



THE HONG KONG  
POLYTECHNIC UNIVERSITY

香港理工大學

Pao Yue-kong Library

包玉剛圖書館

---

## Copyright Undertaking

This thesis is protected by copyright, with all rights reserved.

**By reading and using the thesis, the reader understands and agrees to the following terms:**

1. The reader will abide by the rules and legal ordinances governing copyright regarding the use of the thesis.
2. The reader will use the thesis for the purpose of research or private study only and not for distribution or further reproduction or any other purpose.
3. The reader agrees to indemnify and hold the University harmless from and against any loss, damage, cost, liability or expenses arising from copyright infringement or unauthorized usage.

### IMPORTANT

If you have reasons to believe that any materials in this thesis are deemed not suitable to be distributed in this form, or a copyright owner having difficulty with the material being included in our database, please contact [lbsys@polyu.edu.hk](mailto:lbsys@polyu.edu.hk) providing details. The Library will look into your claim and consider taking remedial action upon receipt of the written requests.

**HIGH-PERFORMANCE 3D CERAMIC  
INTERPOSERS WITH ALUMINUM  
NITRIDE USING GREEN CHEMISTRY  
APPROACH FOR MICROELECTRONIC  
APPLICATIONS**

**KOK WAI HOONG**

**PhD**

**The Hong Kong Polytechnic University**

**2019**

**The Hong Kong Polytechnic University**  
**Department of Industrial and Systems Engineering**

**High-performance 3D Ceramic Interposers with Aluminum  
Nitride using Green Chemistry Approach for  
Microelectronic Applications**

Kok Wai Hoong

A thesis submitted in partial fulfilment of the requirements for  
the degree of Doctor of Philosophy

February 2019

# CERTIFICATE OF ORIGINALITY

I hereby declare that this thesis is my own work and that, to the best of my knowledge and belief, it reproduces no material previously published or written, nor material that has been accepted for the award of any other degree or diploma, except where due acknowledgement has been made in the text.

\_\_\_\_\_ (Signed)

      KOK WAI HOONG       (Name of student)

# Abstract

Thermal management of electronic devices related to heat removal has been a continual challenge since it affects the performance and long term reliability of electronic systems. This heat removal issue is especially crucial for high-performance electronic devices such as 3D Integrated Circuits and all electronic modules where heat dissipating rate is critical under air cooling.

A 3D interposer consists of (i) a substrate with (ii) embedded interconnecting metals to form the functional circuitry. (i) Organic substrate is commonly used but its poor heat dissipation has limited its use in high-performance electronics. As such, organic substrates are commonly replaced with higher thermal conductivity aluminum oxide ( $\text{Al}_2\text{O}_3$ ) ceramic substrates. However, for advanced applications that require a higher heat dissipation performance, aluminum nitride (AlN) is a possible choice to replace  $\text{Al}_2\text{O}_3$  due to its higher thermal conductivity by nature. (ii) The common interconnecting metals for 3D interposer are copper but it might not be suitable for ceramic interposer due to its low melting temperature. Molybdenum (Mo) is a refractory metal that can withstand high-temperature and therefore is a good candidate for co-sintering with AlN ceramic to form the 3D ceramic interposer. Besides, the current process of producing 3D ceramic interposers involves multiple steps that require extensive use of solvents, which is costly and not environmental-friendly. Therefore, a simpler and greener processing technology is much needed, and additive manufacturing could be developed to

replace the current process technology.

The aim of this work is to develop a high-performance 3D ceramic interposer with AlN ceramic substrates and Mo interconnecting metal for microelectronic applications using additive manufacturing, an alternative processing technology based on green chemistry approach.

First part of this research work focused on the green chemistry approach using eco-friendly material to form AlN ceramic substrate. A sustainable natural protein, ovalbumin is used to produce high thermal conductivity AlN ceramic substrates. AlN substrate with bimodal particle size distribution (1:1 mixture of 0.5  $\mu\text{m}$  and 1  $\mu\text{m}$  AlN) was found to produce its highest thermal conductivity value of 21 W/mK after sintering for 6 hours at 1600°C, compared to a thermal conductivity of 0.2 W/mK for the organic substrate.

In the second part, Mo metal was developed using the same gelcasting process like AlN ceramics with ovalbumin as the gelcasting monomer. The sintering of the Mo gelcast for 6 hours at 1600°C produces Mo metal with an electrical resistivity of  $4.1 \times 10^{-4} \Omega \cdot \text{cm}$ , slightly lower than copper plate ( $3.3 \times 10^{-4} \Omega \cdot \text{cm}$ ) but is sufficient for most of the applications. The XRD result shows only the presence of pure Mo metal phase and the oxide phases are not seen. This result shows that treating Mo powder with stearic acid forms a protective layer that allows gelcasting of Mo using aqueous-based monomer, ovalbumin.

The final part of this research adapted an additive manufacturing approach, called direct gelcast 3D printing, to print multi-materials by design that forms the

green body of 3D interposer from the CAD system directly. It was confirmed that multi-material that consists of AlN ceramic and Mo metal can be printed concurrently and co-sintered at 1600°C to produce high-performance functional 3D ceramic interposer. The product can power up a light emitting diode (LED), demonstrating the functionality of 3D ceramic interposer.

Overall, this research work has successfully developed an eco-friendly process technology by incorporating 3D printing to produce multi-materials including ceramics, metal or a mixture thereof, directly from the CAD system. The overall result also shows the use of a natural protein with minimum waste as the core processing component. The technology is versatile, allowing combinations of compatible materials to be co-produced, be recycled, and enables in-situ production of multi-materials using a simple process.

# Publications arising from the thesis

## Journal papers:

1. WH Kok, Winco K.C. Yung, Desmond TC Ang (2018), Green gelcasting of aluminum nitride using environmental sustainable ovalbumin natural binder, *Journal of the Australian Ceramic Society*, Volume 55, Issue 1, pp 169-177, March 2019. DOI: 10.1007/s41779-018-0222-3
2. WH Kok, Winco K.C. Yung, Desmond TC Ang, Non-toxic gelcasting of molybdenum using an environmentally sustainable low-cost natural protein monomer, *Academia Journal of Scientific Research* (Accepted. To be published)
3. WH Kok, K.H. Cheung, Winco K.C. Yung, Desmond TC Ang (2018), Direct gelcast3D Printing of Multi-material AlN Interposer and Mo, *Journal of Engineering Research and Application*, Vol. 8, Issue 9 (Part -IV) Sep 2018, pp 25-31. DOI: 10.9790/9622-0809042531
4. WH Kok, Winco K.C. Yung, Desmond TC Ang, Eco-friendly direct gelcast 3D Printing for multi-layer ceramic application, submitted for publication to *Journal of Material Processing Technology*.



## **Conferences:**

1. WH Kok, Winco K.C. Yung, Desmond TC Ang (2016), Characterization of AlN Green Parts by Gelcasting with Egg-protein. Paper presented at the 2nd *International Congress on Technology - Engineering & Science (ICONTES)*, 28-29 July, 2016, Kuala Lumpur, Malaysia, p168.
2. WH Kok, Winco K.C. Yung, Desmond TC Ang (2018), Direct 3D Printing of Aluminum Nitride Using Ovalbumin As The Natural Binder. Paper presented at the *14<sup>th</sup> International Ceramics Congress, CIMTEC 2018*, 4-8 June 2018, Perugia, Italy, p85.

## **Award**

PolyU Micro Fund 2016 Entrepreneurship Award with a grant of HK\$ 120,000 in recognition of outstanding business proposition for “Heat Dissipation Solutions for Advance Electronics”.

# Acknowledgements

I am greatly grateful to my supervisor, Professor Dr. Winco K.C. Yung, Professor of the Department of Industrial and Systems Engineering, for his constant guidance, support, and encouragement for the entire duration of my PhD study. The project is very difficult and requires a lot of hard work but it is an invaluable experience for my research. Without his guidance, this thesis could not be completed.

I am also deeply grateful to my co-supervisor Dr. Desmond T.C. Ang, visiting scholar from School of Physical & Mathematical Science SPMS-CBC, Nanyang Technology University, Singapore for his constant guidance, encouragement and support throughout the whole period of my PhD study.

I would also deliver my sincere gratitude to my colleagues, Dr. Henry Choy, Mr. Ran Bi, Mr. Huang Junfeng, Dr. Karpagam Subramanian, Ms. Ting Yu, Ms. Lida Zhang, Mr. Kenneth Cheng, Mr. Chan Cho Yee and all the staff in PCB Center of the Hong Kong Polytechnic University. I am especially thankful to Associate Professor Dr. Wang Yuhong, Mr. Wen Yong, Associate Professor Dr. Thomas Lee Ming Hung and Ms. He Qijin that supported the instrument used in this study. Also, I owe sincere thanks to my friends Ms. Li Chen, Ms. Elsie, Ms. Titi, Dr. Minaketan Tripathy and Dr. Sushri Tripathy for their valuable ideas and advice.

Finally, I greatly appreciate all the support given by my beloved family, my wife, Ms. Hiap Poh Tin, my sons Mr. Kok Zhi Wei and Mr. Kok Zhi Sheng, and my

siblings. I would never successfully complete this work without their understanding and patience.

# Table of contents

<b>Abstract .....</b>	<b>ii</b>
<b>Publications arising from the thesis .....</b>	<b>v</b>
<b>Acknowledgements .....</b>	<b>vii</b>
<b>Table of contents .....</b>	<b>ix</b>
<b>List of figures .....</b>	<b>xiii</b>
<b>List of tables .....</b>	<b>xvii</b>
<b>List of abbreviations.....</b>	<b>xix</b>
<b>Chapter 1 Introduction .....</b>	<b>1</b>
1.1 Microelectronic packaging .....	1
1.1.1 CMOS scaling .....	2
1.1.2 Challenges in CMOS scaling.....	3
1.1.3 Potential technologies beyond CMOS.....	6
1.2 High-performance microelectronic packaging .....	7
1.2.1 Advantage of using 3D integration technology .....	11
1.2.2 Types of 3D integration .....	12
1.3 Interposer technology .....	14
1.3.1 Drivers for interposer .....	16
1.3.2 Thermal management issue .....	17
1.3.3 Interposer substrate materials .....	19
1.4 Additive manufacturing (AM).....	20
1.5 Research challenges (More details are given in Section 2.5).....	26
1.6 Research objectives .....	28
1.7 Organization of this thesis .....	29
<b>Chapter 2 Literature review .....</b>	<b>31</b>
2.1 Interposer materials .....	31
2.1.1 Low-CTE organic interposer .....	33
2.1.2 Silicon interposer with TSV .....	34
2.1.3 Glass .....	38
2.1.4 Polycrystalline silicon .....	38
2.1.5 Ceramics .....	40
2.1.6 Concluding remarks.....	43

2.2	Ceramics substrate fabrication .....	44
2.2.1	Ceramic filler fabrication techniques .....	48
2.2.2	Gelcasting .....	49
2.2.3	Green gelcasting technology .....	52
2.2.4	Concluding remarks.....	53
2.3	Interconnecting material for the interposer .....	54
2.3.1	Copper metallization .....	55
2.3.2	Refractory metals.....	58
2.3.3	Gelcasting .....	59
2.3.4	Concluding remarks.....	61
2.4	Multi-layer ceramics process for interposer .....	61
2.4.1	High-temperature co-fired ceramics (HTCC) .....	62
2.4.2	Low-temperature co-fired ceramics (LTCC).....	63
2.4.3	Conventional multi-layer ceramic process .....	64
2.4.4	Additive manufacturing (AM) process .....	64
2.4.5	Concluding remarks.....	69
2.5	Research gaps .....	69
<b>Chapter 3 Research methodology .....</b>		<b>76</b>
3.1	Green gelcasting of AlN ceramic substrate .....	76
3.1.1	Green chemistry approach in developing ceramic processing technology .....	77
3.1.2	High thermal conductivity ceramic powders.....	79
3.1.3	Gelcasting of the ceramic substrate .....	80
3.1.4	Characterization and testing .....	81
3.2	Interconnecting metal compatible with AlN green gelcasting process .....	82
3.2.1	Compatibility of copper (Cu) with AlN green gelcasting process .....	83
3.2.2	Compatibility of molybdenum (Mo) with AlN green gelcasting process .....	84
3.2.3	Characterization.....	84
3.3	Direct gelcast 3D printing to produce 3D ceramic interposer .....	85
3.3.1	Parameters for direct gelcast 3D printing .....	86
3.3.2	Direct gelcast 3D printing of multi-material 3D ceramic interposer....	87
3.4	Characterization instrument and testing .....	87
3.4.1	Density balance .....	87
3.4.2	Thermogravimetric (TGA) characterization.....	88
3.4.3	X-ray diffraction (XRD) characterization .....	89
3.4.4	Flexural strength test .....	92
3.4.5	Thermal conductivity measurement .....	93
3.4.6	Scanning electron microscope (SEM) characterization .....	94

3.4.7 Four-point probe electrical characterization.....	96
3.4.8 Dynamic light scattering (DLS) .....	97
3.4.9 Dynamic shear rheometer (DSR) .....	99
<b>Chapter 4 Green gelcasting of aluminum nitride (AlN) ceramics substrate.....</b>	<b>102</b>
4.1 Introductory remarks .....	102
4.2 Experimental.....	104
4.2.1 AlN feedstock preparation .....	104
4.2.2 Casting.....	106
4.2.3 Characterization.....	107
4.3 Results and discussions .....	109
4.3.1 AlN/ovalbumin ceramic slurry .....	109
4.3.2 Gelcasted AlN ceramics .....	110
4.3.3 AlN particle size mixing.....	115
4.3.4 Ceramic particle size mixing .....	125
4.3.5 Effect of AlN solid loading.....	127
4.4 Concluding remarks.....	130
<b>Chapter 5 Interconnecting metals compatible with the AlN green gelcasting</b>	
<b>process.....</b>	<b>132</b>
5.1 Introductory remarks .....	132
5.2 Experimental.....	134
5.2.1 Preparation of metal slurry .....	134
5.2.2 Metal forming process .....	136
5.2.3 Characterization.....	137
5.3 Results and discussions .....	139
5.3.1 Gelcasting of copper (Cu) powder .....	139
5.3.2 Gelcasting of molybdenum (Mo) powder .....	142
i) Mo/ovalbumin gelcasting slurry .....	142
ii) Thermal analysis of Mo/ovalbumin green body .....	145
iii) Evaluation of sintered Mo metal.....	148
5.4 Concluding remarks.....	152
<b>Chapter 6 Direct gelcast 3D printing of 3D ceramic interposer for</b>	
<b>microelectronic application .....</b>	<b>154</b>
6.1 Introductory remarks .....	154
6.2 Experimental.....	156
6.2.1 AlN/ovalbumin gelcasting paste.....	156
6.2.2 Recycling of AlN/ovalbumin ceramics .....	157

6.2.3 Metal/ovalbumin gelcasting paste preparation .....	157
6.2.4 3D printing process and sintering .....	158
6.2.5 Characterization.....	160
6.3 Results and discussions .....	160
6.3.1 Direct gelcast 3D printing of AlN ceramics .....	160
i) Direct gelcast 3D printing parameters .....	160
ii) Direct gelcast 3D printing of AlN/ovalbumin.....	165
iii) Recycling of AlN ceramics .....	168
6.3.2 Direct gelcast 3D printing of 3D ceramic interposer.....	170
i) AlN Ceramic substrate with Cu as the interconnecting metal .....	170
ii) Hybrid SiAlN ceramic substrate with Cu as interconnecting metal	172
iii) 3D printing of functional AlN ceramic interposer .....	181
6.4 Concluding remarks.....	185
<b>Chapter 7 Conclusions and suggestions for future research .....</b>	<b>187</b>
7.1 Overall conclusions .....	187
7.2 Significance of the study .....	193
7.3 Suggestion for future research.....	195
<b>Appendix I: Thermal conductivity measurement report.....</b>	<b>198</b>
<b>Appendix II: Ceramic sample information .....</b>	<b>204</b>
<b>References.....</b>	<b>211</b>

# List of figures

Figure 1.1 Types of advanced electronic packaging

Figure 1.2 List of 23 key technology areas

Figure 1.3 Growth of electronic packaging technologies

Figure 1.4 Potential markets for 3D IC

Figure 1.5 Progresses to TSV 3D-SiP Era

Figure 1.6 3D integration in electronic packaging

Figure 1.7 Types of 3D electronic packages

Figure 1.8 Interposer configurations

Figure 1.9 Comparison of IC packages (a) conventional (b) with interposer.

Figure 1.10 Schematics of different interposer structures

Figure 1.11 Application for 3D interposers: (a) logic-memory, (b) die breakup, and (c) heterogeneous integration

Figure 1.12 Potential thermal solutions for electronic packages

Figure 1.13 Generic process of CAD to part, showing all eight stages

Figure 2.1 First silicon interposers without TSVs

Figure 2.2 TSV silicon interposer cross-section

Figure 2.3 Xilinx advanced logic with silicon interposer

Figure 2.4 Polymer-lined TSV

Figure 2.5 Through-silicon hole (TSH) using air as a dielectric liner

Figure 2.6 Potential for cost-reduction

Figure 2.7 Fabrication process for (a) 2-metal layer and (b) 4-metal layer RDL

Figure 2.8 Cross-section of a 4-metal layer RDL

Figure 2.9 Flow chart of ceramic substrate fabrication



Figure 2.10 Process flow of a typical gelcasting process

Figure 2.11 Copper-oxygen phase diagram

Figure 2.12 DBC process flow for oxygen-bearing ceramic.

Figure 2.13 Active metal brazing (AMB) process flow

Figure 2.14 Multi-layer ceramics fabrication process

Figure 2.15 Proposed 3D Printing for LTCC

Figure 2.16 Barriers, challenges and promising directions for AM

Figure 2.17 Layout of the research study

Figure 3.1 Experimental approaches in developing high thermal conductivity AlN ceramic substrate based on green chemistry approach.

Figure 3.2 Ceramic gelcasting process (a) conventional (b) ovalbumin

Figure 3.3 Schematic of unimodal and bimodal distributions

Figure 3.4 Metal molds for gelcasting of AlN

Figure 3.5 Debinding and sintering profile for AlN ceramic substrate

Figure 3.6 Experimental approaches in developing interconnecting metals that are compatible with the AlN green gelcasting process

Figure 3.7 Experimental approach in direct gelcast 3D printing of 3D ceramic interposer

Figure 3.8 Arrangement of components in a TGA

Figure 3.9 Bragg's law

Figure 3.10 Flexural test with 3-point configuration

Figure 3.11 Thermogram plot of laser pulse vs time of a typical ceramic sample

Figure 3.12 Interaction of highly speed electrons on the surface

Figure 3.13 Four-point resistance measurements

Figure 3.14 Schematic of a typical DLS system

Figure 3.15 Schematic of a DSR system

Figure 4.1 Gelcasting of AlN ceramics with ovalbumin monomer

Figure 4.2 AlN/ovalbumin gelcasting slurry

Figure 4.3 Gelcasted AlN ceramics

Figure 4.4 Debinding and sintering profile of AlN/ovalbumin ceramics

Figure 4.5 AlN powders: (a) 0.1  $\mu\text{m}$ , (b) 0.5  $\mu\text{m}$ , (c) 1.0  $\mu\text{m}$ , and (d) 5.0  $\mu\text{m}$

Figure 4.6 Viscosity of AlN/ovalbumin slurry with different particle size

Figure 4.7 XRD pattern of AlN/ovalbumin gelcast

Figure 4.8 TGA analysis of AlN/ovalbumin gelcast

Figure 4.9 Effect of nanoparticles on the thermal conductivity of AlN ceramics

Figure 4.10 Taguchi Main Effects Plot obtained using Minitab 14

Figure 4.11 Effect solid loading on the viscosity AlN/ovalbumin slurry

Figure 5.1 Process flow of the gelcasting of Cu powder using ovalbumin protein

Figure 5.2 Process flow of the gelcasting of Mo powder using ovalbumin protein

Figure 5.3 Debinding and sintering profile for Cu/ovalbumin gelcast

Figure 5.4 Debinding and sintering profile for Mo/ ovalbumin gelcast

Figure 5.5 XRD pattern of the Cu/ovalbumin gelcast

Figure 5.6 Agglomeration of Cu after sintering at 1600°C

Figure 5.7 Rheology of Mo/ovalbumin slurry for 0.1  $\mu\text{m}$ , 1  $\mu\text{m}$  and 3  $\mu\text{m}$  Mo particle size

Figure 5.8 TGA analysis of Mo/ovalbumin gelcast

Figure 5.9 XRD pattern of Mo/ovalbumin gelcast

Figure 5.10 SEM images (5,000x) of sintered Mo sample with an average particle size of  
a) 0.1  $\mu\text{m}$ , b) 1  $\mu\text{m}$  and c) 3  $\mu\text{m}$

Figure 6.1 Preparation of AlN/ovalbumin paste

Figure 6.2 Recycling of AlN/ovalbumin (green state)

Figure 6.3 Preparation of metal paste

Figure 6.4 Thick paste extruder (ZMorph 2.0)

Figure 6.5 Debinding and sintering temperature profile of HTCC (Mo-AlN) Interposer

Figure 6.6 Voxelizer software for 3D printing

Figure 6.7 Show schematics of 3D printing of AlN ceramics using paste prepared with ovalbumin natural protein

Figure 6.8 3D printed structures of AlN ceramics

Figure 6.9 3D printing of AlN on a hot surface without hot air blow

Figure 6.10 3D printing of AlN on a hot surface with hot air blow

Figure 6.11 (a) AlN green state, (b) crushed using mortar and pestle, (c) 3D printed of recycled AlN

Figure 6.12 3D printing of recycled AlN

Figure 6.13 3D printing using recycled AlN for the fourth time

Figure 6.14 Sintering of AlN-Cu at (a) 1400°C and (b) 1250°C

Figure 6.15 Effect of Si/AlN ratios on thermal conductivity after sintering at 1000°C.

Figure 6.16 REO effect on thermal conductivity and sintering temperature

Figure 6.17 Effect of sintering temperature on the density of hybrid SiAlN (20/80) ceramics

Figure 6.18 Co-sintering of hybrid SiAlN (20/80) ceramic substrate with Cu interconnect at 1000°C

Figure 6.19 Voxelizer software showing the CAD drawing

Figure 6.20 Direct gelcast printing of multi-material using the CAD design

Figure 6.21 Direct gelcast printing sequence using Voxelizer software

Figure 6.22 Actual sample printed using direct gelcast 3D printing of multi-layer materials (a) AlN interposer, (b) Mo interconnect, (c) AlN interposer on top of Mo interconnect.

Figure 6.23 Functional interposer with AlN with embedded Mo conducting line (a) before applying current (b) LED turn on when applying DC current

# List of tables

Table 1.1 IC junction temperature limits

Table 1.2 Working principles of AM processes

Table 2.1 Material properties of different interposer materials

Table 2.2 Physical properties of possible materials in interposer applications

Table 2.3 Melting points of ceramics for application as electronic substrates.

Table 2.4 Types of processes used to form ceramic substrates

Table 2.5 Comparison of gelcasting with other ceramic forming processes

Table 2.6 Properties of refractory metals

Table 3.1 Comparison of conventional gelcasting monomer, acrylamide and ovalbumin

Table 4.1 Mixing of AlN powder with different particle sizes

Table 4.2 Thermal conductivity measurement of AlN ceramics

Table 4.3 Repeatability of thermal conductivity measurement

Table 4.4 The density, porosity, shrinkage and thermal conductivity results of different AlN particle mixing

Table 4.5 SEM images of AlN ceramics with different particle size mixing

Table 4.6 SEM images of Unimodal and Bimodal AlN particle mixing

Table 4.7 Composition of samples to study the effect of multimodal distribution

Table 4.8 Thermal conductivity result for multi-modal distribution

Table 4.9 Effect of solid loading on thermal conductivity on AlN ceramics

Table 5.1 Gelcasting of different types of Cu powder

Table 5.2 Parameters of sintered Mo samples

Table 6.1 The 3D Printing parameters

Table 6.2 Physical parameters of AlN sintered samples

Table 6.3 AlN green sample prepared using a different paste mixing method

Table 6.4 Comparison of flexural strength of sintered AlN prepared using virgin and recycled AlN ceramics

Table 6.5 Gelcasting of pure Cu powder

Table 6.6 Parameters of hybrid SiAlN ceramics after sintered at 1000°C

Table 6.7 Effect of REOs and sintering temperature on hybrid SiAlN (20/80) ceramics

Table 6.8 Sintering of hybrid SiAlN ceramics at 1200°C

Table 6.9 Parameter optimization for hybrid SiAlN ceramics

Table 6.10 Sintering of hybrid SiAlN (20/80) ceramics at 1600°C

# List of abbreviations

3D	: Three Dimension
3D IC	: Three Dimensional Integrated Circuit
3D WLP	: Three dimensional Wafer Level Packaging
AlN	: Aluminum Nitride
AM	: Additive Manufacturing
AMB	: Active Metal Brazing
ASIC	: Application Specific Integrated Circuit
BCB	: Benzocyclobutene
BEOL	: Back End of Line
BGA	: Ball Grid Array
BN	: Boron Nitride
BSA	: Bovine Serum Albumin
CAD	: Computer Aided Design
CAGR	: Compound Annual Growth Rate
CMOS	: Complementary Metal Oxide Semiconductor
CMP	: Chemical Mechanical Polishing
CNT	: Carbon Nanotube
CNTFET	: Carbon Nanotube Field Effect Transistors
COP	: Coefficient of Performance
CoWoS	: Chip on Wafer on Substrate
CSP	: Chip Scale Package
CT	: Computer Tomographs
CTE	: Coefficient of Thermal Expansion
CVD	: Chemical Vapor Deposition
DBC	: Direct Bonded Copper

DDM	: Direct Digital Manufacturing
DP	: Direct Printing
DRAM	: Dynamic Random Access Memory
DRIE	: Deep Reactive Ion Etching
EDA	: Electronic Design Automation
EQCA	: Electrical Quantum Dot Cellular Automata
FDM	: Fused Deposition Modeling
FEOL	: Front End of Line
FET	: Field Effect Transistors
FI-WLP	: Fan In Wafer Level Packaging
FO-WLP	: Fan Out Wafer Level Packaging
FPGA	: Field Programmable Gate Array
HEMA	: 2-hydroxyethyl methacrylate
HPL	: High-performance Loader
HSU	: Heat Storage Unit
HTCC	: High-temperature Co-fired Ceramic
I/O	: Input/ Output
IBM	: International Business Machines
IC	: Integrated Circuit
ICDD	: International Centre for Diffraction Data
IEEE	: Institute of Electrical and Electronic Engineers
IGBT	: Insulated Gate Bipolar Transistor
ILD	: Interlayer Dielectric
IoT	: Internet of Things
ITRI	: Industrial Technology Research Institute
ITRS	: International Technology and Roadmap for Semiconductors
LM	: Layer Manufacturing

LTCC	:	Low Temperature Co-fired Ceramic
MAM	:	Methacrylamide
MBAM	:	N,N',-Methylenebisacrylamide
MCM	:	Multi Chip Modules
MCP	:	Multi Chip Package
MEMS	:	Micro Electro Mechanical Systems
MF	:	Microfluidic
MQCA	:	Magnetic Quantum Dot Cellular Automata
MTCC	:	Medium Temperature Co-fired Ceramic
MtM	:	More than Moore
Nichrome	:	Nickel-Chrome
NIST	:	National Institute of Standards and Technology
NWFET	:	Nano Wire Field Effect Transistors
ORNL	:	Oak Ridge National Laboratory
PBO	:	Polybenzoxazole
PCB	:	Printed Circuit Board
PCM	:	Phase Change Material
PDA	:	Personal Digital Assistant
PDF	:	Powder Diffraction File
PoP	:	Package on Package
PWB	:	Printed Wiring Board
RCA	:	Radio Corporation of America
RDL	:	Redistribution Layer
RF	:	Radio Frequency
RM	:	Rapid Manufacturing
RP	:	Rapid Prototyping
RT	:	Rapid Tooling



RTD	:	Resonant Tunneling Diodes
SEJ	:	Single Electron Junctions
SEM	:	Scanning Electron Microscope
SFF	:	Solid Freeforming
SiC	:	Silicon Carbide
SiP	:	System in Package
SL	:	Stereolithography
TC	:	Thermal Conductivity
TCE	:	Thermal Conductivity Enhancer
TGA	:	Thermo Gravimetric Analyzer
TIM	:	Thermal Interface Material
TPV	:	Through Package Via
TSH	:	Through Silicon Holes
TSMC	:	Taiwan Semiconductor Manufacturing Company
TSV	:	Through Silicon Via
UV	:	Ultra Violet
V/V	:	volume/ volume
WB	:	Wire Bonding
WL-CSP	:	Wafer Level Chip Scale Package
WLOptic	:	Wafer Level Optics
WPC	:	Wheat Protein Concentrate
XRD	:	X-ray Diffraction

# Chapter 1 Introduction

The electronics industry is one in which each new generation of product provides performance improvement at a lower cost. As a consumer, we are spoiled into believing that each generation of electronic devices will be smaller, faster, cheaper, more reliable, with better functionality and connectivity.

## 1.1 Microelectronic packaging

The constant progress in electronic hardware performance can be attributed to the continued miniaturization of ICs (Integrated Circuits), according to Moore's Law (Moore 1965), which was articulated by Gordon Moore in 1965, that predicted the doubling of transistor's density every year. He predicted that the trend would continue to at least 1975 reaching 64,000 transistors; a bold prediction since ICs only had about 65 transistors at the time.

Today, predictions of future advancements are based on two different concepts of scaling: (1) "More Moore", which continues the scaling theory by further reducing the vertical and horizontal physical dimensions and (2) "More than Moore", which emphasizes the progression and expansion of function (Dennard, Gaensslen, et al. 1974). The scaling trend, which has continued for more than four decades, is predicted to hit its limit by 2022 when 3-dimensional integrated circuits (3DICs) will be fueling the next stage of development. With the scaling trend coming to an

end, the ever-increasing pressure for miniaturization of electronic devices has resulted in the need to go into the third dimension at both device and package levels (Haron and Hamdioui 2008).

Several different packaging technology platforms have emerged in the past couple of decades and enabled the growth of Advanced Packaging. Figure 1.1 highlights the various technology platforms available today, ranging from well-established technologies such as flip chip, fan-in, and 3D wafer-level packaging (WLP), to newer platforms such as embedded dies in printed circuit board (PCB)/ laminate, Fan-out WLP, WL Optics, and 3D and 3D IC (Baron 2012).

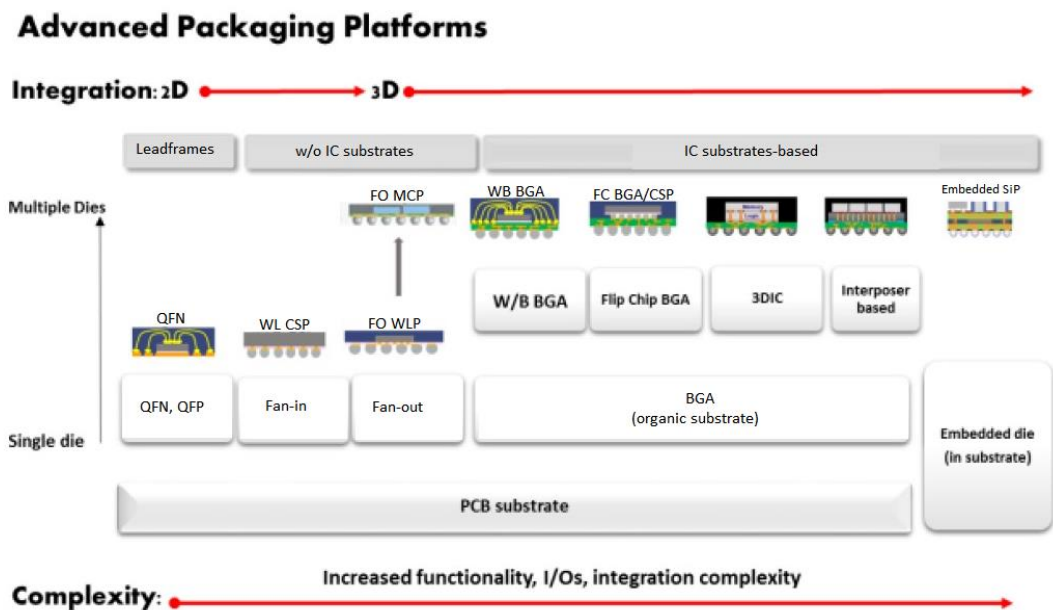


Figure 1.1 Types of advanced electronic packaging (Garrou 2015).

### 1.1.1 CMOS scaling

The consistent increase in CMOS transistor density has been crucial for the

development of silicon chip technology over the past 40 years. Nevertheless, the semiconductor industry only began applying these theories a decade later to CMOS transistors that enable integration of even more transistors into a single chip (Chen 2006).

The scaling of CMOS transistors has overcome many challenges, but the ITRS (ITRS 2007) predicts that it will reach its limit at 22nm by the end of this century (Iwai 2004) when the boundaries in quantum mechanics are reached. Other factors, such as economics, could also cause the end of CMOS transistor advancements (Chen 2006).

#### 1.1.2 Challenges in CMOS scaling

NZB Haron and S.Hamdioui address five categories of challenges that could hinder the future utilization of CMOS technology (Haron and Hamdioui 2008):

##### i) Physical challenges

The miniaturization of devices increases current leakages that reduce the performance of CMOS devices. A channel length of 100nm or less will require a 3nm thick oxide layer which only consists of a few atomic layers (Taur 2002), and is approaching the vital limits of 1 to 1.5nm (Isaac 2000). This oxide layer will cause gate leakage due to quantum-mechanical tunneling that increases exponentially with reduced thickness of the oxide layer; and will cause damage leading to fallible of the dielectric (Tyagi 2007).

## ii) Material challenges

New materials that can give better electrical insulation and conduction are required as this scaling trend will affect the chip reliability. Current materials used; Silicon (Si), Aluminum (Al), Silicon dioxide (SiO<sub>2</sub>) and Copper (Cu) will not be useful if the inherent limits of their physical parameters are exceeded. These parameters include relative dielectric constant ( $\epsilon$ ), carrier saturation velocity ( $v_s$ ), carrier mobility ( $\mu$ ), breakdown field strength ( $E_c$ ) and conductivity (Wang, Han, et al. 1998). Iwai (Iwai 2004) reported that the thinning of the SiO<sub>2</sub> layer could cause a reliability issue. Cu, when used as interconnecting wires, have issues with open defects even though it is less prone to electromigration compared to Al. Tyagi et al. (Tyagi 2007) reported that high-permittivity (high-k) materials can replace silicon SiO<sub>2</sub> as the material for gate dielectric as it can minimize the current leakage problem due to the thinner dielectric being used. However, these materials are not stable as its property will change under the high-temperature environment (Buchanan 1999).

## iii) Power-thermal challenges

As the number of transistors per-unit-area increases, it not only creates higher power but also more heat. Lundstrom et al. (Lundstrom 2003) reported that a 10 kW microprocessor will produce 1 kW/cm<sup>2</sup> of heat. This thermal issue can be observed from the development of Intel® microprocessor, where its power density grows with every new generation, and the projection is that processors will be too hot when it reaches the end of the scaling trend. This issue has caused Intel® to cancel its 4

GHz Pentium® 4 in 2001 and alternatively introduce the dual-core processors.

iv) Technological challenges

As microelectronic devices miniaturize, the lithography techniques are also reaching its limit because the required resolution will be below the wavelength of light. Lithography techniques are used for patterning CMOS transistors onto the wafer and are one of the main drivers of transistor scaling. However, it is now facing difficulty in controlling the gap between the mask and wafer, and uniformity of exposure. The other problems include wafer thinning by polishing has difficulty maintaining a uniform thickness and the problem with mask reliability (Gupta and Kahng 2003). Fabrication of features smaller than the wavelength of light requires careful design and the complexity will increase the cost of the masks (Skotnicki, Hutchby, et al. 2005).

Most recent technologies reported 9nm devices using a 248 nm radiation, but the process is not economically feasible due to the complexity of the processes. An alternative patterning method that does not use radiation, nanoimprint lithography can be a good alternative, but further development is required to improve its feasibility at use (Pease and Chou 2008).

v) Economic challenges

The cost of production increases with technology advancement due to the higher cost of equipment, facilities (clean room), and the growing complexity of lithography process that can reach a point of not economically viable to manufacture (Isaac 2000). Conventionally, IC fabrication for a 90nm process will require more

than 35 masks and 700 steps; and the same trend also applies to DRAM (Trybula 2003). In order to be economically viable, each mask set will need 3000 to 5000 wafers, 1500 wafers for microprocessors, and 500 wafers or less for SICs and SOCs (Harriott 2001). Besides, the mask will be one of the significant cost contributors when the feature size goes below the exposure wavelength as more design revisions will be required and lower productivity output from each mask (Hillenius 2004). This problem has led to the sharing of the wafer production facility and other cost reduction strategy such as alliances between companies, university participation with government funding.

Another major cost contributor is the testing cost, as smaller size circuits are vulnerable to defects and will need thorough quality testing, which in turn will require more complex test method being developed with possibly more steps and longer time (Benware 2004).

### 1.1.3 Potential technologies beyond CMOS

The alternative devices that could replace CMOS are categorized into three classes (Cotofana 2009):

i) Electrical nanodevices

Electrical nanodevices use either ballistic transport for an electron to travel free of resistivity, or tunneling, where electron pass through potential energy barrier using the quantum-mechanical process, or electrostatic, which uses the interaction between electrons in an electric field (Zhirnov, Hutchby, et al. 2005). Examples

include CNTFET (carbon nanotubes field-effect transistors), SEJ (single electron junctions), RTD (resonant tunneling diodes), NWFET (semiconductor nanowire field-effect transistors), and EQCA (electrical quantum-dot cellular automata) (Goser, Glösekötter, et al. 2004, Zhirnov, Hutchby, et al. 2005).

ii) Magnetic nanodevices

Magnetic nanodevices use the magnetic or spin phenomena, instead of electrons for the transport of data. It uses either magnetic dipole or the spin-polarized electrons transportation for manipulation of the signal. Examples of the system in this category include MQCA (magnetic quantum dot cellular automata) and spin-FET (spin field-effect transistors) (Zhirnov, Hutchby, et al. 2005).

iii) Mechanical nanodevices

Mechanical nanodevices use the mechanical changes of polymer structure according to the input signal. An example includes molecular memory (Cotofana 2009).

## **1.2 High-performance microelectronic packaging**

3D integration has advantages of shorter and therefore faster connections; higher density of interconnections, higher bandwidth, lower power consumption and better flexibility in integration compared to conventional techniques, such as system-on-chip (SoC) (Beica 2015).



<b>Market Category</b>	<u>Life Sciences</u> (21)	<u>Computational Biology and Bioinformatics</u> (22)	<u>Medical Robotics</u> (23)
<b>Technologies</b>	<u>Computer Vision and Pattern Recognition</u> (20)		
	<u>Machine Learning and Intelligent Systems</u> (19)		
	<u>Big Data and Analytics</u> (18)		
	<u>Natural User Interfaces</u> (16)		<u>3D Printing</u> (17)
	<u>High-Performance Computing</u> (13)	<u>Cloud Computing</u> (14)	<u>Internet of Things</u> (15)
	<u>Networking &amp; Interconnectivity</u> (11)		<u>Software-Defined Networks</u> (12)
<b>Human Capital</b>	<u>Massively Online Open Courses</u> (4)		
	<u>Open Intellectual Property Movement</u> (2)		<u>Sustainability</u> (3)
	<u>Security Cross-Cutting Issues</u> (1)		

Figure 1.2 List of 23 key technology areas (Milojičić 2013).

The 3D integration is a “More than Moore” approach which is a new paradigm for the semiconductor package advancements. In a report by IEEE entitled “2022 Report”, 3D IC is one of the key technologies that could disrupt the industry. Figure 1.2 shows the 23 technologies that could potentially change the world by 2022 in which 3D IC together with 3D printing was listed (Milojičić 2013).

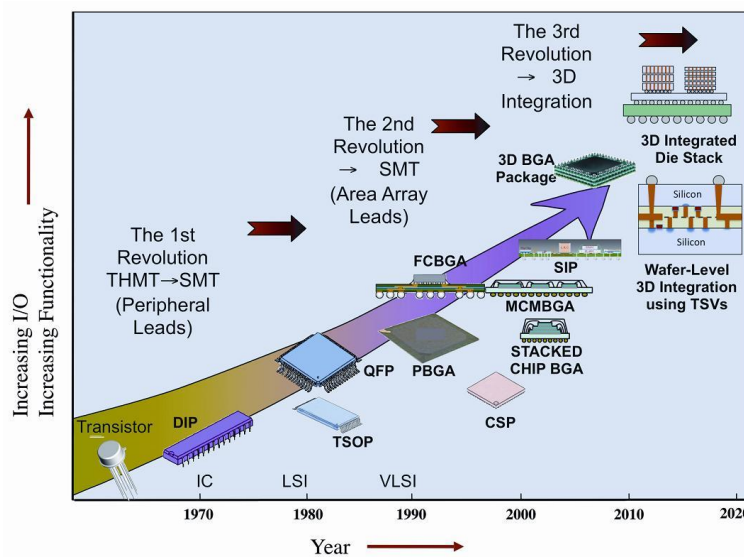


Figure 1.3 Growth of electronic packaging technologies (Gotro 2018).

High growth of the packaging technologies in the coming six years (18% CAGR in wafer units), will be driven primarily by 3D packaging technologies such as 3DIC, embedded technologies, 3D system in package (SiP), fan-out wafer level packaging (FOWLP) and interposer (Figure 1.3).

3D IC is expected to be introduced in various products, and each has its specifications, challenges, and individual roadmaps (Hellings, Scholz, et al. 2015). High volume adoption is expected for mobile products, smartphones, tablets, followed by computers, consumer market, gaming, and industrial products and lower volumes for automotive and medical packages (Figure 1.4).



Figure 1.4 Potential markets for 3D IC (Baron 2012).

However, it has its own set of challenges and heat removal from integrated circuits (ICs) is the limiting factor. This heat removal problem is critical because vertically integrated packages are now required to remove heat from multi-layers

rather than form a single plain (Shorey and Lu 2016). Interposer technology using 3D, also known as 3D interposers could be the key to 3D IC technology as it can provide better yield, better heat dissipation, and improved electrical performance. Substantial effort has been made that include conventional interposers such as FOWLP to lower the cost (Yoon, Tang, et al. 2013).

The 3D integration technology is a significant technology development for “More than Moore” technology as the transistor scaling is coming to an end (Kondo, Kada, et al. 2016). New nanodevices to replace CMOS such as carbon nanotubes, spintronics, and molecular switches will not be ready for another 10 – 15 years and therefore, 3D integration technology is currently the most viable solution.

Figure 1.5 illustrates the historical development for IC packaging technologies that show technological revolution that happens every ten years, since the 1970s, that started with a 3D system in package (3D-SiP), to the current through-Si-via (TSV) for 3D IC.

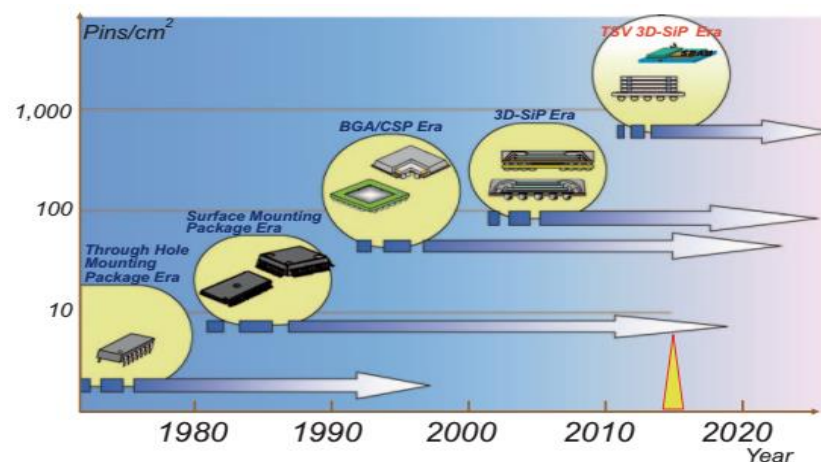


Figure 1.5 Progresses to TSV 3D-SiP Era (Kondo, Kada, et al. 2016).

TSV is an integration of the silicon wafer process in the semiconductor packaging process that allows the electron to pass through the silicon wafer (or chip). “More than Moore” also represents the evolution of packaging technology in addition to solving the limitation of “More Moore” (Kondo, Kada, et al. 2016). Comparison of 3D integration packaging technologies using conventional wire bonding (WB) and TSV is shown in Figure 1.6.

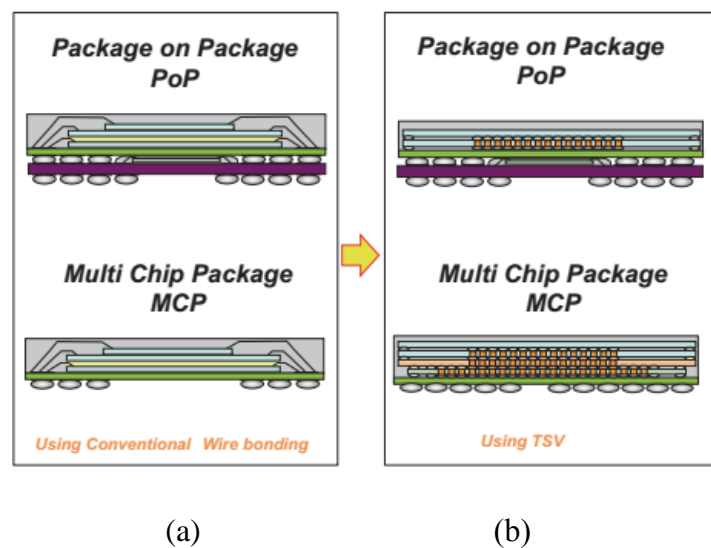


Figure 1.6 3D integration in electronic packaging (Kondo, Kada, et al. 2016).

### 1.2.1 Advantage of using 3D integration technology

The solution to achieving similar improvement aligning with Moore’s Law (without reducing the size), is by having more functions performed by individual ICs separately and integrated into a single package in 3D packaging structures. These TSVs can reduce the interconnect distance and increase the density of interconnection by 1000 times as compared to the conventional wire bond (WB)

method. The flexibility of 3D integration architecture is not limited to ‘like’ technologies and therefore allows the possibility of unique functionalities by the combination of ICs and micro-electro-mechanical systems (MEMS) devices (Guenin 2009).

### 1.2.2 Types of 3D integration

The 3 categories of the 3D package are shown in Figure 1.7.

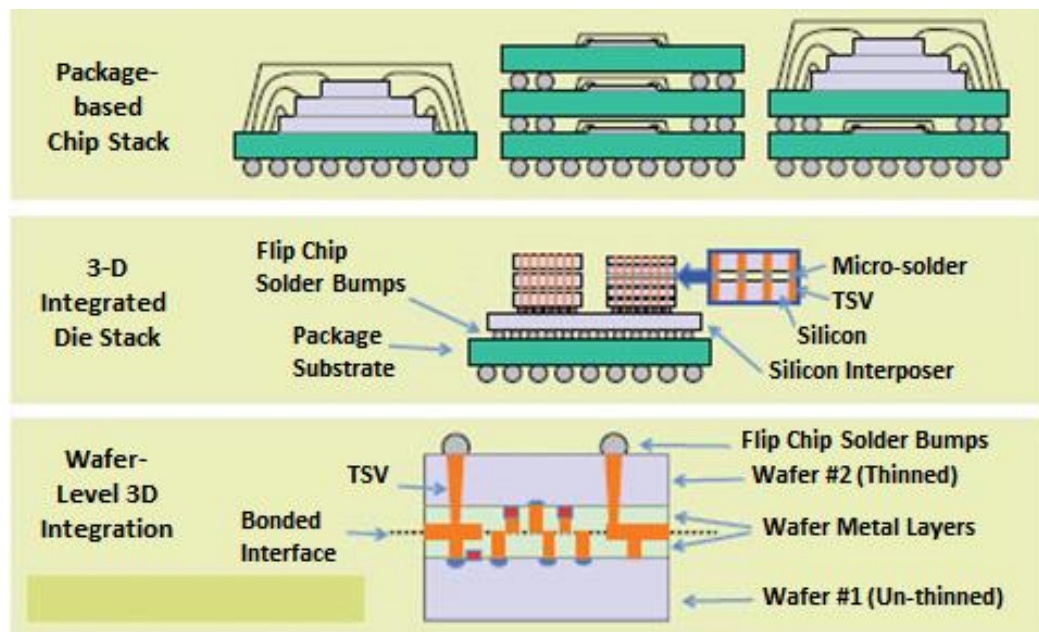


Figure 1.7 Types of 3D electronic packages (Guenin 2009).

#### i) Package-based chip stack

In package-based chip stack, also known as package-on-package (PoP), either wire bond or solder balls or a combination of both is used for connecting the third dimension. It is currently used in stacked memory chips and in mobile applications where compactness is essential. The current wire bonded (WB) packages can use

thinned chips, as thin as 50 $\mu$ m and stack up to 5 levels high. Even though a PoP design could not match the compactness of stacked chips but it has the advantage that each chip can be tested individually before stacking for better quality control and signal integrity (Guenin 2009).

ii) Integrated 3D chip stack

The integrated 3D chip stacks with TSVs, to provide the electrical connection between each chip, will be assembled in standard wafer-level packaging foundries. The process will start with the formation of TSVs by using laser ablation or deep reactive ion etching (DRIE) and followed by insulator coating on the side walls. The conductor will then be deposited, and C4 bump, low profile solders or thermo-compression bonds are used for electrical interconnection between adjacent chips. This integration can achieve higher densities (three orders of magnitude) compared to package-based stacking technology that can accommodate a larger number of chips within a space with better signal integrity (Bernstein, Andry, et al. 2007).

iii) Wafer-level 3D integration chip

The ultimate type of integration is the 3D wafer-level integration, where multi-layer wafers with circuit interconnections were fabricated using high-resolution CMOS technology. It incorporates the standard CMOS fabrication process to construct 3D wafer, one layer at a time, sequentially bonding the wafers and then followed by forming the TSVs for use in electrical connection. In a 45nm CMOS technology, a pitch of 400nm for the TSVs can be fabricated and this integration can maintain or even exceed the rate of Moore's Law scaling trend (considering

volumetric efficiency at the system level). This TSV development also has significant cost reduction because interconnections are made parallel at the wafer level (Guenin 2009).

### 1.3 Interposer technology

An interposer is a substrate that connects the top and bottom side of a die with electrical interconnections. It has a through-via connection, TSVs or through-package vias (TPVs) and has multiple layers of wiring called redistribution layers (RDLs). The motivations for using 3D interposers are the better yield, improved electrical performance, and lower cost.

The 3D interposers are quite similar to silicon multichip module technology but with the addition of TSV. Figure 1.8 shows the possible configuration of interposer either by TSV or by RDL to connect the chips.

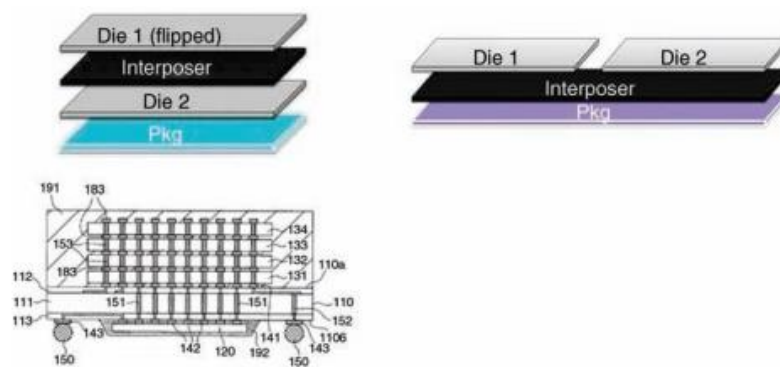


Figure 1.8 Interposer configurations (Guenin 2009).

The side-by-side connection is a better thermal solution as a heat sink can be attached for cooling (Garrou, Koyanagi, et al. 2014).

Figure 1.9 shows the comparison of the IC package for (a) conventional configuration and (b) with an interposer. Typical wiring includes connecting the ICs at the top to (ball grid array (BGA) or printed wiring board (PWB)) to the bottom of the package. The use of interposer, with interconnections along the same plane, allows for a side-by-side connection that replaces the bridge between the pitch of the chip and the board. Interposers typically have a thickness of 50 – 300  $\mu\text{m}$  and pitch of 10-200  $\mu\text{m}$  (V. Sundaram 2014).

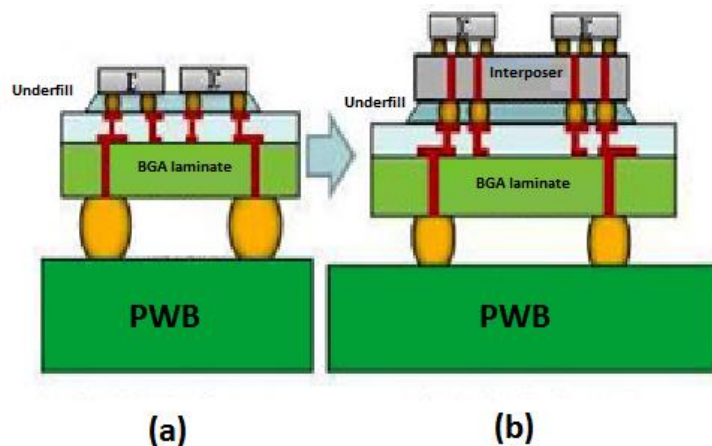
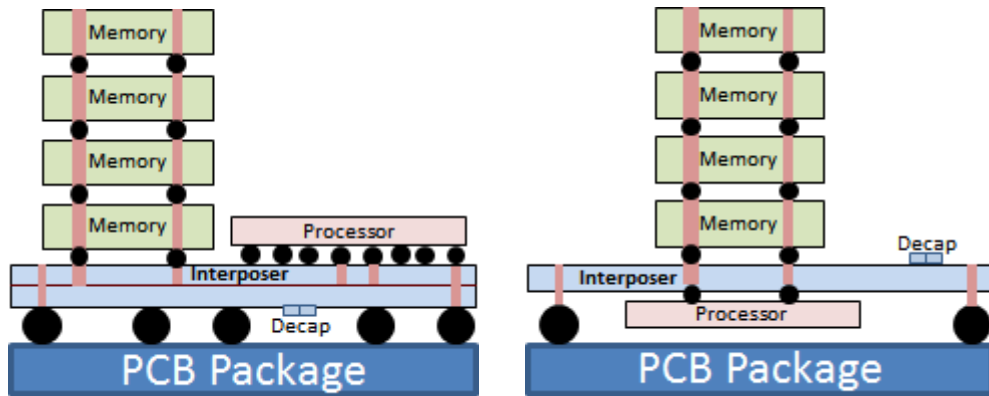


Figure 1.9 Comparison of IC packages (a) conventional (b) with interposer (Garrou, Koyanagi, et al. 2014).

Figure 1.10a shows the “side-by-side” configuration in which multiple ICs are placed at the side of each other with interconnection to the top of the interposer. Alternatively, ICs can be on both sides of the interposer connected using TSVs as shown in Figure 1.10b. Larger interposers are attached to the BGA, and smaller interposers are mounted directly to the motherboard.

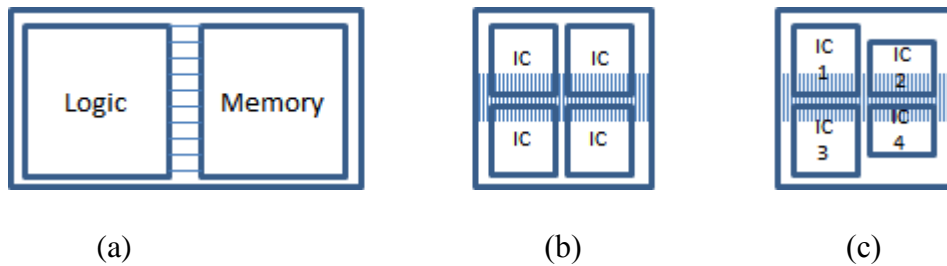




(a) (b)  
 Figure 1.10 Schematics of different interposer structures (Guenin 2009).

### 1.3.1 Drivers for interposer

The main advantage of the interposer technology is the ability to increase I/O density that matches the scaling trend. High-density fine-pitch interposers will be required when the IC nodes go down to 7nm, I/O pitch of 10-50  $\mu\text{m}$  for the ICs and, 100-150  $\mu\text{m}$  for the IC packages. The demand for 3D interposer solutions is due to the issues faced by 3D IC stacking on heat dissipation, lack of testing procedure and low yield. Figure 1.11 shows the three types of applications for high-density interposers: (a) logic-to-memory bandwidth improvements; (b) “die breakup” and (c) multiple heterogeneous IC integration (Garrou, Koyanagi, et al. 2014).



(a) (b) (c)  
 Figure 1.11 Applications for 3D interposers: (a) logic-memory, (b) die breakup, and (c) heterogeneous integration (Garrou, Koyanagi, et al. 2014).

### 1.3.2 Thermal management issue

Thermal management will not be an issue for low-power applications such as low-power flash memory but can create significant impact for applications that require higher power such as processors. The increase in temperature reduces the semiconductor carriers' mobility and increases the resistivity of metal that increases the time constant. Therefore, the supply voltages have to be increased to maintain the clock frequency to be constant, which will cause additional power dissipation and temperature increment (Jain and Ramanathan 2006).

The component lifetime (L) reduces exponentially with temperature (T) in accordance with the Arrhenius law:

$$L(T) = A(e^{\frac{Ea}{kT}} - 1) \quad (1.1)$$

where A is the system-specific constant, Ea is the activation energy and k is the Boltzmann's constant. Therefore, raising the temperature by 20°C will cause a reduction of system lifetime by a factor of two. Table 1.1 shows the maximum allowable junction temperatures for ICs.

Table 1.1 IC temperature limits (Sweetland, M. and Lienhard, J.H 2003).

Application	Temperature limit (°C)
High-performance logic	95
Low-performance logic	125
Memory devices	125
Handheld devices	125
Automotive electronics	175

The heat dissipation in 3D packages involves all layers sharing a common thermal path and therefore, the compounding effects of aggregated power and long-distance results in a large thermal gradient. This 3D package is different from conventional side-by-side multi-chip packages where heat transported to the heat sink is proportional to the number of devices in their thermal path.

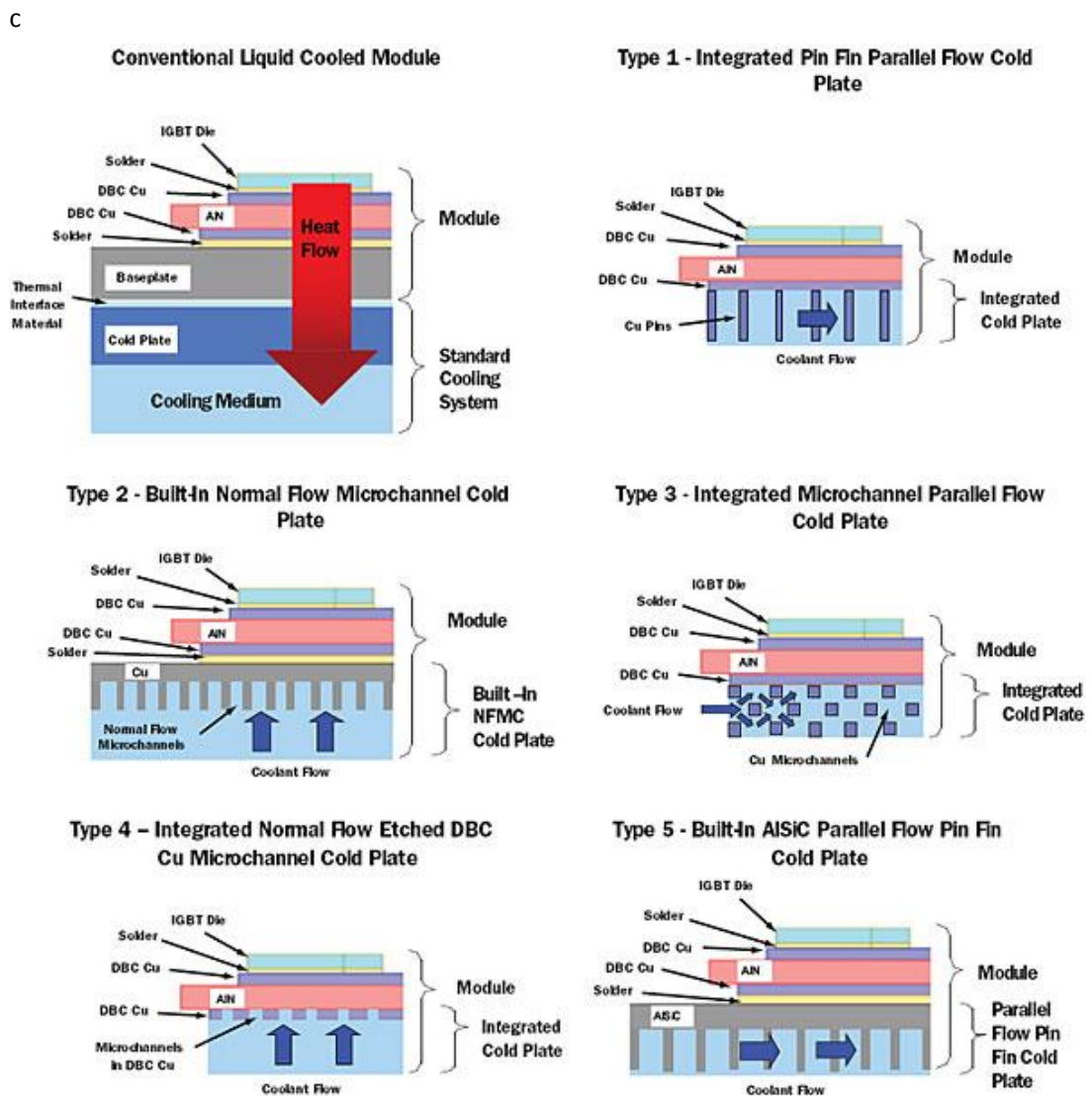


Figure 1.12 Potential thermal solutions for electronic packages (Moore and Shi 2014).

Figure 1.12 describes some of the methods to tackle the challenge of thermal management in electronic packages. All these methods use some form of heat sink related technology to dissipate the heat at the cost of space (Moore and Shi 2014).

### 1.3.3 Interposer substrate materials

The materials used for interposer should be robust, chemically inert, high thermomechanical reliability, high interconnection density, and high thermal conductivity. Currently, the most widely used materials are organics due to its good reliability and cost but it has the problem with line density because the high coefficient of thermal expansion (CTE) that does not match the silicon die and low thermal conductivity.

Silicon interposers is popular for application in 3DIC due to its good dimensional stability but it has low electrical resistivity that can cause signal loss and current leakage for sensitive applications like radio frequency (RF). Glass has high electrical resistivity, good dimensional stability, adjustable CTE, chemically inert but has low thermal conductivity and therefore less effective in heat dissipation. Heat dissipation capability, i.e. thermal conductivity, has become important in high-performance electronics to overcome the thermal management issue.

S. Cho et al. (Cho, Joshi, et al. 2013) has compared and found a notable difference in the temperature profile around chips placed on the interposer with two different materials, silicon, and glass. The silicon interposer has a uniform surface

temperature, but glass interposers show temperature drop across the chip boundary and interposer boundary. This is because the silicon interposer has higher thermal conductivity ( $\sim 150$  W/mK) compared to glass ( $\sim 1$  W/mK).

The maximum temperature value for glass interposer is also higher ( $129^{\circ}\text{C}$ ) than silicon interposer ( $75^{\circ}\text{C}$ ). However, silicon has a higher electrical resistivity of  $6.40 \times 10^2 \Omega \cdot \text{m}$  (at  $20^{\circ}\text{C}$ ) compared to glass,  $10 \times 10^{10}$  to  $10 \times 10^{14} \Omega \cdot \text{m}$  (at  $20^{\circ}\text{C}$ ), and therefore not suitable for telecommunication applications due to the problem of signal loss (Bansal and Doremus 2013).

Multi-layer ceramic packages could be a viable alternative due to their characteristics such as good mechanical strength, high reliability, higher thermal conductivity, matching CTE, hermeticity, and cost. Aluminum nitride (AlN) will be the suitable material due to its high thermal conductivity (theoretical  $320$  W/mK) and high electrical resistivity (resistivity  $\sim 10^{13} \Omega \cdot \text{cm}$ ), lower dielectric constant ( $8.0 - 9.2$  at  $1$  MHz), higher dielectric strength ( $14-27$  kV/mm) and lower CTE that matches silicon ( $\sim 4 \times 10^{-6}/^{\circ}\text{C}$ ) (Watari, Hwang, et al. 1996).

#### **1.4 Additive manufacturing (AM)**

The traditional manufacturing approach is based on mass-production to produce large-quantity of identical parts using a complicated assembly process that results in material wastage and higher cost for low-volume production. The mass-customization approach of additive manufacturing (AM) process is based on direct

part production from the design data that allows the creation of complex geometric structures without part-specific tooling such as molds and dies.

Additive manufacturing (AM), also known as 3D printing, prints layers after layers of materials on top of each other to form a three-dimensional (3D) structure directly from the 3D model data. The standard definition, according to ASTM F2792-12a for AM, is the “process of joining materials to make objects from 3D model data, usually layer upon layer, as opposed to subtractive manufacturing methodologies, such as traditional machining” (Standard 2012). This first AM technology, stereolithography (SLA), developed in 1986 by Charles Hull has led the development of other techniques such as powder bed fusion, fused deposition modeling (FDM) and inkjet printing. The key advantage of the AM technique is its high freedom to design that allows fast prototyping with mass customization, waste minimization and fabrication of highly complex structures (Ngo, Kashani, et al. 2018).

#### 1.4.1 Principles of additive manufacturing (AM)

The AM process starts with the creation of mathematical layer information and followed by physical layer model using mathematical layer information (Prakash, Nancharaih, et al. 2018), and can further be broken into 8 steps shown in Figure 1.13 (Gibson, Rosen, et al. 2010).

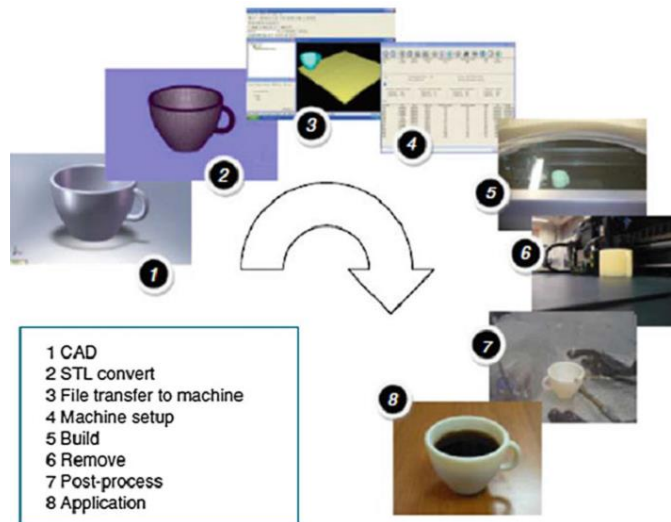


Figure 1.13 Generic process of CAD to part, showing all eight stages (Gibson, Rosen, et al. 2010).

#### Step 1: Computer Aided Design (CAD)

All AM parts start from a software model (CAD) with detailed geometry description and output in 3D solid representation.

#### Step 2: STL format

The 3D CAD files are then converted to the STL file formats that are readable by AM machines.

#### Step 3: File transfer to AM machine

The STL file with the corrected size, position, and orientation of build was sent to the AM machine.

#### Step 4: AM machine setup

Like all machines, AM machines have to be properly configured to the building parameters.

#### Step 5: Build

The parts are then built in the AM machines automatically. Only superficial monitoring of machine is needed, such as ensuring no errors due to material shortage, and software glitches.

#### Step 6: Remove

After the products are built, they will be removed from the AM machine for the next process. This may include the removal of safety interlocks.

#### Step 7: Post-process

Depending on the AM process, additional post process such as cleaning and supporting feature removal might be required.

#### Step 8: Application

Parts are now ready to be used after some additional treatment such as priming and painting.

### 1.4.2 Types of AM processes

The working principles of AM processes can be categorized based on the starting material as shown in Table 1.2.

#### 1) Liquid

Stereolithography (SLA), developed by Charles Hull in 1986 was the first commercial AM technology (Jacobs 1992). It uses the principle of ultraviolet (UV) light to solidify liquid photosensitive resin into a solid. The 3D structure was built by scanning the UV light onto a layer of resin to solidify it, followed by the stage descending to allow a fresh layer thickness of resin to cover it. The UV light will



then scan the top of the fresh resin to solidify another layer, and this process continues until the final 3D structure is formed. An alternative to SLA, digital micromirror device (DMD) that uses light exposure to cure a whole layer of photo-curable polymer and is faster and cheaper compared to SLA (Sun, Fang, et al. 2005).

Table 1.2 Working principles of AM processes (Guo and Leu 2013)

State of starting material	Process	Material preparation	Layer creation technique	Phase change	Typical materials	Applications
Liquid	SLA	Liquid in vat	Scanning by laser or light	Polymerization by light exposure	Resin curable by UV	Prototyping, casting, soft tool
	MJM	Liquid in jet	Ink-jet printing	Polymerization by light exposure	Acrylic and wax curable by UV	Prototyping, casting
	RFP	Liquid in nozzle	Droplet deposition	Freezing to solidify	Water	Prototyping, casting
Filament / Paste	FDM	Polymer filament	Extrusion	Cooling to solidify	Thermoplastics, waxes	Prototyping, casting
	Robo casting	Liquid paste	Extrusion	-	Ceramic paste	Prototyping, parts
	FEF	Paste	Extrusion	Cooling to solidify	Ceramic paste	Prototyping, parts
Powder	SLS	Powder in bed	Scanning by laser	Partial melting	Thermoplastics, metal, ceramic	Prototyping, casting, parts
	SLM	Powder in bed	Scanning by laser	Melting	Metal	Tools, parts
	EBM	Powder in bed	Scanning by electron beam	Melting	Metal	Tools, parts
	LMD	Powder in nozzle	Laser melting	Melting	Metal	Tools, parts
	3DP	Powder in bed	Printing by binder	-	Polymer, Metal, ceramic, other powders	Prototyping, casting
Solid sheet	LOM	Laser cutting	Adhesion of sheets	-	Paper, plastic, metal	Prototyping, casting

Multi-jet modeling (MJM) (Chua, Leong, et al. 2010) uses multiple nozzles to dispense UV curable ink on demand and followed by a UV lamp to flash on the surface to solidify the polymer, and rapid freeze prototyping (RFP) (Sui and Leu 2003) uses freezing water droplets to build parts layer by layer.

## 2) Filament/ paste

Fused deposition modeling (FDM) (Crump 1991), the most popular AM

process at the moment, uses heat, to slightly melt the plastic filament. The melt filament is then extruded via a nozzle and deposited onto a cooled substrate using a movable head. Robocasting (Cesarano 1997) was developed at Sandia National Laboratories uses an extruder to extrude successful layers of pastes to form 3D parts. An alternative to robocasting, freeze-form extrusion fabrication (FEF) (Huang, Mason, et al. 2005), developed at the Missouri University of Science and Technology (Missouri S&T), uses freezing technique to solidify the aqueous paste.

### 3) Powder

Powder systems use high energy source to solidify powders layer-by-layer using processes such as selective laser sintering (SLS) to partially melt the powder, selective laser melting (SLM) that fully melts the powder, laser metal deposition (LMD) that melts locally deposited powders, and electron beam melting (EBM) that uses electron instead of laser light as the energy source. Another type of powder system, three-dimensional printing (3DP), uses a liquid binder to selectively spray and solidify a layer on the powder bed (Guo and Leu 2013).

### 4) Solid sheet

Laminated object manufacturing (LOM) (Mueller and Kochan 1999) process involves cutting and attaching the solid materials in sheet form.

#### 1.4.3 AM for electronics

Currently, most of the AM processes are limited by the availability of compatible materials. However, recent research interest includes the development of more sophisticated system such as insertion of electronic components into cavities

of fabricated structures, fabrication of functional materials, and embedding solid conductors in polymer substrates using ultrasonic or thermal energy for high-performance electrical interconnect (Espalin, Muse, et al. 2014). Lopes et al. (Lopes, MacDonald, et al. 2012) reported using the hybrid stereolithography (SLA) and direct printing (DP) system to produce 3D structures with embedded electronic circuits in a single-step process. Palmer et al. (Palmer, Jokiel, et al. 2006) reported using SLA with micro-wire electro-discharge machining ( $\mu$ EDM) to produce switches. Wicker et al. (Wicker, Medina, et al. 2004) modified an existing SLA system to produce multiple materials for application in tissue engineering.

### **1.5 Research challenges (More details are given in Section 2.5)**

Heat removal issue in electronics always ranks high among the major technical problems hindering higher data processing speeds. This issue arises because high-temperatures and more substantial thermal gradients affect chip performances and reliability. This problem is worsened in 3D ICs as the requirement now is to remove heat from multi-layer instead of a single plane. Even though the power dissipation per transistor for 3D ICs is smaller, the higher packing densities will cause greater power density that increases the thermal resistance and consequently increase in temperature. Also, the additional integration layer forces heat to travel greater distances that further impede heat dissipation.

Most recent methods of cooling require an additional feature that reduces routing

space and limits the density of interconnections within the interposer. Therefore, there is a need for the interposer material itself to be more efficient in distributing the heat generated from electronic devices and reduce hot spots. High thermal conductivity ceramic materials with low electrical conductivity property will be required to improve the heat dissipation performance of electronic devices.

The common interconnecting metals for interposer are copper but it has a melting point lower than ceramics which make it unsuitable for co-sintering to form the 3D ceramic interposer. Therefore, metals that can withstand high-temperature with good electrical conductivity are required for co-sintering with the ceramic substrate to form the 3D ceramic interposer.

The traditional multi-layer ceramic process for producing ceramic interposers is a multi-step process with extensive use of solvents to form layers of ceramics and interconnect metals that are costly and not environmental-friendly. Additive manufacturing (AM) offers an attractive proposition to this problem as it can build complex-shaped parts with simple steps and minimum post-processing requirements. However, the current AM technology has difficulty in building dense ceramics with superior physicochemical properties.

Also, recently, there is a need for the development of a green process using sustainable materials. This need could be fulfilled using AM process technology, but it will require the integration of different functional materials.

## 1.6 Research objectives

Interposers are crucial to solve the heat dissipation issue faced by advanced electronic devices, but the current interposer material is not able to meet this demand. Besides, the push for greener and environmental-friendly processes has spurred research on the use of alternative materials that are green and sustainable. This study focuses on discovering better interposer materials using a green chemistry approach to produce high-performance 3D interposers that meet the following objectives.

- 1) To study the gelcasting of AlN ceramic substrate using a green chemistry approach.

Aluminum nitride (AlN) is selected for use as the ceramic substrate in the 3D interposer due to its non-toxic nature, high electrical resistivity, high thermal conductivity, and a good coefficient of thermal expansion (CTE). The green chemistry approach using natural protein will be evaluated to produce AlN ceramic substrate with good thermal conductivity. The use of protein ovalbumin as the monomer for gelcasting will be selected as it has many advantages such as no chemical additive needed for the initiation, complete gelation, low amount of binder left in the dried green body (0.6 – 4.0%), non-toxic and biodegradable.

- 2) To study the compatibility of interconnect metals with the AlN green gelcasting process.

3D ceramic interposer consists of the ceramic substrate, in this study, using AlN and interconnects metals to form functional circuitry. In the process for producing

the 3D ceramic interposer, the ceramic substrate and the interconnect metal will be co-sintered to produce the functional circuitry. Therefore, suitable interconnect metals that are compatible with AlN during co-sintering are important to ensure the integrity and performance of the 3D ceramic interposer.

3) To investigate an additive manufacturing (AM) process for multi-material direct printing of 3D ceramic interposer for microelectronic application

The additive manufacturing (AM) process technology produces three-dimensional (3D) structures by directly printing layers of materials on top of each other that correspond to the CAD design. The modified AM process, direct gelcast 3D printing, uses the gelcast slurry for producing complex multi-material 3D structures is an eco-friendly process due to less waste produced and use of sustainable natural protein monomer, ovalbumin, as compared to the subjective manufacturing process. The versatile direct gelcast 3D printing process will allow a high degree of customization tailored to different design requirements of microelectronic devices.

## **1.7 Organization of this thesis**

This thesis explores the possibility of using a green chemistry approach to produce high-performance AlN 3D ceramic interposers for microelectronic applications.

Chapter 1 provides an introduction to the background of the work and objective of this study. Chapter 2 provides a comprehensive review of the current

interposer materials, the ceramic substrate fabrication process, high-density interconnections compatible with ceramics processing, existing methods used for producing multi-layer ceramics and identifies the research gaps in the area. Chapter 3 describes the approach and the methodology used to achieve all the set objectives, including materials, processing equipment and characterization equipment used in this study. Chapter 4 discusses the approach in using green chemistry, natural protein ovalbumin to produce AlN ceramics substrate with good thermal conductivity. Chapter 5 discusses the selection of interconnect metals that are compatible with the green gelcasting process of AlN ceramic substrate. The green gelcasting process to produce copper metal and molybdenum metal was evaluated for its electrical performance and process suitability. Chapter 6 present the versatility of the additive manufacturing process, direct gelcast 3D printing to produce multi-material components directly from the CAD system to produce a functional AlN-Mo 3D ceramic interposer. Finally, chapter 7 outlines the overall conclusion of this study, the significance of this research work and recommendations for future work.

# Chapter 2 Literature review

## 2.1 Interposer materials

Ceramics, alumina was the initial choice of materials for electronic substrates but was replaced by organics due to the limited I/O density and high processing cost of ceramics. Organics is currently the most widely used electronic substrate material worldwide. However, organics are not suitable as interposer materials due to its limited line density caused by their high coefficient of thermal expansions (CTEs) that mismatch with the semiconductor die.

Silicon interposers have good dimensional stability that allows fine-pitch and small TSVs, but their disadvantages include the low electrical resistivity of silicon that causes signal loss and current leakage, especially in sensitive radio frequency (RF) application, and the high cost of processing in the wafer fab at the back-end-of-line (BEOL). Therefore, several alternative interposer materials were being investigated, such as glass (Sukumaran, Bandyopadhyay, et al. 2012) and polycrystalline silicon (Chen, Bandyopadhyay, et al. 2011).

Table 2.1 shows the comparison between various interposer materials evaluated on their electrical, mechanical, thermal, physical and manufacturing viability including cost. Interposer materials should be robust, chemically inert, with high thermomechanical reliability in addition to having high I/O interconnection density. Glass is a good candidate for interposer material as it has high electrical resistivity, available in large panel, good dimensional stability and surface finish, customizable



CTE (3-10ppm/°C), chemically inert, and high thermal stability (V. Sundaram 2014).

However, glass is not good in heat dissipation (low thermal conductivity).

Table 2.1 Material properties of different interposer materials (V. Sundaram 2014).

Characteristic	Materials						
	Ideal Properties	Glass	SC Si	Poly Si	Organic	Metal	Ceramics
Electrical	<ul style="list-style-type: none"> <li>High resistivity</li> <li>Low loss</li> </ul>	√√	X	√	√√	X	√√
Physical	<ul style="list-style-type: none"> <li>Smooth surface finish</li> <li>Large area availability</li> <li>Ultrathin</li> </ul>	√√	√	√√	√	√	√
Thermal	<ul style="list-style-type: none"> <li>High conductivity</li> <li>CTE match with Si</li> </ul>	√	√√	√√	X	√√	√
Mechanical	<ul style="list-style-type: none"> <li>High strength</li> <li>High modulus</li> </ul>	√	√	√	X	√√	√
Chemical	<ul style="list-style-type: none"> <li>Resistance to process chemicals</li> </ul>	√√	√	√	√	X	√
Manufacturable high TPVs	<ul style="list-style-type: none"> <li>Low-cost via formation and metallization</li> </ul>	√	X	√	√	X	X
Cost/mm <sup>2</sup>	<ul style="list-style-type: none"> <li>At 25 μm pitch</li> </ul>	√	X	√	X	X	X

SC Si: Single crystal Si      √√ GOOD      √ FAIR      X POOR  
 Poly Si: Polycrystalline Si

Table 2.2 lists the properties of possible materials that have excellent heat dissipation property for application in interposers. Beryllium Oxide (BeO) has the highest thermal conductivity among the material in the list, but it is not widely used because of the toxicity associated with the BeO powder. Aluminum Nitride (AlN) is identified as promising material as it is an insulator (high electrical resistivity) with excellent heat dissipation ability (high thermal conductivity) and thermal expansion capacity that matches the semiconductor dies (low CTE value).

Table 2.2 Physical properties of possible materials in interposer applications (V. Sundaram 2014).

PHYSICAL PROPERTY	Current Interposer Material			Ceramics								
	Si	Glass	Organic	BeO	AlN	WC	TiB <sub>2</sub>	SiC	BN	Al <sub>2</sub> O <sub>3</sub>	B <sub>4</sub> C	Si <sub>3</sub> N <sub>4</sub>
Thermal Conductivity (W/mK)	149	1.38	0.2-0.8	200-330	170-220	71-121	96	41	30	30	28	27
Thermal expansion coefficient (ppm/°C) (TCE Si: 3.5 - 4 ppm/°C)	3.5-4	0.55-10	50-90	7.4-8.9	4.5	5.9	6.4-9.2	5.12	11.9	6.7	5.54	3.4
Electric resistivity (Ω.cm)	2.3 x 10 <sup>5</sup>	>10 <sup>10</sup>	>10 <sup>14</sup>	>10 <sup>14</sup>	>10 <sup>14</sup>	>10 <sup>14</sup>	>10 <sup>14</sup>	108	>10 <sup>12</sup>	>10 <sup>14</sup>	>10 <sup>14</sup>	1013
Density (g/cm <sup>3</sup> )	2.33	2.2-4	1.76	3.01	3.26	15.6	4.52	3.21	1.9	3.95	2.51	3.31

### 2.1.1 Low-CTE organic interposer

The majority of substrate materials used in the semiconductor packaging today are organic materials. The reason for the popularity of organic materials is because of low-cost, availability, good reliability and general market acceptance. The limitations of standard organic packages are i) limitation in the I/O density because of poor dimensional stability, ii) warpage because of low elastic modulus, iii) poor heat dissipation, and iv) interconnection reliability due to CTE mismatch with semiconductor die (Sunohara, Tokunaga, et al. 2008).

Low-CTE organic was developed to overcome the limitations of traditional organic packages such as mismatch and warpage for use in thinner package applications (Yim, Strode, et al. 2011). By using advanced resins and inorganic fillers, the current low-CTE organics can achieve CTE less than 10 ppm/°C (Amou, Shimizu, et al. 2012).

### 2.1.2 Silicon interposer with TSV

IBM and Bell Labs developed the first silicon interposer in the 1980s, but it was not commercially viable compared to low cost material at that time (Figure 2.1). Silicon interposers are actively being developed to replace organic interposers due to the limitation of I/O density, poor heat dissipation, warpage and mechanical stress of organic interposer as a result of large CTE mismatch (Sunohara, Tokunaga, et al. 2008).

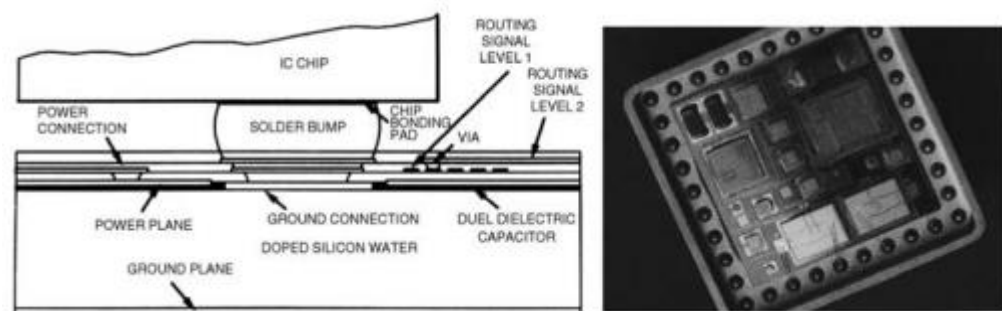


Figure 2.1 First silicon interposers without TSVs (Ho, Chance, et al. 1982).

TSMC developed the first commercial high-density silicon interposers for Xilinx, which is a field-programmable gate array (FPGA) modules that use the chip-on-wafer-on-substrate (CoWoS) technology (Banijamali, Ramalingam, et al. 2011). The process starts with Bosch etching to form blind vias in the thick silicon wafers, the vias are filled with metal using chemical vapor deposition (CVD) technique and BEOL  $\text{SiO}_2$ -Cu damascene processes. A temporary bonding adhesive is used to bond the carrier wafer for backgrinding process to polish and reveal the TSV at the backside. The RDLs on the backside are fabricated using BEOL process or wafer-

level Cu-polymer RDL process. The TSV design rules are shown in Figure 2.2 (V. Sundaram 2014).

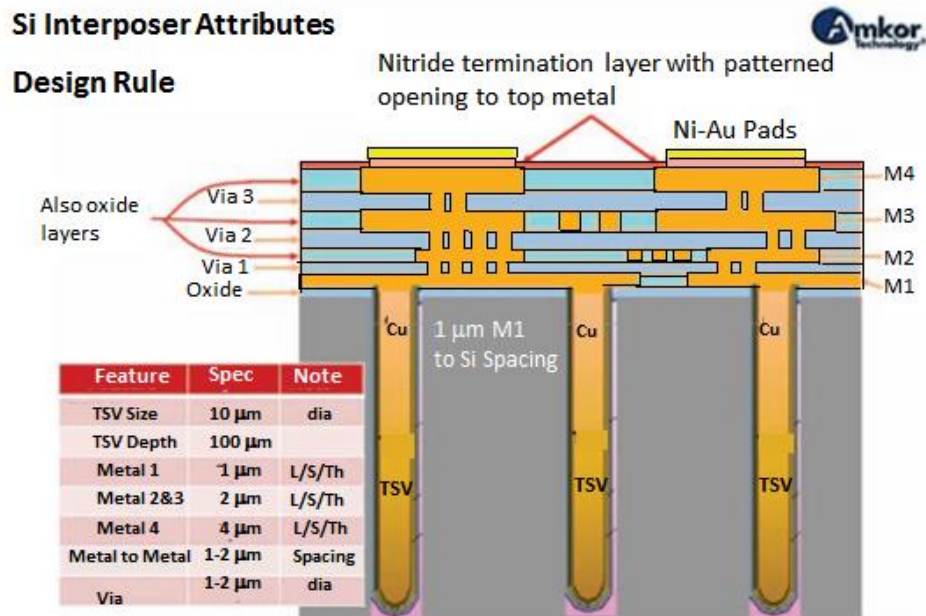


Figure 2.2 TSV silicon interposercross-section (V. Sundaram 2014).

The TSV silicon interposer, with only TSV, is better than the conventional 3D stacking approach because of its manufacturing simplicity that lowers its cost as well. The first commercial application of 3D silicon interposer, Xilinx Virtex 7 made using the TSMC 65nm process, is shown in Figure 2.3 (Kim, Wu, et al. 2011). With the design rules for 65nm, smaller feature size by a factor of 100 – 1000x can be achieved as compared to conventional package substrates, showing high interconnect density can significantly reduce latency and power consumption.

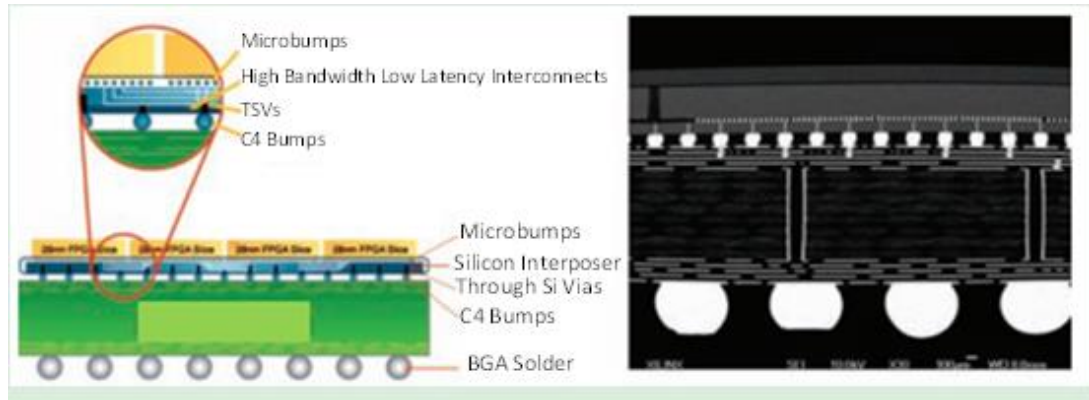


Figure 2.3 Xilinx advanced logic with silicon interposer (Kim, Wu, et al. 2011).

One of the most compelling applications for silicon interposers is the high bandwidth interconnections required in smartphones and tablets. Conventional wire-bonded PoP has a limited bandwidth of less than  $8 \text{ GBs}^{-1}$  but a 3D interposer with a  $2\text{-}4 \mu\text{m}$  line width and  $50 \mu\text{m}$  pitch die-to-interposer interconnections that can achieve a bandwidth over  $25 \text{ GBs}^{-1}$  with 50% power savings.

The current challenges for silicon interposers are the high fabrication cost due to the requirement of a wafer fabrication facility and electrical losses of TSVs due to thin oxide liners. Current research includes the development of alternative liner materials to reduce electrical loss but at the same time, able to improve reliability using a thicker coating. ST Microelectronics has reported that the use of a polymer liner can have a lower electrical loss and higher reliability (Figure 2.4) (Chausse, Bouchoucha, et al. 2009).

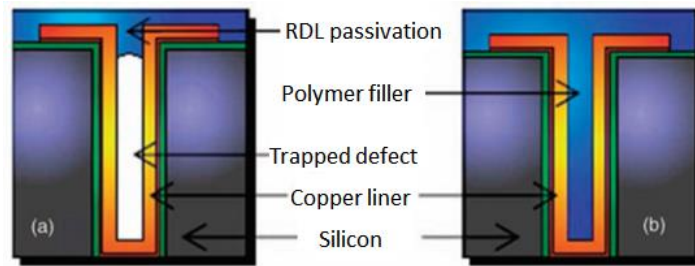


Figure 2.4 Polymer-lined TSV (Chausse, Bouchoucha, et al. 2009).

ITRI Taiwan has developed another alternative approach to reduce electrical loss, by using air as the dielectric material, as shown in Figure 2.5. The through-silicon hole (TSH) structure has copper interconnection made using a modified wire-bonding technique (Wu, Lau, et al. 2012).

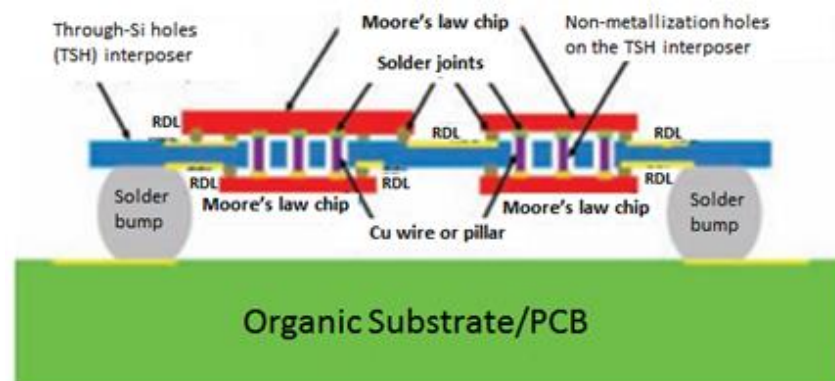


Figure 2.5 Through-silicon hole (TSH) using air as a dielectric liner (Wu, Lau, et al. 2012).

A low-cost interposer is a requirement for applications that are sensitive to cost such as mobile and internet of thing (IoT) devices. Figure 2.6 shows the potential driver that can lower the cost and increase the density of interposers, and large panel processing is the primary reason for cost-reduction.

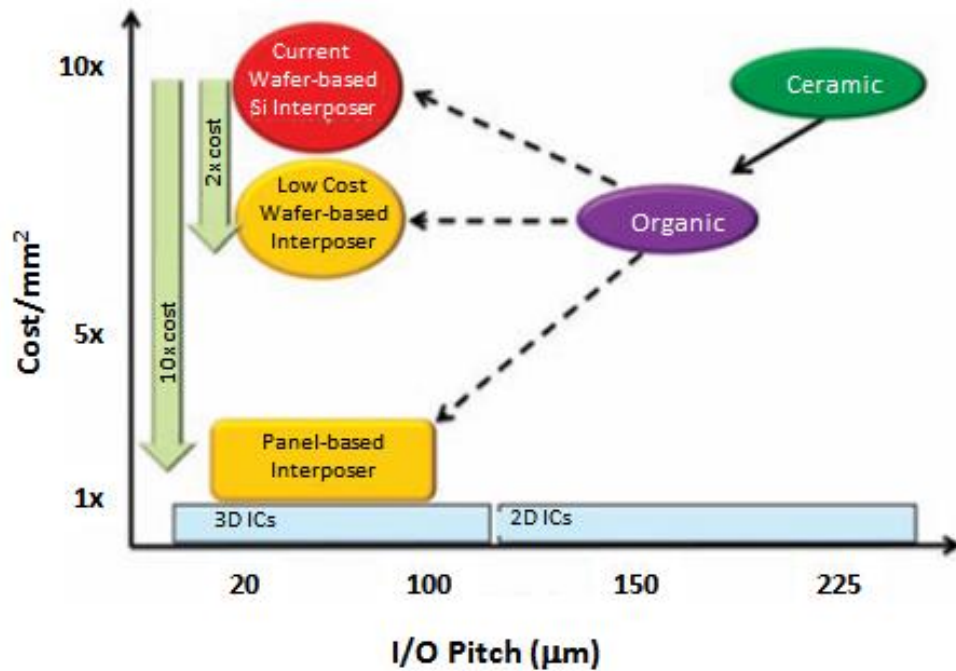


Figure 2.6 Potential for cost-reduction (Tummala and Sundaram 2011).

### 2.1.3 Glass

Glass has several good material properties. It is an insulator and therefore, has a low loss in electrical signal and has high stiffness with less issue on warpage, and a tunable CTE to match the semiconductor die. Also, glass is cost-effective as the glass forming process allows the fabrication in a panel format (Shorey and Lu 2016).

However, the limitation of glass is its low thermal conductivity and brittleness. Besides, it also has some engineering challenges such as sensitivity while handling ultra-thin glass, the production rate of small TPVs and reliability, due to CTE mismatch between copper and glass.

### 2.1.4 Polycrystalline silicon

The development of polycrystalline silicon interposer is to reduce the cost of

silicon interposer (10x cheaper than single-crystal silicon wafers). Figure 2.7 shows the process of fabricating the polysilicon interposers (Chen, Bandyopadhyay, et al. 2011). The method of making the polysilicon interposer starts with ablating the polysilicon surface using a 355nm UV laser to form the TSV, followed by filling the polymer using dry film vacuum lamination. The surface is selectively ablated again to form the inner via, followed by electroless plating of copper to form a thin copper layer before using copper electroplating to build up the conductor layer, where excess Cu will be removed using chemical etching process. The next process is photolithography to form the pattern of the metal traces, plated using electrolytic plating to make RDLs on the silicon interposer. Figure 2.8 shows the cross-section of a four-metal-layer interposer developed by Georgia Tech (Sundaram, Chen, et al. 2012).

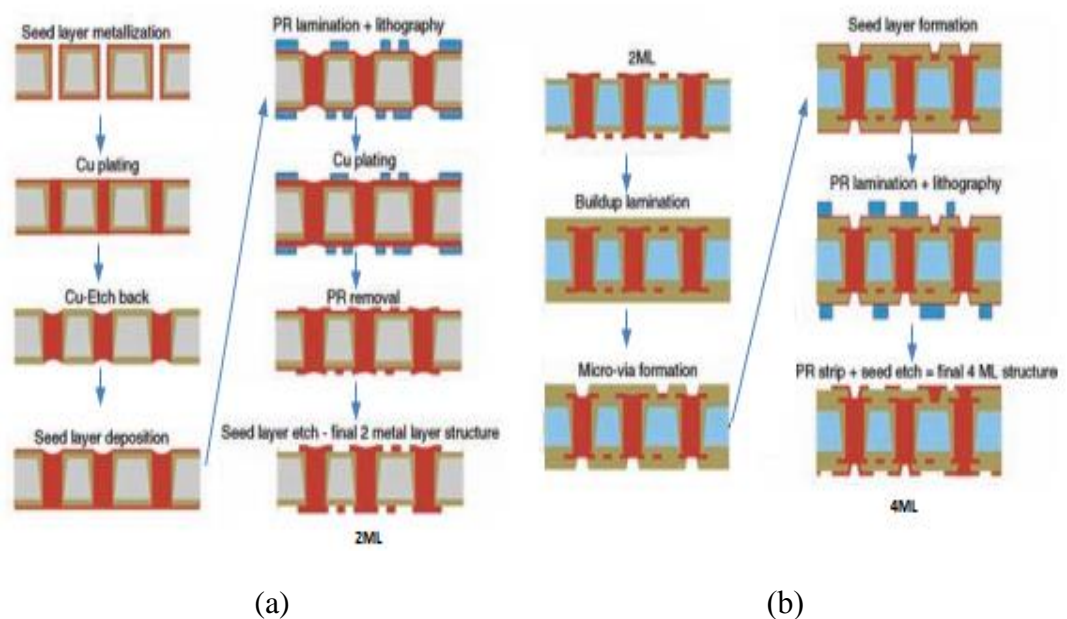


Figure 2.7 Fabrication process for (a) 2-metal layer and (b) 4-metal layer RDL (Chen, Bandyopadhyay, et al. 2011).



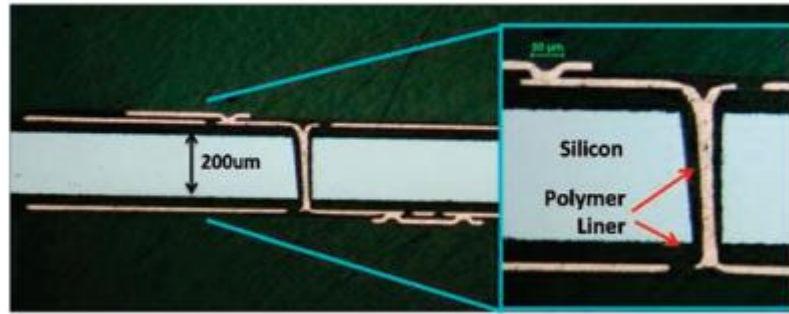


Figure 2.8 Cross-section of a 4-metal layer RDL (Sundaram, Chen, et al. 2012).

The fabrication of 3D ICs will need the costly wafer fabrication facility, typically using the depreciated 200 and 300mm wafer facility that is capable of producing 20 to 50  $\mu\text{m}$  pitch interconnection (vs. 150  $\mu\text{m}$  pitch for 2D ICs). Therefore, the cost of 3D ICs might be too much for smartphone and consumer electronics. Some of the reasons for high cost include lesser availability of interposer, the high cost of BEOL wafer fab process, slow DRIE process and the extra cost of the insulating liner. For polysilicon panels, it can achieve better cost performance as compared to silicon wafer due to the scale-up of up to 10 times higher in throughput, the polysilicon wafer thickness go down to 220  $\mu\text{m}$ , lower cost of producing TPV without DRIE and lower cost of double-sided RDL (Chen, Bandyopadhyay, et al. 2011).

### 2.1.5 Ceramics

Ceramics have long played a significant role in electronics. They continue to be a material that enables the advancement of electronic systems. The key technologies are thick film, thin film, high-temperature co-fired ceramics (HTCC), and low-

temperature co-fired ceramics (LTCC). It is interesting how there is no single one best technology, and all have attributes that make them the right choice for different applications. The prevalence of thick film has continued to grow since the 1970s. While, initially, it was just a low-cost alternative for less critical applications, it has significantly advanced over the years, and processes like etching have allowed for a significant reduction in line widths. Thermally enhanced thick film materials like direct bonded copper (DBC) are an essential part of the construction of isolated gate bipolar transistor (IGBTs) (W.T Minehan 2016).

In power semiconductor packaging, the use of a ceramic substrate as the basic building block for an IGBT is widespread, especially for the current and voltages above a given threshold. Ceramic grinding, lapping, milling, and other finishing processes may be specified to obtain the required flatness, roughness, angle, or other physical attributes. A copper layer applied onto the ceramics needs to ensure a stable metallic interface for solder or sinter attachment of the power die and pads for electrical interconnect, typically wirebonds.

The ceramic material most commonly used for electronic substrates is aluminum oxide ( $\text{Al}_2\text{O}_3$ ), generally known as alumina. While alumina does not provide the highest bulk thermal conductivity value of the various ceramics typically used for these applications, it is available in high-quality grades from many suppliers and is relatively inexpensive. Some important physical properties include excellent electrical characteristics, high strength, reasonable thermal conductivity, and a long and well-proven record for processing, metallization, and reliability in

semiconductor packaging. Alumina is a well-characterized substrate material due to the extent of use of this ceramic across the electronics industry for both high-temperature co-sintering ceramics (HTCC) and low-temperature co-sintering ceramics (LTCC).

Other ceramics utilized for semiconductor substrates for power electronics packaging include silicon carbide (SiC), aluminum nitride (AlN), and silicon nitride (Si<sub>3</sub>N<sub>4</sub>). The AlN ceramic material has high thermal conductivity, and a coefficient of thermal expansion (CTE) value that matches well with silicon and other semiconductor die materials. Therefore, AlN is a suitable substrate material for high power and multichip modules.

Multi-layer co-fired ceramics differ from other ceramic technologies in the way they are processed and manufactured. Conventionally, ceramic powders are formed by tape casting and then printed with conductive metal patterns. The metal/ceramic composite is fired simultaneously to produce a monolithic circuit configuration, hence the term “co-fired.” Alternatively, thick film, thin film and direct bond circuits were deposited on post-fired ceramic substrates. The multi-layer co-fired process developed in the 1960s known as HTCC utilizes alumina “green” tape and refractory metal inks. Later, other materials systems were used including LTCC. The HTCC circuits for alumina and AlN are compatible with refractory metals, such as tungsten and molybdenum, which have attractive electrical performance. The technology has been explored and utilized in many other materials system include inductors, capacitors, solid oxide fuel cells, and batteries. The essential elements of

co-fired materials systems are a) compatible firing temperature; b) compatible thermal expansion of the materials; and c) limited reaction of the materials at firing temperature. Co-fired solutions continue to be developed with ceramics such as silicon nitride (Barlow III and Elshabini 2007).

The HTCC process has highly reliable mechanical strength, good metallization adhesion, good hermeticity, high-temperature performance and the ability to braze at high-temperatures, better than other ceramic packaging technologies. Also, the form factor for multi-layer technology has the greatest latitude. For example, co-fired processing permits the formation of blind vias, as-fired cavities, and high layer count devices. Combining HTCC with other technologies such as thick film, thin film, and complex metal components provide compelling and unique solutions. Materials development of other metal systems such as platinum can expand the application of alumina-based technology (Karbasi, et al. 2013, Chen, Neudeck, et al. 2016).

#### 2.1.6 Concluding remarks

The choice of material for future interposers should take into considering heat dissipation as the critical criteria, and inorganics are currently the only choice. Ceramics, especially AlN-based with unique properties of higher electrical resistivity, higher thermal conductivity, and a CTE that matches with semiconductor dies is found to be a suitable candidate that can be developed as the new interposer material.

## 2.2 Ceramics substrate fabrication

Table 2.3 shows the list of potential ceramic materials that can be used as interposer substrates. All the ceramics in the list have a high melting point of more than 2000°C and therefore, will require high sintering temperatures to make the interposer substrates.

Table 2.3 Melting points of ceramics for application as electronic substrates.

Material	Melting Point (°C)
Silicon Carbide (SiC)	2700
Boron Nitride (BN)	2732
Aluminum Nitride (AlN)	2232
Beryllium Oxide (BeO)	2570
Alumina (Al <sub>2</sub> O <sub>3</sub> )	2000

Figure 2.9 shows the typical process of fabricating ceramic substrates. The initial steps are similar; in which materials were ground to a fine powder with fluxing and binding glasses. In the first fabrication method (Figure 2.9a), organic binder and plasticizers were mixed, and the ball mill is used to grind the slurry and remove agglomerates for consistent mixing. The slurry is then used to form a sheet using tape casting, called green state and then dried to form a roll. Holes and other geometries are then punched to the desired shape and size. The second method (Figure 2.9b) is the same as the first method up to producing the green sheets. The green sheets will then be fired slowly with increasing temperature to allow for full removal of the organics followed by sintering the particles together. In the third method (Figure 2.9c), the difference is that the substrate is formed in a mold which

is under pressure (Sergent and Harper 1995, Barlow III and Elshabini 2007).

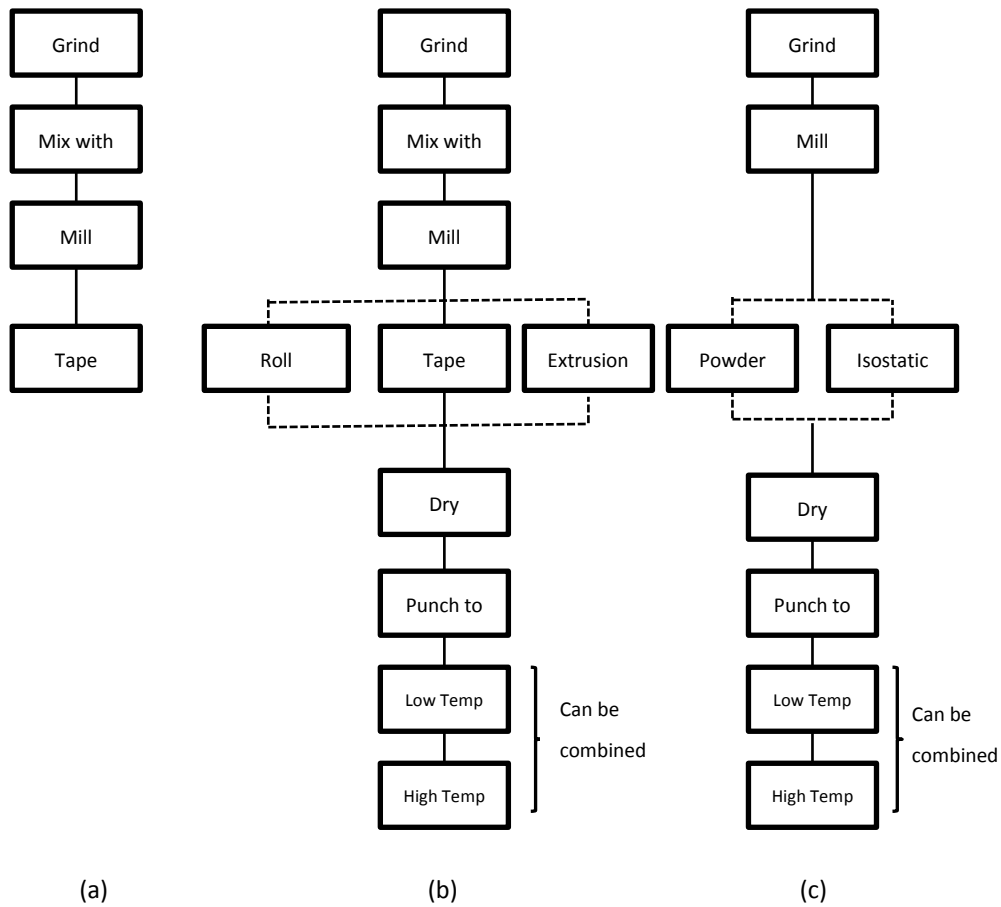


Figure 2.9 Flow chart of ceramic substrate fabrication (Barlow III and Elshabini 2007).

The temperature profiles are conducted in two stages, the first stage is called debinding to remove the polymer binders and the second stage is sintering for complete removal of organics in the ceramic. All organics have to be removed from the ceramics to avoid the formation of the void which is caused by incomplete removal of organics. Depending on the type of ceramics, the oxidizing atmosphere will be used to improve the efficiency of organic burnout to form CO<sub>2</sub> gas. For nitride ceramics, a nitrogen atmosphere is required to prevent oxidation of the

ceramics. Shrinkage will occur due to the organic burnout and densification of the ceramics during sintering. The typical shrinkage will range from 10% (powder) up to 22% (sheet casting) (Jabbari, Bulatova, et al. 2016).

Table 2.4 describes the individual steps in the form of ceramic substrates. Tape casting is widely used to fabricate multi-layered ceramic packages. It produces a thin layer of ceramics that can be stacked and laminated into multi-layers. The rheological of the slurry and material flow determines the final properties and quality of the cast product.

Table 2.4 Types of processes used to form ceramic substrates (Barlow III and Elshabini 2007).

Process	Description
Tape casting	Sheets are formed when the ceramic slurry is dispensed onto the moving belt with a knife edge to control the thickness, under relatively low-pressure.
Powder pressing	The ceramic powders are forced under very high pressure (up to 20,000 psi) in a hard die cavity to produce high dense parts with very good as-fired tolerance. However, pressure variations could cause excessive warpage.
Isostatic powder pressing	The ceramic powders are compressed (up to 10,000 psi) in a flexible die. The process has better pressure uniformity and less warpage compared to the powder pressing process.
Extrusion	Low viscosity ceramic slurry is forced through a die. The process does not have good tolerance but is economical and able to produce thinner parts compared to other methods.
Roll compaction	Ceramic slurry is dispensed onto a flat surface, partially dried, and passing through a pair of rollers to form a uniform sheet.

Yung and Liem (Yung and Liem 2007) have reported bi-modal filler mixing will improve packing density and therefore, thermal conductivity of the boron nitride (BN) ceramic. Bimodal particle size mixing of hBN samples with particle sizes of 0.4 and 0.2  $\mu\text{m}$  can increase the thermal conductivity by up to 133%. Besides, bimodal mixing of cubic boron nitride (cBN) with a particle size of 1  $\mu\text{m}$  has shown improvement of up to 217%, reaching 19 W/mK as a result of the increased surface area of the filler by maximizing the addition of cBN into the hBN resin. Silane surface treatment of the filler can reduce the CTE by 43%. JP Hong et al. (Hong, Yoon, et al. 2012) has reported that the best mixing ratio of AlN:BN is 1 to 1 in order to achieve high thermal conductivity in the epoxy composite. GW Lee et al. (Lee, Park, et al. 2006) have reported that hybrid fillers with different shapes and sizes are effective in improving the heat dissipation performance (thermal conductivity) of the polymer composite. The improved mixing is because of the enhanced connectivity by structuring filler with a high aspect ratio in the hybrid filler. Also, larger and surface treated particles not only improve heat dissipation but also lower the CTE of composites.

V. Onbattuvelli et al. (Onbattuvelli, Purdy, et al. 2010) have reported that bimodal powder mixtures with nano- and micron-sized particles of AlN and SiC can increase the solids loading in the powder injection molding system. The addition of nanoparticles also improved the sinterability of SiC and AlN by reducing the liquid phase formation to 1800°C and 1500°C respectively. Around 99.3% density is obtained for the bimodal micro-nano AlN system when pressure-less sintered at



1650°C. With the tendency to agglomerate, nanoparticles exhibit poor packing density, but the addition of nanoparticles to the bimodal distribution has shown to increase the solids loading. Also, adding nanoparticles to micron-sized particles can lower the suspension viscosity (Onbattuvelli, Enneti, et al. 2013). JY Qiu et al. (Qiu, Hotta, et al. 2006) reported that the addition of nanoparticles could enhance the density and thermal conductivity of AlN ceramics. However, Onbattuvelli et al (Onbattuvelli, Enneti, et al. 2013) reported that bimodal nano-micro (20nm/ 1 µm) AlN system has low debinding rates because of the higher filler content and smaller particle size.

#### 2.2.1 Ceramic filler fabrication techniques

Fabrication techniques which are used to form complex shape ceramics include machining, gelcasting, slip casting, injection molding, and pressure casting. All these techniques use slurry for casting except machining. Machining is generally avoided due to the high strength of ceramics that makes the process time consuming and expensive (Omatete, Janney, et al. 1997). Injection molding is the most common high precision shape forming process, but its drawbacks include long debinding time (removal of binder), it can take up to 7 days, non-uniform drying of thick and thin sections that cause cracks, and size limitation to only less than 3cm in diameter (White and Dee 1974). The recent improvement in injection molding technology was able to reduce the debinding time, but it still was not able to increase the size of products (Novich and Sundback 1991).

Therefore, for large size ceramic casting, either slip casting or pressure casting are used. The disadvantage of slip casting is that the forming time is long, which can take a few hours and non-uniform density distribution. Pressure casting is an improved version of slip casting by speeding up the casting process but still has the issue of density uniformity. Therefore, there is a need for a new casting process, and gelcasting, developed in Oak Ridge National Laboratory (ORNL) could potentially provide a good alternative for forming highly reliable near-net-shape of large parts.

### 2.2.2 Gelcasting

Gelcasting is an improvement from slip casting that couple with polymer chemistry to overcome the long binder time needed to form near-net-shape of large parts. The gelcasting process consists of mixing a high concentration of ceramic powder with the monomer to form a slurry. The slurry is then poured into a mold where in-situ polymerization can take place to form the green body in the near-net-shape form. In gelcasting, the removal of solvent (water) is by drying, followed by pyrolysis to remove the binder, also known as debinding (Omatete, Janney, et al. 1997).

The gelcasting concept was first successfully demonstrated by Janey et al. using acrylate monomer as organic solvents (Janney 1990). The ceramic powder was slurried together with the organic solvents, and the slurry was transferred into a mold, followed by polymerization using free-radical initiation to form gels. The gel can hold the powder and keep it near-net-shape with the cavity of the mold. The

cast was then demolded to form a green body, followed by debinding to remove all the organics and sintering to reach full density.

However, due to environmental and cost concern on the use of solvents, the water-based solution was being explored, and the search has led to the discovery of acrylamide gel system (Janney and Omatete 1991, Janney and Omateta 1992). The detailed study on alumina using the acrylamide gel system was successfully demonstrated by Young et al. (Young, Omatete, et al. 1991) and the gelcasting process is shown in Figure 2.10.

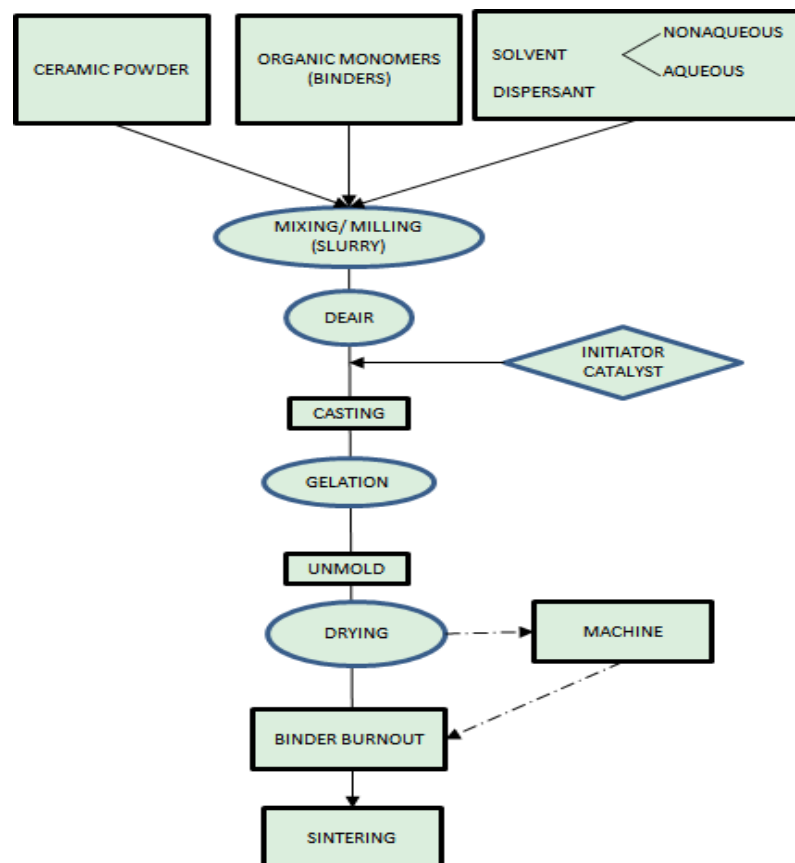


Figure 2.10 Process flow of a typical gelcasting process (Omatete, Janney, et al. 1997).

Gelcasting is different from the sol-gel process as it uses high solid loadings and the organic monomers will form a gel upon polymerization and hold the powders together. As a comparison, the sol-gel process has low solid loading, and the solids are usually produced as a by-product.

Table 2.5 Comparison of gelcasting with other ceramic forming processes (Janney, Ren, et al. 1998).

Property	Gelcasting	Slip casting	Injection molding	Pressure casting
Time	5-60 min	1-10 hour	1-2 min	10 min-5 hour
Strength (green body)	Good	Poor	Not applicable	Poor
Materials for mold	Metal, glass, plastic, wax	Plastic	Metal	Plastic
Time for binder burnout	2-3 hours	2-3 hours	Up to 7 days	2-3 hour
Defects due to molding	Not significant	Not significant	Significant	Not significant
Maximum size	1m	1m	~30cm	~ 0.5m
Warpage	Minimum	Minimum	Can be severe	Minimum
Product with thick/thin sections	Not much problem	Time increases for thick section	Binder removal problem	Time increases for thick section
Effect of reducing particle size	Viscosity increases	Casting time increases	Viscosity increases	Casting time increases

Table 2.5 shows the comparison between injection molding, slip casting, pressure casting, and gelcasting. Gelcasting fare well in all categories, and its significant advantages include fast forming cycle, good green body strength, the flexibility of using a different material for mold, large size product (> 1m) with thin and thick sections and low molding defects (Janney, Ren, et al. 1998).

### 2.2.3 Green gelcasting technology

The drive for the use of environmental-friendly materials for processing of ceramic has triggered the development of water-based binder for the conventional forming technology such as injection molding (Fanelli, Silvers, et al. 1989). Binder is one of the most critical components in ceramic forming that will affect the surface charge of particles, solid loading, the green body strength, dimensional stability, and defects. The ideal system uses a small amount of binder and yet has high green body strength (Dhara and Bhargava 2001).

Gelcasting is not widely used in the industry due to safety concern because the acrylamide monomer is a neurotoxin (Omatete, Janney, et al. 1991, Young, Omatete, et al. 1991). Therefore, this has triggered efforts to look for a low-toxicity gelcasting monomer system. The alternative monomer for acrylamide was desired to be water soluble (at least 20 wt% for mono-functional monomers and 2 wt% for difunctional monomers) with high solubility, low toxicity and inexpensive (Janney, Omatete, et al. 1998).

Some natural binders that have been reported include gelatin (Xie, Chen, et al. 2000), bovine serum albumin (BSA), agarose (Xie, Yang, et al. 1999), whey protein concentrate (WPC), albumin and polysaccharide (Olhero, Tari, et al. 2000). Lyckfeldt et al (Lyckfeldt, Brandt, et al. 2000) have reported that low albumin content of 5-8 wt% causes weaker gels.

Ovalbumin has recently been introduced as the low-cost environmentally sustainable source of monomer for gelcasting. The advantage of ovalbumin is that

the polymerization started in-situ upon heating to a temperature below 100°C without the need for an initiator. Besides, the low content of the net binder in the dried green body (0.6 – 4.0%), together with being biodegradable, and wide availability make it an attractive monomer for gelcasting (Dhara and Bhargava 2001).

However, gelcasting of AlN ceramics using aqueous monomer such as ovalbumin is generally not appropriate due to the tendency for AlN to hydrolyze that can reduce the thermal conductivity of the AlN ceramics. Therefore, the gelcasting of AlN reported in the literature uses non-aqueous monomer. L. Shen et al. (Shen, Xu, et al. 2016) reported using a modified non-aqueous gelcasting technique with 1-methyl-2-pyrrolidinone. C Jiang et al. (Jiang, Gan, et al. 2013, Jiang, Zhang, et al. 2014) used hydantion epoxy resin that can accommodate solid loading of up to 58 vol% AlN. The gelcasting of AlN ceramics using natural aqueous-based monomers has not been reported previously. It will require some form of protection or inhibition mechanism that prevents AlN from hydrolyzing.

#### 2.2.4 Concluding remarks

Environmental issues related to global warming and pollution are globally significant problems. Therefore, green manufacturing technologies and the use of sustainable materials are preferred. Green gelcasting using ovalbumin is a sustainable source of material that has an excellent potential to meet this demand.

### 2.3 Interconnecting material for the interposer

Copper is a suitable metallization material because of its good electrical conductivity, high thermal conductivity, and relatively low-cost. It also has good solderability, electroplating availability, good corrosion resistance, and patterning availability using machining or chemical etching.

Copper is one of the elements with the lowest resistivity ( $1.72 \times 10^{-6} \Omega\text{-cm}$ ), second only to silver ( $1.59 \times 10^{-6} \Omega\text{-cm}$ ) (Matula R.A 1979). However, silver has the problem of silver migration that causes device failure (Yang, S. and Christou, A. 2007). Therefore, copper is well suited to be used for high-density interconnections and low electrical resistivity.

However, copper is easily oxidized in the air that will prevent reliable soldering and wire bonding, and therefore, nickel or gold are plated to act as a protective layer. Also, copper has high CTE ( $16.8 \text{ ppm}/^\circ\text{C}$ ), more than twice the value of ceramics that can cause mismatch at the joints leading to fractures. Therefore, the thermomechanical design has to be addressed early in the design of the chip and its packaging (Krum 2007).

The interconnection metals used commonly for high-temperature co-fired ceramics (HTCC) are W, Mo, Pt, and Pd due to their high firing temperature of 1450 to 1880°C. These high-temperature metals are used since noble metals such as Au, Ag, and Cu could not be processed at these temperatures (Greig 2007).

### 2.3.1 Copper metallization

Copper metallization using direct bond copper (DBC) technology is able to produce copper substrates with good mechanical properties. The technology is fast, creating copper layers, in hundreds of micrometers, with a single processing step (Hromadka, Stulik et al. 2014). DBC is a patented process that uses copper to eutectically bond to oxygen-bearing ceramics without adhesion or bonding material (Kuneman and Dickson 1986). Figure 2.11 shows the copper-oxygen phase diagram that illustrates the eutectic point for copper and oxygen at 1065°C, in which only 0.39% oxygen is present. Therefore, copper will fuse with oxygen-bearing ceramics in the temperature between 1065 °C and 1083°C, 1083°C is the melting point of copper.

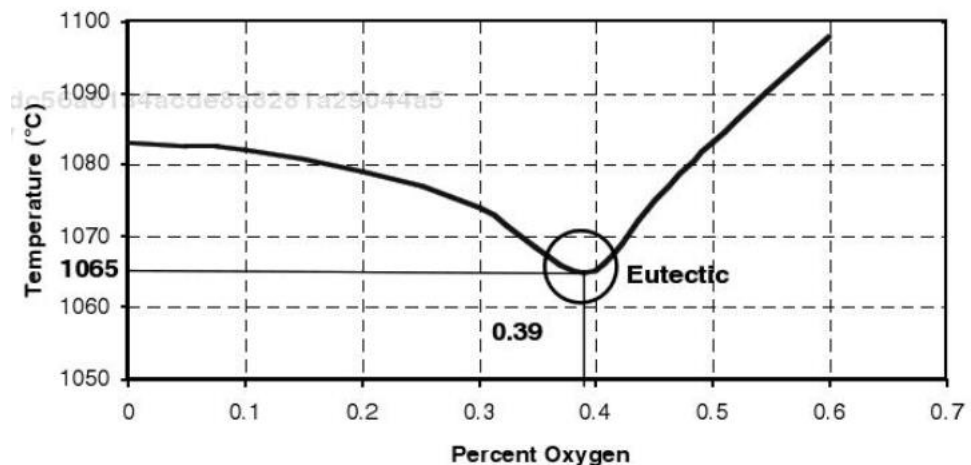


Figure 2.11 Copper-oxygen phase diagram (Barlow III and Elshabini 2007).

Figure 2.12 shows the DBC process flow for oxygen-bearing ceramics. First, the copper foil (25-50  $\mu\text{m}$ ) is cut into the desired size that complements the ceramic.



Next, the copper foil is oxidized and touches the ceramics. The copper will be fused with the ceramics in the furnace in temperature between 1065°C to 1083°C. The sample is then cooled and taken out of the furnace. Wet etching process with photoresist exposure for selective area etching will be employed to define the circuit pattern. Nickel or gold will then be plated onto the sample as a protective layer.

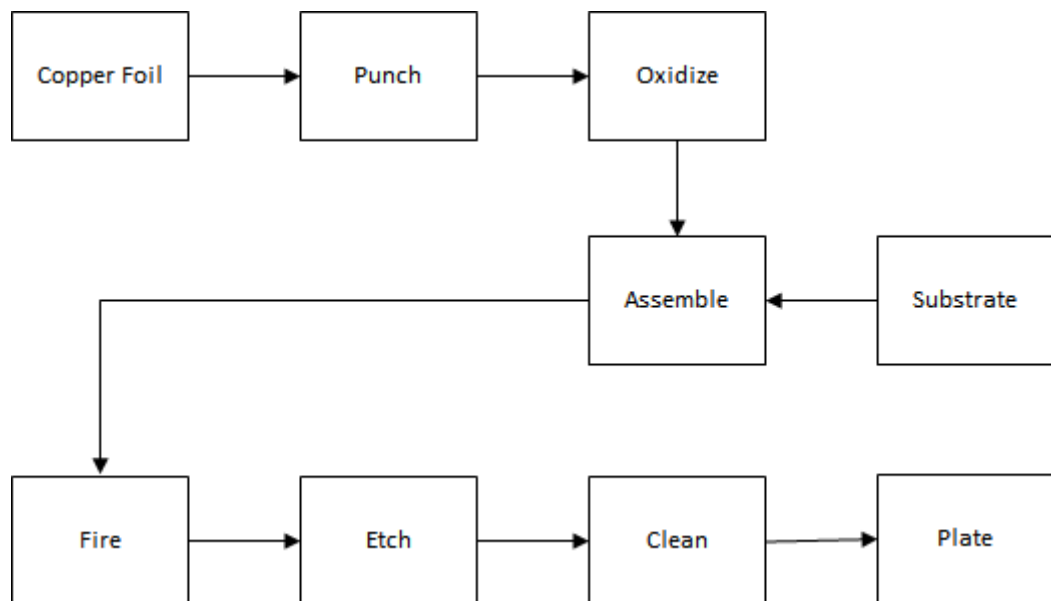


Figure 2.12 DBC process flow for oxygen-bearing ceramic.

Active metal brazing (AMB) is to braze metals to ceramics without the need to metalize the ceramic. It has higher adhesive strength as compared to DBC but less critical furnace temperature setting and does not rely on oxide formation (Zhang, Di, et al. 2006). The process starts by applying braze materials (titanium, hafnium or zirconium) in the form of film, powder, or paste (Figure 2.13). Then the combination of copper, braze material and ceramics were placed in the vacuum

furnace with a vacuum level of  $10^{-3}$  torr to prevent copper oxidation, where a liquidus material is formed from the reaction between brazing alloy and ceramics that bond the metal to the ceramic. When the parts are cooled, it will be plated in the same manner as DBC and followed by etching to form the desired pattern.

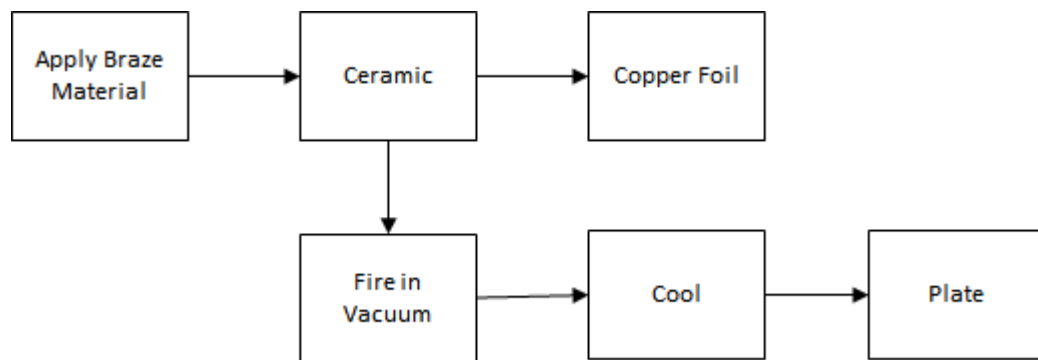


Figure 2.13 Active Metal Brazing (AMB) process flow.

Copper can also be deposited either by screen printing or etching. For screen printing, the copper ink is forced through a screen with pre-defined patterns, dried and fired in dry nitrogen to avoid copper oxidation. It is then selectively etched using the photolithography process, the line width achievable can be as narrow as 25  $\mu\text{m}$  (Barlow III and Elshabini 2007).

There are two methods of copper electroplating on ceramics. The first method is by having an adhesion or seed layer using either evaporation or sputtering, followed by gold deposition deposited on top of the seed layer and later copper electroplating to build up the thickness that will be followed by electroplating of the protective nickel layer. The other method involves the selective electroplating of

copper onto selective conductors. Fine line widths of 50  $\mu\text{m}$  are achievable using the second method (selectively plated copper process) and minimum line width of 125  $\mu\text{m}$  is achievable using the first method (etched blanket-coated copper substrates) (Barlow III and Elshabini 2007).

In electroless copper plating, alkali metal compounds are used to treat the ceramic surface followed by surface exposure in an acid halide solution (Sard, 1970). The next step is copper plating is an electroless copper bath to deposit a thin layer of copper on the ceramic, followed by the photolithography process to expose the selected area for selective electrolytic copper plating. After the photoresist is removed, nickel was plated to form a protective layer (Barlow III and Elshabini 2007).

### 2.3.2 Refractory metals

The characteristic of refractory metals is that they are all solids at a temperature of around 2500°C that makes it suitable for co-sintering with ceramics. Properties of refractory metals are shown in Table 2.6 (Shabalin 2014). Molybdenum (Mo) has the highest electrical conductivity in the series and is often the choice of refractory metal for HTCC AIN. HTCC AIN is suitable for 5G phased array packaging due to its high thermal conductivity (Sturdivant 2018). The challenge with current low-cost 5G phased arrays is the lack of heat dissipation capability. Therefore, the alternative is to use HTCC and LTCC technology to replace organic panel-based

technology. HTCC is preferred due to better heat dissipation performance.

Table 2.6 Properties of refractory metals.

Refractory Metals	Density (g/cm <sup>3</sup> )	Melting Point (°C)	Electrical Conductivity (%IACS)	Electrical resistivity (μΩ·cm)	Thermal Conductivity (W/mK)
Tungsten (W)	19.3	3410	31	5.5	166
Rhenium (Re)	21.0	3180	9.3	19.1	71
Tantalum (Ta)	16.6	2996	13.9	13.5	54
Molybdenum (Mo)	10.2	2610	34	5.7	146
Niobium (Nb)	8.6	2468	13	14.1	52
Titanium (Ti)	4.5	1668	5.5	42	22
Copper (Cu)	8.96	1083	100	1.7	393

The current method of metalizing refractory metals is by applying thick-film paste that consists of either W or Mo using screen printing to fill via on the ceramic sheet. The layer of filled green ceramic sheets is then stacked, followed by lamination using thermal compression, typically at 30MPa and 80°C, a temperature slightly above the glass transition temperature of the binder-plasticizer system of the green tape (Hellebrand 1996). The laminated sheets are then co-fired in the sintering furnace to produce the ceramic circuit board with exposed metal for further metalization with appropriate plating.

### 2.3.3 Gelcasting

Gelcasting process produces near-net-shape form and has the advantage of lower cost of machining, fast fabrication process, and complex shape formation widely reported for use in ceramics. There were not many studies on the use of gelcasting for metal powders, and most of the study was related to optimizing

gelcasting parameter for metal powder in non-aqueous media (Bekouche, Jia, et al. 2016, Bekouche, Wang, et al. 2016). The key factors to form an excellent green body of copper using non-aqueous gelcasting are the solid content, viscosity, and consistency of the metal powder.

J. Tang et al. (Tang, Ji, et al. 2016) had reported that the increase in particle size of copper powder decreases the viscosity of the gelcasting system, causes inhomogeneity of the green body and reduces the flexural strength and density of the sintered body. The gelcasted copper green body sintered at 975°C for 5 hours in a nitrogen atmosphere was reported to have good flexural strength 39.93 MPa compared to the green body using 29 µm Cu powder.

Liu et al. (Liu, Jia, et al. 2008) reported the study on solid loading of anhydrous alcohol-based copper gelcasting. The viscosity of Cu slurries was found to be reduced with an increase in the dispersant and 61% solid loading is optimum with the sintering temperature of 910°C.

The water-based gelcasting system is generally not appropriate for metal powder due to oxidation that leads to the use of non-aqueous gelcasting of metal powder. However, Y. Li et al. (Li, Guo, et al. 2008) have reported using water-soluble cellulose ether (CE) for gelcasting of iron powder. Gelcasting of Mo metal has not been reported but the gelcasting of Mo/Cu alloy using 2-hydroxyethyl methacrylate (HEMA)-1,6-hexanediol diacrylate (HDDA) monomer has been reported by Bohua et al. (Bohua, Chengkang, et al. 2018).

#### 2.3.4 Concluding remarks

Simpler fabrication processes which utilizes alternative methods and materials that can be more environmental-friendly with reduced waste is an attractive technology to be developed. The conventional copper deposition processes including plating process uses many chemical processing steps that can lead to undesirable effluent which will require further treatment before it can be disposed to the environment. AM process of directly printing gelcasted metals onto a substrate that uses eco- friendly aqueous binders and meets the green technology demand will be developed.

#### **2.4 Multi-layer ceramics process for interposer**

Multi-layer ceramics can be used to produce high-density electronic substrates with high-density interconnection, low electrical loss, stability in high-temperatures and has the ability for making 3D structures. These multi-layer ceramic packages are used in a variety of applications because of their desirable characteristics, which include mechanical strength, reliability, thermal conductivity, CTE match, hermeticity, and cost. One of the key advantages of these materials is their intrinsic hermetic property and high thermal conductivities, which is more than 100 times better than conventional organic substrates.

Multi-layer ceramics was first used in capacitors, in the late 1940s (Howatt, Breckenridge, et al. 1947). HTCC was then developed a decade later with IBM

being the early adopters (Schwartz and Wilcox 1967). This technology is still being used for single-chip packaging applications and as multi-layer substrates for high-density electronics (Barlow III and Elshabini 2007).

#### 2.4.1 High-temperature co-fired ceramics (HTCC)

HTCC is described as multi-layer ceramics fired at temperatures above 1500°C that include ceramics such as aluminum oxide, AlN and other materials for application in electronic packaging. The difference between HTCC and LTCC is the difference in firing temperature of 600°C. Recently, a mid-firing multi-layer ceramics, known as medium-temperature co-fired ceramic (MTCC) is developed (I. Labadie 2013).

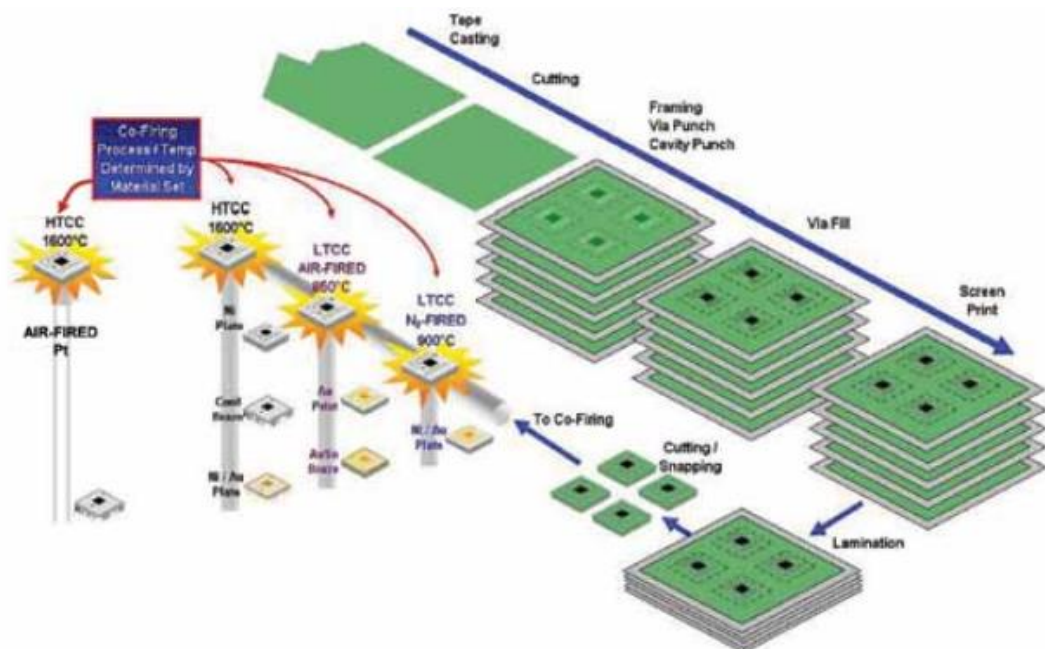


Figure 2.14 Multi-layer ceramics fabrication process (I. Labadie 2013).

Figure 2.14 shows the common multi-layer ceramic fabrication process applied to HTCC, AlN, and LTCC though the firing conditions are quite different. High-volume productions are often fully automated but must also couple with the “art” required for producing high-quality packages.

#### 2.4.2 Low-temperature co-fired ceramics (LTCC)

LTCC was developed to complement HTCC that has problems with high conduction loss in RF products. The lower firing temperature of 800°C to 1000°C can allow the use of non-refractory metals with high electrical conductivity such as silver, gold, and copper. The use of noble metals with LTCC is especially crucial for multi-chip modules (MCM) that require high speed, high-frequency analog processing that could not endure the power losses due to metallization of HTCC technology (Scrantom and Lawson 1999).

Therefore, LTCC often has better electrical performance compared to HTCC but has inferior mechanical and thermal performance due to the glass-ceramic composition in LTCC. Thus, a compromise is required in selecting the right material for the correct application. Recent advances in LTCC includes the development of new dielectric with ultra-low sintering temperature (<650°C) that can save on energy, reduction in processing time and the capability for more integration options with semiconductors, metals, and plastics. HTCC and LTCC have many advantages as packaging substrates which include high mechanical strength and thermal conductivity, excellent electrical resistance, hermetic, good in



refractory metallization, and reliable in brazing (Yu, Liu, et al. 2015).

#### 2.4.3 Conventional multi-layer ceramic process

The fabrication of multi-layer ceramic used a parallel process, where individual layers are produced separately, collated and co-fired to form the final product (Figure 2.23). First, the roll of ceramic/ glass particles in the polymer matrix was tape casted, and the roll was blanked into individual sheets with the size ranging from 75mm square to 200mm square. Each substrate consists of 6 to 50 sheets of individual layers with its circuitry and vias for interconnection. The layers are then carefully collated and aligned before getting co-fired to form 3D blocks of ceramics with embedded electrical circuitry (Barlow III and Elshabini 2007).

The industrial applications for communications and automotive have driven the growing variety of ceramic tape systems available today. HTCC packages uses refractory metals such as tungsten, molybdenum, and platinum as conductor traces, are typically fired at temperatures between 1550°C – 1850°C, and the most prevalent ceramics used are  $Al_2O_3$  and AlN for high-reliability circuits. LTCC, fired between 800 °C – 1000°C, generally uses Cu, Ag or/ and Au as conductors (I. Labadie 2013).

#### 2.4.4 Additive manufacturing (AM) process

Printed circuit boards (PCBs) are commonly used as connectivity between ICs and electronic components using conductive traces on a non-conductive substrate for conventional electronics. Continuous innovations are required to meet the ever demanding development of ICs and electronic devices. PCBs have its limitation in

freedom of placement that results in more space requirement for the placement of components. This limitation could be solved by using embedded electronic circuits with multi-layer substrates fabricated using additive manufacturing technology of direct-write (DW) or direct-print (DP) (Piqué and Chrisey 2001, Joe Lopes, MacDonald, et al. 2012). ASTM F2792-12a has defined AM as the “process of joining materials to make objects from 3D model data, usually layer upon layer, as opposed to subtractive manufacturing methodologies, such as traditional machining” (Standard 2012).

Recent research has started to focus on the fabrication of final end-use products for 3D printing by democratizing the manufacturing process to produce products with unit-level customization. Some research group has reported embedding electronic components, and electrical interconnects into 3D printed structures, but not much has been reported on electromechanical functionality built with a single AM build sequence. Also, the previously reported use of conductive ink for electrical interconnect has demonstrated the poor conductivity of printed conductive ink.

The limitation for ceramic materials produced by the conventional method, is its limited geometric complexity, high cost, and difficulty to produce small individual parts, and AM can narrow this gap by providing possible solutions to these constraints (Homa and Schwentenwein 2015).

It is an undeniable fact that further advancement of ceramic materials will depend on the capability of technologies to produce complex 3D geometry. Post-

machining of ceramics is normally avoided because ceramic materials are hard and brittle that requires careful and time-consuming machining, using specialized and expensive tools (Klocke 1997). Also, the limited prototyping capability of ceramics will also result in lack of quick test parts that limit its use, all these issue led to the emergence of AM technologies that could fill these gaps in the technology (Travitzky, Bonet, et al. 2014).

There are three classes of AM technologies for ceramics: i) technologies for porous ceramics, ii) technologies for fully dense ceramic bodies with dimensional restriction, and (iii) technologies for fully dense ceramic bodies without dimensional restrictions. Current AM technologies for ceramics still face the challenge to fabricate fully dense ceramics mainly due to the difficulty in removing binders in the ceramic suspension or pastes (Zocca, Colombo, et al. 2015).

There are a number of AM techniques for ceramics. The initial development for ceramics uses powder-based techniques that are limited by its limited availability of compositions (Leuven 2014, Travitzky, Bonet, et al. 2014). The other three-dimensional (3D) printing systems are selectively curing by UV, selective binding using adhesives and selective fusion using lasers (Zocca, Colombo, et al. 2015). However, all these techniques involve a time-consuming and inefficient binder removal process. The low strength and poor reliability are caused by cracks, pores, and inhomogeneities of the additively manufactured ceramic part (Eckel, Zhou, et al. 2016).

In 2014, Strandjord (Strandjord 2014) proposed usage of 3D Printing of multi-

layered ceramics (Figure 2.15). The use of 3D Printing could create a simple ceramic and conductor LTCC, fabricated using a single system that use CAD diagrams instead of tooling. Besides, 3D Printing will be able to simultaneously create additional features such as chip cavities, channels, pipes and also functional materials into the same part.

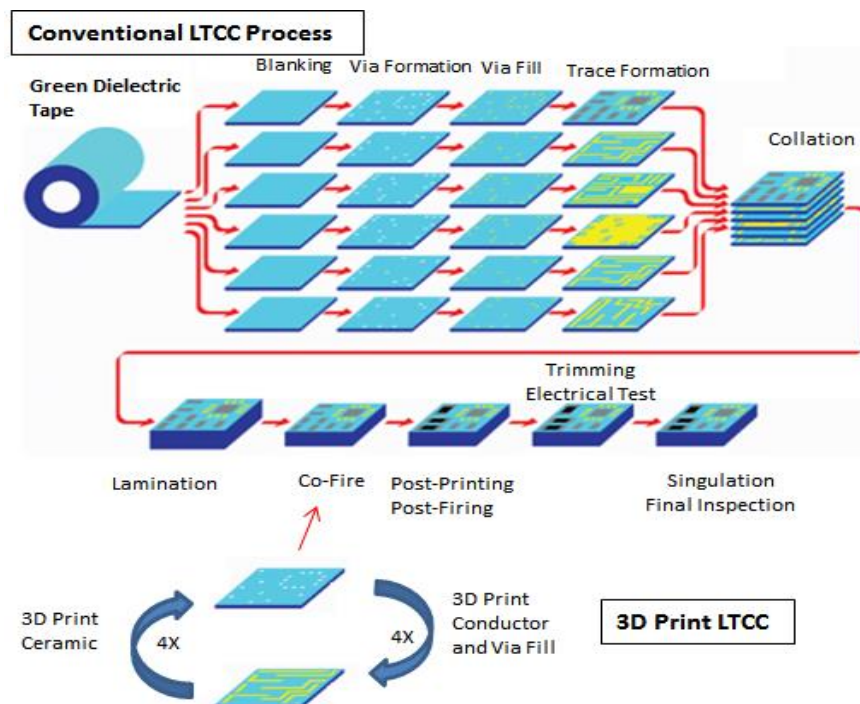


Figure 2.15 Proposed 3D Printing for LTCC (Strandjord 2014).

The SLA process currently has the best surface finishing, but it is costly and limited in materials range, in addition to the potential environmental hazards of using solvents. 3D direct printing, on the other hand, can only achieve limited surface quality but it allows the broadest range of feedstock materials. Also, 3D printing has the extended function of controlling the composition, microstructure, and properties of the component. In a recent development, Z.C. Eckel et al. (Eckel,

Zhou, et al. 2016) have reported the use of preceramic monomers that can be pyrolyzed with uniform shrinkage and without porosity using ultraviolet light in a stereolithography 3D printer.

The recent development of AM for ceramics include NanoParticle Jetting (NPJ) technology claim to produce ceramics with physical properties equivalent to conventional process and have a smoother surface finish as compared to stereolithography, DLP, and binder jetting (Levi 2018). Tucker et al. (Hensen, Aguirre, et al. 2018) have introduced Direct Coagulation Printing that is a binderless, extrusion-based AM to fabricate alumina ( $\text{Al}_2\text{O}_3$ ) parts from nanopowder. Eqtesadi et al. (Eqtesadi, Motealleh, et al. 2018) have reported using robocasting to print  $\text{B}_4\text{C}$  green pieces to near net shape from ink, followed by subsequent pressureless spark plasma sintering. Zhang et al. (Zhang, Chen, et al. 2017) have reported usage of selective laser gasification on frozen slurry to produce 3D ceramic parts.

Chen, L et al. (Chen, L. Deng, C., et al. 2019) reported 3D printing of lithium-calcium-silicate bioceramic scaffolds that has dual bioactivities. Golaszewski, M., et al. (Golaszewski, M., Grygoruk, R., Giorgio,, et al. 2019) has reported printing metamaterials which allow for displacements at micro-level. Kuang, X., et al. (Kuang, X., Chen, K.,, et al. 2018) introduced novel 4D printing of highly stretchable with shape memory and self-healing elastomer. Sultan, S. et al. (Sultan, S., Abdelhamid, H. N., et al., 2019) reported the one-pot synthesis of 3D printable hydrogel containing the metal-organic framework of zeolitic imidazolate.

#### 2.4.5 Concluding remarks

The conventional multi-layer fabrication process, HTCC, and LTCC are fundamentally parallel processes that require multiple steps, and each step requires dedicated tools and equipment. AM offers a more straightforward and flexible fabrication process that will also be using fewer chemicals besides the capability to build complex shapes with unique features directly from the CAD design.

### **2.5 Research gaps**

High-performance 3D integration of electronic devices is currently facing the following challenges:

- I) The need for a high thermal conductivity insulator material that can be used as an electronic interposer substrate.

The electronic chips and functional electronics has its own maximum allowable rated junction temperature, between 85°C to 120°C, for its safe and reliable operation (Kandasamy, Wang, et al. 2008). Overheating of electronic component will affect its reliability, and a 4% improvement is observed for every 1°C drop in operating temperature (Mithal 1996).

The challenge with vertically integrated packages like 3D integration is the absence of technique to remove heat from multi-layer and not just from a single plane. Therefore, highly efficient heat dissipation methods are required to prevent temperature rises above the limit. Even though the power dissipation per transistor for 3D ICs are smaller, however, the higher packing densities produce higher power

densities and higher thermal resistance that generate substantial temperature rise (Rahman and Reif 2001). Also, heat has to travel farther due to the additional integration layer in 3D ICs that further impedes heat dissipation (Goplen and Sapatnekar 2006).

The cooling methods can be categorized as active cooling and passive cooling. Active cooling includes a heat sink that uses direct contact to extract heat transferred by free convection, forced convection, liquid cooling and any combination thereof. The current active method of solving the thermal issue in 3D ICs is by the aggressive microfluidic (MF) cooling that uses a liquid as opposed to the conventional air (Kearney, Hilt, et al. 2012, Zhang and Bakir 2013, Serafy, Bar-Cohen, et al. 2016). Other methods include incorporating thermal vias (Goplen and Sapatnekar 2006, Cho, Sundaram, et al. 2015), fabrication of silicon carriers with embedded fluidic channels (Yu, Khan, et al. 2008) and forced convective interlayer cooling (Brunschwiler, Michel, et al. 2008).

However, all these methods will take up valuable routing space that limits the density of interconnections within the interposer. Veitl (Veitl and Dohn 2010) has proposed a change of concept by using high thermal conductivity ceramics as heatsink, circuit carrier and part of the product design to make the interposer material itself to be more efficient in distributing the heat generated from multi-chip ICs to reduce the development of hot spots and at the same time have high-density interconnection to ensure high-performance 3D integrated packaging.

II) The need for green aqueous-based metal forming process.

The aqueous-based feedstock systems are a potential solution to environmental-friendly processing technology but are not generally used for metal forming. The gelcasting method generally uses water-soluble binders and the results prove to be better than slip casting, injection molding and pressure casting (Janney, Omatete, et al. 1998). The gelcasting process was widely reported for application in ceramics but rarely for application in metal forming.

The gelcasting of metals reported previously used non-aqueous monomer; Y. Tang et al. (Tang, Ji, et al. 2016) reported using HEMA monomer and PBO solvent to gelcast copper, H. Yuan et al. (Yuan, Jia, et al. 2015) used HEMA monomer and PBO solvent to gelcast porous Al-Cu alloy, and D. Bohua et al. (Bohua, Chengkang, et al. 2018) also reported using HEMA monomer and PBO solvent for gelcasting Mo/Cu alloy powders.

The reason that the water-based gelcasting system is generally not appropriate for metal powder is due to metal oxidation that causes corrosion and poor electrical performance. The use of environmental-friendly gelcasting monomer to produce near-net-shape metals will encourage green manufacturing of metal components. As the use of synthetic non-aqueous gelcasting monomer is less environmental-friendly, an aqueous-based metal forming process will be desirable.

III) The need for a green process for building electronic components using a simpler step.

A new paradigm is required for making complex shape parts using high-performance materials that have excellent strength and durability. High-



performance material, especially ceramics are difficult to machine and therefore not easily fabricated into complex 3D geometries that limit its application. Thus, AM can fill this gap as it is an effective method for making complex geometries product.

Figure 2.16 shows a review of the current challenges and trends in AM technologies (Gao, Zhang, et al. 2015). Ceramics are hard and brittle solids that can withstand high temperatures and are chemically inert. Therefore, post-machining of ceramics is generally avoided as it is a time-consuming and expensive process. The difficulty in post-processing of ceramics has caused the need to produce complex-shaped ceramic parts directly from computer-aided design (CAD) files for quick fabrication of newly designed test parts. This has led to the development of additive manufacturing (AM) techniques for ceramics.

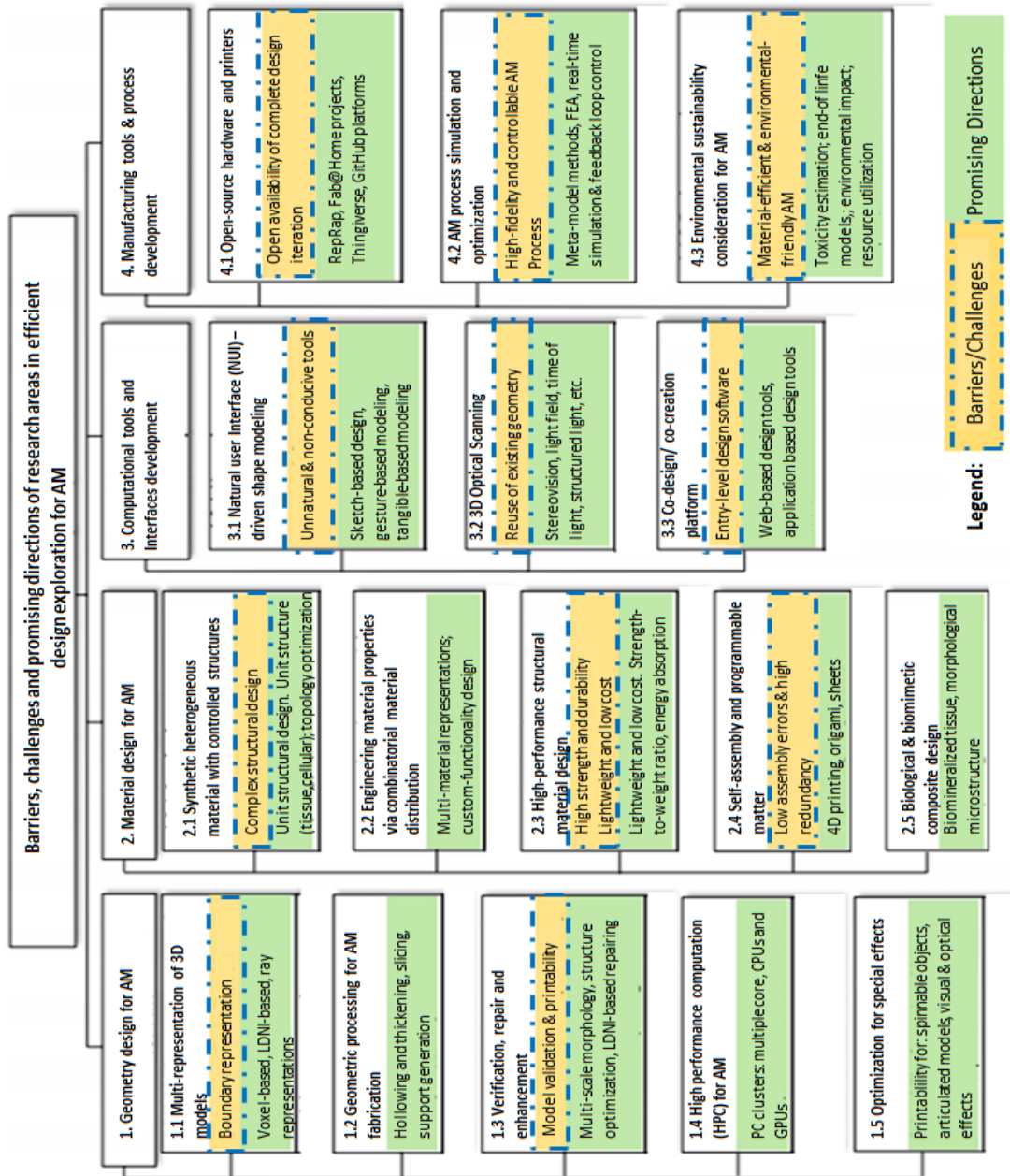


Figure 2.16 Barriers, challenges and promising directions for AM (Gao, Zhang, et al. 2015).

One problem with the use of powders that are too small (sub-micron) is the low flowability that causes difficulty in forming thin layers, in addition to the problem with agglomeration and electrostatic charging resulting in cracking. The theoretical density for packing of particles with sizes with ranging from 20 to 100  $\mu\text{m}$  is below 50% (Zocca, Gomes, et al. 2014).

The high proportion of organic binders (40% to 60%) used in most ceramic suspension for AM process causes the inefficient removal of binders and consequently affects the density of the sintered parts (Homa and Schwentenwein 2015). Currently, the liquid phase densification was identified as the best way for fast densification in AM for ceramics, but it might not produce parts with the desired phase that can affect the final desired physical property (Mühler, Gomes, et al. 2015). The AM of slurry-based ceramic uses the features of tape casting and slip casting process with organic binders (Tang and Yen 2015, Yen 2015). Therefore, there is a need for producing embedded electronics with ceramics as substrates using aqueous-based process.

The layout of the research study is presented in Figure 2.17.

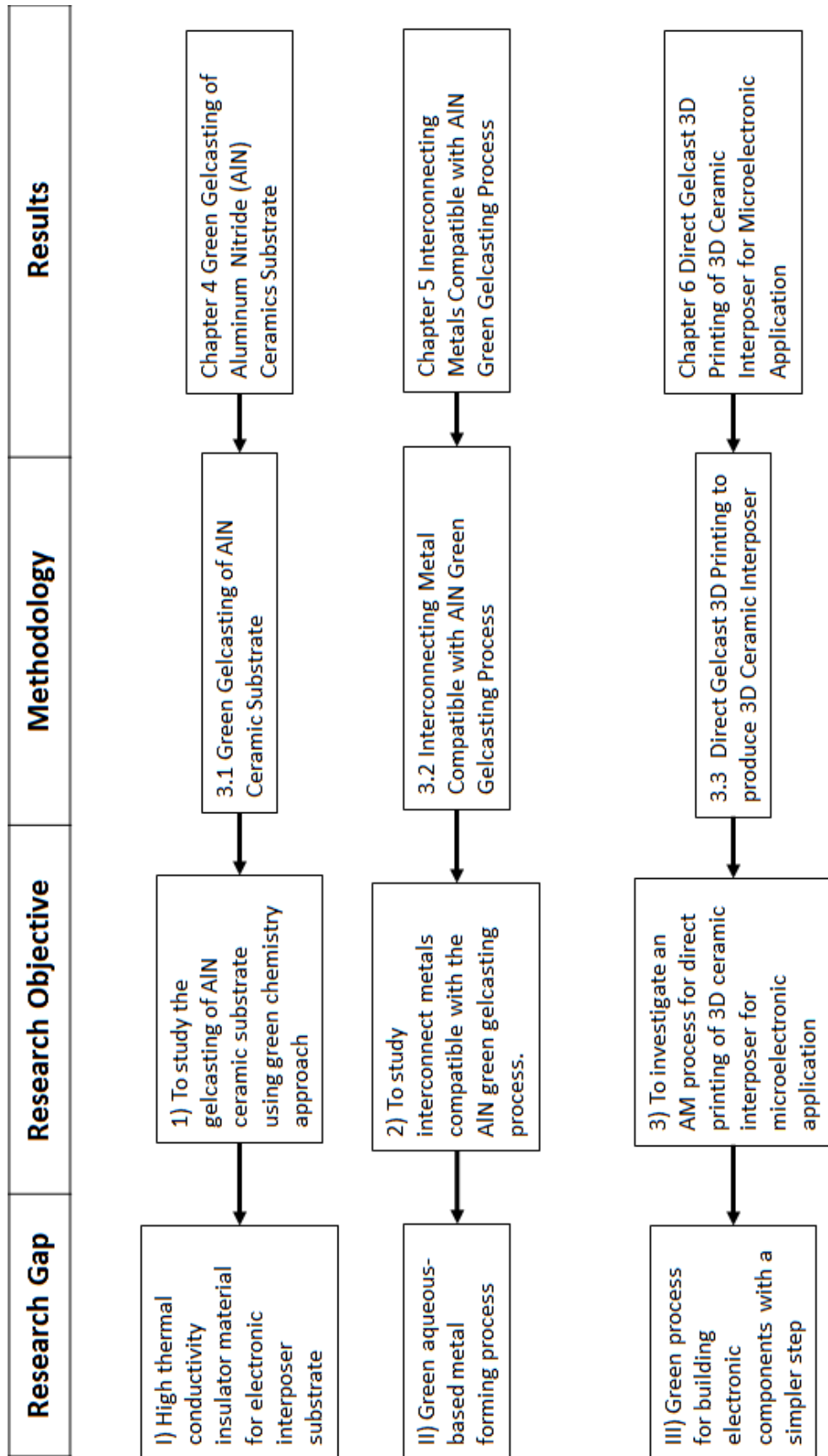


Figure 2.17 Layout of the research study

# Chapter 3 Research methodology

## 3.1 Green gelcasting of AlN ceramic substrate

In order to meet the need for high thermal conductivity insulator material for use as electronic interposer, the objective of the study is to develop high thermal conductivity AlN ceramic substrate using green chemistry approach. Figure 3.1 shows the experimental approach and it consists of 4 parts:

- 1) Green chemistry approach in developing environmental-friendly ceramic processing technology.
- 2) Selection of high thermal conductivity ceramics powders.
- 3) Development of a suitable debinding profile for the 3D ceramics.
- 4) Characterization and testing of the ceramic substrate.

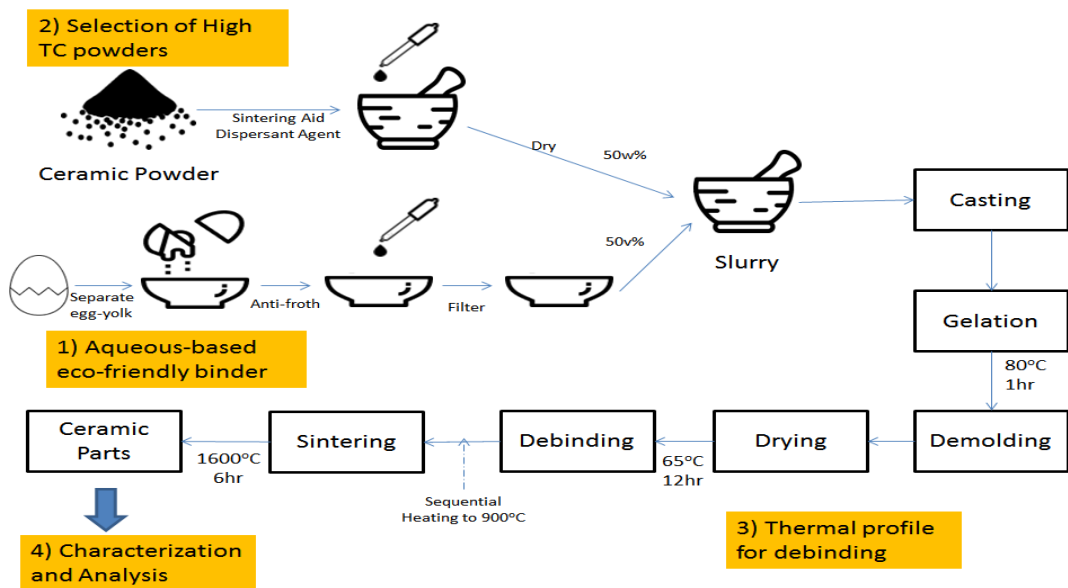


Figure 3.1 Experimental approaches in developing high thermal conductivity AlN ceramic substrate based on green chemistry approach.

### 3.1.1 Green chemistry approach in developing ceramic processing technology

Aqueous-based feedstock systems are potential solutions for an environmental-friendly ceramic fabrication technology. Gelcasting process technology using water-soluble binders was selected as they have better characteristics compared to other casting technologies.

The first part of this study is to develop an environmental friendly gelcasting monomer system for the fabrication of near-net-shape and high thermal conductivity ceramics. The initial formulation of gelcasting uses acrylamide as the gelcasting monomer, a known neurotoxin and therefore, an eco-friendly gelcast monomer is desirable. The comparison of conventional gelcasting monomer, acrylamide and the green monomer, ovalbumin is shown in Table 3.1.

Table 3.1 Comparison of conventional gelcasting monomer, acrylamide and ovalbumin

Properties	Conventional monomer	Green monomer
Chemical name	Acrylamide	Ovalbumin
Source	Synthesis from hydrocarbon process	Obtained from natural egg after separation from the yolk
Chemical safety	Toxic	Non-toxic
Catalyst	MAM, MBAM	Not required, gelation by heating more than 80°C
Medium	Aqueous	Aqueous

Natural protein ovalbumin, a green chemical obtained by separating the egg white from its egg yolk is a common binder used to making foodstuff is used in this study. The egg yolk was separated from the egg white because egg yolk contains fat

and rich in alkali metals such as calcium and magnesium. The introduction of alkali metals into the gelcast could co-sinter with AlN and affect its material property (Lyckfeldt, Brandt,, et al. 2000).

The advantage of using ovalbumin as the gelcasting monomer is its in-situ polymerization by heating to 80°C without the need for additional catalyst and initiator (Figure 3.2). The stirring of ovalbumin mixture causes froth and therefore anti-froth agents will be added to reduce the froth generation prior to mixing with the AlN ceramic powders to form the gelcasting slurry.

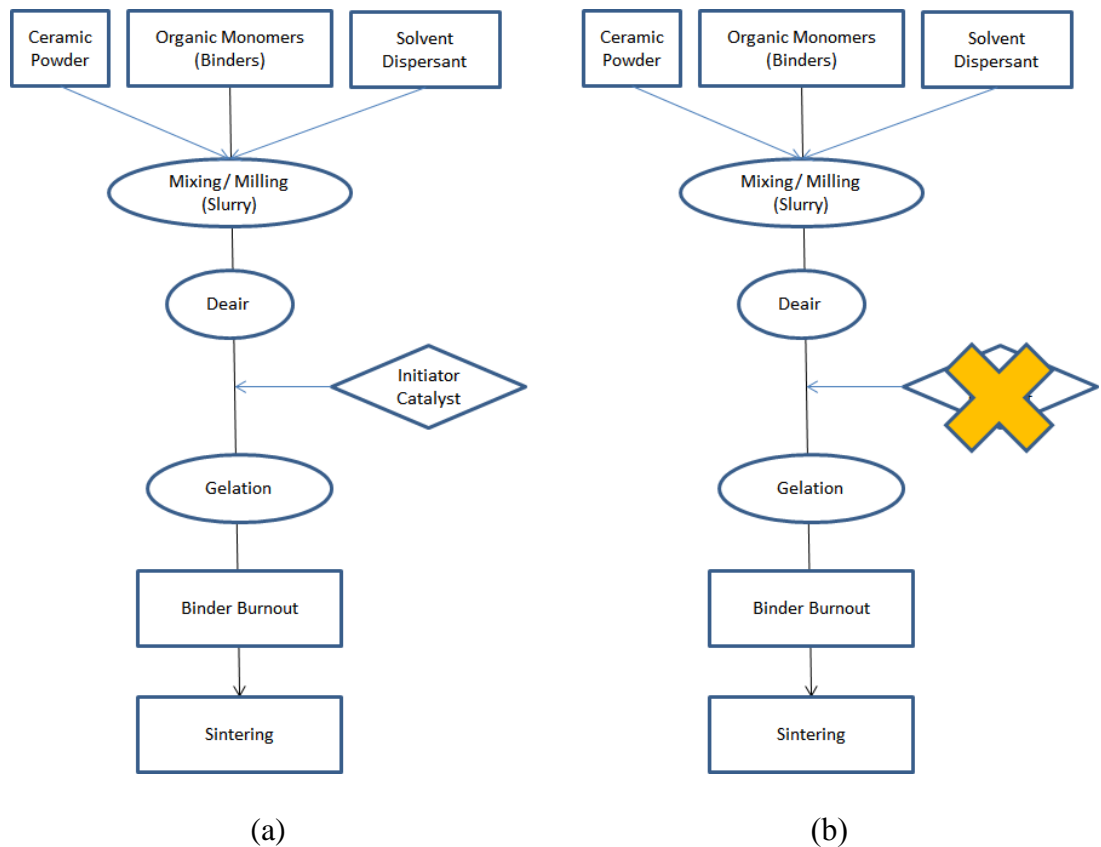


Figure 3.2 Ceramic gelcasting process (a) conventional (b) ovalbumin.

### 3.1.2 High thermal conductivity ceramic powders

The previous study has shown that mixing the ceramic powders with different particle size will improve densification due to better particle packing as smaller particles are able to fill in the void between bigger particles (Figure 3.3).

High thermal conductivity ceramic powders of aluminum nitride (AlN) of various sizes (0.04  $\mu\text{m}$ , 0.1  $\mu\text{m}$ , 1  $\mu\text{m}$ , 3  $\mu\text{m}$ , and 5  $\mu\text{m}$ ), boron nitride (BN) with particle size of 0.5  $\mu\text{m}$  and 15  $\mu\text{m}$  and silicon carbide (SiC) with particle size of 0.1 $\mu\text{m}$  is used in this study.

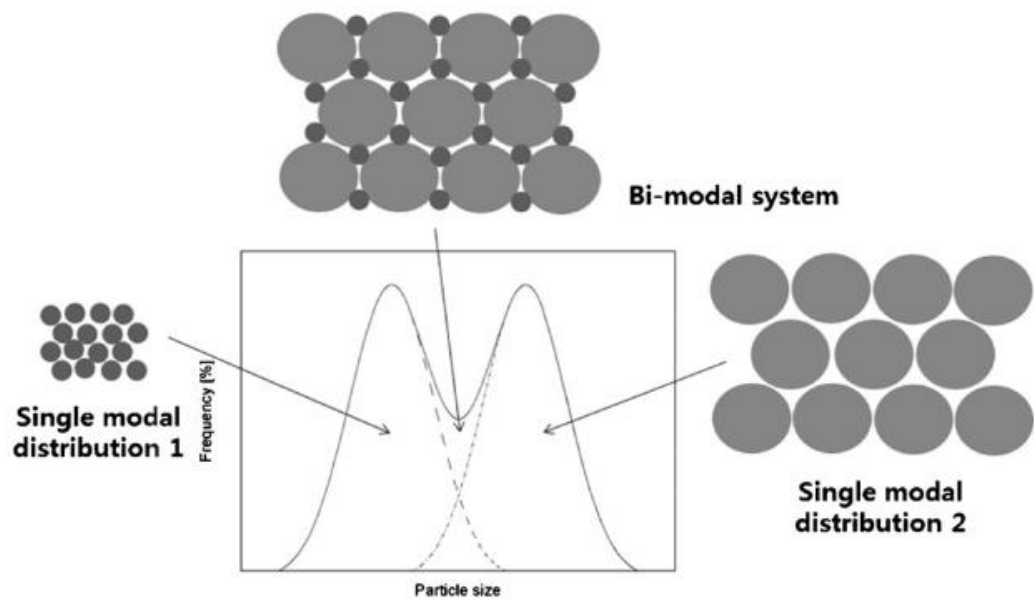


Figure 3.3 Schematic of unimodal and bimodal distributions (Hong, Yoon, et al. 2012).

Statistically designed experimental tools are used to optimize the process parameter using a full factorial design that consists of all combinatory possibilities of the parameters. The Design of Experiment (DoE) software, Minitab 14 is used to



create a full factorial design of experiment to determine the type of particles that can improve the thermal conductivity of the final sintered product. The particle size is analyzed using the Dynamic Light Scattering (DLS) system to determine the particle size distribution of the incoming raw materials.

### 3.1.3 Gelcasting of the ceramic substrate

The ceramic powders were mixed using either a ball mill (Deco PBM-H-0.4L) or mortar pestle with dispersant agents and sintering aid added before mixing with the ovalbumin gelcast monomer to form the gelcasting slurry.

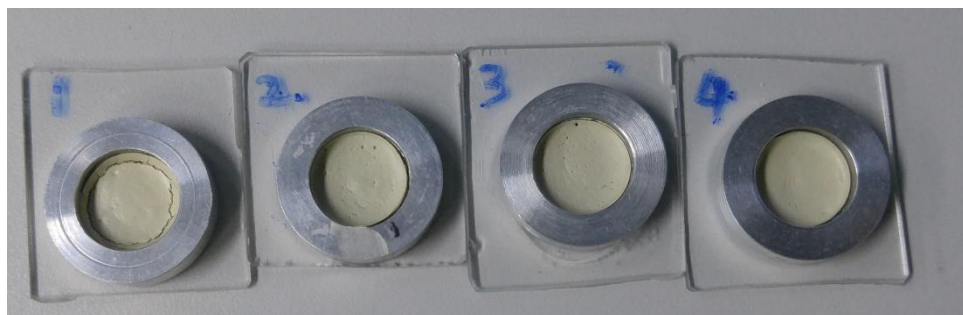


Figure 3.4 Metal molds for gelcasting of AlN.

The ceramic slurry was then poured onto the metal mold, dried and then demolded (green state) before further analysis (Figure 3.4).

The gelcasted ceramics in the green state was then analyzed using the thermogravimetric analyzer (TGA) to determine the thermal degradation profile. Once the thermal degradation profile was obtained, the debinding profile is developed for binder removal with less stress on the sample to avoid causing cracks

on the sample.

The gelcasted products in the green state are then be dried before pyrolysis to remove all the binders, followed by sintering at 1600°C in the nitrogen-filled atmospheric furnace (Zhengzhou Protech PT-M1700-A) to form the product with the desired property. The thermal conductivity of the sintered parts is measured to determine its heat dissipation capability. The physical strength of the ceramic substrate is evaluated using a 3-point flexural strength measurement system. Scanning electron microscope (SEM) is used to observe the microstructure and its packing in the ceramic substrate.

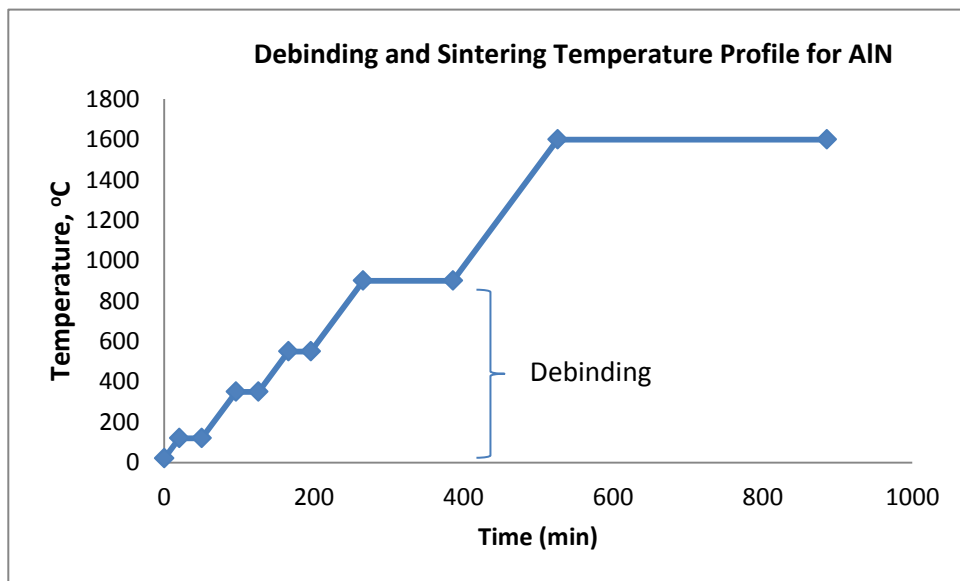


Figure 3.5 Debinding and sintering profile for AlN ceramic substrate. (Dhara and Bhargava 2001)

#### 3.1.4 Characterization and testing

The list of characterization and test equipments used are listed below:

- i) Thermal conductivity measurement to determine the heat dissipation performance of the ceramic substrate.
- ii) Thickness measurement using a caliper to measure the shrinkage of the substrate after sintering.
- iii) Microstructure analysis by using a scanning electron microscope (SEM).
- iv) Particle size analysis by using dynamic light scattering spectrometer (DLS).
- v) Rheology of the slurry by dynamic shear rheometer (DSR).
- vi) Flexural strength measurement (3-point) to determine the toughness of the sample to withstand physical process such as post polishing, etc.
- vii) Density meter to analyze sample density, which is required for analysis of the thermal conductivity and information on the particle packing of the ceramics.
- viii) X-ray diffraction (XRD) analysis to detect the presence of the hydrolyzed species of AlN.

### **3.2 Interconnecting metal compatible with AlN green gelcasting process**

In order to meet the need for green aqueous metal forming process, the objective of the study is to study interconnect metals that is compatible with the AlN green gelcasting process. Figure 3.6 describe the experimental approach and are mainly consists of three parts:

- 1) Compatibility of Cu with AlN green gelcasting process.
- 2) Compatibility of Mo with AlN green gelcasting process.
- 3) Characterization of gelcasted metals.

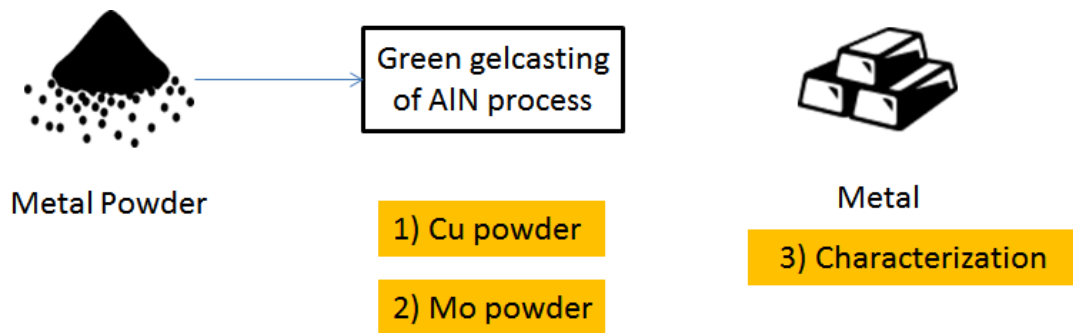


Figure 3.6 Experimental approaches in developing interconnecting metals that are compatible with the AlN green gelcasting process.

### 3.2.1 Compatibility of copper (Cu) with AlN green gelcasting process

Copper (Cu) is the most common material used for interconnecting metals in electronic devices due to its high electrical conductivity (second only to silver), and resistance to electromigration. The 3D ceramic interposer production involves co-sintering of the ceramic substrate and interconnecting metals. Therefore, similar processing parameters are desirable to avoid compatibility issues between the ceramic and metals. The green gelcasting of Cu using the process similar to the one described in section 3.1.1 is used in this study.

Cu has a melting point of 10835°C and is lower than the sintering temperature of 1600°C for AlN ceramic substrate. Therefore, the effect of heating Cu to the

sintering temperature of 1600°C is evaluated for determining the suitability of using Cu as the interconnecting metal with AlN ceramic substrate.

### 3.2.2 Compatibility of molybdenum (Mo) with AlN green gelcasting process

High melting temperature refractory metals are evaluated for its compatibility with AlN ceramics substrate process. Molybdenum (Mo) has the highest electrical conductivity as compared to other refractory metals and will be evaluated in this study. The different particle size of Mo will be evaluated on its effect on the electrical and thermal conductivity of the sintered Mo parts.

### 3.2.3 Characterization

The list of characterization and test equipment used are given below:

- i) Electrical resistivity measurement using a 4-point probe electrical measurement system.
- ii) Thickness measurement using a caliper to measure the shrinkage of the substrate after sintering.
- iii) Microstructure analysis by using a scanning electron microscope (SEM).
- iv) Rheology of the slurry by dynamic shear rheometer (DSR).
- v) Flexural strength measurement to determine the toughness of the sample that can withstand physical process such as post polishing, etc.
- vi) Density meter to analyze sample density, which is required for analysis of the thermal conductivity and information on the particle packing of the ceramics.

- vii) X-ray diffraction (XRD) analysis to detect the presence of the metal oxidation phase and correlate with the process parameter.

### 3.3 Direct gelcast 3D printing to produce 3D ceramic interposer

In order to meet the need for green process for building electronic components with a simpler step, the objective of the study is to investigate using additive manufacturing (AM) process for direct printing of 3D ceramic interposer. Figure 3.7 shows the experimental approach for developing interconnecting metal that is compatible with the AlN green gelcasting process already described in Section 3.1. It mainly consists of 2 parts:

- 1) Direct gelcast 3D printing parameters.
- 2) Functional 3D ceramic interposer.

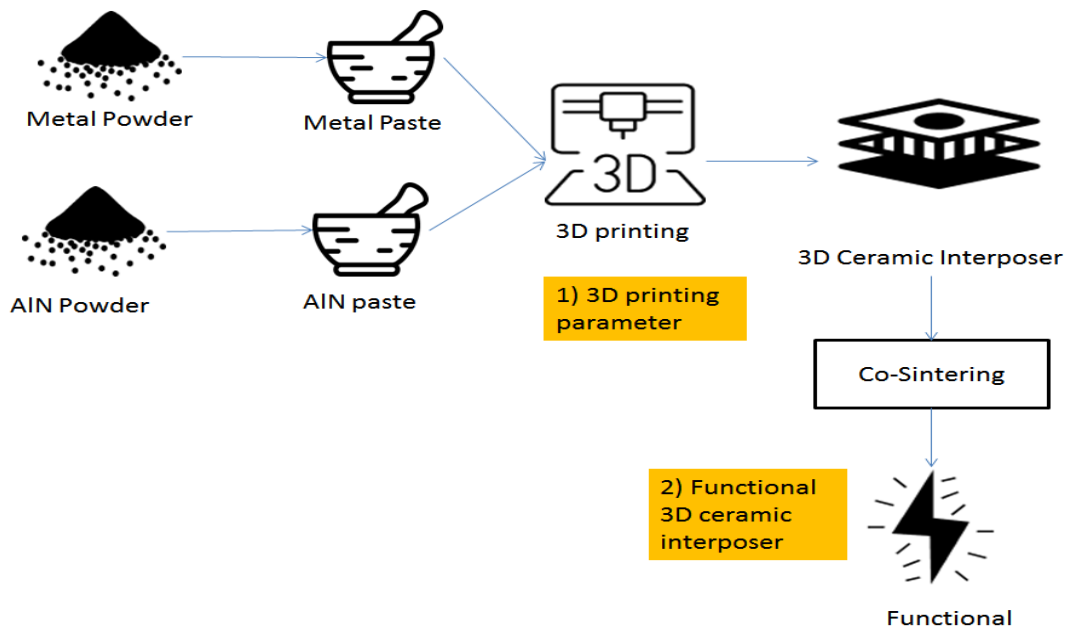


Figure 3.7 Experimental approaches in direct gelcast 3D printing of 3D ceramic interposer.

### 3.3.1 Parameters for direct gelcast 3D printing

The ovalbumin gelcast slurry will solidify when heated up to 80°C and therefore, the base temperature of the 3D printing system is evaluated to achieve optimum layer formation. Separate syringes for different slurry are used to avoid cross-contamination that could affect the final property of the 3D ceramic interposer. The 3D ceramic interposer is built layer by layer using separate slurry syringes concurrently to produce the 3D structure.

The momentum of flow rate,  $\dot{M}$  with  $\rho$  is the fluid density is subject to the following equation (Hoath 2016).

$$\dot{M} = \rho U_{ave}^2 A \quad (3.1)$$

The parameter in the direct gelcast 3D printing include

i) Layer height

Layer height will determine the resolution of the print and depends on the nozzle size of the syringe. The smaller the layer height, the higher is the resolution. The nozzle of the syringe has a diameter of 2mm.

ii) Temperature

The temperature of the base plate can be heated to 140°C and could be tuned to increase the speed of gelation for the ovalbumin slurry.

iii) E-speed

E-speed is the speed of lateral printing. Faster E-speed will increase the resolution but have to be optimized to avoid discontinuity in printing. Too slow E-speed will deposit more material resulting in poorer resolution.

### 3.3.2 Direct gelcast 3D printing of multi-material 3D ceramic interposer

The direct gelcast 3D printing system will be optimized for the printing of different materials in a single process to produce the 3D ceramic interposer followed by co-sintering to form the final interposer with desired properties. Also, the compatibility of the co-sintered multi-material will be evaluated on its compatibility and functionality.

The direct gelcast 3D printing process is used to print a 3D interposer directly from the CAD system with functional circuitry. The functionality of the circuitry is evaluated using a light emitting diode (LED).

## **3.4 Characterization instrument and testing**

The following characterization method is chosen to evaluate and monitor the progress of the research. These characterization methods are used for process monitoring and final product characterization.

### 3.4.1 Density balance

The measurement of the density of the interposer materials is important in providing information on the packing density of the materials that affect the thermal conductivity of the materials. Lattice waves are the dominating factor that



determines the thermal conductivity of insulator (ceramic) that was determined by the packing density of the particles in the interposer. Also, the density data of the sample is required for the measurement of its thermal conductivity.

Density is a physical property of matter and it is based on the mass of the substance occupying a specific space (volume). The symbol for density,  $\rho$  given mathematically as

$$\rho = \frac{m}{V} \quad (3.2)$$

where  $m$  is the mass, and  $V$  is the volume.

For a pure substance, the density is like its mass concentration, and densities of many substances are compared to the density of water. The density balance measures density of materials using the Archimedes' principle (buoyancy method), in which the fluid loss by a body immersed in a fluid is the amount of the weight of the fluid that it displaces. It can be used to determine the density of solids, viscous and pasty substances, as well as liquids.

#### 3.4.2 Thermogravimetric (TGA) characterization

Thermogravimetric analysis (TGA) is an important tool to study the binder decomposition profile of the interposer material. It will give information to optimize the debinding profile and ensure smooth decomposition of binders.

TGA measures the mass loss of the sample with increasing temperature. Besides, it is also able to obtain heat flow information to determine if the events are endothermic or exothermic and provides accurate melting points of high purity

standard reference materials. Temperature range is typically from room temperature up to 1200°C or higher with various purge gases available to make the environment inert or reactive (Prime, Bair, et al. 2009).

The thermo-balance is the critical component of TGA to measure sample mass in relation to temperature and time. A schematic representation of a typical TGA is shown in Figure 3.8.

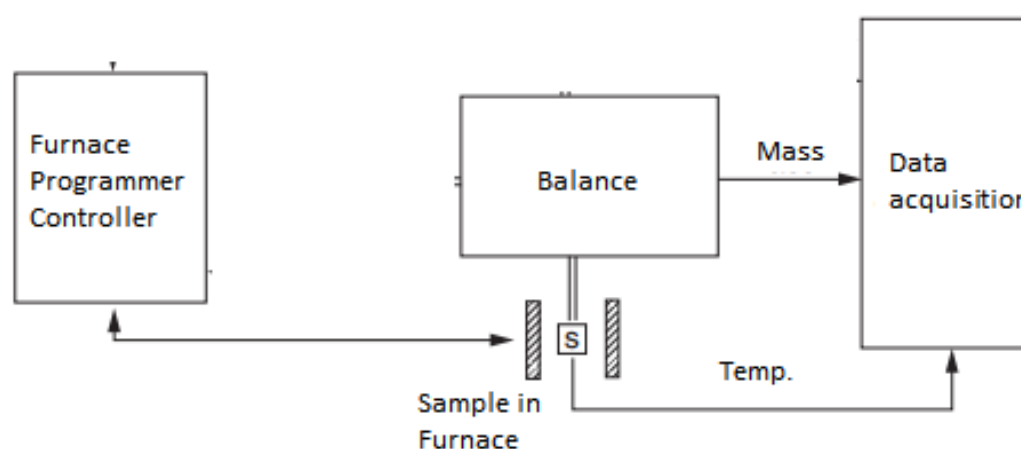


Figure 3.8 Arrangement of components in a TGA.

TGA analysis provides quantitative information on the composition of polymeric materials and the multi-component system. The separation is carried out in different decomposition temperature. Other application of TGA includes measurement of weight loss at a specific temperature and gas environment to determine the groups that are volatilizing, and measurement of total weight loss to determine the mass of the compound present in the sample.

#### 3.4.3 X-ray diffraction (XRD) characterization

X-ray diffraction (XRD) characterization is a non-destructive method to study the

phases of materials and identify potential impurities that are present in the interposer. It will be used to determine the effectiveness of the gelcasting process in preventing metal oxidation, which could affect its electrical performance.

XRD is a powerful tool to identify minerals in complex mixtures. The XRD signal was obtained due to the constructive interference of monochromatic X-rays that was diffracted from the crystal plane of the samples that satisfy Bragg's Law. The x-rays source, generated in the cathode ray tube are filtered to produce monochromatic radiation that collimates to focus the x-ray beam and are directed towards the sample for interaction.

Crystals have long-range order, started with a single repeating unit called the unit cells that will repeat itself billions of times in 3D to form the crystals producing a sharp peak in the XRD pattern. Amorphous materials such as glass only have a short-range order and therefore would not get the same quality of diffraction effects as that of crystals.

The incidence primary X-ray beam will scatter in all direction when it hits the sample if there is no diffraction effect. Therefore, the diffraction phenomena redistribute the intensity from the whole scattering sphere into distinct paths and cause intensity peaks rising in a certain direction, and the paths between peaks and intensity decrease drastically.

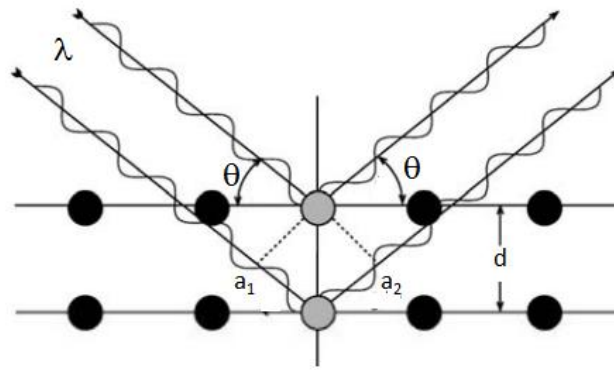


Figure 3.9 Bragg's law.

Figure 3.9 shows the geometric derivation of Bragg's law. Constructive interference, or Bragg reflection, occurs when the path of the two scattered wavelengths in the upper and lower plane vary by an integer number of wavelength  $\lambda$ . It causes a reflection in accordance with the following equation:

$$n\lambda = 2d \sin\theta \quad (3.3)$$

where  $\lambda$  is the radiation wavelength,  $n$  is an integer,  $\theta$  is the angle between the lattice planes and the incident radiation and  $d$  is the distance between the lattice planes that causes diffraction.

XRD patterns are obtained by scanning the  $2\theta$  angles to collect all possible diffraction occurrences that will form peaks as a result of the constructive interference between different lattice planes (d-spacing). As the d-spacing is unique for each type of minerals, it can be identified by comparing with standards, obtained from the International Centre for Diffraction Data (ICDD) powder diffraction file (PDF). The ICDD database (release 2016) has more than 848,000 unique materials represented by the PDF. Each PDF entry has information on the diffraction pattern,

crystallographic data, and information on how the data was obtained.

#### 3.4.4 Flexural strength test

The mechanical property of the interposer is evaluated using flexural strength measurement to obtain information on the physical toughness of the product. As ceramics has very low ductility, the mechanical properties cannot be measured using the conventional tensile test. Therefore, brittle materials such as ceramics are typically tested using the flexural test with the three-point flexural jig (Figure 3.10).

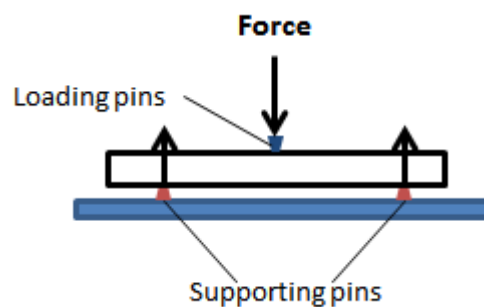


Figure 3.10 Flexural test with 3-point configuration.

The samples are placed on top of two supporting pins that are parallel to each other. A loading force is applied to the middle of the sample until the point of fracture where the force is recorded. When the pin applies force to the sample at the point of fracture, the fracture that occurs as a result of this test is called flexural strength ( $\sigma_{fs}$ ) or modulus of rupture (MOR).

Samples with rectangular cross-section have fracture strength given by (Quinn, Sparenberg, et al. 2009):

$$\sigma_{fs} = \text{MOR} = F_f L / \pi R^3 \quad (3.4)$$

where

- $F_f$  is the load on fracture in N
- $L$  is the length between supporting pins in mm,
- $R$  is the specimen radius in mm

#### 3.4.5 Thermal conductivity measurement

The thermal conductivity of materials directly determines the heat dissipation capability of the ceramics and metals produced. The parameters that determine the ability of materials to store and transfer heat is determined by its thermal conductivity, thermal diffusivity, and specific heat capacity. These values are essential for the modeling of heat transfer and heat management.

The thermal conductivity,  $\kappa$ , governed by Fourier's Law is as follows:

$$\kappa = \frac{Q/A}{\Delta T/L} \quad (3.5)$$

$Q$  = heat flow through the disc

$A$  = area

$\Delta T$  = temperature drop

$L$  = thickness of disc

The thermal conductivity measurement using light or laser flash methods (LFA) has the most extensive measurement range and is suitable for moderate to high conductivity materials. The technique measures the temperature rise from short energy pulse through the thin disc samples (Figure 3.11).

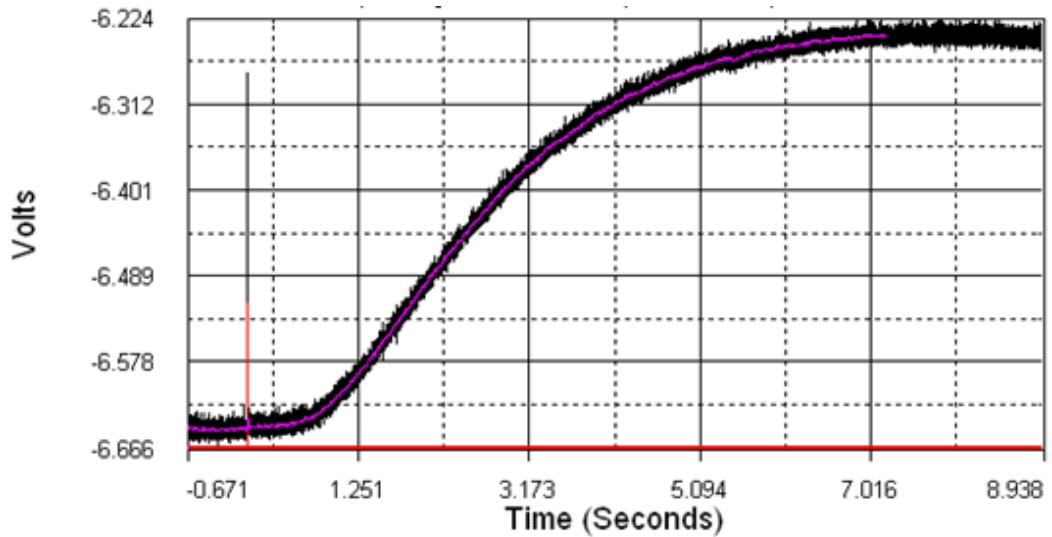


Figure 3.11 Thermogram plot of laser pulse vs time of a typical ceramic sample

It measures the thermal diffusivity ( $\alpha$ ), a ratio of the amount of heat conducted and the amount of heat stored in a sample. The thermal diffusivity results are obtained after fitting the thermogram with theoretical predictions using least squares model and are related to thermal conductivity using the following equation (Koski, 1981):

$$\alpha = \frac{\kappa}{\rho C_p} \quad (3.6)$$

$\rho$  = density of the material

$C_p$  = specific heat capacity at a specific temperature

### 3.4.6 Scanning electron microscope (SEM) characterization

Scanning electron microscope (SEM) observation is important to study the morphology of a product that gives microstructure information to understand the effect of different processing parameters.

Scanning electron microscope (SEM) uses electron as the source of radiation to obtain morphological information of the surface of the sample. It is a powerful magnification tool that produces high-resolution, three-dimensional images to gather information on the topographical, morphological and compositional. The high resolution is because electrons have a wavelength that is shorter than visible light by five orders of magnitude which gave the electron microscopes superior resolving power.

The electron gun in the SEM first generates a beam of energetic electrons that are accelerated down the column and focused using electromagnetic lenses before reaching the sample surface. Figure 3.11 shows the phenomena that can occur when an incident electron hits onto the surface of the sample. When high-speed electrons impact the sample surface, energetic electrons are released, and causes scatter patterns. X-rays that are emitted from the sample surface can give information on the elements that are present on the surface. SEM produces images with a good depth of view with resolution down to 10nm (Claudionico~commonswiki 2013).



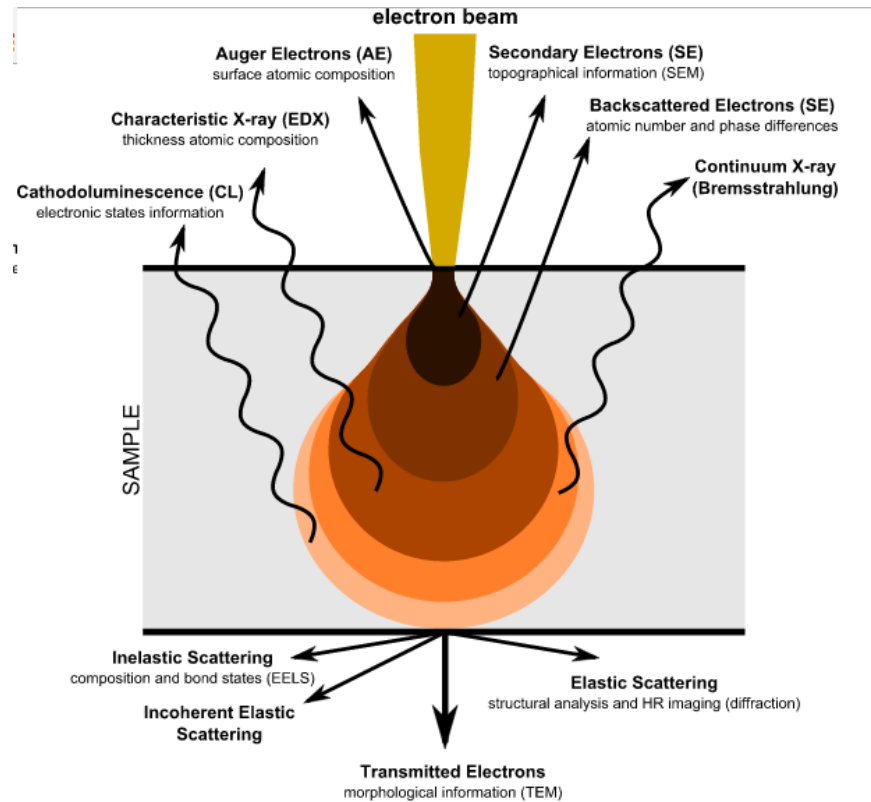


Figure 3.12 Interaction of highly speed electrons on the surface (Claudionico 2013).

### 3.4.7 Four-point probe electrical characterization

The interconnecting metal in the 3D ceramic interposer is used to conduct electricity in a functional circuitry. The four-point probe electrical characterization system can evaluate the electrical performance of these interconnecting metals.

The four-terminal sensing (4T sensing), or 4-point probes, also known as Kelvin sensing, measures the electrical impedance of a sample using a discrete pair of current and voltage electrodes. This configuration is more accurate than the simple two-terminal (2T) sensing device (Bowler N. and Huang Y, 2005). The reason is that the separate current and voltage electrodes can eliminate the lead and consequently contact resistance from the measurement, allowing accurate

measurement at low resistance values. It is the recommended method for measurement of resistance below 100 ohms.

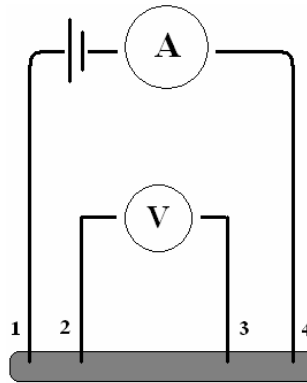


Figure 3.13 Four-point resistance measurements (Vessels, 2007).

Figure 3.12 shows the configuration of a typical 4-point probe system. When current is supplied in a Kelvin connection, the current leads causes a drop in voltages, and the impedance was measured using Ohm's law as follows:

$$V = IR \quad (3.7)$$

The device fabricated is tested by way of electrical conductivity of multiple layers in the device.

#### 3.4.8 Dynamic light scattering (DLS)

The particles size of the powder is important because it will affect the packing density of the final product. Therefore, the highly accurate dynamic light scattering (DLS) system is important to determine the particle size distribution of the incoming raw powders.

Dynamic light scattering (DLS) is used to measure the sizes of particles and its distribution by means of analyzing the temporal fluctuations caused by the intensity of photon auto-correlation function (or quasi-elastic light scattering, QELS). Using the Fourier transform of the time domain, the auto-correlation function (ACF) will decay from zero delay time with the smaller particles having faster dynamics change and faster decorrelation of the scattered intensity. This technique commonly measures particle sizes in the micron region up to 1 nm.

When the laser light hits a particle in the solution, it will scatter in all directions (Rayleigh scattering), and this scattering intensity fluctuates due to Brownian motion over time that will experience constructive or destructive interferences, expressed using the Stokes-Einstein equation (Pecora 2013):

$$D = \frac{kT}{3\pi\eta D_H} \quad (3.8)$$

where  $D$  = Diffusion speed,  $k$  = Boltzman's constant,  $T$  = absolute temperature,  $\eta$  = viscosity, and  $D_H$  = hydrodynamic radius.

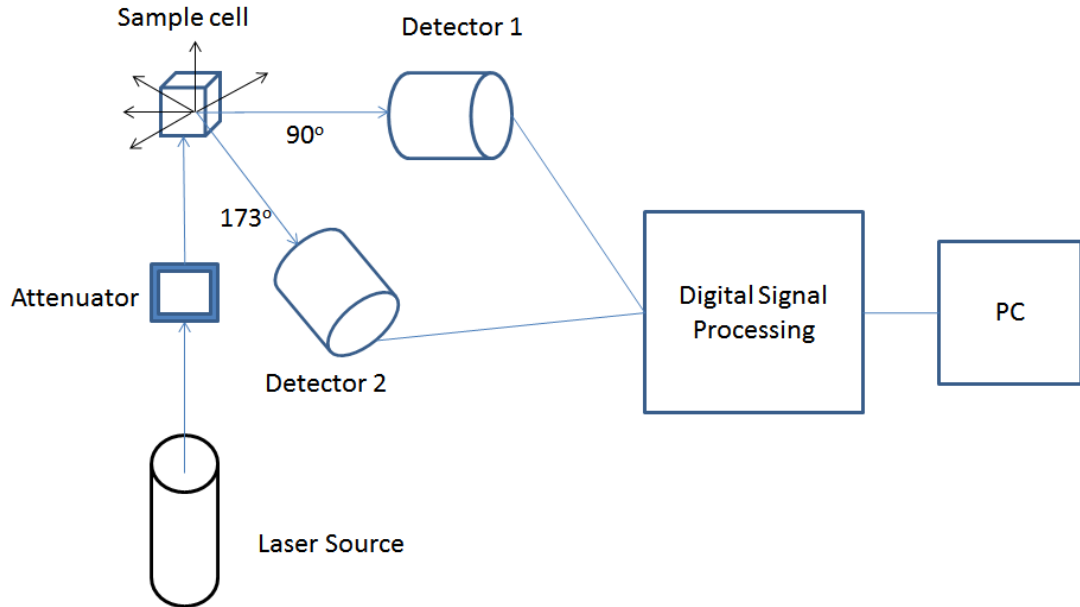


Figure 3.14 Schematic of a typical DLS system.

The instrument setup shown in Figure 3.13 includes a monochromatic light source (typically 250nm laser) that will irradiate and pass through a polarizer before reaching the sample. The DLS system consists of (1) laser, (2) measurement cell, (3) detector, (4) attenuator, (5) PC for data handling. The configuration of the detector is either standard 90° or at a wider angle to increase sensitivity at 173° (Pecora 2013).

#### 3.4.9 Dynamic shear rheometer (DSR)

DSR is used to study the rheology property of the slurry that could help in optimizing the printing parameters in 3D printing. A suitable rheology profile is important for consistent printing of the materials.

Rheology evaluates the material responses to applied forces, stress (force per area), and strain (deformation per length). Stress ( $\sigma$ ), in units of Pascals (Pa), is

dependent on the direction of the force impacting on the surface. Normal stress is when the force is perpendicular to the surface, shear stress for force direction that is parallel to the surface, and strain is the relative deformation of the material (Tabilo-Munizaga and Barbosa-Cánovas 2005).

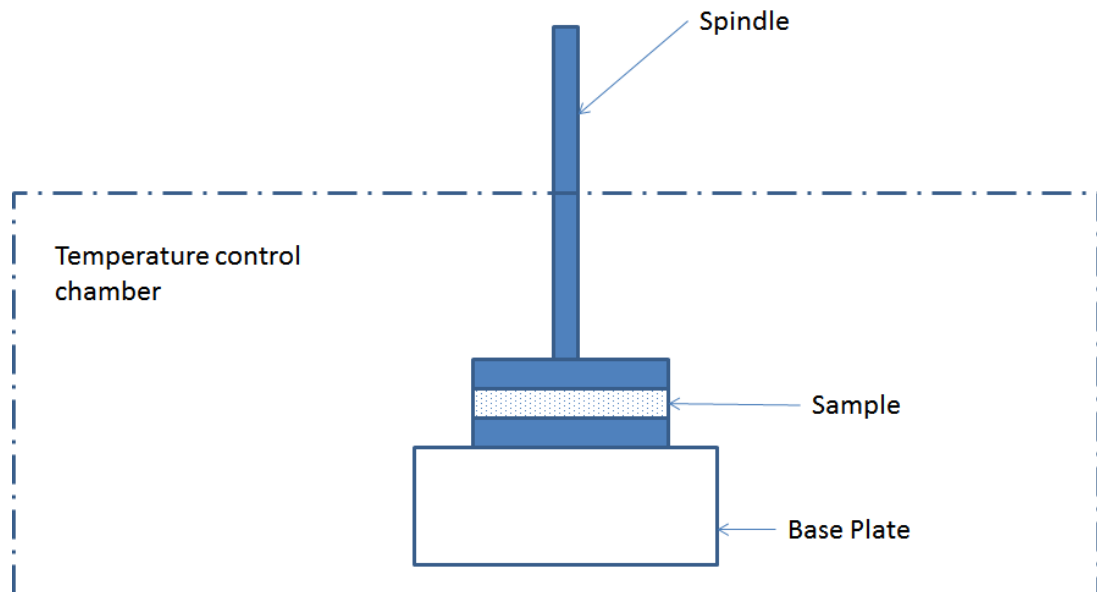


Figure 3.15 Schematic of a DSR system.

Figure 3.14 presents the schematic diagram of the DSR. Samples are placed in between two parallel plates (spindle), where a sinusoidal oscillatory stress-strain force are applied and the corresponding force and deformation as a function of time are measured (Airey, Hunter, et al. 2002).

The parameters obtained from the dynamic rheological tests includes  $G'$  (storage modulus) and  $G''$  (loss modulus).  $G'$  is the measurement of stored deformation energy and  $G''$  is the deformation energy used in the sample that represents the elastic behavior and viscous behavior of the sample accordingly. The loss factor,

$$\tan \delta = \frac{G'}{G''} \quad (3.9)$$

where  $\delta$  is the phase angle.

The sample is said to be elastic, more like a solid if  $G' \gg G''$  and more like a liquid (viscous) if  $G'' \gg G'$  (Rao, 1999). Therefore,  $\tan \delta = 0$  indicate an elastic response while  $\tan \delta = \infty$  represent a viscous response. The material is viscoelastic when the phase angle,  $\delta$  is within  $0 < \delta < 90^\circ$  (Schramm 1994).

Fluids can be classified as solids, gels, suspension, and emulsions. It has no shape of its own and will take the form of the container. The flow of fluids that causes deformation under normal and tangential stresses describes the rheological properties of the fluid and viscosity is the parameter used to measure the internal friction or tendency of the fluid to resist flow. In Newtonian fluids, the shear rate is directly proportional to the shear stress, while all other types of fluids are categorized as the non-Newtonian type (Kamal, M. R., and Mutel, A. 1985).

# Chapter 4 Green gelcasting of aluminum nitride (AlN) ceramics substrate

## 4.1 Introductory remarks

Both aluminum nitride (AlN) and beryllium oxide (BeO) ceramics are widely used in high-performance electronic application that requires good heat dissipation characteristic due to their excellent thermal conductivity values. The BeO powder has better thermal conductivity than AlN but is toxic, which restricted its use (Chen, Perisse, et al. 1994). On the other hand, AlN is non-toxic and is the preferred material for use as high-performance dielectric material. Some characteristics of AlN are high thermal conductivity and high electrical resistivity, low dielectric constant, high dielectric strength and CTE that matches silicon (Watari, Hwang, et al. 1996).

The aqueous-based additives were introduced into ceramic processing due to its environmental-friendly characteristic. This approach includes aqueous-based additives for injection molding (Fanelli, Silvers, et al. 1989), tape-casting (Yuping, Dongliang, et al. 2000) and gelcasting (Omatete, Janney, et al. 1991). The gelcasting process was first developed by Omatate et al. (Omatete, Janney, et al. 1991) in 1991 to solve the problems related to injection molding processes. Gelcasting is a near-net-shape process that is superior to other casting methods such as slip casting, pressure casting and injection molding (Janney, Omatete, et al. 1998).

The original gelcasting formulation include the acrylamide,  $C_2H_3CONH_2$  and difunctional  $N,N'$ -methylenebisacrylamide,  $(C_2H_3CONH)_2CH_2$  (MBAM) monomer, ammonium persulfate  $(NH_4)_2S_2O_8$  as the initiator to promote the free-radical initiated vinyl polymerization and  $N,N,N',N'$ -tetramethylethylenediamine (TEMED) as the catalyst to form cross-linked polymer to bind the ceramic powder (Young, Omatete, et al. 1991). The hydrogel is not toxic, but the monomer, acrylamide is a known neurotoxin (Omatete, Janney, et al. 1991). The drive to replace this poisonous monomer has encouraged the development of nontoxic natural protein system such as polysaccharides, as a gelcasting monomer (Millán, Moreno et al. 2002), egg white (Dhara and Bhargava 2001), agarose (Adolfsson 2006); protein such as bovine serum albumin (BSA), albumen, and whey protein concentrate (WPC) (Lyckfeldt, Brandt, et al. 2000). The advantage of using ovalbumin as the gelcasting binder is that there is no requirement for any initiator or catalyst for the gelation. Also, ovalbumin is a natural, nontoxic protein that is obtained from a sustainable source (He, Su, et al. 2011). The gelation of ovalbumin is purely initiated by heat energy. When ovalbumin is heated to a temperature of  $80^\circ C$ , individual ovalbumin protein molecules start to denature and forms a covalent bonded gel network (Mine 1995). The previous study on the gelcasting of AlN includes usage of an aqueous binder (Jian, Tai, et al. 2012) and non-aqueous binders such as sorbitol polyglycidyl ether/ tetraethylenepentamine (Jianfeng, Manjiang, et al. 2010) and 1-methyl-2-pyrrolidinone (Shen, Xu, et al. 2016) processes.



## 4.2 Experimental

### 4.2.1 AlN feedstock preparation

The AlN ceramic slurry was prepared according to the process shown in Figure 4.1. The preparation of the ovalbumin binder starts with separating ovalbumin from egg-yolk in raw egg. Then, 1 wt% of silicon oil (Unichem), as the froth reducing agent, was added to this mixture. The ovalbumin mixture was stirred for 30 minutes with a magnetic stirrer and this mixture is used as the binding solution for the ceramic powder.

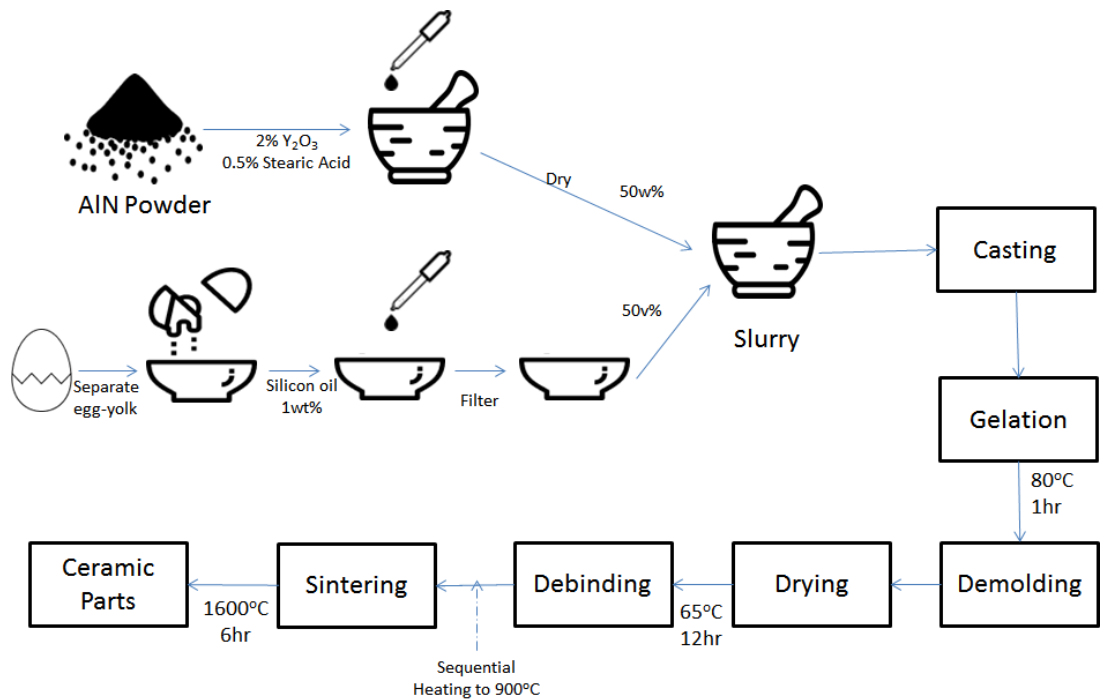


Figure 4.1 Gelcasting of AlN ceramics with ovalbumin monomer.

For the preparation of the AlN powder, the AlN powder obtained from HWNano, China, with particle sizes of 0.1 $\mu$ m, 0.5 $\mu$ m, 1 $\mu$ m, 3 $\mu$ m, and 5 $\mu$ m and the combination thereof has been investigated as shown in Table 4.1.

Table 4.1 Mixing of AlN powder with different particle sizes.

Type of mixing	Aluminum Nitride (AlN) particle sizes
Unimodal	0.1 $\mu$ m
	0.5 $\mu$ m
	1 $\mu$ m
	5 $\mu$ m
Bimodal	0.1 $\mu$ m & 0.5 $\mu$ m
	0.1 $\mu$ m & 1 $\mu$ m
	0.1 $\mu$ m & 5 $\mu$ m
	0.5 $\mu$ m & 1 $\mu$ m
	0.5 $\mu$ m & 5 $\mu$ m
	1 $\mu$ m & 5 $\mu$ m
	3 $\mu$ m & 5 $\mu$ m
Trimodal	0.1 $\mu$ m & 0.5 $\mu$ m & 1 $\mu$ m
	0.1 $\mu$ m & 0.5 $\mu$ m & 5 $\mu$ m
	0.1 $\mu$ m & 1 $\mu$ m & 5 $\mu$ m
	0.5 $\mu$ m & 1 $\mu$ m & 5 $\mu$ m
Quad-modal	0.1 $\mu$ m & 0.5 $\mu$ m & 1 $\mu$ m & 5 $\mu$ m

The AlN powder mixtures were added with 2 wt % Y<sub>2</sub>O<sub>3</sub> powder (Acros, 99.99%) as the sintering aid, 10 w% of PEG-4000 (Unichem) as the dispersant agent and 0.5 %wt of stearic acid/ethanol (Arachem) were mixed in a mortar pestle for 15 min. Finally, 50 wt% ovalbumin premix was added and mixed in the mortar pestle for 15 min to form the ceramic slurry. Figure 4.2 shows the slurry is thick but can flow into molds for casting to form different shapes and sizes. As a control comparison, aluminum oxide powders were prepared using a similar method.



Figure 4.2 AlN/ovalbumin gelcasting slurry.

#### 4.2.2 Casting

The ceramic slurry prepared as described previously in section 4.2.1 is poured into the designated metal mold, followed by heating to 80°C for 1 hour to initiate gelation (Figure 4.3). The gelcast is demolded after cooling to room temperature and dried in an oven at a temperature of 65°C for 6 hours (green body). The green body that is formed at this stage has sufficient strength for light machining and polishing with improved surface characteristics.

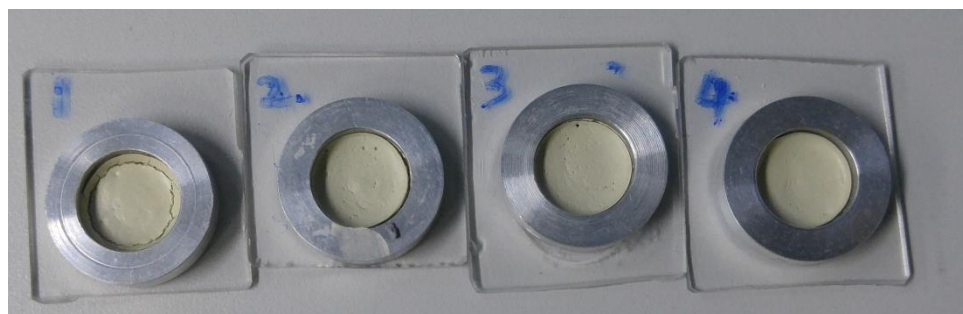


Figure 4.3 Gelcasted AlN ceramics.

The green body is then subjected to debinding and sintering using the PT1700 Atmosphere Furnace from Zhengzhou Protech with a 5°C per min heating rate in 0.08MPa nitrogen atmosphere. The debinding and sintering profile is shown in Figure 4.4.

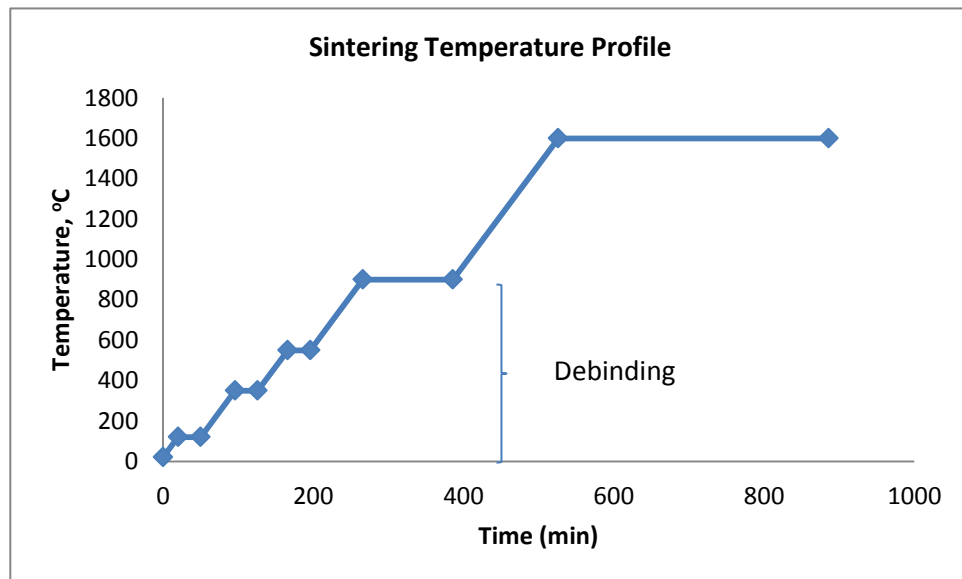


Figure 4.4 Debinding and sintering profile of AlN/ovalbumin ceramics (Dhara and Bhargava 2001).

#### 4.2.3 Characterization

The particle size of the AlN powder is analyzed using dynamic light scattering (DLS) system; model Zetasizer Nano ZS from Malvern Instruments.

The rheology of the ceramic slurries was characterized using a dynamic shear rheometer (MCR702, Anton Paar, Austria) using a pair of 50 mm diameter parallel plate and pre-sheared at 100 s<sup>-1</sup> for 10s at a temperature of 25°C prior to the measurement. The measurement was from 0.1 to 1000 s<sup>-1</sup>.

Thermogravimetry analyzer, TGA (TGA/DSC 3+, Mettler Toledo) is used to study the binder degradation to determine the debinding profile of the binder. The weight loss of the sample is measured when heated from 25°C to 1000°C at a heating rate of 10°C per min in the 0.1 MPa nitrogen atmospheres.

The X-ray diffractometer (XRD), Rigaku SmartLab, is used to determine the type of crystal phases that is present in the samples. The X-ray source used monochromatic Cu K $\alpha$  (0.15418 nm) with 2 $\theta$  scan range from 20 – 80 deg at a step size of 0.02 deg and a scanning speed of 5 deg per min. The XRD pattern is matched with data from the International Centre for Diffraction Data (ICDD) PDF-2 to determine the crystalline phase present in the sample.

A fused deposition modeling machine (FDM) model (Flashforce 3D Printer) is used to 3D print the plastic mold for flexural strength measurement with a cavity of 5x2x1 mm. The three-point bending experiment is conducted using Instron Model 5565 at 0.5 mm per min crosshead speed, and the flexural strength is determined from the displacement curve.

The Flashline TM 2000 thermal conductivity measurement apparatus is used to determine the thermal conductivity of the sample using Pyroceram as the drift correction standard. The density balance, JA203M (Changzhou Xingyun Electronic Equipment Co., Ltd), based on the Arrhenius method was used for density measurement of the samples. The scanning electron microscope (SEM), VEGA 3 (Tescan) is used to study surface morphology and microstructures of the samples.

## 4.3 Results and discussions

### 4.3.1 AlN/ovalbumin ceramic slurry

Figure 4.5 shows the particle size of the AlN powder obtained from HWNano, China, measured using Malvern Zetasizer Nano ZS. The size distribution is found to be within the specified particle size range reported by the supplier.

The rheology characterization of bimodal AlN/ovalbumin ceramics slurry (0.5  $\mu\text{m}$  & 1  $\mu\text{m}$  and 3  $\mu\text{m}$  & 5  $\mu\text{m}$ ) is shown in Figure 4.6.

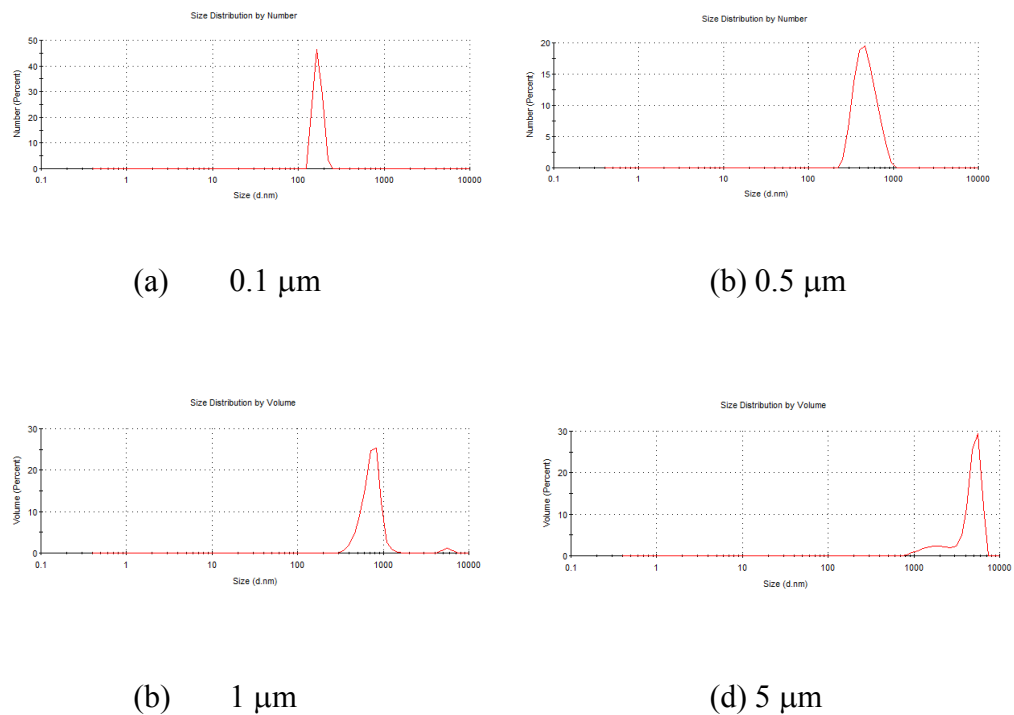


Figure 4.5 AlN powders: (a) 0.1  $\mu\text{m}$ , (b) 0.5  $\mu\text{m}$ , (c) 1.0  $\mu\text{m}$ , and (d) 5.0  $\mu\text{m}$ .

The figure shows that as the shear rate increases, the viscosity decreases, which is consistent with the shear thinning characteristic of non-Newtonian fluid (Kamal, M. R., and Mutel, A. 1985).

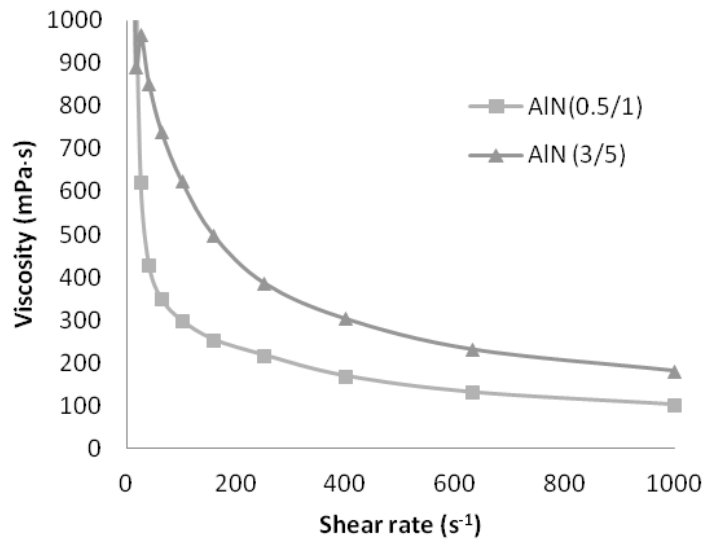


Figure 4.6 Viscosity of AlN/ovalbumin slurry with different particle size.

The AlN bimodal slurry of 0.5  $\mu\text{m}$  & 1  $\mu\text{m}$  mixture has lower viscosity as compared to the bimodal mixture of 3  $\mu\text{m}$  & 5  $\mu\text{m}$  (298 mPa·s vs 624 mPa·s). The lower viscosity is due to smaller particles having more surface area in contact with the liquid phase that resembles suspension with lower concentration.

#### 4.3.2 Gelcasted AlN ceramics

Figure 4.7 shows the XRD pattern of the ovalbumin gelcasted AlN ceramics. The main phases identified in the pattern are AlN and the aluminum yttrium oxide phase. The yttrium oxide ( $\text{Y}_2\text{O}_3$ ) is used as the sintering aid to increase the densification of AlN. It is removed in the form of the gas at the final sintering stage. First, it will undergo liquid phase densification with AlN by reacting with the  $\text{Al}_2\text{O}_3$  molecules that are present the AlN surface to form AlN- $\text{Al}_2\text{O}_3$ - $\text{Y}_2\text{O}_3$  liquids. The

oxygen content is lowered by precipitation of yttrium and  $Y_2O_3-Al_2O_3$  compounds in the grain boundary followed by vaporization to improve thermal conductivity (Watari, Hwang, et al. 1999).

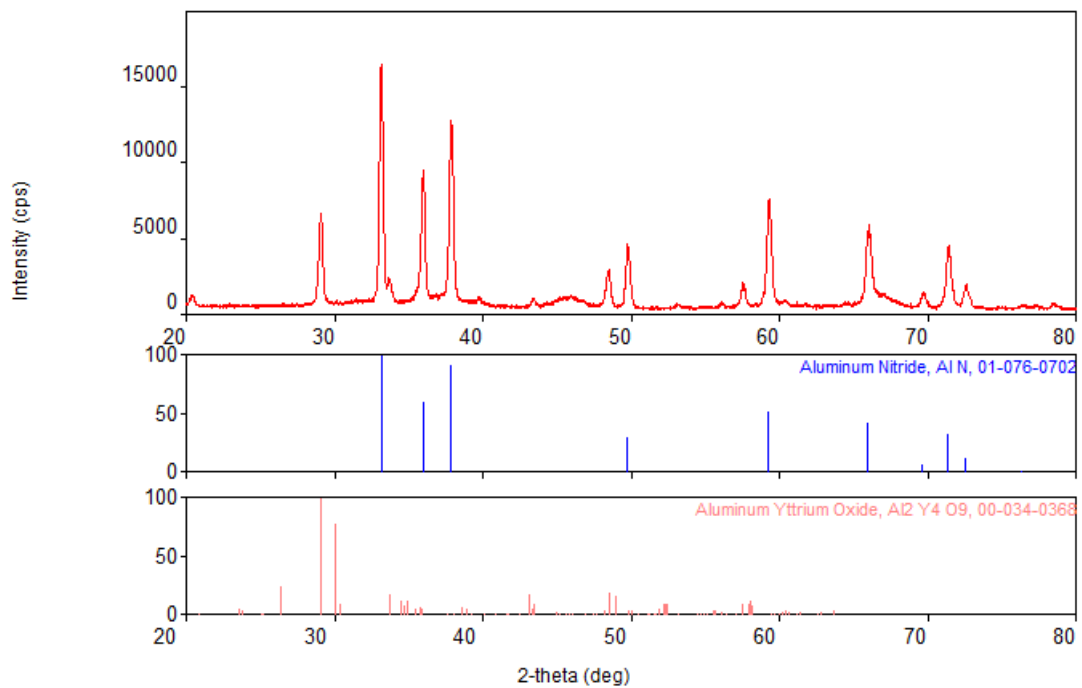


Figure 4.7 XRD pattern of AlN/ovalbumin gelcast.

The analytical method used for studying the progress of hydrolysis on AlN particles reported in the literature is XRD and can be broken down into three stages (Kocjan, Dakskobler, Krnel, & Kosmač, 2011). The first stage is the induction stage with only a very thin layer of 3nm thick amorphous gel was formed on the surface of the AlN. The actual progression of hydrolysis is in the second stage, where the hydrolysis rate is accelerated to form a porous layer of boehmite particles ( $\gamma$ -AlO(OH)) and finally the last stage of hydrolysis involve the formation of



bayerite  $\text{Al}(\text{OH})_3$  in the shape of large conical somatoids.

AlN has been reported to be easily hydrolyzed in the presence of moisture to form the  $\gamma\text{-AlOOH}$ ,  $\text{Al}(\text{OH})_3$  or  $\gamma\text{-Al}_2\text{O}_3$  species that could lower the thermal conductivity of the AlN ceramics (Nicolaescu, Tardos, & Riman, 1994). Ovalbumin consists of 80% water, and since 50% of ovalbumin mixtures are used to prepare the ceramic slurry, 40% of the slurry comprises of water. However, AlN does not react readily at room temperature with the  $\gamma\text{-AlOOH}$  phase and are formed only when heated for more than  $100^\circ\text{C}$ . It will only be converted to the oxide phases after prolonged contact with water: 80% of AlN was hydrolyzed after 24 hours in contact with water, and the crystalline phase of bayerite,  $\text{Al}(\text{OH})_3$  was detected after 16 hours of contact with water (M. He, et al. 2002). Stearic acid was reported to be effective in creating a protective layer to passivate metal and ceramic particles (Kwon, Gromov, et al. 2007). The hydrolyzed phases of AlN were not observed in the XRD analysis indicating that there was no apparent hydrolysis of AlN. Therefore, the addition of stearic acid is shown to be useful in creating a protective layer to passivate the AlN particles.

Ceramics generally has very low ductility, and therefore, the conventional tensile test method for metals is not suitable for determining its mechanical strength. Flexural strength test would be a suitable test for the strength of brittle materials such as ceramics (Ćurković, Bakić, et al. 2010). The flexural strength of the ovalbumin gelcasted AlN green body is only 3 MPa but it is sufficient for light post-processing. The result is similar to the flexural strength of the alumina green body

reported by X.He et al. (He, Su, et al. 2011). One of the significant issues with ceramic processing is the huge time consumed and the high cost of post-processing after sintering. Therefore, post-processing of the green body is preferred compared to sintered ceramics. Also, some of the problems related to the post-processing of hard sintered ceramics are chipping (Song and Evans 1997) and sub-surface microcracks due to its brittleness (Monaghan and Brazil 1997).

Fig. 4.8 shows the TGA profile of the ovalbumin gelcasted AlN green body. It can be observed that decomposition started at 200°C and ended at 625°C, and consists of 3 steps. The first decomposition is a slow decay and has a weight loss of 2.4 % (25°C to 235°C), followed by the second decomposition having a weight loss of 8.6 % (235°C to 375°C) and the final, the third decomposition domain has a weight loss of 7.6 % (375°C to 625°C).

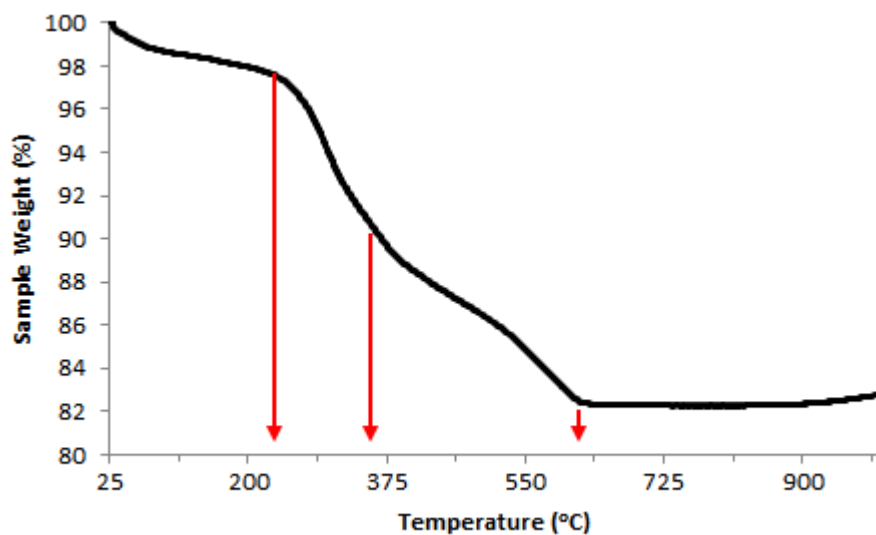


Figure 4.8 TGA analysis of AlN/ovalbumin gelcast.

The first decomposition domains from 25°C to 235°C are mainly due to water evaporation and decomposition of stearic acid and partial decomposition of PEG. The second decomposition domains from 235°C to 375°C are primarily due to the decay of PEG, ovalbumin and silicon oil. The third decomposition domains from 375°C to 625°C are mostly due to the decay of PEG, ovalbumin and silicon oil.

Stearic acid has a boiling point of 198°C, and in the nitrogen atmosphere, the degradation of stearic acid occurs at a range from 175°C to 275°C with two endotherms, melting at 70°C and the highest rate loss happens at 265°C. This decomposition domain corresponds to the combustion and subsequent volatilization of organic species such as CH<sub>3</sub>COOH from stearic acid (Bagheri, Shameli, et al. 2013).

PEG has a melting point of 40°C and is stable at a temperature below 400K (127°C). It will start decomposing at 350°C and complete decomposition at temperatures above 450°C (Kou, Wang, et al. 2019). In the previous study reported by Knapp et al. (Knapp and Halloran 2006), the PEG degradation in inert nitrogen atmosphere, starts with the first 4% mass loss that happened at the temperature range from 40°C to 285°C, followed by majority of the mass loss from 285°C to 410°C, and the final 1.5 wt% organics pyrolyzed within the temperature range of 415°C to 500°C.

The first exothermic peak for ovalbumin is reported to be at 330°C, due to the oxidative decomposition of ovalbumin, and the second decomposition is at a temperature of 560°C and 630°C (Dhara 2005).

For silicon oil, there is two domain of decomposition. The first domain is up to 350°C, where volatile matters were volatilized at this temperature. The second domain is from 350°C to 700°C that indicate the presence of different volatile matters which decompose at different temperature zones (Mehmet 2008).

#### 4.3.3 AlN particle size mixing

Table 4.2 shows the thermal conductivity result of the AlN particle size mixing. It is observed that bimodal particle size mixing of a ratio of 1.5 (3 μm & 5 μm) to 2 (0.5 μm & 1μm) have the highest thermal conductivity value. The reason is that bimodal particle size distribution has better packing efficiency as smaller half-sized particles can fit nicely onto the interstitial spaces between larger particles (Hong, Yoon, et al. 2012).

Table 4.2 Thermal conductivity measurement of AlN ceramics.

Type of mixing	AlN particle size	Thermal Conductivity (TC) W/mK	Specific Heat (J/kg.K)
Unimodal	0.1μm	12	847.2
	0.5μm	8	906.3
	1μm	8	898.5
	5μm	8	769.8
Bimodal	0.1μm & 0.5μm	11	838.9
	0.1μm & 1μm	14	793.0
	0.1μm & 5μm	11	931.1
	0.5μm & 1μm	18	813.2
	0.5μm & 5μm	9	387.6
	1μm & 5μm	8	942.6
	3μm & 5μm	17	904.3
Trimodal	0.1μm & 0.5μm & 1μm	10	813.0
	0.1μm & 0.5μm & 5μm	12	787.8
	0.1μm & 1μm & 5μm	15	829.0
	0.5μm & 1μm & 5μm	10	718.1
Quad-modal	0.1μm & 0.5μm & 1μm & 5μm	13	790.8

This result correlates well with the simulation result of Shi et al. (Shi and Zhang 2008), conducted using spherical particles that are mono-size, bimodal and Gaussian distribution based on a loose packing numerical simulation model to conclude that higher packing density is obtained when the optimum ratio of particle size is 1.5 to 2. The computation method uses dropping and rolling rules when a sphere was dropped into a dimension-specified box from a random selection of sphere pre-generated from a continuous particle-sized distribution. The sphere was first given a random  $(x,y)$  and  $z$  starts from the top of the box. The computation starts with each sphere moving on a linear trajectory, i.e.  $(x,y)$  constant and  $z$  are decreasing until the sphere touches the floor or on another sphere. If the sphere touches the floor, it is its final position, and if it touches another sphere, rolling rules apply. Using the rolling rules, the sphere will roll down vertically, downward touching two spheres. Once it touches the third sphere, the status is examined to ensure a stable position and avoid gravity potential. When the sphere stabilizes, the final position is fixed and a new sphere is generated, and the process continues. Also, the model uses periodic boundaries to prevent the problem with wall effects as a smooth wall will induce partial ordering during packing. The result shows that a larger ratio of particle size has higher packing density because small particles can fit into voids that are left by bigger particles and reduces the coordination number significantly.

The results also indicate that multi-modal distributions have thermal conductivity up to 2 times higher than that of unimodal distributions. In the case of large ratio of particle size, i.e. 2.0 and 3.0, a higher amount of small particles will

increase the packing density and coordination number but this phenomenon is less obvious for smaller particle size ratios of 1.1 and 1.5. At higher particle size ratios, although large particle that is in contact with many small particles have higher coordination number, this situation reduces the contact points of small particles and causes overall smaller average coordination number. Even though a higher packing density is generally important, however, for ceramic sintering, the low coordination number will cause loose contact of particles that lowers the strength and therefore, thermal conductivity of the ceramics.

Table 4.3 shows the thermal conductivity measurement of AlN ceramics prepared and sintered at a different time to determine the repeatability of the ovalbumin gelcasted AlN process. The results show a variation of standard deviation between 0 to 3 W/mK. The thermal conductivity of the optimum bimodal mixture of 0.5  $\mu\text{m}$  & 1  $\mu\text{m}$  ranges from 14 W/mK to 18 W/mK or  $\pm 12.5\%$ . Shinzato and Baba (Shinzato and Baba 2001) reported the accuracy of the laser flash method to be  $\pm 3\%$  for thermal conductivity,  $\pm 2\%$  for thermal diffusivity and within 1% for the specific heat of molybdenum. Therefore, the precision of producing high thermal conductivity ovalbumin gelcasted AlN ceramics within  $\pm 10\%$  is acceptable for commercial applications. As the thermal conductivity measurement is a critical parameter to evaluate the effectiveness of the material for heat dissipation performance, information such as the thermogram plot (laser signal against time) in the sample report might be used for the understanding of the sample condition (refer to section 3.4.5). A sample thermal conductivity measurement report, for a

unimodal AlN sample with a thermal conductivity value of 11.19 W/mK is shown in Appendix I. All the thermal conductivity measurement in this research has a similar report.

Table 4.3 Repeatability of thermal conductivity measurement.

Mixing type	Particle sizes	Thermal Conductivity (TC) W/mK				
		Aug-16	Sep-16	Nov-16	Average	Standard Deviation
Unimodal	0.1 $\mu$ m	11	-	12	12	0.5
	0.5 $\mu$ m	8	-	8	8	0
	1 $\mu$ m	-	8	5	6	3
	5 $\mu$ m	8	-	8	8	0
Bimodal	0.1 $\mu$ m & 0.5 $\mu$ m	9	-	11	10	2
	0.1 $\mu$ m & 1 $\mu$ m	11	-	14	12	2
	0.1 $\mu$ m & 5 $\mu$ m	13	11	13	12	1
	0.5 $\mu$ m & 1 $\mu$ m	16	14	18	16	2
	0.5 $\mu$ m & 5 $\mu$ m	8	8	-	8	0
	1 $\mu$ m & 5 $\mu$ m	-	-	8	8	-
Trimodal	0.1 $\mu$ m & 0.5 $\mu$ m & 1 $\mu$ m	10	-	-	10	-
	0.1 $\mu$ m & 0.5 $\mu$ m & 5 $\mu$ m	-	12	12	12	-
	0.1 $\mu$ m & 1 $\mu$ m & 5 $\mu$ m	-	12	15	14	2
	0.5 $\mu$ m & 1 $\mu$ m & 5 $\mu$ m	-	-	10	10	-
Quad-modal	0.1 $\mu$ m & 0.5 $\mu$ m & 1 $\mu$ m & 5 $\mu$ m	11	13	-	12	1.5

The physical characteristics of the AlN/ovalbumin particle mixing are shown in Table 4.4. The theoretical density of AlN is  $3.26 \text{ g/cm}^3$ , based on the cell dimensions  $a = 3.111 \text{ \AA}$  and  $c = 4.980 \text{ \AA}$  (Taylor and Lenie 1960). Sintering at  $1600^\circ\text{C}$  significantly increases the density of the AlN ceramics from 50 % to 80 %. The shrinkage of the AlN ceramics ranges from 12 % to 20% and porosity of the ovalbumin gelcasted AlN ceramics ranges from 40 % down to 14 %.

Table 4.4 The density, porosity, shrinkage and thermal conductivity results of different AlN particle mixing.

Type of particle mixing	Aluminum Nitride (AlN) particle sizes	Density before sintering ( $\text{g/cm}^3$ )	Density after sintering ( $\text{g/cm}^3$ )	Relative Density (before sintering) (%)	Relative Density (after sintering) (%)	Porosity (%)	Shrinkage (%)	Thermal Conductivity (W/mK)
Unimodal	0.1 $\mu\text{m}$	1.658	2.630	51	81	19	18	12
	0.5 $\mu\text{m}$	1.189	2.263	36	69	31	16	8
	1 $\mu\text{m}$	1.213	2.460	37	75	25	20	8
	5 $\mu\text{m}$	1.185	2.336	36	72	28	13	8
Bimodal	0.1 $\mu\text{m}$ & 0.5 $\mu\text{m}$	1.472	2.581	45	79	21	15	11
	0.1 $\mu\text{m}$ & 1 $\mu\text{m}$	1.628	1.970	50	60	40	17	14
	0.1 $\mu\text{m}$ & 5 $\mu\text{m}$	1.531	2.801	47	86	14	13	13
	0.5 $\mu\text{m}$ & 1 $\mu\text{m}$	1.589	2.675	49	82	18	18	18
	0.5 $\mu\text{m}$ & 5 $\mu\text{m}$	1.357	2.536	42	78	22	18	8
	1 $\mu\text{m}$ & 5 $\mu\text{m}$	1.753	2.543	54	78	22	16	8
	3 $\mu\text{m}$ & 5 $\mu\text{m}$	1.715	2.640	53	81	19	17	17
Trimodal	0.1 $\mu\text{m}$ & 0.5 $\mu\text{m}$ & 1 $\mu\text{m}$	1.584	2.397	49	74	26	19	10
	0.1 $\mu\text{m}$ & 0.5 $\mu\text{m}$ & 5 $\mu\text{m}$	1.590	2.705	49	83	17	20	12
	0.1 $\mu\text{m}$ & 1 $\mu\text{m}$ & 5 $\mu\text{m}$	1.472	2.472	45	76	24	14	15
	0.5 $\mu\text{m}$ & 1 $\mu\text{m}$ & 5 $\mu\text{m}$	1.208	2.220	37	68	32	12	10
Quad-modal	0.1 $\mu\text{m}$ & 0.5 $\mu\text{m}$ & 1 $\mu\text{m}$ & 5 $\mu\text{m}$	1.607	2.471	49	76	24	18	13



The porosity was calculated with the assumption that all voids were filled with air using the following equation (Morrow and Lockner 2001):

$$\emptyset = 1 - \frac{\rho^{bulk}}{\rho^{particle}} \quad (4.2)$$

Figure 4.9 shows the effect of the bimodal ratio and nanoparticles on the thermal conductivity performance of the AlN ceramics. The AlN ceramics produced using nanoparticle AlN (0.1  $\mu\text{m}$ ) show better thermal conductivity value compared to micron-sized particles. This is because the nano-sized particles can adequately fill the interstitial void in the powder packing that improved packing density and thermal conductivity.

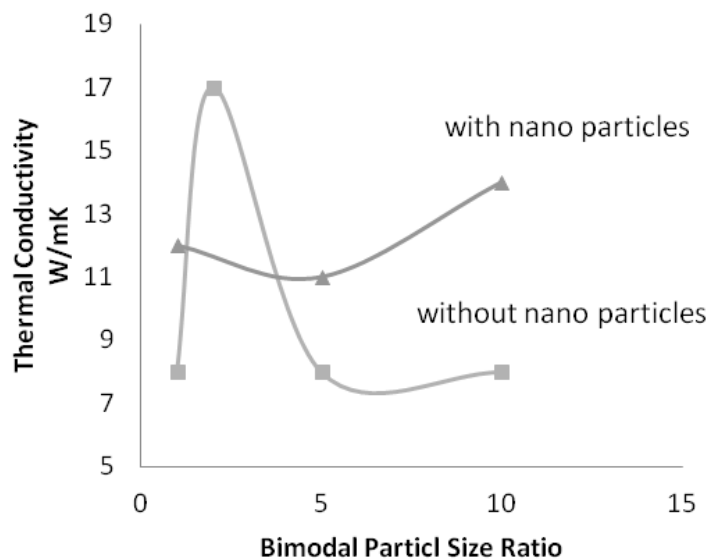


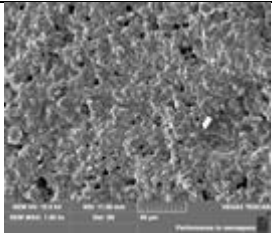
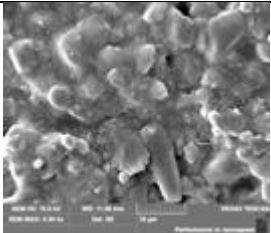
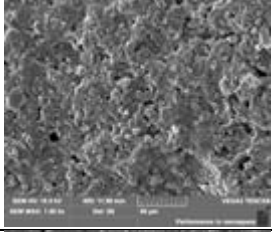
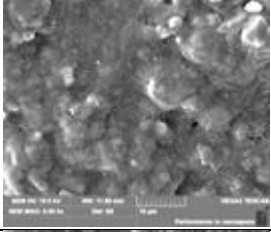
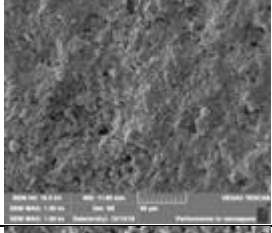
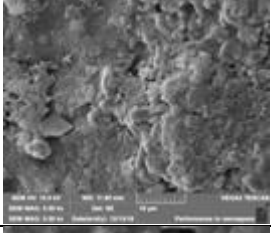
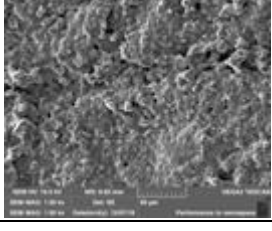
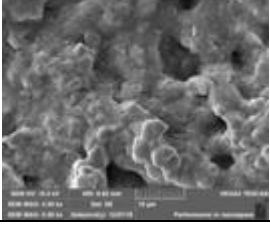
Figure 4.9 Effect of nanoparticles on the thermal conductivity of AlN ceramics.

Table 4.5 shows scanning electron microscope (SEM) images of the gelcasted AlN ceramics at a magnification of 1,000x and 5,000x respectively. It is observed

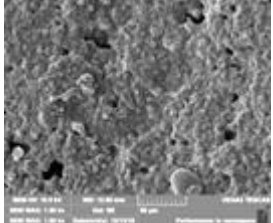
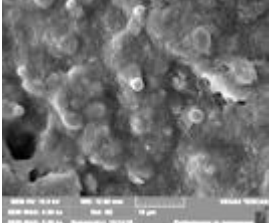
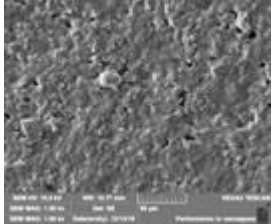
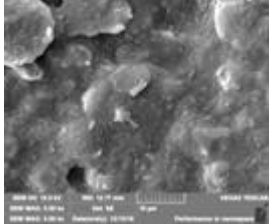
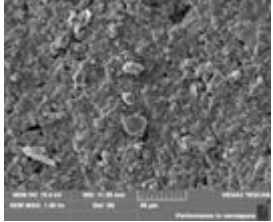
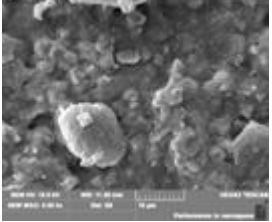
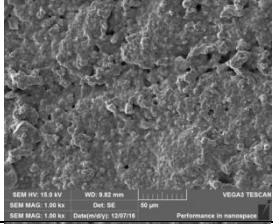
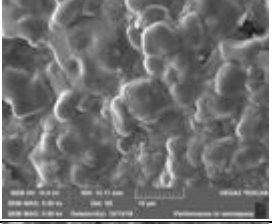
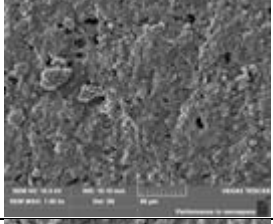
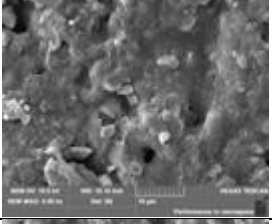
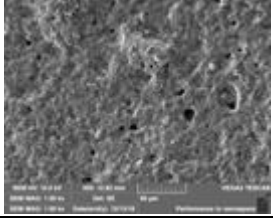
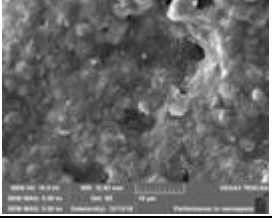
that samples with high thermal conductivity have more compact microstructures due to better packing efficiency. There were loose particles observed with unimodal distributions except for nano-sized AlN. The SEM images show that samples with higher thermal conductivity have a more compact structure, which is consistent with better packing density.

Table 4.5 SEM images of AlN ceramics with different particle size mixing.

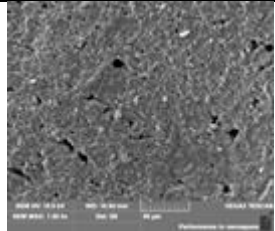
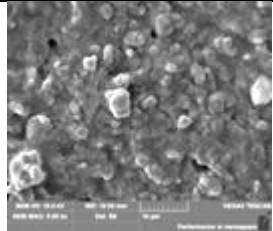
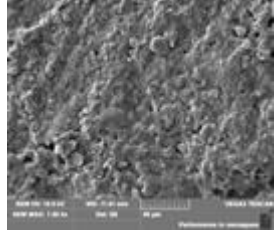
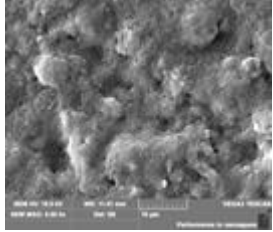
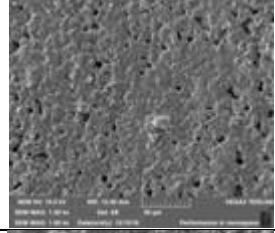
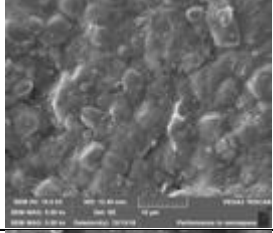
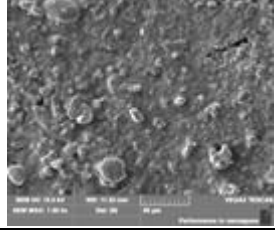
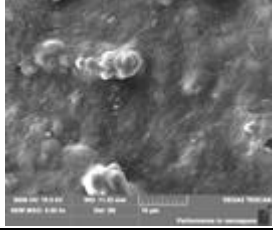
Unimodal

AlN particle sizes	1,000x	5,000x	Thermal Conductivity (W/mK)
0.1 $\mu\text{m}$			12
0.5 $\mu\text{m}$			8
1 $\mu\text{m}$			8
5 $\mu\text{m}$			8

Bimodal

AlN particle sizes	1,000x	5,000x	Thermal Conductivity (W/mK)
0.1 $\mu$ m&0.5 $\mu$ m			11
0.1 $\mu$ m&1 $\mu$ m			14
0.1 $\mu$ m &5 $\mu$ m			13
0.5 $\mu$ m &1 $\mu$ m	 SEM HV: 15.0 kV WD: 9.82 mm VEGA3 TESCAN SEM MAG: 1.00k X OC: 0 50 $\mu$ m SEM MAG: 1.00k X Defocus: 13.07116 Performance in nanoscale		18
0.5 $\mu$ m &5 $\mu$ m			8
1 $\mu$ m &5 $\mu$ m			8

Trimodal

AlN particle sizes	1,000x	5,000x	Thermal Conductivity (W/mK)
0.1 $\mu$ m&0.5 $\mu$ m&1 $\mu$ m			10
0.1 $\mu$ m&0.5 $\mu$ m &5 $\mu$ m			12
0.1 $\mu$ m&1 $\mu$ m&5 $\mu$ m			15
0.5 $\mu$ m&1 $\mu$ m&5 $\mu$ m			10

Quadmodal

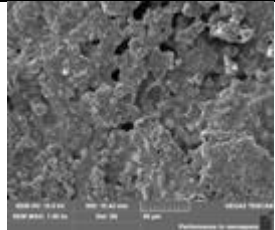
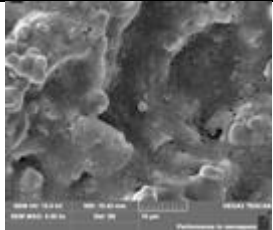
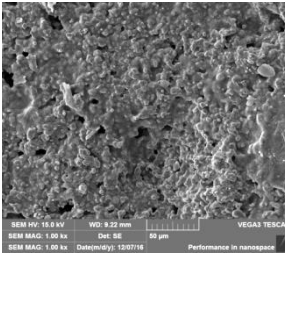
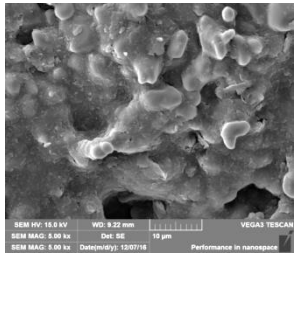
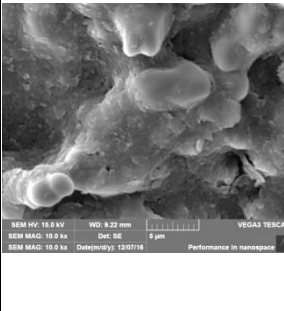
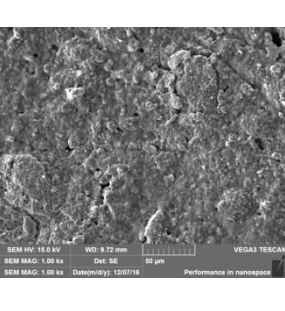
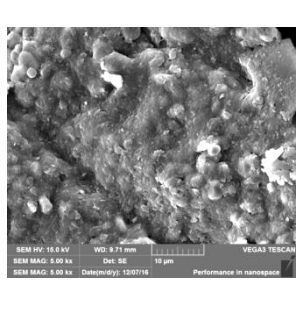
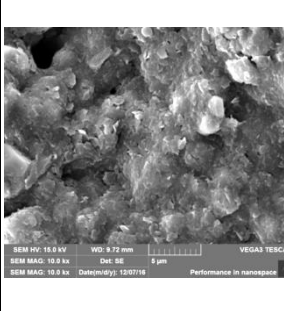
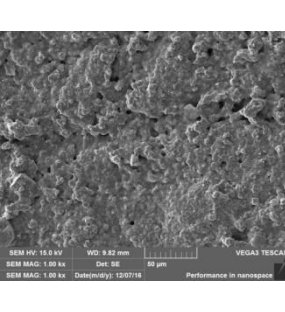
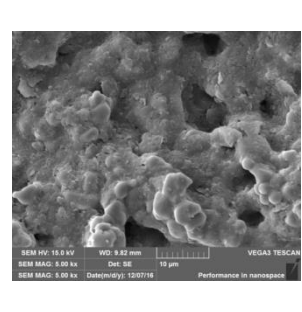
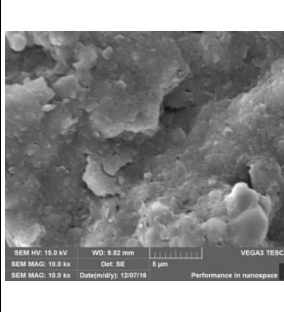
AlN particle sizes	1,000x	5,000x	Thermal Conductivity (W/mK)
0.1 $\mu$ m&0.5 $\mu$ m&1 $\mu$ m&5 $\mu$ m			13

Table 4.6 shows the SEM images of unimodal and bimodal AlN ceramics at a higher magnification of up to 10,000 times. The bimodal distribution clearly seems

to have better microstructures, and the presence of loose particles in unimodal samples lower the thermal conductivity value. The highest thermal conductivity achieved is 18 W/mK using a bimodal distribution of 0.5  $\mu\text{m}$  & 1  $\mu\text{m}$  AlN particle.

Table 4.6 SEM images of Unimodal and Bimodal AlN particle mixing.

Description	1,000x	5,000x	10,000x
<p>Sample 8 <b>Unimodal</b> AlN 0.5<math>\mu\text{m}</math></p> <p>(TC 8 W/mK)</p>			
<p>Sample 10 <b>Unimodal</b> AlN 1<math>\mu\text{m}</math></p> <p>(TC 8 W/mK)</p>			
<p>Sample 4 <b>Bimodal</b> AlN 0.5<math>\mu\text{m}</math> &amp; 1<math>\mu\text{m}</math></p> <p>(TC 18 W/mK)</p>			

#### 4.3.4 Ceramic particle size mixing

Table 4.7 shows the effect of the multi-modal distribution of different type of high conductivity ceramics such as AlN, BN, and SiC was studied using Taguchi Orthogonal Array Design L12 (9 factors and 2 levels) distribution design of experiment.

Table 4.7 Composition of samples used to study the effect of multimodal distribution.

No.	AlN (g)					Al(g)	BN (g)		SiC (g)
	0.04 $\mu$ m	0.1 $\mu$ m	0.5 $\mu$ m	1 $\mu$ m	5 $\mu$ m	-	0.5 $\mu$ m	15 $\mu$ m	0.1 $\mu$ m
1	-	-	-	-	-	-	-	-	-
2	-	-	-	-	-	1.250	0.156	0.156	0.156
3	-	-	1.250	1.250	1.250	1.250	-	-	-
4	-	1.000	-	1.000	1.000	-	-	0.125	0.125
5	-	1.000	1.000	-	1.000	-	0.125	0.000	0.125
6	-	0.833	0.833	0.833	-	0.833	0.104	0.104	-
7	0.125	-	1.000	1.000	-	-	-	0.125	0.125
8	0.125	-	1.000	-	1.000	-	0.125	0.125	-
9	0.104	-	-	0.833	0.833	0.833	0.104	-	0.104
10	0.125	1.000	1.000	-	-	1.000	-	-	0.125
11	0.156	1.250	-	1.250	-	-	0.156	-	-
12	0.125	1.000	-	-	1.000	1.000	-	0.125	-

The thermal conductivity of the green body before sintering was analyzed and the results are tabulated in Table 4.8. The green body was then subjected to debinding to remove the organic binders and sintering at 1600°C for 6 hours to form the final part. The thermal conductivity value of the final part is listed in Table 4.8.

The results indicate that samples without AlN as fillers are unstable and difficult to be gelcasted using ovalbumin (sample 2). They are fragile and easily broken.

This sample fragility is due to the incompatibility of the low density of BN and nano-sized SiC. The results also show that the sintered ceramics have a ten-fold increase in thermal conductivity when compared to the green state. The Taguchi analysis using Minitab 14, as depicted in Figure 4.10, indicates that the factors that contribute to the increase in thermal conductivity are AlN particle sizes with sizes of 0.04  $\mu\text{m}$ , 0.1  $\mu\text{m}$ , and 1  $\mu\text{m}$ , and BN with particle size 0.5  $\mu\text{m}$ .

Table 4.8 Thermal conductivity result for multi-modal distribution.

No.	Density ( $\text{g}/\text{cm}^3$ )		TC ( $\text{W}/\text{mK}$ )		Remarks
	Before Sintering	After Sintering	Before Sintering	After Sintering	
1	NA	NA	NA	NA	Can't gelcast without filler
2	Broken	Broken	NA	NA	Sample Broken
3	0.688	1.166	0.68	8.01	
4	0.445	1.025	<0.1	<0.1	
5	0.600	1.084	0.68	9.63	
6	0.426	0.661	<0.1	4.9	
7	0.591	0.959	0.51	5.1	
8	0.380	0.829	0.60	6.8	
9	0.452	0.680	0.52	5.4	
10	0.479	Broken	<0.1	NA	Sample broken
11	0.553	1.105	1.83	14	
12	0.618	Broken	0.41	NA	Sample broken

However, this thermal conductivity value is less than the bimodal distribution of AlN particle size of 0.5  $\mu\text{m}$  & 1  $\mu\text{m}$  (ratio 2), and 3  $\mu\text{m}$  & 5  $\mu\text{m}$  (ratio 1.5) that has the thermal conductivity value of 18  $\text{W}/\text{mK}$  and 17  $\text{W}/\text{mK}$  respectively. Therefore, the bimodal distribution of AlN (0.5  $\mu\text{m}$  & 1  $\mu\text{m}$  and 3  $\mu\text{m}$  & 5  $\mu\text{m}$ ) is the preferred ceramic powder to be used for producing high-performance 3D interposer.

Additional samples information is listed in Appendix II.

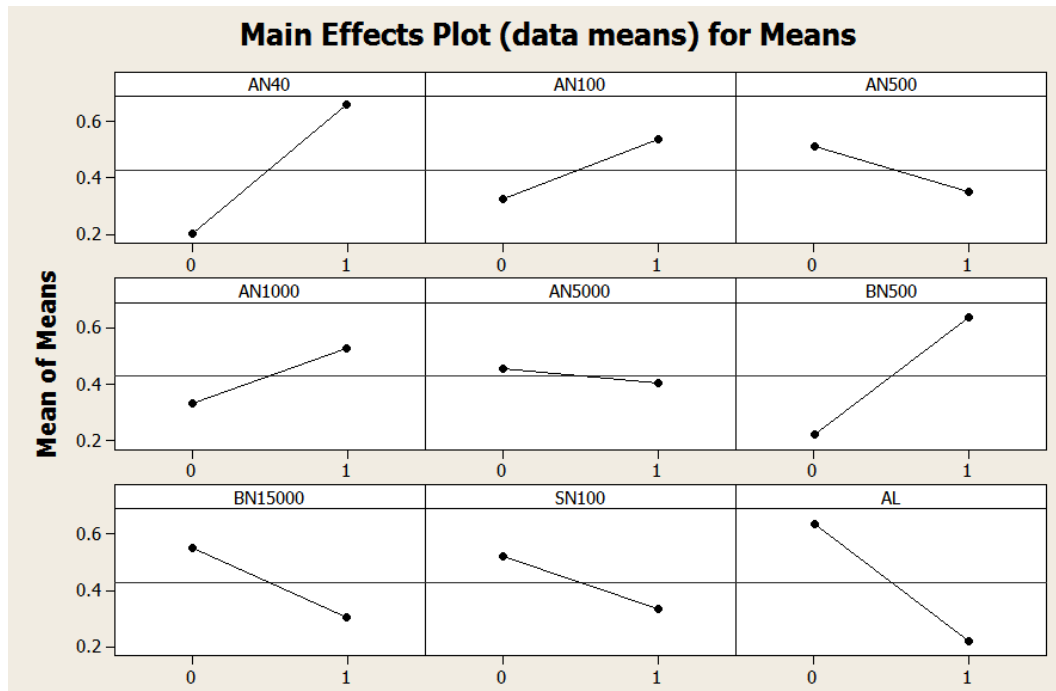


Figure 4.10 Taguchi Main Effects Plot obtained using Minitab 14.

#### 4.3.5 Effect of AlN solid loading

Figure 4.11 shows that higher AlN solid loading will increase the viscosity of the AlN/ovalbumin slurry. The result, with a standard error bar of +/- 5% is consistent with the previous results reported by Shen et al. (Shen, Xu, et al. 2016) on the shaping of AlN ceramics using non-aqueous gelcasting. This phenomenon can be explained that by increasing the incidence of particle contact, it also increases the flow resistance and therefore, increases in the viscosity of the slurry when the solid loading is high. Also, higher solid loading reduces voids between particles which consequently increase particle contact.



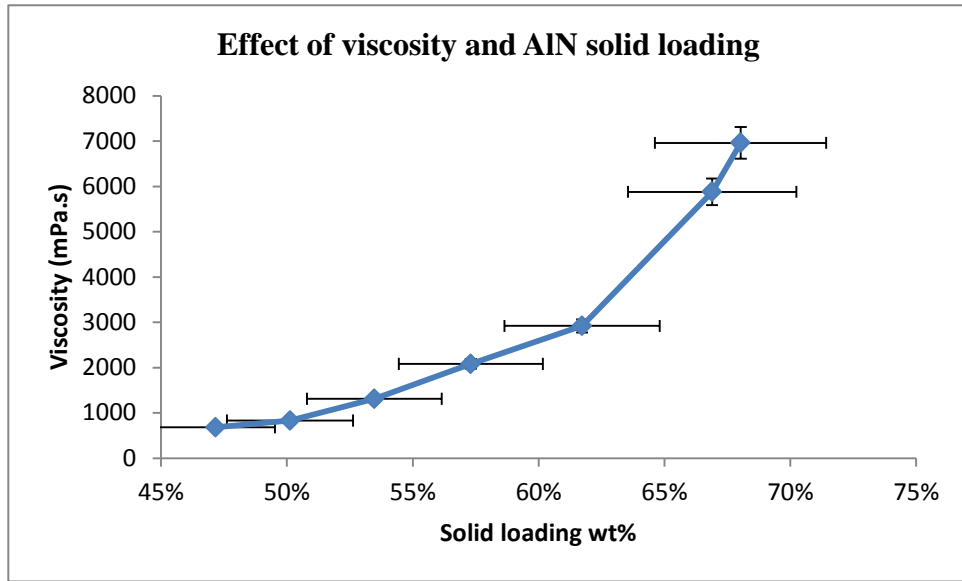
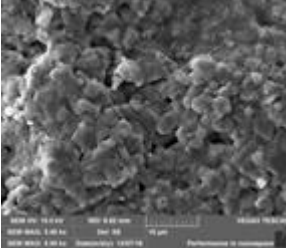
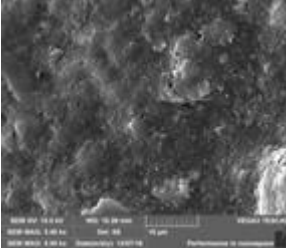
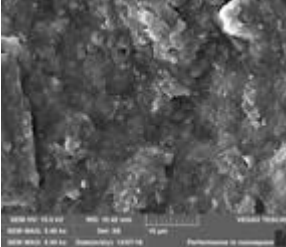


Figure 4.11 Effect solid loading on the viscosity AlN/ovalbumin slurry.

Table 4.9 shows the effect of AlN/ovalbumin solid loadings on the thermal conductivity, density and SEM microstructure of the ovalbumin gelcasted AlN samples. A bimodal AlN particle size distribution of 0.5  $\mu\text{m}$  & 1  $\mu\text{m}$  is used and ovalbumin premix is added to the desired solid loading.

The result shows that increasing solid loading also increases the relative density, which is consistent with the previous report by Wang et al. (Wang, Wang, et al. 2015) is associated to the post-contraction process. There is also a direct correlation that higher relative density also increases the thermal conductivity of the sintered AlN ceramics. Heat is transmitted via the lattice effect for insulators such as AlN and therefore, the higher density increases the compactness of the particles that assist in heat conduction.

Table 4.9 Effect of solid loading on thermal conductivity of AlN ceramics.

No.	Solid loading %	Relative Density %	SEM Images 5,000x	Thermal Conductivity W/mK	Viscosity @ 25°C mPa.s
1	50	73		18	800
2	55	81		19	2000
3	60	86		21	2900

Onbattuvelli et al. (Onbattuvelli, Purdy, et al. 2010) have reported similar findings, that increasing the solids loading of the casting slurry will increase the density of the ceramic part, and in turn, improve thermal conductivity. They reported that the maximum powder content for the injection molding process using bimodal SiC powder is 87 wt.% (65.5 vol%), and for bimodal AlN is 90 wt% (71 vol%) but they recommend the optimal solids loading to be 59 vol% (82 wt %) and 64 vol% (81 wt%) for bimodal  $\mu$ -n SiC and AlN feedstocks respectively.

For additive manufacturing, using robocasting for ceramics, Peng, et al. (Peng, Zhang, et al. 2018) recommended a ceramic solid loading of more than 40 vol% (50

wt%) for good control of viscoelastic behavior, and an organic additive < 3 vol% to minimize post-printing shrinkage. Feilden et al. (Feilden, Blanca, et al. 2016) have reported the use of solid content as high as 36 vol%  $Al_2O_3$  and 39 vol% SiC inks respectively. Their results show that a solid loading of less than 30 vol% will cause the problem of densification during sintering due to the low green densities and drying cracks. However, higher solid loading of more than 45 vol% causes poor printability due to prohibitive high viscosity. The optimum AlN/ovalbumin solid loading used in this study is 60 wt%.

#### **4.4 Concluding remarks**

The study has shown that ovalbumin, a sustainable natural protein material, can be used as the gelcasting monomer to produce high thermal conductivity AlN ceramics substrate with the thermal conductivity of 21 W/mK, compared to 0.2 W/mK used in the conventional organic interposer. The flexural strength of the AlN/ovalbumin green body of 3 MPa is sufficient for post-processing before the final sintering. The AlN/ovalbumin gelcast was successfully sintered at 1600°C for 6 hours in the nitrogen atmosphere with a weight loss of 18%, a density of 86% and shrinkage of about 20%.

The study also shows that bimodal particle size mixing is important for obtaining the highest thermal conductivity for the AlN ceramic substrate, consistent with packing simulation result reported by Shi & Zhang (Shi and Zhang 2008). The AlN particle size ratio of between 1.5 (1  $\mu\text{m}$  & 3  $\mu\text{m}$ ) and 2 (0.5  $\mu\text{m}$  & 1  $\mu\text{m}$ )

produced the best thermal conductivity of 18 W/mK and 17 W/mK respectively with a 50 wt% solid loading. Unimodal, trimodal and quadmodal mixing was not able to produce good packing and have a lower thermal conductivity compared to bimodal mixing. Mixing the AlN particles with other ceramic powders having high thermal conductivity; like boron nitride (BN) and silicon carbide (SiC) does not improve the thermal conductivity. The addition of nano-sized AlN particle (0.1  $\mu\text{m}$ ) increases the thermal conductivity of the AlN ceramics but is still lower than the optimal bimodal mixing ratio of 1.5 and 2.0. Another important parameter that affects the gelcasting of AlN/ovalbumin is solid loading. Increasing the solids loading from 50 wt% to 60 wt% increases the thermal conductivity of the AlN ceramic substrate from 18 W/mK to 21 W/mK. Therefore, the bimodal mixing of AlN particles with a mixing ratio of between 1.5 (1  $\mu\text{m}$  & 3  $\mu\text{m}$ ) and 2 (0.5  $\mu\text{m}$  & 1  $\mu\text{m}$ ) is suitable as the ceramic substrate to produce high-performance 3D interposer.

# **Chapter 5 Interconnecting metals compatible with the AlN green gelcasting process**

## **5.1 Introductory remarks**

A 3D ceramic interposer consists of the ceramic substrate with embedded interconnecting metals to form the functional circuits. Copper (Cu) is usually the preferred interconnecting metal due to its excellent electrical conductivity but it has a low melting temperature of 1085°C that make it not suitable for high-temperature co-firing with the ceramic substrate. Therefore, the firing temperature of the interposer has to be optimized taking into account both the ceramic and metallic components.

Molybdenum (Mo) is a refractory metal that keeps its crystal structure (body-centered cubic, bcc) from low temperature up to its melting temperature of 2610°C. The series of Mo-alloys have excellent stability, creep resistance and thermal conductivity (Liu, Zhang,, et al. 2013). In addition, its properties such as low thermal expansion coefficient (CTE), and high thermal and electrical conductivity make Mo an important material for high-temperature semiconductor components; from vacuum tubes, emitters for flat panel displays and multi-layer ceramics (MLC) package technology (Shields and Lipetzky 2000).

The Mo components are usually produced using the powder metallurgy (PM) process, that sinters Mo powder at high temperature to form high-density

components (Mueller, Bianco,, et al. 2000, Kolobov, Kieback,, et al. 2003). However, such a process has issues related to deformability and weldability (Huang and Hwang 2002). The problem with this process is mainly due to the reactivity on oxidation, thus limits its application as a structural material (Briant 2000).

Gelcasting, a fast forming near-net-shape process technology was first introduced by Omatate et al. (Omatete, Janney, et al. 1991) for alumina ceramics, and has since been successful in forming articles using other ceramics such as aluminum nitride, zirconia, and silicon carbide. The original formulation uses aqueous-based slurries has better characteristics compared to other casting processes such as slip casting, injection molding and pressure casting (Janney, Omatete, et al. 1998).

There are limited reports on gelcasting of metals; Li et al. (Li, Wang, et al. 2017) reported gelcasting of porous Ti-Mo alloys for biomedical applications, Bohua (D. Bohua 2017) on Mo-Cu alloy and Bekouche et al. (Bekouche, Wang, et al. 2016) on copper. However, all these studies used a non-aqueous monomer system due to the oxidation of metals in an aqueous environment. Stearic acid has previously been reported to protect metal surfaces from oxidation and corrosion (Wang, Zhang, et al. 2008). Their study here focused on using green and sustainable natural protein as the gelcasting monomer to produce gelcasted metal parts.

## 5.2 Experimental

### 5.2.1 Preparation of metal slurry

The schematics of the Cu gelcasting process are presented in Fig. 5.1. Ovalbumin natural protein is obtained after separation of egg-yolk was added with 1 wt% silicon oil (Unichem). The mixture is stirred for 2 hours using a magnetic stirrer and the froth formed after the mixing is removed before using it to prepare the Cu/ovalbumin slurry.

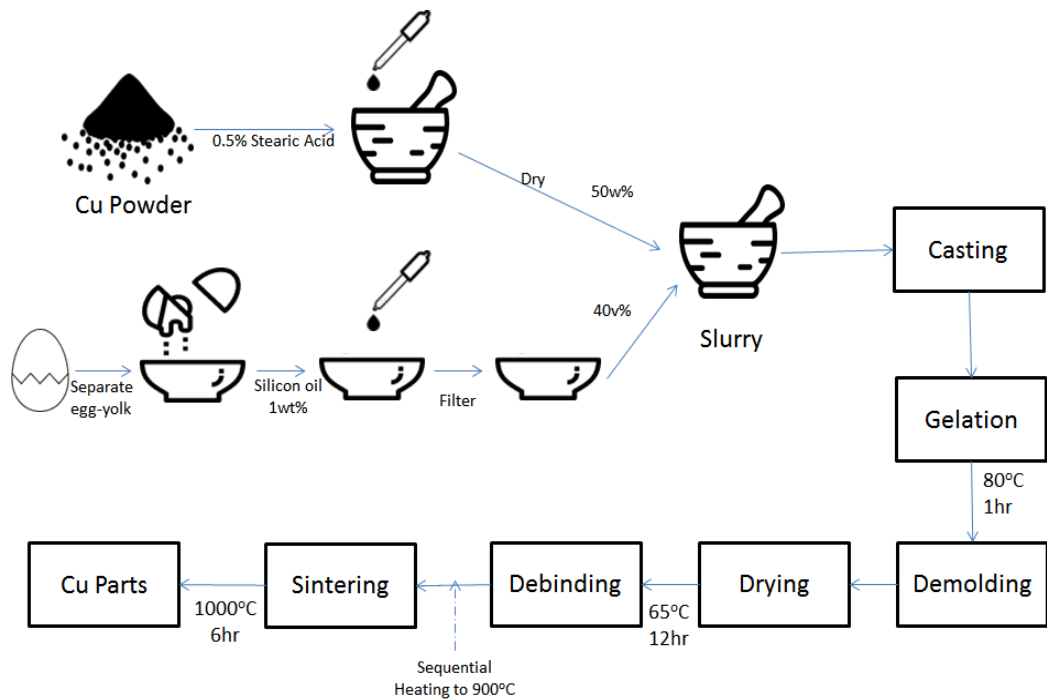


Figure 5.1 Process flow of the gelcasting of Cu powder using ovalbumin protein.

Electrolytic copper powder (1000 mesh, 99.8% Cu) is obtained from Chengdu New Materials Co. Copper (I) Oxide, and Copper (II) Oxide is obtained from Agros. The copper powders are added with 0.05 mo/l of Stearic Acid (Arachem) in

ethanol as the dispersant agent to protect the copper powder from hydrolysis and oxidation. The mixture was ground using a mortar and pestle until the sample dried up. 10 wt% of polyethylene glycol (PEG4000) from Fluka was added as the dispersant. The powder mixture was then ground well in the mortar pestle before adding ovalbumin premix (40 wt%) to form the copper metal slurry. The slurry was mixed thoroughly using the mortar and pestle to ensure homogeneous slurry is formed, before casting to form the final product.

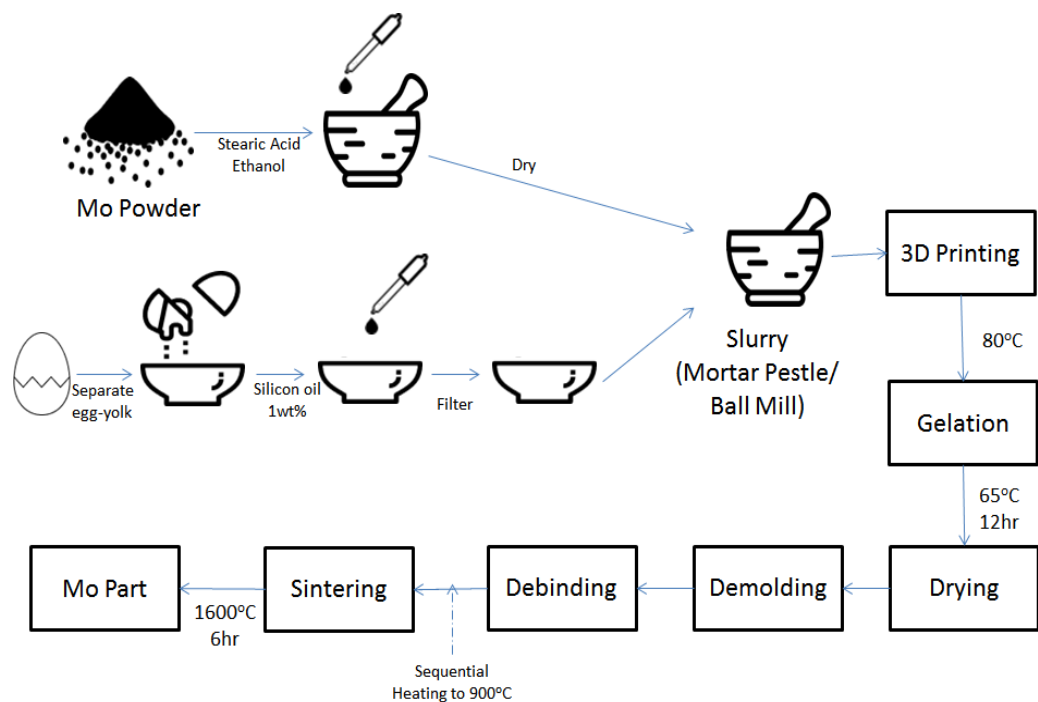


Figure 5.2 Process flow of the gelcasting of Mo powder using ovalbumin protein.

Figure 5.2 shows the gelcasting procedure of Mo powder using ovalbumin as the gelcasting monomer. The Mo powder used in this study is from SAT Nano (China) with an average particle size of 0.1  $\mu\text{m}$ , 1  $\mu\text{m}$ , and 3  $\mu\text{m}$  respectively. The Mo powders were treated using the same procedure as for Cu; firstly, 0.5 wt% of



stearic acid is added to form a superhydrophobic layer on Mo particles for protection against oxidation. Then, 10 wt% of PEG-4000 (Fluka) is added as a dispersant for the slurry before adding the ovalbumin premix (40 wt%) to form Mo metal slurry.

### 5.2.2 Metal forming process

The metal/ovalbumin protein slurry is poured into the casting mold, heated on a hot plate at a temperature of 40°C for 1 hour to start the gelation and increased to 80°C for 1 hour to complete the gelation and finally dried for 12 hours at 65°C. The green body is then demolded and post-processed by mechanical polishing using sandpaper.

The green body is then debinded to remove organic binders in the sample before sintering to form the metal product with the desired properties. The debinding and sintering profile for Cu and Mo is shown in Figure 5.3 and Figure 5.4 respectively. The debinding profile for both Cu and Mo are similar to the same organic binder used and is conducted in a 0.08 MPa nitrogen atmosphere at a heating rate of 5°C per min. The debinding temperatures are maintained for 30 min at a temperature of 120°C, 350°C, and 550°C. This debinding is then followed by firing at 900°C for 2 hours, before sintering using a PT1700 Atmosphere Furnace from Zhengzhou Protech. A metal part was formed after the sintering process.

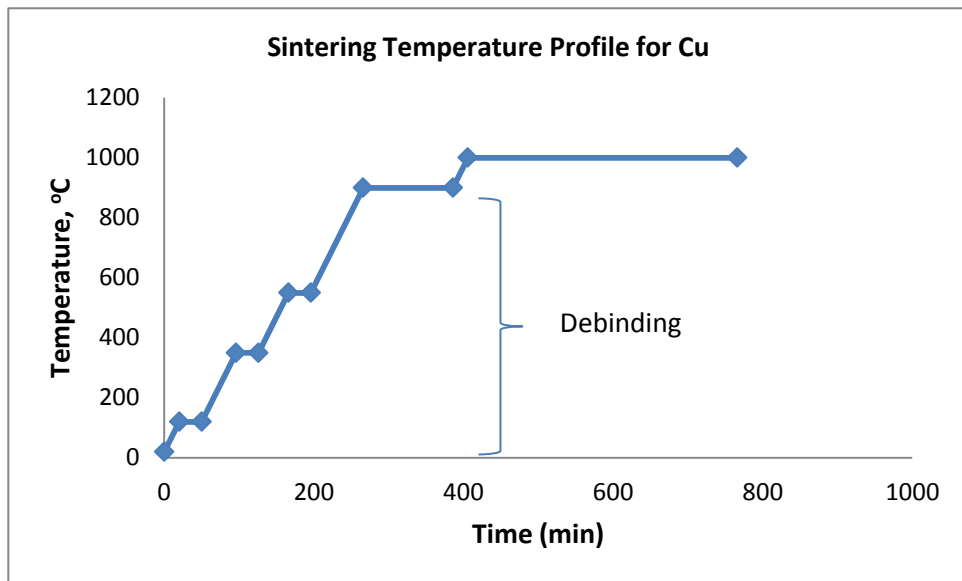


Figure 5.3 Debinding and sintering profile for Cu/ovalbumin gelcast (Dhara and Bhargava 2001).

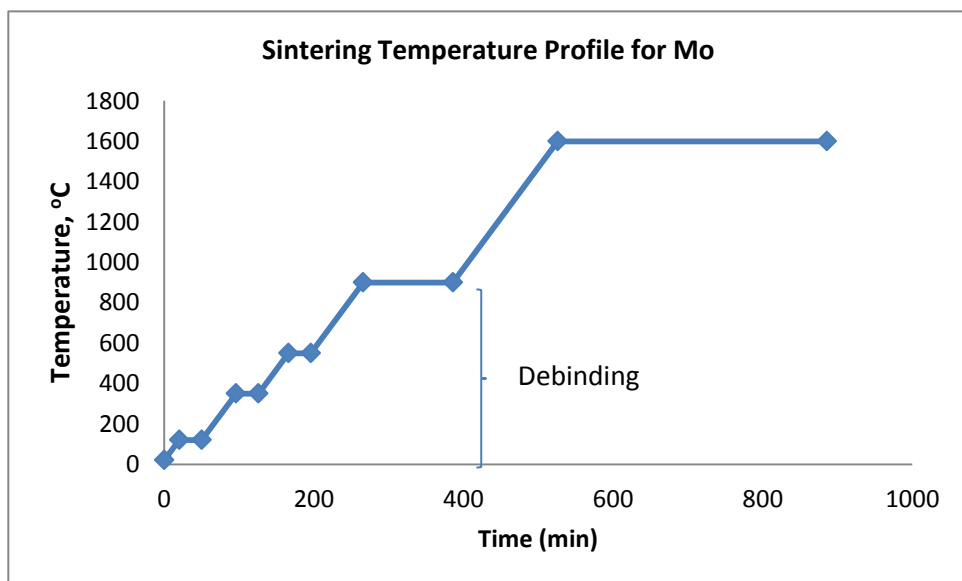


Figure 5.4 Debinding and sintering profile for Mo/ ovalbumin gelcast (Dhara and Bhargava 2001).

### 5.2.3 Characterization

The rheology of Mo slurries was characterized using an MCR702 dynamic shear rheometer (Anton Paar, Austria) with 50mm diameter parallel plate and shear

rate range from 0.1 to 1000 s<sup>-1</sup> at 25°C. Thermogravimetric (TGA) analyzer, model TGA/DSC 3+ from Mettler Toledo was used to study the decomposition behavior of ovalbumin gelcasted Mo green body in a nitrogen atmosphere with a temperature scan range from 25°C to 1000°C and heating rate of 10°C per min.

Rigaku SmartLab X-ray Diffractometer (XRD) system was used to determine crystal phase present in the sample using monochromated Cu K $\alpha$  (0.15418 nm) and 2 $\theta$  scanning from 20 to 80 deg (step size 0.02 deg and 5 deg per min scanning rate). The XRD pattern was then matched with the International Centre for Diffraction Data (ICDD) PDF-2 reference data for crystalline phase identification.







Rectangular shape sintered Molybdenum parts are used to determine the flexural strength using a three-point bending jig with a crosshead speed of 0.5 mm per min (Instron 5565). Flashline TM 2000 thermal conductivity measurement apparatus is used to measure the thermal conductivity of the samples with Pyroceram as the calibration sample for machine drift correction. Density measurement, based on the Arrhenius method is determined using a density balance (JA203M, Changzhou Xingyun Electronic Equipment Co., Ltd). A 4-point probe is used to measure the electrical impedance of the sample using discrete pairs of current and voltage electrodes and an Agilent 43388 milliohmmeter. The surface morphology of the samples is observed using scanning electron microscopy (SEM), model VEGA 3 from Tescan.

### 5.3 Results and discussions

#### 5.3.1 Gelcasting of copper (Cu) powder

A few types of copper powders, copper metal powder (1000 mesh), copper (II) oxide (CuO) and copper (IV) oxide (Cu<sub>2</sub>O) are being investigated on the suitability for gelcasting that matches the AlN ceramics. Table 5.1 shows the gelcasting of copper powder from the different types of copper powder. The green body for all types of copper is found to be not conductive before sintering.

Table 5.1 Gelcasting of different types of Cu powder.

Copper Powder	Before Sintering	After sintering (1000 °C, 2 hr)	Resistivity after sintering (Ω)	Melting Point (°C)
<b>Cu plate (Reference)</b>			<b>0.2</b>	
Cu Powder			<b>0.2</b>	1085
CuO			2000k	1326
Cu <sub>2</sub> O			200k	1232

However, after sintering, all the copper parts are conductive with different resistivity value. It was observed that the higher the oxide content, the lower is the resistivity because the oxide phase is an insulator that reduces electrical conductivity.

The sintering of pure copper/ovalbumin at 1000°C produces a copper metal with good electrical conductivity, similar to the copper plate. These results show that sintering of copper oxide/ovalbumin at a sintering temperature of 1000°C can partially remove oxygen from copper oxide to convert it to electrically conductive copper metal. However, the electrical conductivity is less than bulk copper due to the incomplete conversion and a longer sintering time might be required.

However, even though copper oxides become electrically conductive after sintering, physical integrity is affected as seen from the image after sintering. Cracks were observed on the copper oxide/ovalbumin samples in the green state prior to sintering and therefore are not suitable for use as the starting material to produce interconnect metals.

Figure 5.5 shows the XRD analysis of the ovalbumin gelcasted copper after sintering at 1000°C for 6 hours. The copper phase present mostly consisted of metallic copper with a small residue of copper oxide present. The copper oxide phase is probably due to surface oxidation of the copper when it is exposed to air. Therefore, the results show that the metallic copper was formed after sintering, which contributes to good electrical conductivity. The results also show that stearic acid is able to protect the copper particle from oxidation during the gelcasting process.

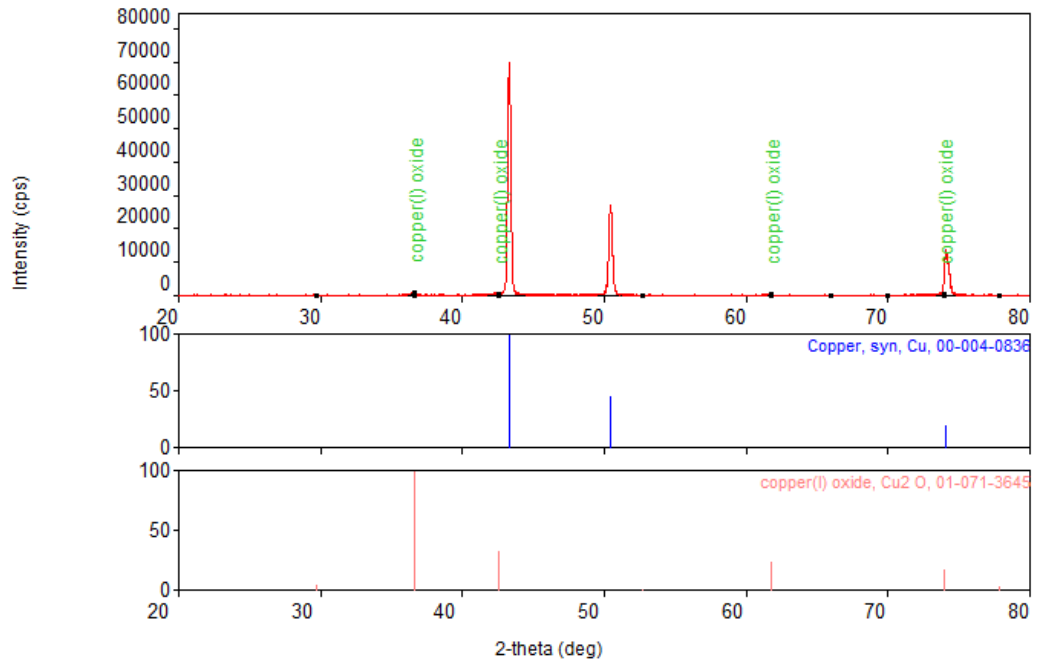


Figure 5.5 XRD pattern of the Cu/ovalbumin gelcast.

However, heating copper to the sintering temperature of AlN ceramics, at 1600°C causes copper agglomeration (Figure 5.6). The copper melts at 1085°C and nucleation occurs when it is cooled back room temperature (25°C).

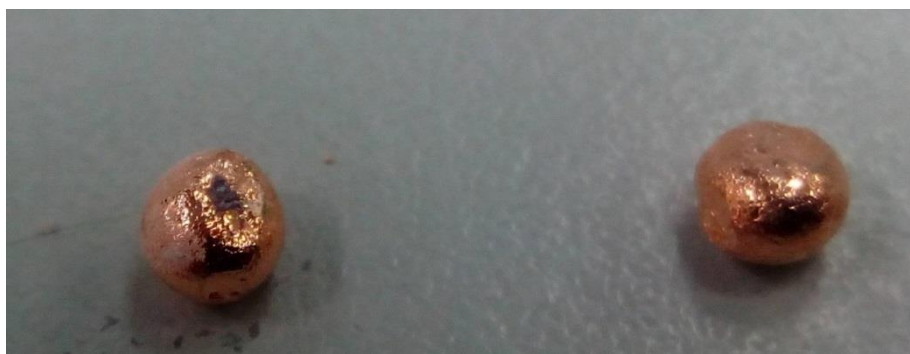


Figure 5.6 Agglomeration of Cu after sintering at 1600°C.

The melting process is initiated at sub-nanometer and sub-nanosecond scales with a size distribution in the three-dimensional percolation of the power law. Zheng (Zheng, An, et al. 2007) reported the sigmoidal profile at the copper solid-liquid interface has a width of 12 Å near the critical nucleation. According to the Johnson-Meh-Avrami law, the growth of melt is accompanied by nucleation (Zheng, An, et al. 2007). Therefore, copper/ovalbumin cannot be used to co-sinter with AlN ceramic substrate at 1600°C.

### 5.3.2 Gelcasting of molybdenum (Mo) powder

#### i) Mo/ovalbumin gelcasting slurry

The refractory metal, molybdenum (Mo), has a melting temperature of 2610°C and is suitable as the interconnect metal to co-sinter with the AlN ceramic substrate, at a sintering temperature of 1600°C. Figure 5.7 shows the rheological curve of the molybdenum slurry, with a particle size of 0.1 µm, 1 µm, and 3 µm respectively. The viscosity of the slurry decreases with increasing shear rate (shear thinning), which is a characteristic of the non-Newtonian behavior (Kamal, M. R., and Mutel, A. 1985).

The result shows that Mo/ovalbumin slurries with smaller particle sizes have lower viscosity. Mo/ovalbumin slurry with 1 µm Mo particle size has a viscosity of 0.353 Pa·s compared to 1.142 Pa·s for Mo/ovalbumin slurry with 3 µm Mo particle size. This result shows that more open spaces are available for the smaller particle size that resembles a suspension with a lower concentration that lowers the

viscosity.

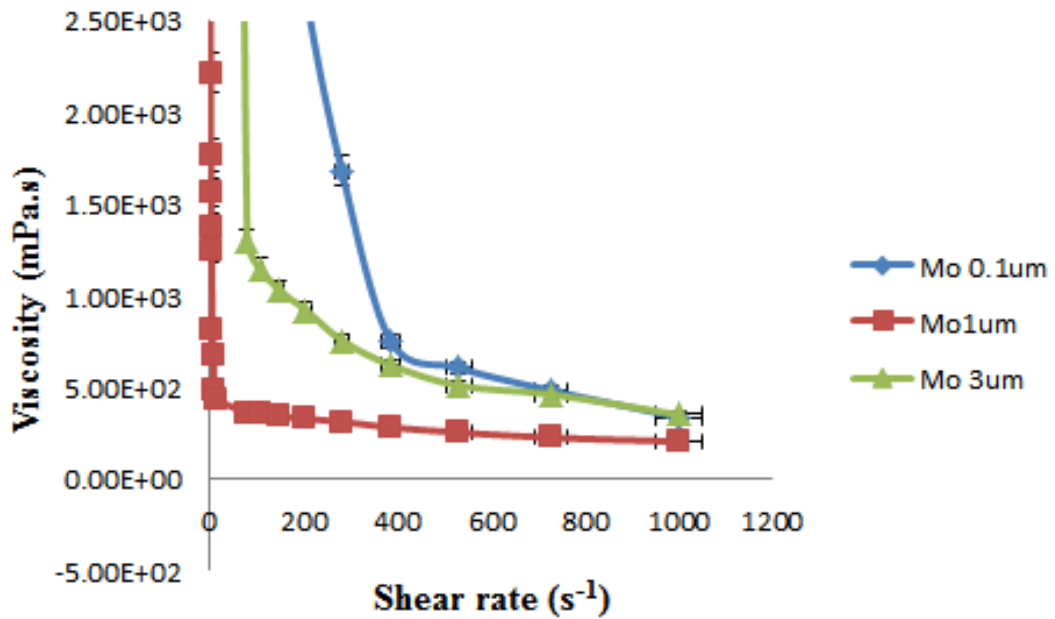


Figure 5.7 Rheology of Mo/ovalbumin slurry for 0.1  $\mu\text{m}$ , 1  $\mu\text{m}$  and 3  $\mu\text{m}$  Mo particle size.

The lower viscosity is favorable for the gelcasting process because it will be able to accommodate more solids, i.e. higher solid loading, and improve the mechanical properties of the sintered products. However, nano-size (0.1  $\mu\text{m}$ ) Mo particle has a thickening effect compared to micron-size particles that increase the viscosity tremendously. The high viscosity value for the nanoparticle Mo slurry is due to nanoparticle agglomeration, commonly occurring in suspension that negatively affects the rheology of the slurry. Once agglomerated, the nanoparticles are difficult to be fragmented again using mortar pestle or millimeter size ball mill. A strong agitator, physical and mechanical dispersion method will be required to disperse the nanoparticles. Ultrasonic dispersion method is found to be better than ball milling in segregating dispersed nanoparticle suspension because ball milling used 50  $\mu\text{m}$  bead



milling and is only useful in suspension with relatively low solid content (Sato, Li, et al. 2008).

Once the powder particles are wetted, it causes individual particles to agglomerate and held together by attractive forces such as van der Waals and liquid surface tension. The effect will be much stronger for nanoparticles due to its extremely high surface area, and these forces must be broken before the agglomerated particles can be dispersed evenly in the liquid media to exhibit its full potential. In the ultrasonic dispersion process, the ultrasonic cavitation will generate mechanical stress that breaks the agglomeration of particles apart for it to be sufficiently wetted. Ultrasonic cavitation occurs when vacuum bubbles in the liquid, that is created by alternating the high-pressure (compression) and low-pressure (expansion) cycles, and collapses violently when the bubble attain a critical volume when they are not able to absorb more energy during a high-pressure cycle. The characteristic of this implosive collapse produces high local heat ( $\sim 5000\text{K}$ ), high-pressure ( $\sim 1000\text{ atm}$ ), extreme heating and cooling rates ( $> 10^9\text{ K/sec}$ ), and liquid streams ( $\sim 400\text{ km/h}$ ) (Hielscher 2012). However, such condition is not suitable for ovalbumin because its gelation is activated by heat to form a polymeric network, and could cause a breakdown. Also, the ultrasonic cavitation can cause bubbles to be trapped in the Mo/ovalbumin slurry during the gelling process that will affect the packing density and the final physical property of gelcasted Mo. Therefore, nano-size Mo ( $1\text{ }\mu\text{m}$ ) is not suitable for gelcasting using ovalbumin monomer.

## ii) Thermal analysis of Mo/ovalbumin green body

The thermal analysis of the green body is essential to determine the debinding protocol for thermal post-processing of the fabricated structures. The mechanisms to remove binder include thermal degradation by either free radical attack, unzipping or chain scission, followed by oxidative degradation and evaporation. However, for pyrolysis, without the presence of oxygen, the thermal degradation occurs by a free radical reaction, and the degradation occurs at a higher temperature compared to degradation in the combustive atmosphere due to the autocatalytic reaction caused by oxygen. For polymers, the degradation mechanisms under pyrolysis condition are first depolymerization, followed by a random scission and finally the elimination of the side group. This degradation causes the migration of low-molecular-weight products to the surface-atmosphere interface before being evaporated. This gas-phase transport and diffusion mechanism is the mechanism for the removal of organic binders from the green body during the debinding heating process. However, if the diffusion is too slow and rate limiting, it will cause the accumulation of gases in the green body. This accumulation of gases, if exceeded the ambient vapor pressure, will cause the parts to bloat and cracks can be formed. Therefore, defects due to the rate limiting diffusion and boiling of organics in the green body are the most significant problem associated with binder removal using the thermal method. The degradation mechanism can be further complicated if side reactions occur, such as cross-linking and cyclization that produces a residue of the carbonaceous-type, that requires a higher temperature for pyrolysis. Besides, the

interaction of the metal surface, especially oxide surfaces, with the degraded polymeric products can also catalyze the decomposition to form smaller molecules that can cause isomerization reactions promoting cross-linking during pyrolysis (Liau, Peters, et al. 2000).

The TGA profile of the Mo green body is shown in Fig. 5.8 has a total weight loss of 5.2%, which is consistent with the characteristic of gelcasting that typically has binder content within 4-10%. There are three decomposition domains; the first domain is from 25°C to 300°C with a weight loss of 0.9%, the second domain from 300°C to 390°C with a weight loss of 2.9% and the second domain was from 390°C to 900°C with a smaller weight loss of 1.5%.

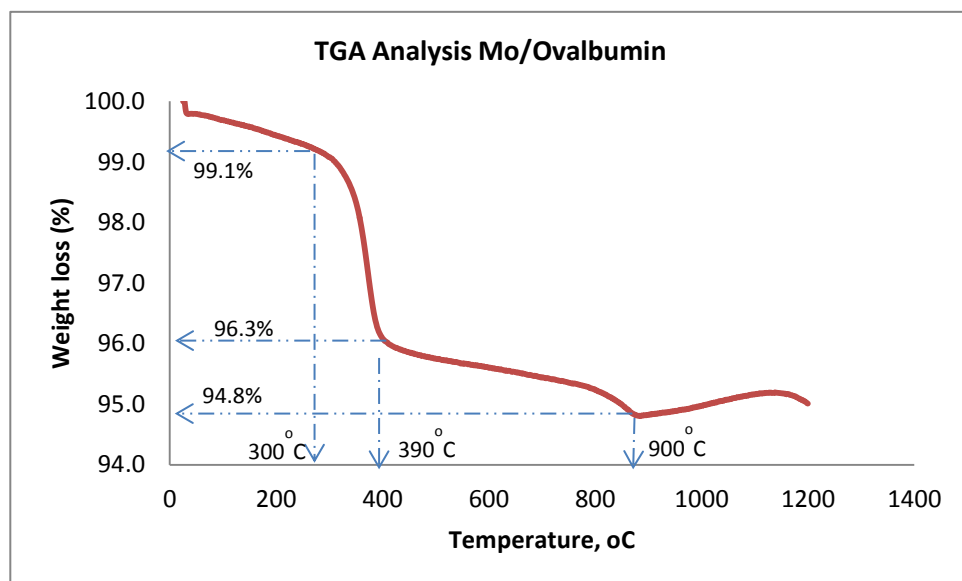


Figure 5.8 TGA analysis of Mo/ovalbumin gelcast.

The organic components in the ovalbumin gelcasted green body include ovalbumin, silicon oil, stearic acid and PEG 4000 as the dispersant. The pH of the

ovalbumin premix is 9.5. The first exothermic peak for ovalbumin has been reported to be at 330°C, due to the first oxidative breakdown of the ovalbumin component. The other exothermic peak at a temperature of 560°C and 630°C is due to the other oxidative decomposition of the remaining ovalbumin (Dhara 2005). Therefore, both degradation domains will have an ovalbumin component.

As for silicon oil, there are two domains of decomposition. The first domain is up to 350°C, where volatile matters were volatilized at this temperature. The second domain is from 350°C to 700°C that indicate the presence of different volatile matters which decompose at different temperature zone (Mehmet2008).

The boiling point for stearic acid is 198°C. In the air atmosphere, stearic acid degradation occurs at 175° to 315°C, which accounts for 80% of the stearic acid compound, and the remaining stearic acid component degrades from 315°C to 500°C with several exothermic reactions. However, in the nitrogen atmosphere, the degradation of stearic acid is simpler with only a single event from 175°C to 275°C with two endotherms. This degradation domain corresponds to the combustion and subsequent volatilization of organic species such as CH<sub>3</sub>COOH from stearic acid (Bagheri, Shameli, et al. 2013).

Kou et al. (Kou, Wang, et al. 2019) reported that PEG is stable at a temperature below 400K and starts to decompose at 623K and ends at a temperature above 723K. These three events occur both in air and nitrogen atmosphere. The melting point of PEG is 40°C. According to Knapp et al. (Knapp and Halloran, 2006), the first 1 wt% of highly volatile materials are degraded and evaporated between 40°C

and 140°C, followed by the significant mass loss between 145°C to 335°C, and the remaining 5 wt% mass loss from 335°C to 455°C with a few exotherms, from the oxidative degradation at 225°C and 260°C in air. In the inert nitrogen atmosphere, evaporation is the primary factor for weight loss. The degradation starts with the initial 4% mass loss occurring at a temperature of 40°C to 285°C, followed by the majority of the mass loss between 285°C to 410°C, and the final 1.5 wt% decomposed at a temperature of 415°C to 500°C.

Therefore, the first degradation domain from 300°C to 390°C in the green body of the Mo/ovalbumin is for the degradation of stearic acid, the oxidative breakdown of the ovalbumin component, volatile matter of silicon oil and major components in PEG. The second degradation domain from 390°C to 900°C is due to the oxidative degradation of remaining ovalbumin, different volatile matter in silicon oil and some minor components of PEG.

### iii) Evaluation of sintered Mo metal

Mo is known to have a low solubility for oxygen that causes it to form surface oxides even at low oxygen pressures. The oxidation of Mo can cause both positive and negative weight change, depending on the temperature and pressure conditions; the formation of MoO<sub>2</sub> causes weight gain where as the formation of volatile MoO<sub>3</sub> causes weight loss (DiStefano, Pint, et al. 2000).

Stearic acid (SA, CH<sub>3</sub>(CH<sub>2</sub>)<sub>16</sub>COOH) is a non-toxic material consists of long-chain saturated fatty acid, the main component of fat (Ng, Wong, et al. 2010).

Studies have shown the use of stearic acid can be used to form a coating on metal surfaces to improve the corrosion resistance characteristics. Wang et al. (Wang, Wang, et al. 2010) have reported immersing etched metal surface, magnesium, in 0.05 mol/l of a stearic acid/ ethanolic solution to create a super-hydrophobic surface by bonding  $\text{CH}_3(\text{CH}_2)_{16}\text{COO}^-$  to the Mg surface with superior water-repellency property. Huang et al. (Huang, Sarkar, et al. 2010) also reported fabricating a super-hydrophobic copper surface using a simplified one-step process with stearic acid.

The XRD analysis of the sintered Mo/ovalbumin gelcast shows that only pure Mo phase is present with no oxide phases of Mo (Fig. 5.9). Therefore, the result shows that Mo powder treated with stearic acid can mitigate the oxidation of Mo during the gelcasting process.

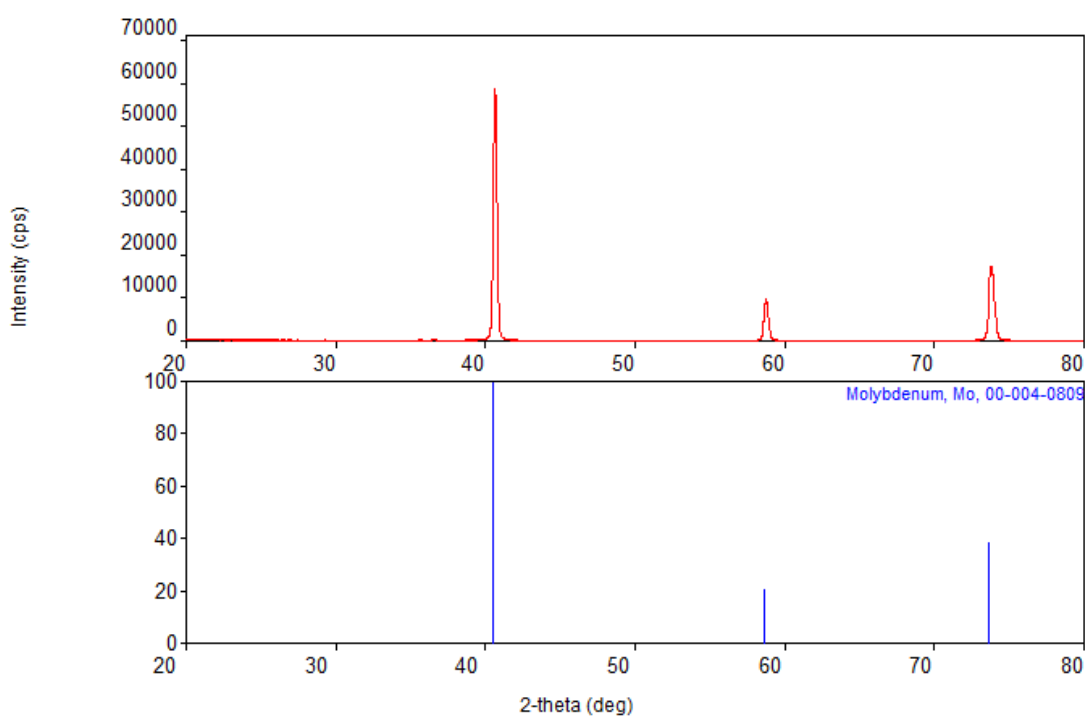


Figure 5.9 XRD pattern of Mo/ovalbumin gelcast.

This is because stearic acid forms a protective layer on the Mo surface that protects it from oxidation during the gelcasting process.

Table 5.2 shows the electrical resistivity, thermal conductivity and flexural strength of the sintered Mo prepared from different Mo particle sizes (1  $\mu\text{m}$  and 3  $\mu\text{m}$ ). All the Mo metals become electrically conductive after the sintering process.

Table 5.2 Parameters of sintered Mo samples.

Parameters	Electrical resistivity ( $\Omega\cdot\text{cm}$ )	Thermal Conductivity (W/mK)	Flexural Strength (MPa)	Relative Density (%)	Shrinkage (%)
Mo (1 $\mu\text{m}$ )	$4.10 \times 10^{-4}$	35	80	83	23
Mo (3 $\mu\text{m}$ )	$5.97 \times 10^{-4}$	39	55	89	21
Cu (reference)	$3.30 \times 10^{-4}$				

The electrical resistivity and flexural strength of the sintered Mo metal using 1  $\mu\text{m}$  Mo particle size ( $4.10 \times 10^{-4}\Omega\cdot\text{cm}$  and 80 MPa ) is better than the sintered Mo metal using 3  $\mu\text{m}$  Mo particle size ( $5.97 \times 10^{-4}\Omega\cdot\text{cm}$  and 55 MPa). However, sintered Mo metal from the bigger, 3  $\mu\text{m}$  particle size has slightly higher thermal conductivity and relative density (39 W/mK and 89% respectively) compared to Mo metal from smaller 1  $\mu\text{m}$  particle size (35 W/mK and 83% respectively). A shrinkage of around 20% is similar to Mo metals prepared from both types of Mo particle size.

The result is consistent with the study by Srivatsan et al. (Srivatsan, Ravi, et al. 2002) that revealed smaller-sized powders have lower density but higher hardness. The smaller particle size of 1  $\mu\text{m}$  has more particles in contact point with

each other and the higher contact points increase the electrical conductivity and flexural strength. However, the bigger 3  $\mu\text{m}$  particles have better packing density which increases heat conduction using the vibration mechanism for a higher thermal conductivity value.

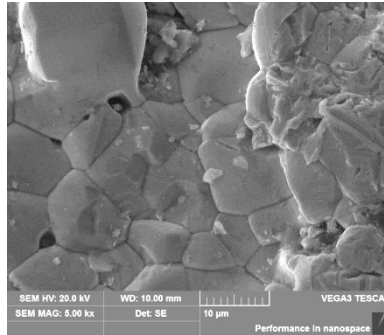
The total thermal conductivity,  $\kappa$ , is the sum of all the excitation factors represented by the following equation (Tritt 2005):

$$\kappa = \sum \alpha K \alpha = K_i \alpha_i + K_j \alpha_j + K_k \alpha_k + \dots \quad (5.1)$$

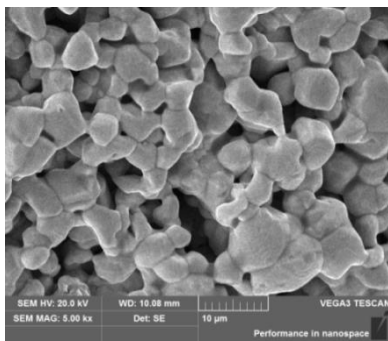
where  $\alpha$  denotes an excitation factor. The excitation factors include electrical carriers (electrons or holes), lattice waves (phonons), electromagnetic waves, spin waves or other excitations. Lattice waves (phonons) are the vibration of atoms coupled with neighboring atoms and are related to the compactness of the crystal lattice and, therefore, the density of the material. The results show that the lattice waves effect contributes more than electrical carriers for the thermal conduction of sintered Mo.

The SEM images for sintered Mo metal with different Mo particle sizes are shown in Fig. 5.10. Mo metal from nanopowder (0.1  $\mu\text{m}$ ) has the most compact structure among the three types of molybdenum particles used in this study due to the better packing density of nanoparticles. Mo metal from 3  $\mu\text{m}$  Mo particle size has a more compact structure compared with Mo metal from 1  $\mu\text{m}$  Mo particle size, which corresponds to higher relative density and better thermal conductivity.

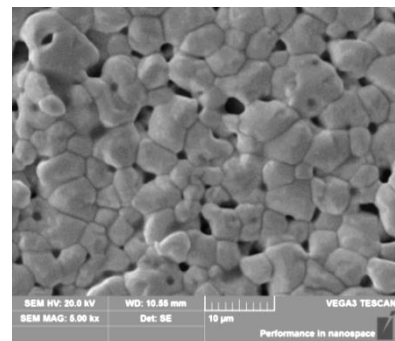




(a)



(b)



(c)

Figure 5.10 SEM images (5,000x) of sintered Mo sample with an average particle size of a) 0.1  $\mu\text{m}$ , b) 1  $\mu\text{m}$  and c) 3  $\mu\text{m}$ .

#### 5.4 Concluding remarks

The natural protein monomer, ovalbumin, can be effectively adopted for gelcasting of Cu and Mo metals (60 wt% solid loading) to produce near-net-shape parts that are electrically conductive after sintering. Stearic acid is proven effective in protecting the metal surface during the debinding stage that ensures good electrical conductivity of the metals after sintering. However, Cu metal is not suitable as the co-sintering metal with AlN ceramic interposer due to its low melting temperature. The refractory metal, Mo was found to be compatible with the

ovalbumin gelcasting process and able co-sinter with AlN ceramic at 1600°C. Nano-sized Mo particle (0.1  $\mu\text{m}$ ) is not suitable for use with ovalbumin due to the agglomeration that causes high viscosity and possible cracks in the gelcasting process. Ovalbumin slurry is not suitable for ultrasonic process used to break this agglomerate as the ultrasonic cavitation can break the ovalbumin polymer network structure and cause bubble formation inside the green body. However, smaller micron-size Mo powder, 1  $\mu\text{m}$  is preferred compared to 3  $\mu\text{m}$  particle size because of lower slurry viscosity that makes it easier to process. Also, the sintered Mo metal using smaller, 1  $\mu\text{m}$  particle size has 30% better electrical resistivity compared Mo metal with 3  $\mu\text{m}$  particle size. This study has shown that 1  $\mu\text{m}$  particle size of Mo powder is suitable to be used as the starting raw material for green gelcasting of Mo metal for 3D interposer application. The Mo/ovalbumin gelcasting process is similar to the AlN/ovalbumin process to ensure compatibility during debinding and co-sintering.

# **Chapter 6 Direct gelcast 3D printing of 3D ceramic interposer for microelectronic application**

## **6.1 Introductory remarks**

The revolution of additive manufacturing (AM), commonly known as 3D printing is one of the driving forces for the realization of the fourth technology revolution that shifted mass production to mass customization. This AM revolution supersedes the previous revolution that used animal to mechanical machinery for production, then mass production into using digital control (Levi 2018).

Some of the critical characteristics of AM technologies are i) capability to produce parts with highly sophisticated design, ii) fewer assembly parts requirement, iii) less time required, iv) less demand for fabrication skills know-how, v) low-cost for small volume, vi) less waste production, vii) ability to create replica and viii) less constraints of creativity (MacCurdy, McNicoll, et al. 2014).

The AM or 3D printing technology has been improving dramatically in the last decade with continual improvement in quality, build size, range of materials and applications. Plastic and metals are the most common materials used for 3D printing in the industry such as automotive, aerospace and electronics with improvement in speed for time-to-market and lower production costs. The technology has evolved from rapid prototyping into manufacturing of functional parts that improve products

that face issues related to less weight, less production time, less tooling cost with highly complex geometries.

However, the use of ceramics in 3D printing is lagging but still is on the rise due to several promising applications. The growth of ceramics in 3D printing has seen impressive demand; the compound annual growth rate (CAGR) of 21.4 % from 2015 to 2017, rising from US\$ 174 million in 2017 to US\$ 544 million by 2022 (Gagliardi 2017), and US\$ 3.1 billion by 2027 globally (Levi 2018).

Aluminum nitride (AlN) is an important technical ceramic with properties such as high thermal conductivity, excellent electrical resistivity, low dielectric constant, high dielectric strength, high melting temperature with good mechanical strength and corrosion resistance (Berger 1996).

There have not been reports of using the gelcast binder system for direct 3D printing and ovalbumin, a natural protein, is selected as the binder of choice due to the simplicity of processing. In addition, the previous study on 3D multi-materials printing used polymers such as material jetting systems, inkjet-based 3D printers with drop-on-demand (DOD) printing method (de Gans, Duineveld, et al. 2004). In this study, direct gelcast 3D printing of multi-materials of ceramics and metal are being investigated.

## 6.2 Experimental

### 6.2.1 AlN/ovalbumin gelcasting paste

Figure 6.1 shows the preparation of the AlN ceramic paste using ovalbumin as the gelcasting monomer. The ovalbumin natural protein was obtained by separating fresh egg yolk, followed by the addition of 1 wt% silicon oil (Unichem) to the mixture. The mixture is then stirred for 2 hours with a magnetic stirrer, to remove froth before using it to prepare the ceramic paste.

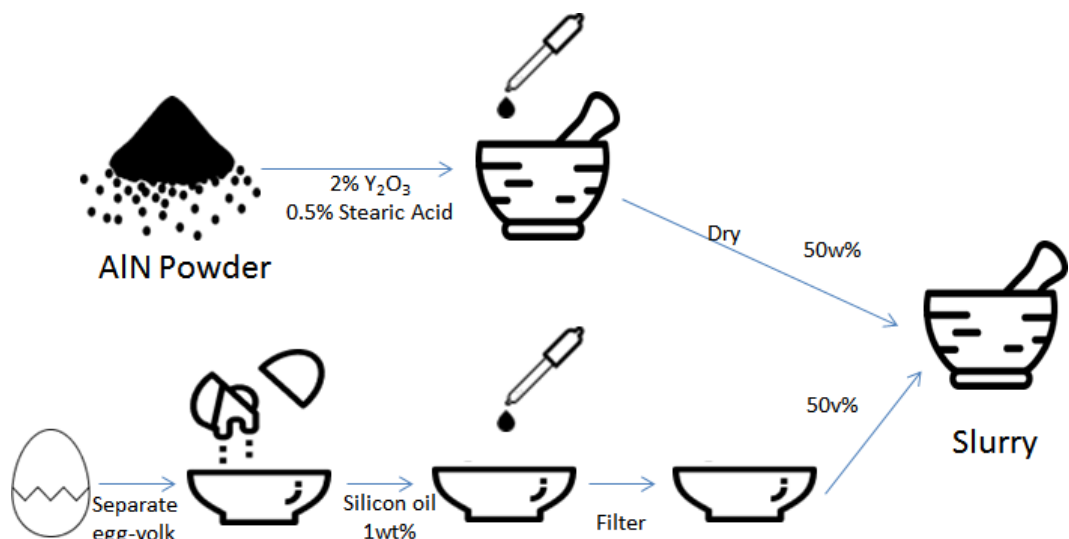


Figure 6.1 Preparation of AlN/ovalbumin paste.

The bimodal AlN powder with the particle size of  $0.5 \mu\text{m}$  &  $1 \mu\text{m}$  (HWNano) is used in this study. The AlN powder is first treated with 0.05 mo/l of stearic acid (Arachem) in ethanol, and the dried mixture is then added with 2 wt% of sintering aid,  $Y_2O_3$  (Acros, 99.99%), 10 wt% polyethylene glycol 4000 (Fluka) as dispersant

and 40 wt% of ovalbumin premix. The mixture is mixed thoroughly using mortar pestle for 15 min or ball mill at 150rpm for 1 hour to form the gelcast paste.

### 6.2.2 Recycling of AlN/ovalbumin ceramics

The possibility of recycling of the AlN/ovalbumin from the green body is investigated. The dried green state of the AlN/ovalbumin ceramics is crushed into a fine powder before adding the ovalbumin premix to form the AlN/ovalbumin paste. The ratio of AlN (recycled): Ovalbumin was 11:7. Figure 6.2 shows the preparation of recycled AlN.

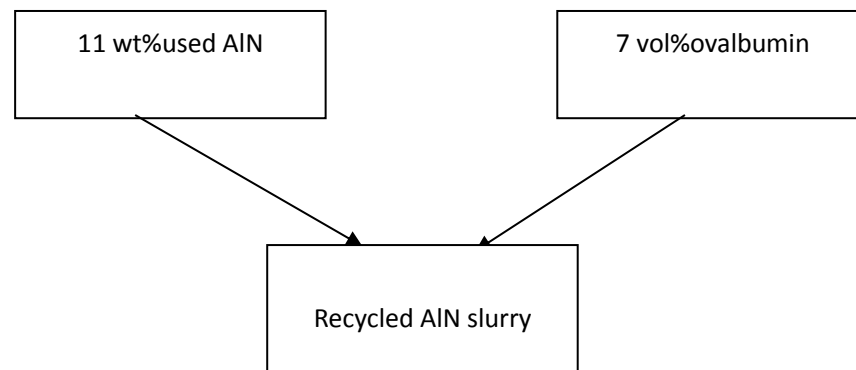


Figure 6.2 Recycling of AlN/ovalbumin(green state)

### 6.2.3 Metal/ovalbumin gelcasting paste preparation

Figure 6.3 shows the preparation of the metal/ovalbumin paste with the ovalbumin natural protein prepared similar to the process described in section 6.2.1. Electrolytic copper powder (1000 mesh, 99.8% Cu) is obtained from Chengdu New Materials (China) and Mo powder (1 $\mu$ m) used in this study is from SAT Nano (China). The metal powder (Cu or Mo) is added with 0.05 mo/l of stearic acid

(Arachem) in ethanol to protect the metal powder from hydrolysis. The mixture is mixed thoroughly grounded using mortar pestle, and the sample is dried in air. Then, 10 wt% polyethylene glycol 4000 (Fluka) is added as a dispersant, and the mixture is grounded thoroughly using mortar pestle, followed by adding 33 wt% of ovalbumin premix to form the gelcast paste for 3D printing. Silicon (Si) powder is obtained from SAT Nano (China) for the study of hybrid ceramic SiAlN.

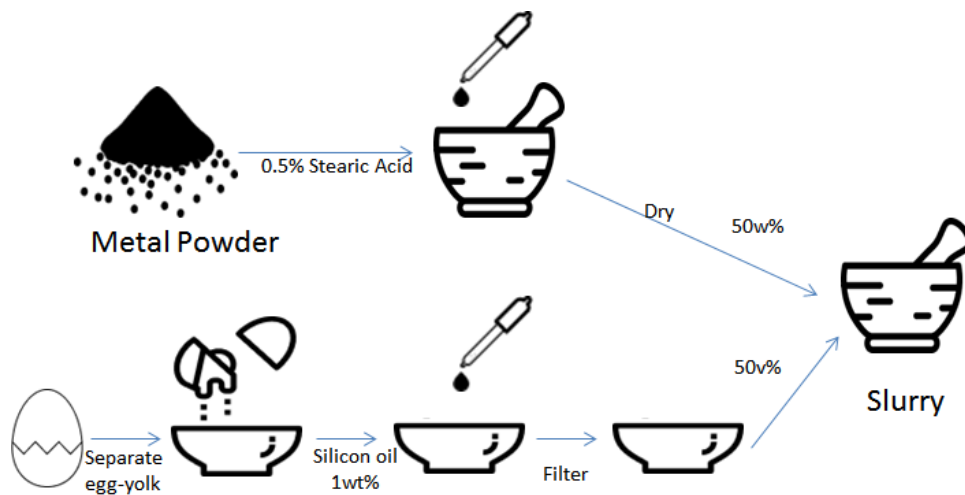


Figure 6.3 Preparation of metal paste.

#### 6.2.4 3D printing process and sintering

The gelcast paste is poured into the syringe, and the printing plate is preheated to 80°C before the printing began using a thick paste extruder, ZMorph 2.0 (Figure 6.4). After printing, the articles are then dried in air for 6 hours before demolding it from the surface.

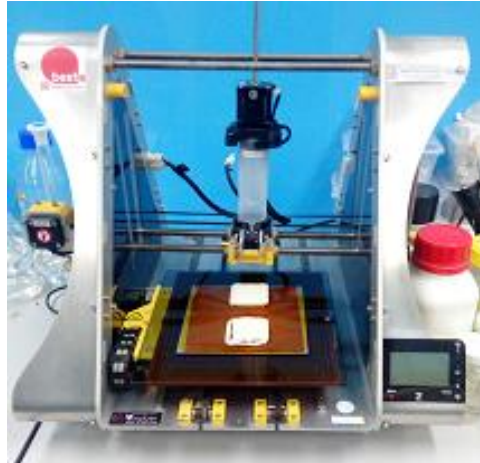


Figure 6.4 Thick paste extruder (ZMorph 2.0).

The dried samples are then debinded and sintered using an atmospheric furnace model PT1700 from Zhengzhou Protech in a 0.08 MPa nitrogen atmosphere to form the final part. The debinding and sintering profiles for Mo-AlN interposer are shown in Figure 6.5.

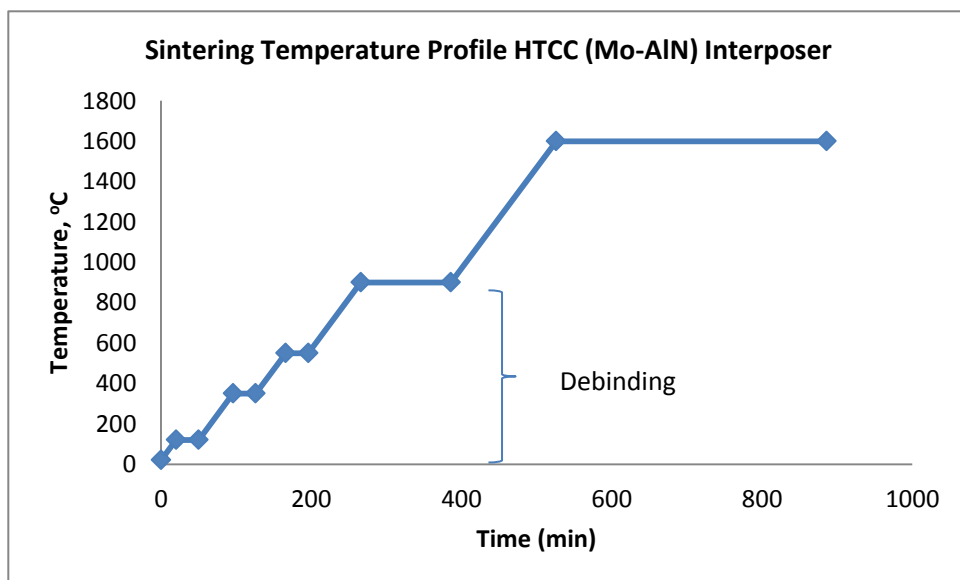


Figure 6.5 Debinding and sintering temperature profile of HTCC (Mo-AlN) interposer (Dhara and Bhargava 2001).



### 6.2.5 Characterization

A digital rotating viscometer, NDJ-5S/8S (Shanghai Pingxuan Instrument Co., Ltd) is used to measure the viscosity of the paste with rotor #4 at a rotating speed of 60 rpm. Flashline TM 2000 is used for measuring the thermal conductivity of the samples using Pyroceram as the calibration sample for drift correction.

Flexural measurement using the (load x displacement) curved obtained with the Instron 5565 testing machine on the printed bars of the samples with dimensions of 25 x 10 x 3mm, is subjected to a three-point bending test at 0.5 mm/min crosshead speed. Sample shrinkage is measured using a digital vernier caliper (Absolute Digimatic, Mitutoyo). A 3W mini power LED light source from Avago is used to test the interposer circuit produced. The LED is attached using silver glue (RS) to the Mo surface before powering up with direct current (DC) from a multimeter (Fluke model 73III).

## 6.3 Results and discussions

### 6.3.1 Direct gelcast 3D printing of AlN ceramics

#### i) Direct gelcast 3D printing parameters

The flowing of fluid through a thick paste extruder is described by a velocity field,  $\vec{v}$ . The vector-valued function of space and time will vary in magnitude and direction within the fluid:

$$\vec{v}(x, y, z, t) = u(x, y, z, t)\hat{x} + v(x, y, z, t)\hat{y} + w(x, y, z, t)\hat{z} \quad (6.1)$$

The volumetric flow rate  $Q$  through an area is

$$Q = \int \vec{v} \cdot \hat{n} \, dA \quad (6.2)$$

If  $U_{ave}$ , the average velocity normal to a planar area  $A$ ,  $Q = U_{ave} \cdot A$  ( $\text{m}^3\text{s}^{-1}$ ) and

therefore, the mass flow rate is

$$\dot{m} = \rho U_{ave} A \quad (6.3)$$

where  $\rho$  is the fluid density.  $\dot{M}$ , the momentum flow rate obtained by multiplying  $\dot{m}$  with fluid velocity (Hoath 2016).

$$\dot{M} = \rho U_{ave}^2 A \quad (6.4)$$

Table 6.1 shows the printing parameter for gelcast printing and Figure 6.6 show the Voxelizer software for controlling the ZMorph thick paste extruder. The temperature of the printing plate was heated to  $80^\circ\text{C}$  prior to printing in order to increase the gelling speed of the paste upon dropping on the printing plate and ensure the integrity of the printed parts. This is because ovalbumin molecules will form a thermo-irreversible gel when heated to  $80^\circ\text{C}$  that are held together by covalent bonds (Mine 1995).

Table 6.1 The 3D Printing parameters.

Parameters	Optimal Value
Layer height	2mm/layer
Infill ratio	25%
Infill type	Rectilinear (to ensure jetting paste in straight lines)
Temperature	$80\text{-}100^\circ\text{C}$
E-speed	5mm/s
XY-speed	200mm/s
Z-speed	20mm/s

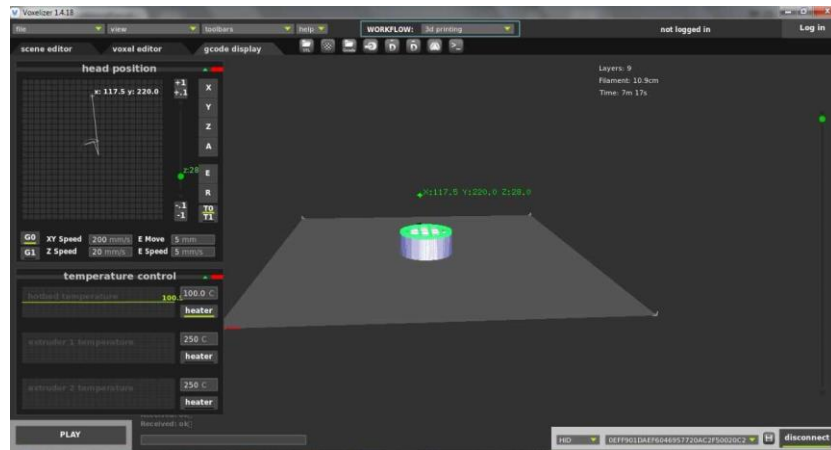


Figure 6.6 Voxelizer software for 3D printing.

Figure 6.7 shows the process of direct gelcast 3D printing of AlN ceramics using the ZMorph 2.0 thick paste extruder and Voxelizer software. After the preparation of the AlN ceramic paste, it is then transferred onto a syringe before setting it onto the extruder. The Voxelizer software is then used to open the selected CAD design file with the suitable printing parameter. The printing stage is then heated to 80°C and the extruder is used to purge out the void from the syringe before actual printing began. Once the temperature of the printing stage reaches 80°C, the 3D printing process started to print the 3D structure according to the CAD design, layer by layer. After the printing is completed, the syringe is removed, and the sample is dried in air for 6 hours before demolding. The green body is then subjected to debinding and sintering according to the sintering profile in Figure 6.5 to form the final part.

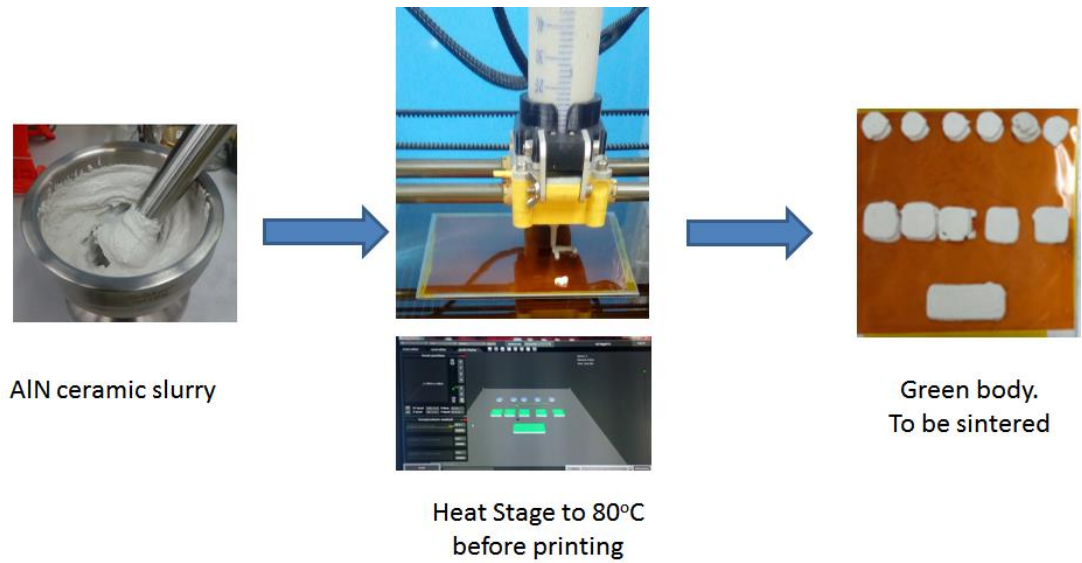


Figure 6.7 Schematics of 3D printing of AlN ceramics using AlN paste prepared with ovalbumin natural protein.

Figure 6.8 shows the 3D structures of AlN ceramics that were successfully printed using the thick paste extruder, Z Morph 2.0. In order to obtain good printing result, the volume of paste that is extruded through the nozzle should fit the line width perfectly during printing (Peng, Zhang, et al. 2018). Therefore the preceding layer has to solidify before dispensing another layer on top of it to build up the 3D structure.



Figure 6.8 3D printed structures of AlN ceramics.

In the ovalbumin system, hot air blow can be used to accelerate the gelation of the ovalbumin in the preceding layer so that the ceramic paste can be printed on top of it and ensure a good quality print. If the bottom layer is not sufficiently solidified, the structure could collapse, as shown in Figure 6.9.

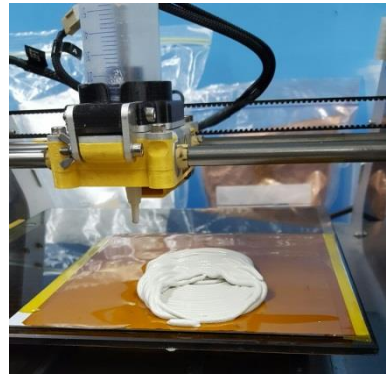


Figure 6.9 3D printing of AlN on a hot surface without hot air blow.

In addition, the mismatch of gelling speed causes non-uniform shrinkage and could produce cracks on the printed structures. Therefore, a uniform solidification of AlN/ovalbumin is important to ensure uniform shrinkage to improve print quality and reduce crack formation. This could be achieved by having hot air flow directed onto the printed surface to increase the gelation speed of the top surface and improve on the gelling.

Therefore, by incorporating hot air blow in the process to accelerate surface solidification, the following layer can be built successfully and the process is repeated to form the 3D structures of AlN ceramic as shown in Figure 6.10.

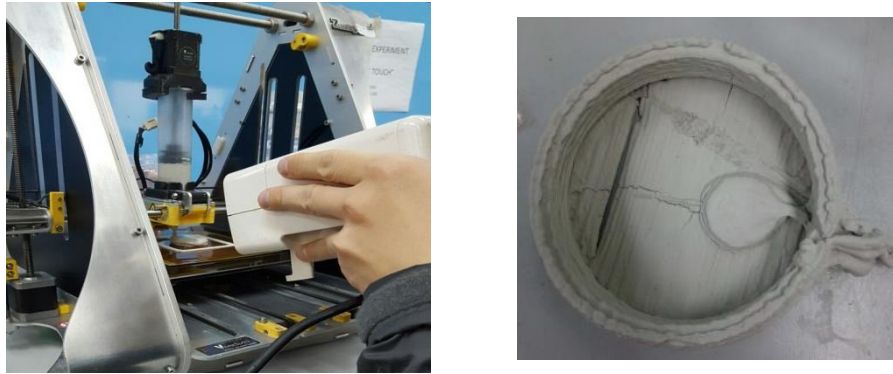


Figure 6.10 3D printing of AlN on a hot surface with hot air blow.

Alternatively, the speed of printing can also be controlled that allows the paste to solidify sufficiently before printing the next layer. In addition, the mismatch of gelling speed causes non-uniform shrinkage and could produce cracks on the printed structures. Therefore, a uniform solidification of AlN/ovalbumin is important to ensure uniform shrinkage to improve print quality and reduce crack formation. This could be achieved by having hot air flow directed onto the printed surface to increase the gelation speed of the top surface and improve on the gelling uniformity.

#### ii) Direct gelcast 3D printing of AlN/ovalbumin

The viscosity of the AlN/ovalbumin (60 wt% solid loading) paste measured at 25°C is 2900 mPa.s using rotor #4. Table 6.2 shows the effect on the type mixing of the AlN paste; ball milling and mortar pestle. The physical parameters of the sintered AlN ceramics prepared using 3D printing and mold casting are similar (density 91% vs 86%, flexural strength 8.27 MPa vs 8.00 MPa, and thermal



conductivity of 19 W/mK vs 21 W/mK). This is because the slurry compositions for both methods are the same.

Table 6.2 Physical parameters of AlN sintered samples.

Type of paste mixing	Molding Method	Density after sintering	Relative Density	Flexural Strength (MPa)	Thermal Conductivity (W / mK)
		( g / cm <sup>3</sup> )	( % )		
MortarPestle	3D printing	2.960	91	8.27	19
Ball mill (150 rpm)	3D printing	1.970	52	5.00	10
Mortar Pestle	Mold casting	2.793	86	8.00	21

Table 6.3 shows images of the AlN/ovalbumin gelcast prepared using different mixing method. It is observed that samples prepared using ball mill mixing has significantly more pores and this will weaken the AlN ceramic structure, indicated by the 40% lower in flexural strength and density.

Table 6.3 AlN green sample prepared using a different paste mixing method.

Mixing method	Green state	Quality
Ball Milling		Relatively lower, more frequent to have air bubbles
Mortar & Pestle (MP)		Relatively higher, almost no air bubbles occur

The reason is because mixing by ball mill created more bubbles that were trapped in the paste, which turn into pores upon drying. This phenomenon can be explained from the study by S.Maleksaeedi, et al. (Maleksaeedi, Paydar, et al. 2009) on centrifugal de-airing of ceramic paste. The study shows that during centrifugal de-airing, the bubble agglomerates and sink to the bottom instead of rising up. When the centrifugal force is absent, the intra-agglomerate bubble will start to rise to the surface but will be trapped by the surrounding particles and could not escape to the atmosphere. As a result, the lower critical bubble coordination number will increase with the sinking of the bubbles. The critical coordination number depends on the ratio between the bubble and particle size, and solid loading. The bubble removal time will increase with increasing solid content. At a low centrifugal acceleration of 10g, a paste with the volume fraction of 0.3 and 0.6, will need 3 hours and 13 hours respectively to remove 5  $\mu\text{m}$  bubbles from the ceramic paste. Also, higher centrifugal speed will reduce the bubble removal time.

The process of mixing by ball milling is similar to centrifugation, where bubbles that are formed will start to sink to the bottom of the container. Also, the periodic change of rotational direction during ball milling will cause more bubble formation that are trapped in the paste. When the ball milling stops, the bubble will go back into the paste from the bottom and trapped in the highly viscous paste. The trapped bubbles will form pores when dried and weaken the structural integrity of the AlN ceramic substrate. As compared to ball milling, the mixing by mortar pestle is much



gentler that created less bubbles and is easier for the atmosphere for a more compact AlN/ovalbumin gelcast.

The 3D printed AlN ceramics after sintering has excellent heat dissipation property with a high thermal conductivity value of 19 W/mK, which is higher than the conventional organic substrate that has a thermal conductivity of 0.2 W/mK. The shrinkage of the 3D printing process is around 20%, which is similar to casting using a metal mold, and is consistent with the previous study. Sun et al. (Sun, Shimai, et al. 2014) have reported shrinkage of around 15% using a nontoxic, water-soluble copolymer of isobutylene and maleic anhydride for gelcasting alumina of low shrinkage.

### iii) Recycling of AlN ceramics

The AlN green body formed after drying of the paste can be crushed and reused by adding ovalbumin premix. Figure 6.11 shows the recycling process; first, the AlN green body is crushed using mortar pestle and ground to finer particle size.

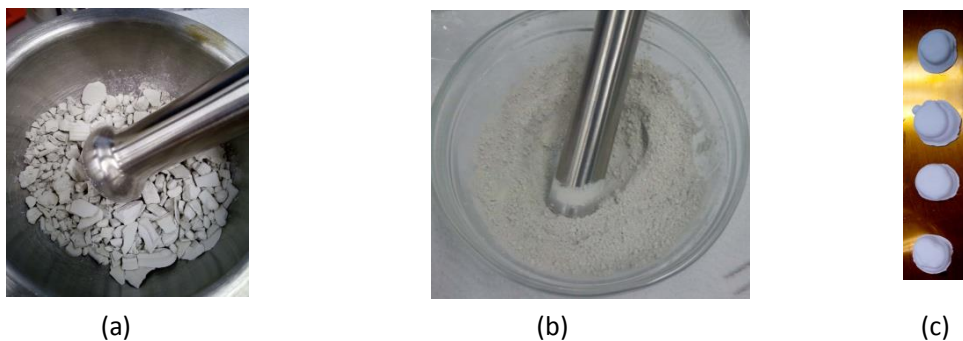


Figure 6.11 (a) AlN green state, (b) crushed using mortar and pestle, (c) 3D printed of recycled AlN.

Then, the ovalbumin mixture is added to the powder to form the printing paste. The paste can then be used to 3D print AlN ceramic structures using the thick paste extruder to the desired shape and size.

Figure 6.12 shows the 3D printing of recycled AlN for 1<sup>st</sup> and 2<sup>nd</sup> time. The physical outlook for both prints is similar. However, even though the quality of the print can be maintained using recycled material, the flexural strength of the recycled AlN ceramic drops drastically as shown in Table 6.4. This is mainly due to the decrease in the solid content of recycled AlN.

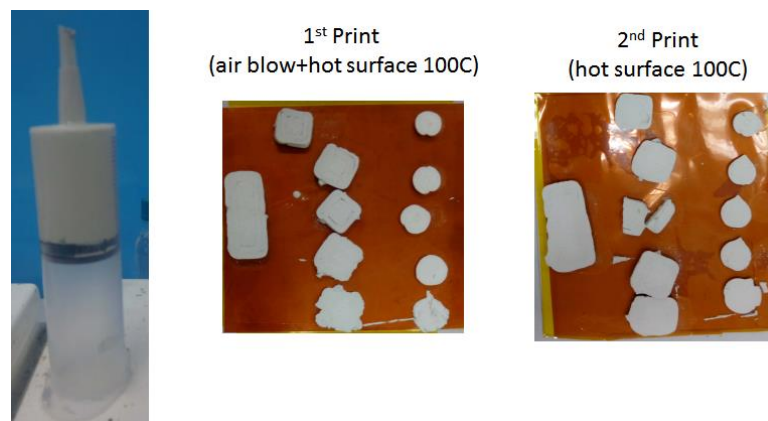


Figure 6.12 3D printing of recycled AlN.

Table 6.4 Comparison of flexural strength of sintered AlN prepared using virgin and recycled AlN ceramics.

AlN source	Relative Density (%)	Flexural strength (MPa)
Virgin materials	94	3.9
Recycled material (1x)	65	0.6
Recycled material (2x)	50	0.5
Recycled material (3x)	40	0.3

The print quality for recycled AlN material can be used only up to 3 times. On the 4<sup>th</sup> print, the quality drops drastically as the solid content is too low for it to be printed (Figure 6.13).





Figure 6.13 3D printing using recycled AlN for the fourth time.

### 6.3.2 Direct gelcast 3D printing of 3D ceramic interposer

#### i) AlN Ceramic substrate with Cu as the interconnecting metal

Table 6.5 shows the gelcasting of pure Cu powder that was not conductive before sintering and becomes conductive after sintering. The electrical resistance measured using the multimeter is similar to a copper plate, which is 0.2  $\Omega$ .

Table 6.5 Gelcasting of pure Cu powder.

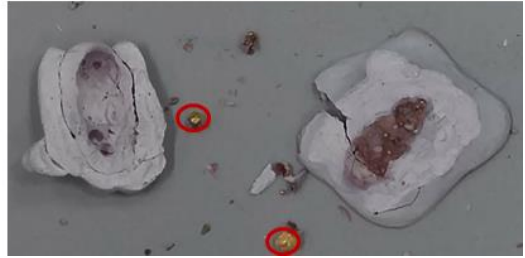
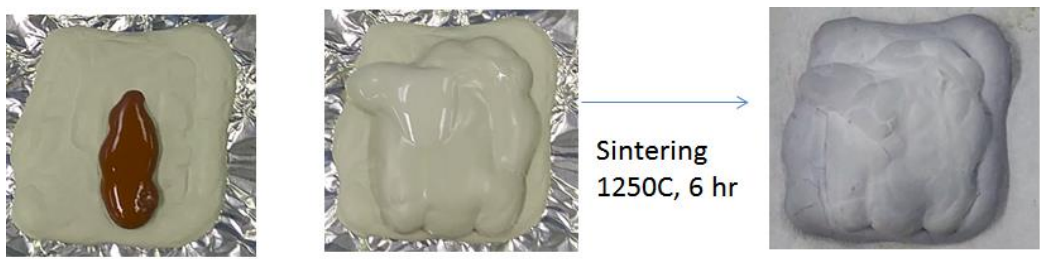
Material	Before Sintering	After sintering (1000°C, 6 hr)	Electrical resistance before sintering ( $\Omega$ )	Electrical resistance after sintering ( $\Omega$ )
Cu Powder			Not conductive	0.2

In order to form a functional interposer, the AlN ceramics and interconnecting metals have to be co-sintered to achieve the desired property. Figure 6.14 (a) shows that co-sintering of AlN ceramics with Cu metal at 1400°C causes cracks. This is because Cu, with a melting temperature of 1085°C, melts at this temperature and agglomerates upon cooling. The agglomeration of Cu upon cooling broke the electrical integrity of the sintered Cu metal.

However, a lower sintering temperature of 1250°C also cracks the interposer and leading to the loss of electrical integrity (Figure 6.14 (b)). Therefore, Cu is found to be not compatible to co-sinter with AlN ceramics at a temperature of more than 1200°C, and hence, an alternative approach is required.



(a)



(b)

Figure 6.14 Sintering of AlN-Cu at (a) 1400°C and (b) 1250°C.

ii) Hybrid SiAlN ceramic substrate with Cu as interconnecting metal

An alternative, hybrid approach of mixing silicon (Si) with AlN as the ceramic substrate was explored. Si has a melting point of 1414°C, which is much lower the

melting point of AlN, at 2,200°C, and therefore could potentially lower the co-sintering temperature of the SiAlN ceramic. Therefore, the low temperature co-fired ceramics (LTCC) process with sintering temperature between 800°C to 1000°C is being explored. Table 6.6 shows the effect of mixing different ratios of Si and AlN on the thermal conductivity of the hybrid SiAlN ceramics after sintering at 1000°C.

Table 6.6 Parameters of hybrid SiAlN ceramics after sintered at 1000°C.

Si (%)	AlN (%)	Thermal Conductivity (W/mK)	Shrinkage (%)
80	20	0.7	16
60	40	0.49	14
40	60	0.53	8
20	80	0.54	6

Figure 6.15 shows that higher Si content in the hybrid SiAlN ceramic substrate has higher thermal conductivity after sintering at 1000°C due to the dominating Si property. However, higher Si content also causes higher shrinkage of the hybrid SiAlN substrate.

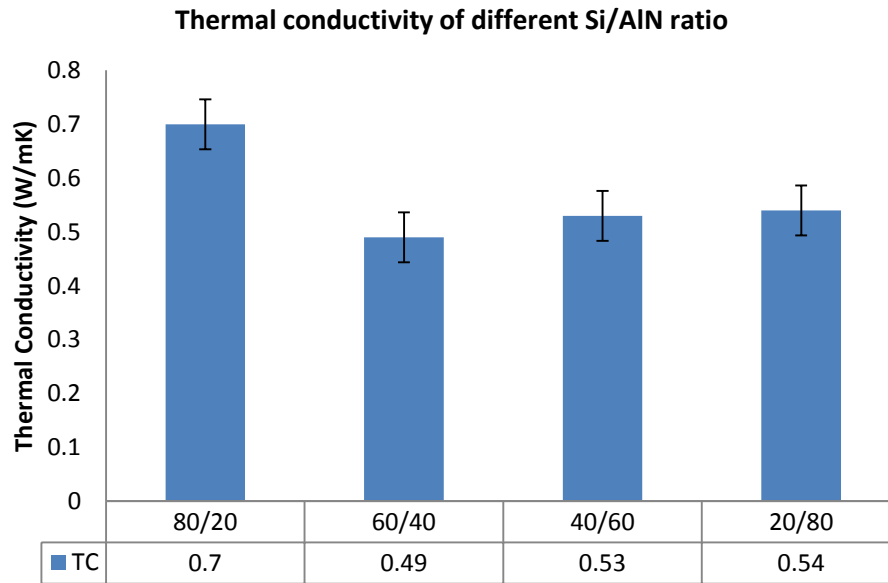


Figure 6.15 Effect of Si/AlN ratios on thermal conductivity after sintering at 1000°C.

Rare earth metal oxides (REOs) are known to lower the sintering temperature of the AlN ceramics (Li, Song, et al. 2015). Therefore, different types of rare earth metal oxides (REOs) are investigated as the sintering aid. The hybrid SiAlN ceramics with a ratio of 20/80 (Si/AlN) is chosen because of the higher AlN content and also due to its lower shrinkage.

Table 6.7 shows that all the REOs investigated are able to improve the thermal conductivity of the hybrid SiAlN (20/80) ceramics at sintering temperatures of 1000°C, 1200°C and 1400°C. The density of the hybrid SiAlN (20/80) ceramics increased with increasing sintering temperature. However, the shrinkage of the hybrid SiAlN (20/80) ceramics reduces with increasing sintering temperature. The hybrid SiAlN (20/80) ceramics after sintered at 1200°C has higher thermal

conductivity when compared to sintering temperature of 1000°C and 1400°C.

Further detail of this progressive sintering study is available in Appendix II.

Table 6.7 Effect of REOs and sintering temperature on hybrid SiAlN (20/80) ceramics.

Sintering Temperature	1000 °C			1200 °C			1400 °C		
	TC (W/mK)	Shrinkage (%)	Density (g/cm <sup>3</sup> )	TC (W/mK)	Shrinkage (%)	Density (g/cm <sup>3</sup> )	TC (W/mK)	Shrinkage (%)	Density (g/cm <sup>3</sup> )
Without REO	0.38	6	0.90	0.87	1	0.99	0.80	2	1.04
REO mixture (Ho/Pr/Dy/Y)	0.48	6	0.99	1.02	2	1.06	0.91	0	1.05
Europium Oxide, Eu <sub>2</sub> O <sub>3</sub>	0.57	5	1.02	1.10	2	1.21	0.72	0	1.14
Dysprosium Oxide, Dy <sub>2</sub> O <sub>3</sub>	0.51	3	0.99	1.31	0	1.12	1.02	1	1.10
Gadolinium Oxide, Gd <sub>2</sub> O <sub>3</sub>	0.59	5	1.17	1.12	3	1.23	0.82	2	1.21
Neodymium Oxide, Nd <sub>2</sub> O <sub>3</sub>	0.74	3	1.01	0.93	6	1.06	0.83	2	1.01
Holmium Oxide, Ho <sub>2</sub> O <sub>3</sub>	0.49	5	1.06	1.16	4	1.11	0.93	0	1.07
Praseodymium Oxide, Pr <sub>2</sub> O <sub>3</sub>	0.57	3	1.05	1.05	3	1.26	0.70	4	1.11
Thulium Oxide, Tm <sub>2</sub> O <sub>3</sub>	0.43	5	1.13	1.29	0	1.24	0.84	4	1.13
Yttrium Oxide, Y <sub>2</sub> O <sub>3</sub>	0.54	6	1.04	1.19	2	1.13	0.92	1	1.12
Erbium Oxide, Er <sub>2</sub> O <sub>3</sub>	0.51	4	0.99	1.21	1	1.26	0.72	1	1.07

Figure 6.16 shows the effectiveness of REO sintering aid to increase the thermal conductivity of SiAlN in the following order Dy<sub>2</sub>O<sub>3</sub>> Tm<sub>2</sub>O<sub>3</sub>> Er<sub>2</sub>O<sub>3</sub>> Y<sub>2</sub>O<sub>3</sub>> Ho<sub>2</sub>O<sub>3</sub>> Gd<sub>2</sub>O<sub>3</sub>> Eu<sub>2</sub>O<sub>3</sub>> Pr<sub>2</sub>O<sub>3</sub>> Nd<sub>2</sub>O<sub>3</sub> that correspond to the thermal conductivity value of 1.31, 1.29, 1.21, 1.19, 1.16, 1.12, 1.10, 1.05, 0.93 W/mK respectively, after sintering 1200°C for 6 hours. As a reference, the thermal conductivity of the hybrid SiAlN (20/80) ceramics without the REO sintering aids was only 0.87 W/mK.

Yijun and Tai (Yijun and Tai 2006) reported that Yttrium Oxide (Y<sub>2</sub>O<sub>3</sub>) and Dysprosium Oxide (Dy<sub>2</sub>O<sub>3</sub>) strengthens the grain boundary of AlN ceramic that will improve the bending strength and thermal conductivity. Y<sub>2</sub>O<sub>3</sub> assisted AlN ceramics has higher strength and fracture toughness compared with Neodymium Oxide



(Nd<sub>2</sub>O<sub>3</sub>) and Erbium Oxide (Er<sub>2</sub>O<sub>3</sub>) (Yijun and Tai 2007). Watari et al. (Watari, Tsuzuki, et al. 1992) reported that the thermal conductivity value of sintered AlN ceramics using sintering aid increases in the order of Dy<sub>2</sub>O<sub>3</sub> > Gd<sub>2</sub>O<sub>3</sub> > Er<sub>2</sub>O<sub>3</sub> > Yb<sub>2</sub>O<sub>3</sub> > Nd<sub>2</sub>O<sub>3</sub> > Sm<sub>2</sub>O<sub>3</sub> due to better internal grain structures that promote oxygen removal.

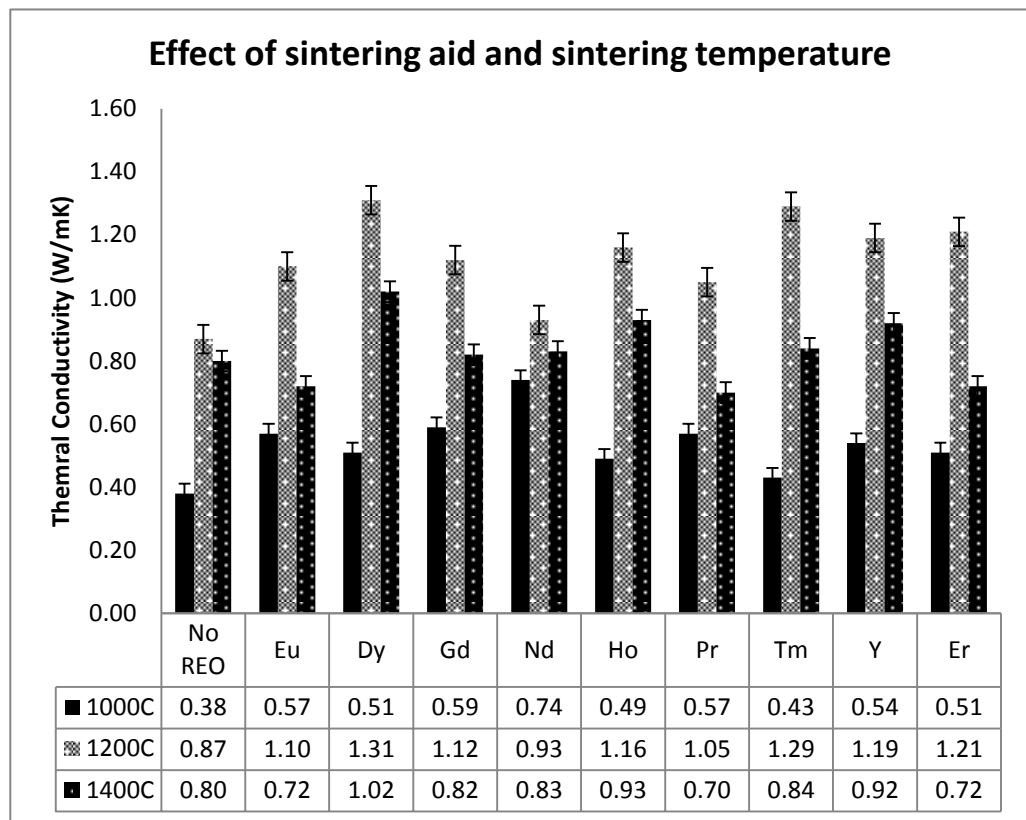


Figure 6.16 REO effect on thermal conductivity and sintering temperature.

The result shows that there is a significant improvement in the thermal conductivity of the SiAlN (20/80) ceramics when the sintering temperature increases from 1000°C to 1200°C, but not much improvement was observed when the sintering temperature increases to 1400°C.

Figure 6.17 shows the effect of sintering temperature on the density of the SiAlN (20/80) ceramics using different REOs as the sintering aid. All the samples exhibit similar characteristic of increasing density when the sintering temperature increases from 1000°C to 1200°C but decreases when sintered at 1400°C. The decrease in density is because Si started to melt when approaching the sintering temperature of 1400°C and agglomerate upon cooling that causes voids and reduces the density. Also, Yijun (Yijun and Tai 2007) has also reported that increasing the temperature will improve AlN transportation along the grain boundaries due to singular growth of AlN grain, which causes the decrease in relative density of the specimens.

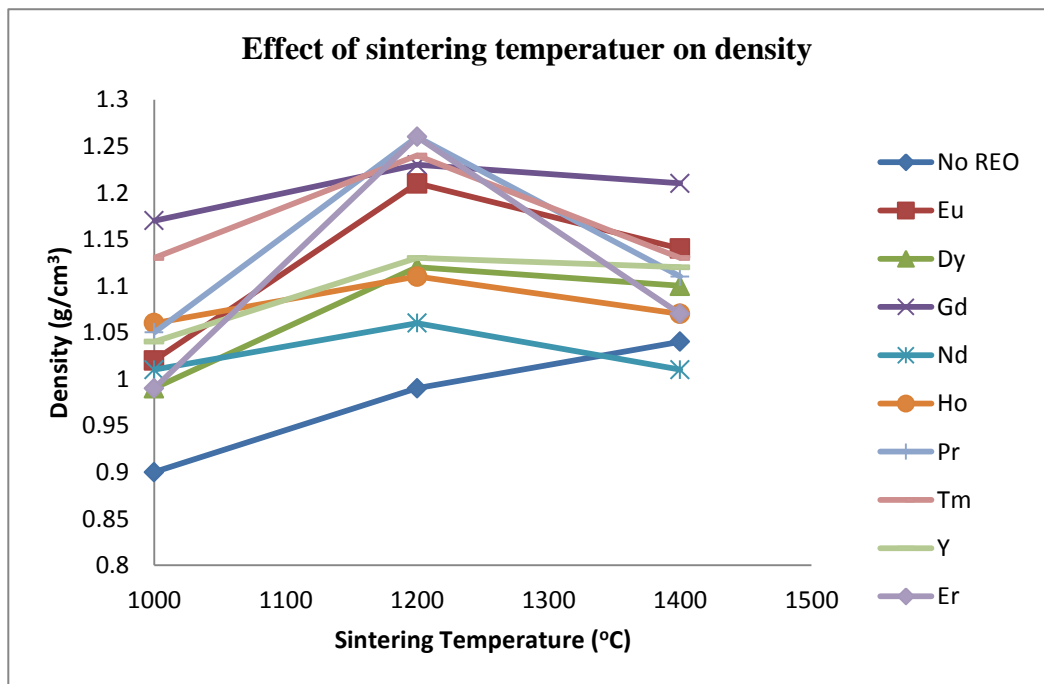


Figure 6.17 Effect of sintering temperature on the density of hybrid SiAlN (20/80) ceramics.

The effect of REOs on higher Si content of the hybrid SiAlN (80/20) was also studied. Table 6.8 shows that the addition of REOs has a negative effect on the hybrid SiAlN (80/20) ceramics with reduced thermal conductivity value after sintering at 1200°C. The only exception is Dy<sub>2</sub>O<sub>3</sub> that increases the thermal conductivity of the hybrid SiAlN (80/20) ceramics by around 30%. Therefore, REOs does not improve the sintering of hybrid SiAlN with higher Si content.

Table 6.8 Sintering of hybrid SiAlN ceramics at 1200°C.

Sintering Aid	SiAlN (20/80)	SiAlN (80/20)
	TC (W/mK)	TC (W/mK)
Without REO	0.87	1.76
Dysprosium Oxide, Dy <sub>2</sub> O <sub>3</sub>	1.31	2.28
Neodymium Oxide, Nd <sub>2</sub> O <sub>3</sub>	0.93	0.79
Thulium Oxide, Tm <sub>2</sub> O <sub>3</sub>	1.29	1.30
Yttrium Oxide, Y <sub>2</sub> O <sub>3</sub>	1.19	1.72
Erbium Oxide, Er <sub>2</sub> O <sub>3</sub>	1.21	1.70

Further optimization of the hybrid SiAlN ceramics with different bimodal AlN powder and higher REO content was shown in Table 6.9. The result shows that bimodal AlN mixture of 0.5 μm & 1 μm particle sizes has a higher thermal conductivity value and density as compared to bimodal AlN mixture of 3 μm & 5 μm particle sizes. The smaller particle size has better packing density that assists in the transfer of heat using lattice waves (phonons). Lattice waves (phonons) are the vibration of atoms coupled with neighboring atoms and is related to the compactness of the crystal lattice and therefore, the density of the material (Tritt 2005).

The highest thermal conductivity of the hybrid SiAlN (20/80), for the sintering temperature of 1000°C, is 0.76 W/mK using 2 wt% of Dy<sub>2</sub>O<sub>3</sub> as the sintering aid and

bimodal AlN particles size distribution of 0.5  $\mu\text{m}$  & 1  $\mu\text{m}$ . Also, the results show that a higher amount of sintering aid has a negative effect on the density and thermal conductivity of the hybrid SiAlN (20/80) ceramics. REOs are a type disappearing sintering aid that enhances densification at the initial stages of sintering by forming liquid phase component at the grain boundaries of the AlN particles after reacting with  $\text{Al}_2\text{O}_3$  at a lower temperature that removes voids and oxygen in the process. It is removed as a gas in the final stages of sintering. However, REOs have low thermal conductivity and if the residue is present in the AlN ceramic matrices, it could reduce the overall thermal conductivity of the AlN ceramics (Watari, Hwang, et al. 1999).

Table 6.9 Parameter optimization for hybrid SiAlN ceramics.

Mixture		Sintering Aid		Sintering at 1000°C		
SiAlN(v/v)	AlN( $\mu\text{m}$ )	Dy <sub>2</sub> O <sub>3</sub>	Y <sub>2</sub> O <sub>3</sub>	Thermal Conductivity (W/mK)	Specific Heat (J/kgC)	Density (g/cm <sup>3</sup> )
20/80	3/5	-	-	0.66	608.4	1.918
40/60	3/5	-	-	0.51	482.1	1.773
20/80	3/5	-	-	0.6	583	2.023
20/80	0.5/1	-	-	0.62	580.2	2.193
20/80	0.5/1	2%	-	0.76	718	2.093
20/80	0.5/1	5%	-	0.72	696.3	1.944
20/80	0.5/1	-	2%	0.76	584.3	2.130
20/80	0.5/1	-	5%	0.48	466.2	1.808
20/80	3/5	2%	-	0.61	440.9	2.107
20/80	3/5	2%	-	0.63	662.7	1.449
20/80	3/5	-	2%	0.6	545.6	1.825
20/80	3/5	-	2%	0.59	523.9	1.664

Table 6.10 shows the effect of raising the sintering temperature of the hybrid SiAlN (20/80) to the sintering temperature for AlN, 1600°C for 6 hours. The highest

thermal conductivity value achieved for the hybrid SiAlN (20/80) is only 3.26 W/mK using Dy<sub>2</sub>O<sub>3</sub> as the sintering aid, much lower than AlN ceramics that has a thermal conductivity value of 19 W/mK. This because Si melts at 1414°C and the agglomeration of the melt when cooled will affects the structure of the ceramics and reduces its thermal conductivity.

Table 6.10 Sintering of hybrid SiAlN (20/80) ceramics at 1600°C.

Tm <sub>2</sub> O <sub>3</sub>	Y <sub>2</sub> O <sub>3</sub>	Thermal Conductivity (W/mK)	Specific Heat (J/kgC)	Density (g/cm <sup>3</sup> )
-	-	1.98	643.4	2.446
-	2%	2.79	527.6	2.565
2%	-	3.26	578.9	0.579

However, the advantage of the hybrid SiAlN (20/80) ceramics is its low shrinkage, 6% after sintered at 1000°C, compared to 20% for AlN ceramics, and a thermal conductivity value of 0.76 W/mK, more than three times higher than the conventional organic substrate (0.2 W/mK).

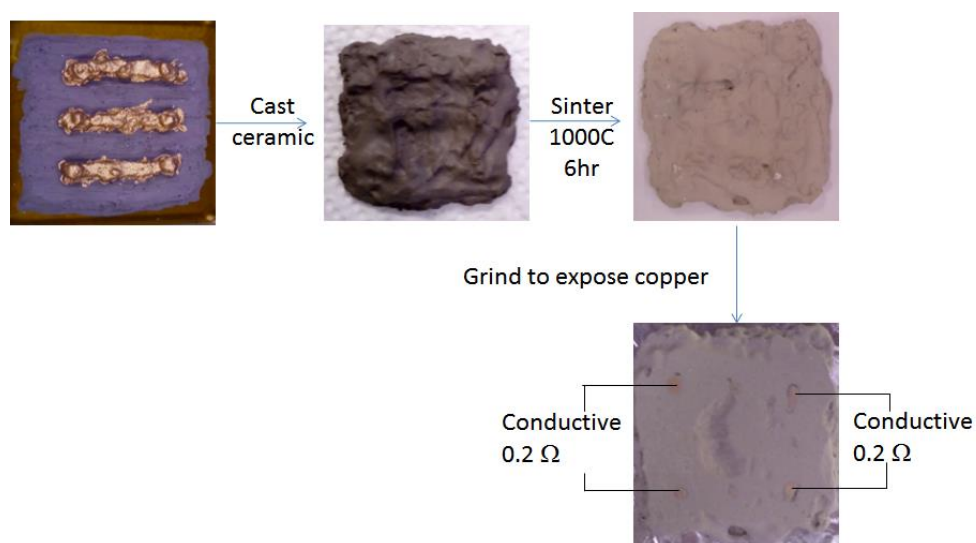


Figure 6.18 Co-sintering of hybrid SiAlN (20/80) ceramic substrate with Cu interconnect at 1000°C.

Figure 6.18 shows the 3D ceramic interposer made using Cu as the interconnect metal and hybrid SiAlN (20/80) as the ceramic substrate, sintered at 1000°C for 6 hours. After polishing of the hybrid SiAlN 3D ceramic interposer to expose the copper metal, the electrical resistance of the Cu interconnects matches that of the copper plate (0.2 Ω). Therefore, eco-friendly direct gelcast 3D printing can be used to produce LTCC SiAlN 3D ceramic interposer for applications that require higher electrical conductivity but can accommodate lower thermal conductivity with reduced shrinkage.

### iii) 3D printing of functional AlN ceramic interposer

Figure 6.19 shows the CAD design for direct gelcast printing of multi-layer multi-material that consists of AlN ceramics and Mo metal.

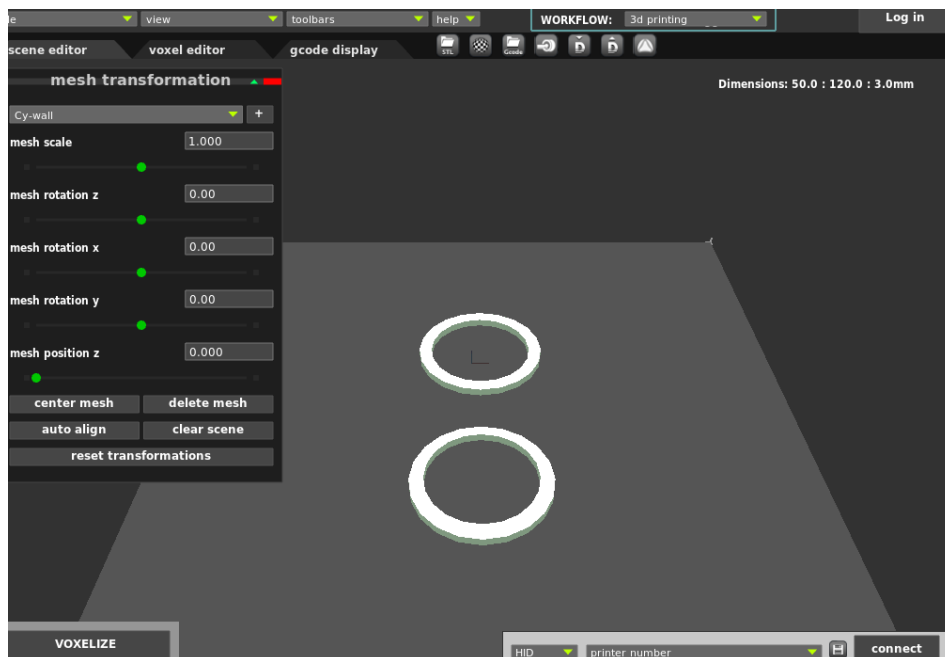


Figure 6.19 Voxelizer software showing the CAD drawing.

Figure 6.20 shows the actual print where firstly Mo/ovalbumin paste was printed from the CAD file; then after changing to the syringe containing AlN/ovalbumin paste, the AlN/ovalbumin is printed on top of the Mo/ovalbumin. The printer was able to print the AlN/ovalbumin ceramics on top of Mo/ovalbumin accurately. The structure is then debinded and sintered to form the sintered multi-material Mo-AlN component. There are no cracks observed showing the good integrity of the printed multi-material structure.

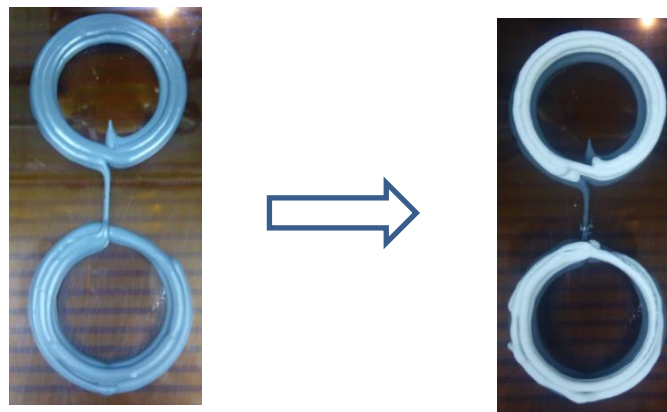


Figure 6.20 Direct gelcast printing of multi-material using the CAD design.

Figure 6.21 shows the step-by-step fabrication of high-performance 3D ceramic interposer with functional circuitry by a direct gelcast 3D printing of multi-layer multi-material AlN ceramic and Mo metal. First, the AlN/ovalbumin gelcast is printed at the base plate with empty cavities for Mo/ovalbumin gelcast. This is followed with the printing of Mo/ovalbumin gelcast onto these cavities and to form the circuit line. Subsequently, AlN/ovalbumin is printed on top of the interconnect

line, leaving the cavity open. Finally, the Mo/ovalbumin gelcast fills the cavities that acts as the electronic terminal and completes the 3D interposer construction.

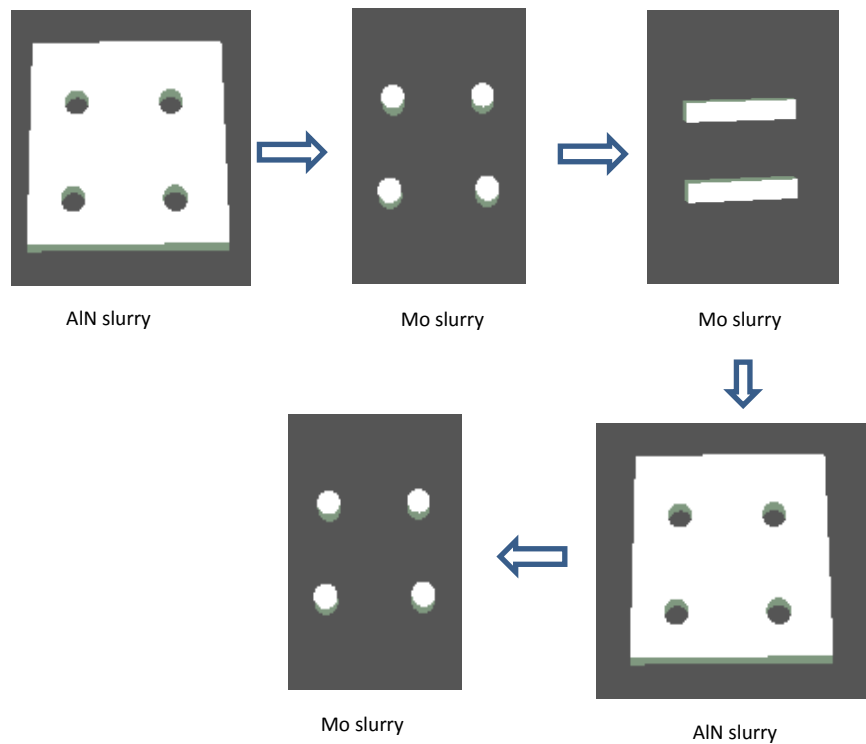


Figure 6.21 Direct gelcast printing sequence using Voxelizer software.

Figure 6.22 shows the actual sample with the print sequence stated previously. The printing can fill the gap correctly and forms a conducting Mo interconnect line that was embedded in the AlN ceramic substrate for electrical conduction. The AlN-Mo 3D ceramic interposer is then sintered using the sintering profile in Figure 6.5 to form the functional interposer circuitry



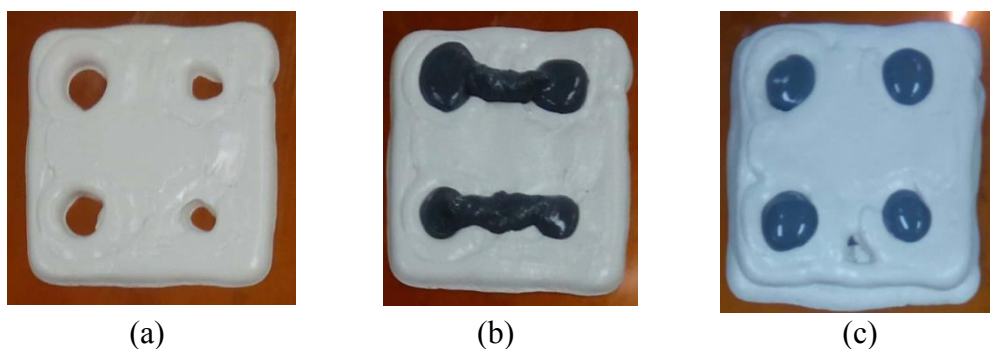


Figure 6.22 Actual sample printed using direct gelcast 3D printing of multi-layer materials (a) AlN interposer, (b) Mo interconnect, (c) AlN interposer on top of Mo interconnect.

A 3W LED (Avago) was attached using silver paste to connect the Mo terminal, and the interposer circuitry was proven to be functional by lighting up the LED using a DC current (Figure 6.23).

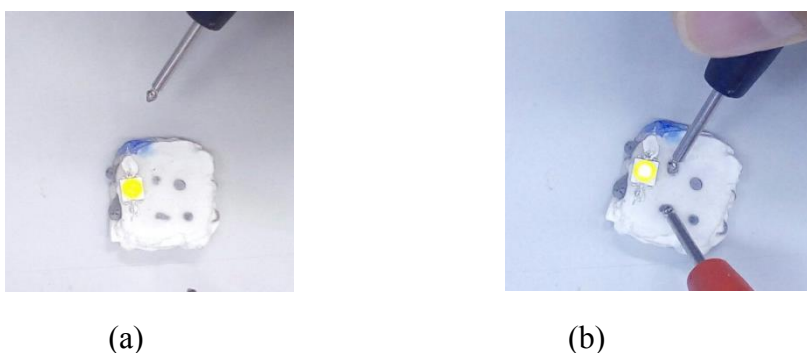


Figure 6.23 Functional interposer with AlN with embedded Mo conducting line (a) before applying current (b) LED turn on when applying DC current.

As both the AlN/ovalbumin and Mo/ovalbumin paste uses the same natural binder, ovalbumin, the same sintering profile can be used for both materials. Therefore, the 3D printed ceramic interposer can be functionalized after co-sintering at 1600°C for 6 hours, which is within the temperature range for high temperature

co-fired ceramics (HTCC). Besides, the coefficient of thermal expansion (CTE) between AlN ( $4.5 \times 10^{-6}/^{\circ}\text{C}$ ) and Mo ( $4.8 \times 10^{-6}/^{\circ}\text{C}$ ) matches closely and therefore, reduces the strain caused during shrinking as both of these materials have similar shrinkage profile. There was no interface crack observed between AlN ceramics and Mo metal indicating that the structure is intact after co-sintering to form the functional 3D ceramic interposer.

#### **6.4 Concluding remarks**

Direct gelcast 3D printing is an eco-friendly and versatile process technology for producing multi-materials, such as hybrid SiAlN ceramics with Cu interconnecting metal and AlN ceramics with Mo interconnecting metal using sustainable natural protein, ovalbumin, as the gelcasting monomer (60 wt% solid loading). Low temperature co-fired ceramics (LTCC) process with sintering temperature from  $800^{\circ}\text{C}$  to  $1000^{\circ}\text{C}$  was demonstrated with the hybrid SiAlN-Cu 3D ceramic interposer and high-temperature co-fired ceramics (HTCC) process with sintering temperature above  $1500^{\circ}\text{C}$  was demonstrated with AlN-Mo 3D ceramic interposer. The high-performance HTCC AlN has a high thermal conductivity value of  $19 \text{ W/mK}$ , and is much higher than the  $0.76 \text{ W/mK}$  for LTCC SiAlN. However, the electrical resistivity of the LTCC Cu/SiAlN of  $3.3 \times 10^{-4} \Omega\cdot\text{cm}$  is better than the  $4.1 \times 10^{-4} \Omega\cdot\text{cm}$  for HTCC Mo/AlN. Therefore, different 3D ceramic interposer system can be produced to suit the specific application depending on the requirement for heat dissipation and electrical conduction.

The 3D multi-material structure can be directly printed from the CAD design demonstrating the versatility of the process in producing complex shape with different types of materials using the same eco-friendly and green monomer, ovalbumin. The process is simple and fast that will contribute significantly to the development of the industry towards mass customization leading to production of specialized high-performance multi-materials. The process can be extended for use with other metals and ceramic system that are compatible in sintering temperatures. Stearic acid is proven effective in protecting metals and the versatility of ovalbumin as the eco-friendly monomer for gelcasting was demonstrated. The use of sustainable natural protein, ovalbumin, as the monomer and when coupled with the additive manufacturing process to reduce waste, direct gelcast 3D printing process, is indeed an eco-friendly manufacturing process.

# Chapter 7 Conclusions and suggestions for future research

## 7.1 Overall conclusions

The quest for developing the ever-improving performance of electronics has driven the development of 3D interposer technology to integrate more functions within a single structure. However, this has created serious thermal management issue because all layers sharing a common thermal path aggregated by the compounding effect and longer distance causes large thermal gradient that is difficult to be fulfilled by heat sink alone. Therefore, there is an urgent need for the interposer material itself to be more efficient in distributing the heat to reduce hot spots that cause device failure.

A 3D interposer consists of (i) a substrate with (ii) embedded interconnecting metals to form the functional circuitry. (i) The most common interposer substrate material is organics due to its cost and proven reliability but it could not fulfill the current demand of heat dissipation performance because of its low thermal conductivity. The development of high thermal conductivity ceramics, aluminum nitride (AlN) having a thermal conductivity of around 100 times better than organics was successfully developed.

(ii) The interconnecting metal in the 3D interposer will need to be compatible with the interposer substrate. The refractory metal, molybdenum (Mo), was successfully developed to be compatible with the processing of AlN ceramic

substrate.

The current multi-layer ceramics process to produce 3D ceramic interposers involves multiple steps with dedicated tools and equipment, and extensive use of solvents that make the process costly and not environmental-friendly. A simpler process of direct gelcast 3D printing was successfully developed using aqueous-based green chemistry approach. The green gelcasting process used the sustainable natural protein, ovalbumin for both AlN ceramic substrate and Mo interconnecting metal. The direct gelcast 3D printing can print multi-material directly from the CAD system that proves to be versatile in producing high-performance 3D ceramic interposer.

### **(1) Aluminum nitride (AlN) ceramic substrate by green chemistry approach**

AlN with different particle sizes and fillers were studied to find the optimized casting parameter to produce the ceramic substrate with the best thermal conductivity. The major findings in this part are given below:

i) The natural protein, ovalbumin, prepared from natural egg white was successfully developed as the gelcasting monomer to make AlN ceramic substrate. The pre-sintered AlN ceramics green body has a flexural strength of 3 MPa that is sufficient for light mechanical polishing before sintering. The XRD spectra of the gelcasted AlN ceramics does not show the presence of hydrolyzed species of AlN such as  $\gamma$ -AlOOH,  $\text{Al}(\text{OH})_3$  or  $\gamma$ - $\text{Al}_2\text{O}_3$  that could hinder the thermal conductivity of the AlN ceramic substrate.

ii) Nano-sized AlN particles (0.1  $\mu\text{m}$ ) were found to perform better than micron-sized AlN particles. However, the best thermal conductivity was obtained from the bimodal mixing ratio of 1.5 (3 $\mu\text{m}$  & 5 $\mu\text{m}$ ) and 2 (0.5 $\mu\text{m}$  & 1 $\mu\text{m}$ ) with a thermal conductivity value of 17 W/mK and 18 W/mK respectively.

iii) The AlN/ovalbumin slurry exhibited a non-Newtonian type of rheology with shear thinning characteristic and slurry with smaller particle size has lower viscosity. It was found that higher solid loading will produce an AlN ceramic substrate with higher density and higher thermal conductivity. The AlN ceramic substrate with a solid loading of 60 wt% achieved its highest thermal conductivity of 21 W/mK in this study, compared to 0.2 W/mK for the organic substrate.

## **(2) Interconnecting metals compatible with AlN green gelcasting process**

Interconnecting metals that are compatible with the AlN green gelcasting process will need to be developed to form the functional 3D Ceramic Interposer. Therefore, the interconnecting metals should be produced using a similar process as that of the AlN ceramic substrates, i.e., gelcasting using ovalbumin as the natural protein monomer. The major findings in this part are as below:

i) The refractory metal, molybdenum (Mo), was gelcasted successfully using similar process parameter as the green gelcasting of AlN ceramic substrate. Sintering of the Mo/ovalbumin gelcast at 1600°C for 6 hours produces Mo metal with an electrical resistivity of  $4.10 \times 10^{-4} \Omega\cdot\text{cm}$ , slightly higher than the copper plate ( $3.3 \times 10^{-4} \Omega\cdot\text{cm}$ ). Therefore, Mo is suitable as the interconnect metal for the

AlN ceramic interposers.

ii) Copper (Cu) powder was successfully gelcasted using ovalbumin as the gelcasting monomer. The gelcasted Cu is not electrically conductive in the green state but is conductive after sintering at 1000°C for 6 hours with an electrical resistance of 0.2Ω. Sintering of gelcasted copper oxide at 1000°C was also found to be conductive but with higher electrical resistance. However, Cu has a low melting temperature of 1085°C that causes cracks due to nucleation when co-sintered with AlN at 1600°C.

iii) Stearic acid pretreatment was found to protect the metal surface from oxidation in the aqueous-based ovalbumin premix. XRD analysis of sintered Mo metal does not show the presence of oxides phases of Mo, whereas XRD spectra for Cu show only a small amount of Cu oxide present due to surface oxidation when Cu is exposed to air.

iv) Gelcasting of molybdenum using 1μm particle size is better than 3μm particle size. The slurry has lower viscosity for easier processing with better flexural strength and lower electrical resistivity. The shrinkage of the sintered molybdenum parts is around 20%, similar to AlN ceramics.

### **(3) Direct gelcast 3D printing of 3D ceramic interposer for microelectronic applications**

The direct gelcast 3D printing process will be optimized for directly producing 3D ceramic interposer followed by sintering to produce the functional

circuit. The major findings in this part are as below

i) Direct 3D gelcast printing using thick paste extruder can be used to produce 3D structures directly from the CAD file. The printing base plate has to be heated to 80°C to allow for quick solidification and gelation of ovalbumin slurry. The preceding layer has to be dried for the subsequent layer to build-up and is assisted by hot air blow.

ii) The 3D printed AlN in the green state can be recycled by crushing it into small particles and added ovalbumin to form the AlN/ovalbumin slurry for re-printing up to 3 times without affecting the print quality but with lower flexural strength. This recycling process will enable savings in the material during the prototyping stage.

iii) Copper is not suitable as the interconnecting metal for AlN ceramic substrate because its melting temperature is lower than the sintering temperature of AlN ceramic.

iv) Hybrid SiAlN ceramics substrate with Si:AlN ratio of 20:80 has a thermal conductivity of 0.76 W/mK after sintering at 1000°C for 6 hours, still better than 0.2 W/mK for the organic substrate. The hybrid ceramics have low shrinkage (5%) and could be co-sintered with copper at 1000°C to produce a functional 3D ceramic interposer.

iv) The direct gelcast 3D printing can be used to produce 3D structures of multi-materials; AlN ceramic, and molybdenum metal. A functional high thermal conductivity 3D ceramic interposer was printed and sintered to form the functional



circuitry that can power up a light emitting diode (LED). The simplified process will be able to reduce the process step in making 3D ceramic interposers for microelectronic applications besides reducing materials wastage when compared to conventional subtractive manufacturing processes.

## 7.2 Significance of the study

The result of the study has proven that direct gelcast 3D printing is an eco-friendly manufacturing technology that uses eco-friendly materials and an eco-friendly process that produces less waste. The eco-friendly material used was ovalbumin, a natural protein obtained from egg white. It is a sustainable, safe and biodegradable material that creates minimal impact on the environment. Also, the monomer is proven to be versatile for use in both metals and ceramics.

The eco-friendly process is the direct gelcast 3D printing process, based on the additive manufacturing process that uses gelcast slurry as the source of material. Additive manufacturing has the flexibility to produce parts on-demand based on CAD design. Therefore, parts with different design could be produced concurrently. Besides, less waste will be generated by the additive manufacturing technology as compared to the conventional subtractive techniques since the processing steps required are lesser.

Also, the green body of the printed parts could be recycled for subsequent printing up to three times before recovering the ceramic or metal powder by way of debinding. The printed parts, in the green body, are brittle, but strong enough for handling. It will be suitable as a prototyping tool to replace some of the plastic 3D printers such as the most popular Fused Deposition Modelling (FDM) systems. There is a growing concern on the popularity of the home FDM 3D printing system that will perpetuate an unhealthy reliance on plastics. The problem with plastics is their resistance to decay; it does not disappear on its own and recycling it the only

option. However, the current technology for recycling plastics is expensive and tedious (Hopewell, et al. 2009). The other problem with plastics is that they are flammable and easily burnt. A study by Illinois Institute of Technology (IIT) (Stephens, Azimi, et al. 2013) have shown that the particle pollution due to the FDM 3D printing is similar to stovetop cooking, burning scented candles, or burning a cigarette that poses risks to the airways and circulatory system that can cause breathing problems, heart attack, and stroke. The plastic filaments used in current 3D printers are mostly acrylonitrile butadiene styrene (ABS) or bio-based polylactic acid (PLA), and the study found that ABS printers produce more ultrafine particles (less than 100nm), 200 billion per minute, compared to PLA with 20 billion per minute. Also, the white fumes from heated ABS plastic are found to be toxic to lab rodents compared to the less toxic corn-based PLA. The exposure of nanoparticles at high concentration poses serious health risk such as total and cardio-respiratory mortality, strokes, and asthma symptoms (Wojtyła, S., et al. 2017). Therefore, the direct gelcast 3D printing system could be a safe alternative for prototyping.

This technology has proved to be versatile and suitable for both ceramics and metals. The capability of multi-material 3D printing is a significant development that will allow useful components to be built using a single printer. The in-situ co-firing of multi-materials allow functional parts to be produced and gets us closer to the concept of “manufacturing of one” that is in line with the Industry 4.0 concept to reduce waste by producing parts only in demand, and not in excess.

### **7.3 Suggestion for future research**

High-performance electronics will require better heat dissipation characteristics and ceramics are popular choices with many times better thermal conductivities than conventional polymer substrates. The current parallel process of producing multi-layer ceramics, since 1965, has not changed much and the process is expensive due to multiple steps and tooling for each step is required. In this work, a modified additive manufacturing process, direct gelcast 3D printing, was developed to directly produce 3D parts from the CAD software design to replace tooling that is required in the conventional method. Also, the process mainly uses the green chemistry approach, using a sustainable natural source, ovalbumin, to make it environmental-friendly to produce.

Although this study can prove the concept of direct gelcast 3D printing and meet all the objectives, there is still some related research that can be undertaken to enhance the process further.

(1) Further study to improve the performance of the thick paste extruder machine used for direct gelcast 3D printing. The current system only has a single nozzle, and therefore, printing of multiple materials require changing of the nozzle manually. The development of multiple nozzle systems will increase the process speed, improve precision and reduce wastage. Also, the current thick paste extruder has a nozzle diameter of 2 mm and therefore, was not able to produce parts with sub-micron precision. Better equipment will need to be developed to produce fine microelectronic components.

(2) Further study could also be conducted to modify the gelcast slurry to fit the 3D inkjet printer system for higher resolution printing as compared to thick paste extruder. Future research could include formulating the gelcasting slurry with reduced viscosity to meet the requirement of high-resolution inkjet printing.

(3) Better sintering technology could be studied to increase the thermal conductivity of the AlN ceramic substrates. Advance sintering system such as microwave sintering and spark plasma sintering has been reported to have short sintering time that greatly enhances densification. Sintering materials using microwave consume less energy, higher heating rates, and higher density with better physical and mechanical properties. The high density and smaller grain size by the SPS method have a direct effect on most of the properties of the sintered materials. Most reported higher densities and lower sintering temperatures when using SPS with additional improvements such as mechanical properties, chemical resistance, microstructure, and electrical properties. This advance sintering technology could probably improve the density of the ceramics and consequently increase its thermal conductivity.

(4) The modern microelectronic devices consist of multiple layers of different materials that are consists of insulators and conductors. The factors that will affect the lifetime of the microelectronic devices include design rules, operating voltage, and maximum switching speeds to ensure functional operation. The microelectronic integration density design will depend on the reliability of the device at the desired

circuit density. Therefore, detailed reliability and stability study of the 3D ceramic interposer will be required for use in the design of microelectronic devices.

## Appendix I: Thermal conductivity measurement report

Thermal conductivity of the unimodal AlN ceramics (0.1  $\mu\text{m}$ ) with a thermal conductivity of 11.19 W/mK (Table 4.3) was measured using the Flashline 2009 thermal conductivity measurement software.

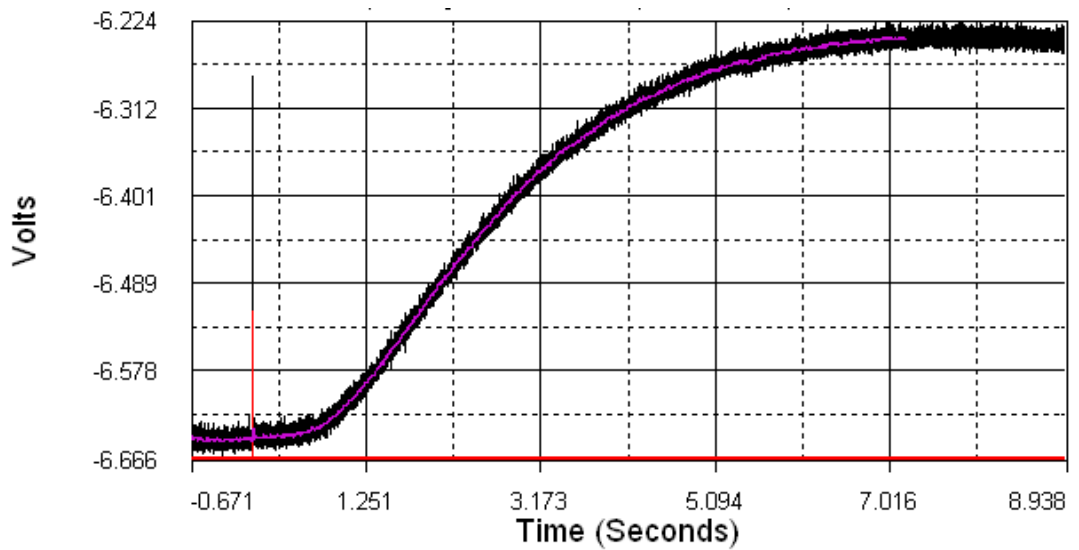
Thickness: 0.2200 (cm)      Specific Heat (J/(kg·K))

Segment	Temperature	Avg
1	26	704.3

Thickness: 0.2200 (cm)      Conductivity (W/(m·K))

Segment	Temperature	Avg
1	26	11.19

Thermogram plot of laser signal vs time at 25.50°C for AlN ceramic



The calculated pulse, from the Cowan model was used to trace the laser pulse plot against time. The diffusivity value is then calculated as follows:

Segment = 1 Specimen = 4 Shot = 1

Thickness (cm): 0.2200 Diameter (cm): 1.1350

Half Time (s): 0.09713 Time Max Temp (s): 0.43580

Temperature (°C) 25.50

Diffusivity, Clark & Taylor (cm<sup>2</sup>/s): 0.067994

Analysis	Diffusivity (cm <sup>2</sup> /s)	Goodness of Fit	SSR	Loss Factor
Clark & Taylor:	0.067994	0.999266	0.0302	0.0142
Parker :	0.069224	0.997212	0.1147	0.0000
Degiovanni:	0.067345	0.997759	0.0921	0.0142
Moment:	0.070012	0.996427	0.1469	0.0142
Logarithmic:	0.071657	0.981012	0.7808	0.0000
Least Squares 1D:	0.068410	0.999573	0.0175	0.0171
Least Squares 2D:	0.068395	0.999573	0.0176	0.0163

#### Analysis Starting at 20%

Analysis	Diffusivity (cm <sup>2</sup> /s)	Goodness of Fit	SSR
Clark & Taylor:	0.067994	0.999573	0.0110
Parker:	0.069224	0.995761	0.1096
Degiovanni:	0.067345	0.997600	0.0621
Moment:	0.061240	0.877346	3.1720
Logarithmic:	0.069211	0.995835	0.1077
Least Squares 1D:	0.000000	0.000000	0.0000
Least Squares 2D:	0.067860	0.999838	0.0042



Clark & Taylor (Original Ratio Calculation ): 0.06801 (cm<sup>2</sup>/s)

Degiovanni (Original Ratio Calculation ): 0.06741 (cm<sup>2</sup>/s)

Cowan (5 x half time 10 x Half Time): 0.06371 (cm<sup>2</sup>/s)

### Ratios

	Clark & Taylor	Degiovanni	Cowan
R1:	0.06849	2/3: 0.06661	5x: 0.06094
R2:	0.06798	1/2: 0.06734	10x: 0.06648
R3:	0.06758	1/3: 0.06829	

Koski: 0.06834 (cm<sup>2</sup>/s) type used: 10

Koski (avg): 0.06834 Max Loss: 0.0162

Koski (.7/.3): 0.06835 Loss: 0.00100 R1: 0.01853 R2: 1.86610

Koski (.8/.2): 0.06886 Loss: 0.00200 R1: 0.01853 R2: 2.71850

Koski (.8/.4): 0.06780 Loss: 0.01621 R1: 0.01853 R2: 1.90837

Koski (Cowan5): 0.09755 Loss: 0.19577 R1: 0.01853 R2: 1.00000

Koski (original modified): 0.06687

Acq Rate = 15000 (Points per Second)

27 pulse width (Number Points)

DA Voltage -0.107 Offset = -6.762 Maximun Temperature Rise (Voltage) 0.660  
0.660

LMV (Pulse Voltage) = 3.259 Carousel 4880 Iris 0 HP 0

Laser Setpoint Voltage: 600 Readback:715

Pulse Width Correction

(Uses Center of Gravity Calculation)

CG: 0.000408 (Seconds)

FPC: 0.000405 (Seconds) Finite Pulse Correction

Cp = 704.324 Specific Heat (J/(kg·K))

k = 11.190 Conductivity (W/(m·K))

Cp Correction: 0.000 Cp Unc: 0.000

Maximum Rise: 0.660503 Simul Max Dimless: 0.838508 Method A:  
0.973134

Cp Dens: 2336.590088 Density (kg/m<sup>3</sup>)

Cp MaxV: 0.660503

Cp DimL: 0.838508

Cp OffS: 1.000000

Cp Sens: -6.761559

Cp Thck: 0.220000

Cp Diam: 1.135000

Ref Cp: 813.149353

Ref Dens: 2555.090576 Density (kg/m<sup>3</sup>)

Ref MaxV: 0.568377

Ref DimL: 0.841377

Ref OffS: 1.000000

Ref Sens: -6.823310

Ref Thck: 0.203200

Ref Diam: 1.270000

In Plane: 0.0000 (cm<sup>2</sup>/s)

SMD: 0.0000 (cm<sup>2</sup>/s)

SHA: 0.0000 0.0000

Santa: 0.0646 (cm<sup>2</sup>/s)

Ratios 0.90000 0.50000

Process Type: 21 Filter: 50.0 20.0

Average Number Points: 51 Trg Type: 2 Pre: 5.0 Post: 85.0

Baseline

B: 0.000000e+000 0.000000e+000 B10 0.000000e+000 0.000000e+000

Ratio - Time

temp. (seconds)

0.100 0.045

0.200 0.059

0.250 0.065

0.300 0.071

0.333 0.075

0.400 0.084

0.500 0.098

0.600 0.113

0.667 0.126

0.700 0.133

0.750 0.146

0.800 0.160

0.833 0.17220

0.900 0.203

1.000 0.000

Unc Thk = 0.220 Uncorrected Thickness (cm)

CT FPC = 0.070

FPC = 1.002 Finite Pulse Correction (Old Style)

Baseline = -6.75991

Clark & Taylor : 6.799362e-002 (cm<sup>2</sup>/s)

-----END-----

## Appendix II: Ceramic sample information

### Ceramic sample information

No.	Sample	Thickness, mm	Density, kg/m <sup>3</sup>	TC W/mK	SH J/kg.K	Tables
1	Unimodal AlN 0.1 $\mu\text{m}$	2.21	1658	NA	NA	Table 4.2
2	Unimodal AlN 0.1 $\mu\text{m}$	1.95	2630	12.2	847.2	Sample 1 after sintering
3	AlN 0.5 $\mu\text{m}$	2.16	1189	NA	NA	Table 4.2
4	AlN 0.5 $\mu\text{m}$	1.99	2263	8.03	906.3	Sample 3 after sintering
5	AlN 1 $\mu\text{m}$	2.02	1213	NA	NA	Table 4.2
6	AlN 1 $\mu\text{m}$	1.86	2460	8.36	898.5	Sample 5 after sintering
7	AlN 5 $\mu\text{m}$	2.01	1185	NA	NA	Table 4.2
8	AlN 5 $\mu\text{m}$	1.85	2336	8.24	769.8	Sample 7 after sintering
9	Bimodal AlN 0.1&0.5 $\mu\text{m}$	2.53	1472	NA	NA	Table 4.2
10	Bimodal AlN 0.1&0.5 $\mu\text{m}$	2.24	2581	11.4	838.9	Sample 9 after sintering
11	Bimodal AlN 0.1&1 $\mu\text{m}$	2.12	1628	NA	NA	Table 4.2
12	Bimodal AlN 0.1&1 $\mu\text{m}$	1.83	1970	13.6	793	Sample 11 after sintering
13	Bimodal AlN 0.1 &5 $\mu\text{m}$	2.55	1531	NA	NA	Table 4.2
14	Bimodal AlN 0.1 &5 $\mu\text{m}$	2.20	2801	10.8	931.1	Sample 13 after sintering
15	Bimodal AlN 0.5 &1 $\mu\text{m}$	1.95	1589	NA	NA	Table 4.2
16	Bimodal AlN 0.5 &1 $\mu\text{m}$	1.60	2675	17.5	813.2	Sample 15 after sintering
17	Bimodal AlN 0.5&5 $\mu\text{m}$	2.35	1357	NA	NA	Table 4.2
18	Bimodal AlN 0.5&5 $\mu\text{m}$	2.17	2536	7.59	387.6	Sample 17 after sintering
19	Bimodal AlN 1 & 5 $\mu\text{m}$	2.33	1753	NA	NA	Table 4.2
20	Bimodal AlN 1 & 5 $\mu\text{m}$	2.17	2543	8.15	942.6	Sample 19 after sintering
21	Bimodal AlN 3 & 5 $\mu\text{m}$	2.47	1715	NA	NA	Table 4.2
22	Bimodal AlN 3 & 5 $\mu\text{m}$	2.05	2640	17	904.3	Sample 21 after sintering
23	Trimodal AlN 0.1 ,0.5,1 $\mu\text{m}$	2.20	1584	NA	NA	Table 4.2

No.	Sample	Thickness, mm	Density, kg/m <sup>3</sup>	TC W/mK	SH J/kg.K	Tables
24	Trimodal AlN 0.1, 0.5, 1 μm	1.99	2397	10.3	813	Sample 23 after sintering
25	Triodal AlN 0.1, 0.5, 5 μm	2.08	1590	NA	NA	Table 4.2
26	Triodal AlN 0.1, 0.5, 5 μm	1.83	2705	12.2	787.8	Sample 25 after sintering
27	Trimodal 0.1, 1, 5	1.39	1472	NA	NA	Table 4.2
28	Trimodal 0.1, 1, 5	1.18	2472	15.3	829	Sample 27 after sintering
29	Trimodal 0.5, 1, 5	2.38	1208	NA	NA	Table 4.2
30	Trimodal 0.5, 1, 5	2.15	2220	9.52	718.1	Sample 29 after sintering
31	Quadmodal AlN 0.1, 0.5, 1, 5 μm	1.54	1607	NA	NA	Table 4.2
32	Quadmodal AlN 0.1, 0.5, 1, 5 μm	1.34	2471	12.9	790.8	Sample 31 after sintering
33	Unimodal AlN 0.1 μm	1.83	3063	11.2	704.3	Table 4.3
34	Unimodal AlN 0.1 μm	2.5	2225	12.4	692.8	Table 4.3
35	Unimodal AlN 0.1 μm	1.42	1731	8.09	673.8	Table 4.3
36	Unimodal AlN 1 μm	1.86	1663	4.92	785.3	Table 4.3
37	Unimodal AlN 5 μm	2.48	1924	7.88	776.2	Table 4.3
38	Bimodal AlN 0.5 & 5 μm	2.1	2071	9.24	797.1	Table 4.3
39	Bimodal AlN 0.1 & 1 μm	2.35	2171	10.8	895.4	Table 4.3
40	Bimodal AlN 0.1 & 5 μm	1.74	2338	12.6	839.9	Table 4.3
41	Bimodal AlN 0.1 & 5 μm	1.54	2442	13.2	694.2	Table 4.3
42	Bimodal AlN 0.1 & 5 μm	1.60	2217	15.81	794.2	Table 4.3
43	Bimodal AlN 0.1 & 5 μm	1.89	2158	13.77	800.3	Table 4.3
44	Bimodal AlN 0.5 & 5 μm	2.10	1712	8.93	1053	Table 4.3
45	Trimodal 0.1, 0.5, 5 μm	1.81	2141	12.92	865.7	Table 4.3
46	Trimodal 0.1, 1, 5 μm	1.74	2338	12.01	804.7	Table 4.3

No.	Sample	Thickness, mm	Density, kg/m <sup>3</sup>	TC W/mK	SH J/kg.K	Tables
47	Quad modal 0.1, 0.5, 1, 5 μm	2.27	2158	12.85	790.8	Table 4.3
48	Multimodal Al, BN 0.5, 15, SiC					Broken
49	AlN 0.5, 1, 5, Al	2.35	688	0.68	1079	Before sintering (Table 4.7)
50	AlN 0.5, 1, 5, Al	2.06	1166	8.01	769.8	After sintering
51	AlN 0.1, 1, 5, BN 15, Si C	1.81	445	<0.1	NA	Before sintering (Table 4.7)
52	AlN 0.1, 1, 5, BN 15, Si C	1.52	1025	<0.1	NA	After sintering
53	AlN 0.1, 0.5, 5, BN 0.5, Si15C17	1.63	600	0.68	1525	Before sintering (Table 4.7)
54	AlN 0.1, 0.5, 5, BN 0.5, Si15C17	1.32	1084	9.63	679.1	After sintering
55	AlN 0.1, 0.5, 1, Al, BN 0.5, 15	2.15	426	<0.1	NA	Before sintering (Table 4.7)
56	AlN 0.1, 0.5, 1, Al, BN 0.5, 15	1.78	661	4.9	625.8	After sintering
57	AlN 0.04, 0.5, 1, BN 15, SiC 0.1	2.31	591	0.51	1525	Before sintering (Table 4.7)
58	AlN 0.04, 0.5, 1, BN 15, SiC 0.1	1.85	959	5.1	615.1	After sintering
59	AlN 0.04, 0.5, 5, BN 0.5, 15	1.58	380	0.6	1322	Before sintering (Table 4.7)
60	AlN 0.04, 0.5, 5, BN 0.5, 15	1.27	829	6.8	500.6	After sintering
61	AlN 0.04, 1, 5, Al BN 0.5, SiC	1.67	452	0.52	1250	Before sintering (Table 4.7)
62	AlN 0.04, 1, 5, Al BN 0.5, SiC	1.56	680	5.4	603.3	After sintering
63	AlN 0.04, 0.1, 0.5, Al, SiC	2.55	479	<0.1		Before sintering (Table 4.7)
64	AlN 0.04, 0.1, 0.5, Al, SiC	2.06	750	<0.1	NA	After sintering

No.	Sample	Thickness, mm	Density, kg/m <sup>3</sup>	TC W/mK	SH J/kg.K	Tables
65	AlN 0.04, 0.1, 1, BN 0.5	2.01	553	1.83	1355	Before sintering (Table 4.7)
66	AlN 0.04, 0.1, 1, BN 0.5	1.62	1105	14	639.5	After sintering
67	Al, BN 0.5, 15, SiC	2.13	618	0.41	1266	Before sintering (Table 4.7)
68	Al, BN 0.5, 15, SiC	Broken				After sintering
70	Bimodal AlN 0.5 & 1 μm	1.17	2639.03	<b>18.12</b>	859.2	50% solid loading (Table 4.9)
71	Bimodal AlN 0.5 & 1 μm	1.77	2420.29	<b>19.80</b>	914.7	55% solid loading (Table 4.9)
72	Bimodal AlN 0.5 & 1 μm	1.87	2825.17	<b>21.05</b>	850.5	60% solid loading (Table 4.9)
73	SiAlN (0.5,1) 20/80 (wo sintering aid)	2.81	904.2	0.38	1179.5	Table 6.7 (after sintering at 1000°C)
74	SiAlN (0.5,1) 20/80 Ho/Pr/DyY	2.32		0.48	1079.6	Table 6.7 (after sintering at 1000°C)
75	SiAlN (0.5,1) 20/80, Eu	4.15	1023	0.57	1244.7	Table 6.7 (after sintering at 1000°C)
76	SiAlN (0.5,1) 20/80, Dy	3.85	996.3	0.51	1244.7	Table 6.7 (after sintering at 1000°C)
77	SiAlN (0.5,1) 20/80, Gd	3.57	1173	0.59	1456.6	Table 6.7 (after sintering at 1000°C)
78	SiAlN (0.5,1) 20/80, Nd	3.95	1059	0.74	1366.1	Table 6.7 (after sintering at 1000°C)
79	SiAlN (0.5,1) 20/80, Ho	3.18	1055		1305.3	Table 6.7 (after sintering at 1000°C)
80	SiAlN (0.5,1) 20/80, Pr	2.47	1110	0.49	1324.1	Table 6.7 (after sintering at 1000°C)
81	SiAlN (0.5,1) 20/80, Tm	3.09	1126	0.57	1029.4	Table 6.7 (after sintering at 1000°C)
82	SiAlN (0.5,1) 20/80, Y	3.65	1036	0.43	1297.5	Table 6.7 (after sintering at 1000°C)
83	SiAlN (0.5,1) 20/80, Er	3.63	963.2		1291.8	Table 6.7 (after sintering at 1000°C)
84	SiAlN (0.5,1) 20/80 (wo sintering aid)	2.48	992	<b>0.87</b>	1075	Table 6.7 (after sintering at 1200°C)
85	SiAlN (0.5,1) 20/80 Ho/Pr/DyY	2.37	1061	<b>1.02</b>	1048	Table 6.7 (after sintering at 1200°C)
86	SiAlN (0.5,1) 20/80, Eu	2.68	1214	<b>1.1</b>	1031	Table 6.7 (after sintering at 1200°C)
87	SiAlN (0.5,1) 20/80, Dy	3.32	1121	<b>1.31</b>	1481	Table 6.7 (after sintering at 1200°C)
88	SiAlN (0.5,1) 20/80, Gd	2.56	1208	<b>1.12</b>	1135.3	Table 6.7 (after sintering at 1200°C)



No.	Sample	Thickness, mm	Density, kg/m <sup>3</sup>	TC W/mK	SH J/kg.K	Tables
89	SiAlN (0.5,1) 20/80, Nd	4.26	Crack	<b>0.93</b>		Table 6.7 (after sintering at 1200°C)
90	SiAlN (0.5,1) 20/80, Ho	3.05	1112	<b>1.16</b>	1376	Table 6.7 (after sintering at 1200°C)
91	SiAlN (0.5,1) 20/80, Pr	2.44	1050.	<b>1.05</b>	1118	Table 6.7 (after sintering at 1200°C)
92	SiAlN (0.5,1) 20/80, Tm	3.52	1008	<b>1.29</b>	1101	Table 6.7 (after sintering at 1200°C)
93	SiAlN (0.5,1) 20/80, Y	2.35	1243	<b>1.19</b>	1067	Table 6.7 (after sintering at 1200°C)
94	SiAlN (0.5,1) 20/80, Er	3.31	11216	<b>1.21</b>	1278	Table 6.7 (after sintering at 1200°C)
95	SiAlN (0.5,1) 20/80 (wo sintering aid)	2.44	1037	0.8	1142	Table 6.7 (after sintering at 1400°C)
96	SiAlN (0.5,1) 20/80 Ho/Pr/DyY	2.36	1054	0.91	1214.7	Table 6.7 (after sintering at 1400°C)
97	SiAlN (0.5,1) 20/80, Eu	2.69	1139	0.72	1018.9	Table 6.7 (after sintering at 1400°C)
98	SiAlN (0.5,1) 20/80, Dy	3.34	1095	1.02	1545.6	Table 6.7 (after sintering at 1400°C)
99	SiAlN (0.5,1) 20/80, Gd	2.51	1228	0.82	1145.3	Table 6.7 (after sintering at 1400°C)
100	SiAlN (0.5,1) 20/80, Nd	3.46	1007	0.83	1007	Table 6.7 (after sintering at 1400°C)
101	SiAlN (0.5,1) 20/80, Ho	3.06	1072	0.93	1389	Table 6.7 (after sintering at 1400°C)
102	SiAlN (0.5,1) 20/80, Pr	2.34	1257	0.7	823	Table 6.7 (after sintering at 1400°C)
103	SiAlN (0.5,1) 20/80, Tm	3.46	1002	0.84	1005	Table 6.7 (after sintering at 1400°C)
104	SiAlN (0.5,1) 20/80, Y	2.26	1128	0.92	1210.9	Table 6.7 (after sintering at 1400°C)
105	SiAlN (0.5,1) 20/80, Er	3.27	1132	0.72	1218.9	Table 6.7 (after sintering at 1400°C)
106	SiAlN (0.5,1) 20/80, w/o sintering aid	2.48	992.11	0.87	1075.8	Table 6.8 (after sintering at 1200°C)
107	SiAlN (0.5,1) 20/80, Dy	3.32	1121.99	1.31	1481	Table 6.8 (after sintering at 1200°C)
108	SiAlN (0.5,1) 20/80, Nd	3.52	1008.79	0.93	1101.7	Table 6.8 (after sintering at 1200°C)
109	SiAlN (0.5,1) 20/80, Tm	2.35	1243.19	1.29	1067	Table 6.8 (after sintering at 1200°C)
110	SiAlN (0.5,1) 20/80, Y	3.31	1121.06	1.19	1278	Table 6.8 (after sintering at 1200°C)
111	SiAlN (0.5,1) 20/80, Er	3.28	1074.83	1.21	1042.7	Table 6.8 (after sintering at 1200°C)

No.	Sample	Thickness, mm	Density, kg/m <sup>3</sup>	TC W/mK	SH J/kg.K	Tables
112	SiAlN (0.5,1) 80/20, without sintering aid	2.65	809.13	1.76	963.6	Tab,e 6.8 (after sintering at 1200°C)
113	SiAlN (0.5,1) 80/20, Nd	4.07	533.12	0.79	1089.7	Tab,e 6.8 (after sintering at 1200°C)
114	SiAlN (0.5,1) 80/20, Dy	2.75	831.02	1.3	933.2	Tab,e 6.8 (after sintering at 1200°C)
115	SiAlN (0.5,1) 80/20, Y	3.65	795.66	1.7	1088.8	Tab,e 6.8 (after sintering at 1200°C)
116	SiAlN (0.5,1) 80/20, Tm	3.81	778.8	2.28	1536.2	Tab,e 6.8 (after sintering at 1200°C)
117	SiAlN (0.5,1) 80/20, Er	3.57	872.91	1.72	1149.7	Tab,e 6.8 (after sintering at 1200°C)
118	SiAlN (3,5) 20/80, without sintering aid	3.44	1773	0.66	608.4	Tab,e 6.9 (after sintering at 1000°C)
119	SiAlN (3,5) 40/60, without sintering aid	2.16	1918	0.51	482.1	Tab,e 6.9 (after sintering at 1000°C)
120	SiAlN (0.5,1) 20/80, 2% Dy	2.8	1093.87	0.76	718.8	Tab,e 6.9 (after sintering at 1000°C)
121	SiAlN (3,5) 20/80, without sintering aid	3.03	1023	0.6	583	Tab,e 6.9 (after sintering at 1000°C)
122	SiAlN (3,5) 20/80, 2% Y	3.37	1664	0.59	523.9	Tab,e 6.9 (after sintering at 1000°C)
123	SiAlN (3,5) 20/80, 2% Dy	3.12	1449	0.63	662.7	Tab,e 6.9 (after sintering at 1000°C)
124	SiAlN (3,5) 20/80, 5% Y	3	1808	0.48	466.2	Tab,e 6.9 (after sintering at 1000°C)
125	SiAlN (0.5,1) 20/80	3.2	2193	0.62	580.2	Tab,e 6.9 (after sintering at 1000°C)
126	SiAlN (0.5,1) 20/80, 5% Dy	3.02	1944	0.72	696.3	Tab,e 6.9 (after sintering at 1000°C)
127	SiAlN (0.5,1) 20/80, 2% Y	2.94	2130	0.76	584.3	Tab,e 6.9 (after sintering at 1000°C)
128	SiAlN (3,5) 20/80, 2% Dy	2.8	2107	0.61	440.9	Tab,e 6.9 (after sintering at 1000°C)
129	SiAlN (3,5) 20/80, 2% Y	2.38	1825	0.6	545.6	Tab,e 6.9 (after sintering at 1000°C)
130	SiAlN (0.5,1) 20/80, without sintering aid	2.53	2446	1.98	643.4	Table 6.10 (after sintering at 1600°C)
131	SiAlN (0.5,1) 20/80, 2% Y	2.91	2565	2.79	527.6	Table 6.10 (after sintering at 1600°C)

<b>No.</b>	<b>Sample</b>	<b>Thickness, mm</b>	<b>Density, kg/m<sup>3</sup></b>	<b>TC W/mK</b>	<b>SH J/kg.K</b>	<b>Tables</b>
132	SiAlN (0.5,1) 20/80, 2% Dy	3.23	2889	3.26	578.9	Table 6.10 (after sintering at 1600°C)

-----END-----

## References

- 1) Adolfsson, E. Gelcasting of zirconia using agarose. *Journal of the American Ceramic Society*, **2006**, 89(6): 1897-1902.
- 2) Agyenim, F., N. Hewitt, P. Eames and M. Smyth. A review of materials, heat transfer and phase change problem formulation for latent heat thermal energy storage systems (LHTESS). *Renewable and Sustainable Energy Reviews*, **2010**, 14(2): 615-628.
- 3) Airey, G., A. Hunter and B. Rahimzadeh. The influence of geometry and sample preparation on dynamic shear rheometer testing. *Proc. of the 4th Europ. Symp. on Performance of Bitum. and Hydraulic Materials in Pavements*, 11 April **2002**, 3-12.
- 4) Amou, S., H. Shimizu and A. Hanawa. Prepreg and its application products for low thermal expansion and low dielectric tangent, *US Patent 8115105B2*. 14 Feb **2012**,
- 5) Bagheri, S., K. Shameli and S. B. Abd Hamid. Synthesis and Characterization of Anatase Titanium Dioxide Nanoparticles Using Egg White Solution via Sol-Gel Method. *Journal of Chemistry* **2013**, 1-5.
- 6) Banijamali, B., S. Ramalingam, K. Nagarajan and R. Chaware. Advanced reliability study of TSV interposers and interconnects for the 28nm technology FPGA. *Electronic Components and Technology Conference (ECTC), 61st, IEEE*. **2011**, 285-290

- 7) Bansal, N. P. and R. H. Doremus. Electrical Conductivity. *Handbook of glass properties*, Elsevier. **2013**, 381-385.
- 8) Barlow III, F. D. and A. Elshabini. Multilayer Ceramics. *Ceramic interconnect technology handbook*, CRC Press. **2007**, Ch 6, 236-284.
- 9) Baron, J. (2012). 3DIC & TSV Interconnects: Applications, Market & Infrastructure Readiness. *Additional Conferences (Device Packaging, HiTEC, HiTEN, & CICMT)*, Jan **2011**, 366-405.
- 10) Beica, R. (2015). 3D integration: Applications and market trends. *IEEE 2015 International 3D Systems Integration Conference*. **2015**, TS5.1.1-7.
- 11) Bekouche, K., C. Jia, Z. Wang and Y. Tang. A Novel Method of Copper Green Bodies Production: Through a Low Toxicity Gelling System in a Non-Aqueous Based Gelcasting Process. *2016 International Conference on Sustainable Energy, Environment and Information Engineering (SEEIE)*, **2016**, 430-437.
- 12) Bekouche, K., Z.-l. Wang, C.-C. Jia, B.-w. Liu and Y. Tang. Effects of process parameters on nonaqueous gelcasting for copper powder. *International Journal of Minerals, Metallurgy, and Materials*, **2016**, 23(5): 542-547.
- 13) Benware, B. R. Achieving sub 100 DPPM defect levels on VDMSM and nanometer ASICs. *IEEE Test Conference, ITC*, **2004**, p 1418
- 14) Berger, L. I. (1996). Aluminum Nitride. *Semiconductor materials*, CRC press. **1996**, 123-124.

- 15) Bernstein, K., P. Andry, J. Cann, P. Emma, D. Greenberg, W. Haensch, M. Ignatowski, S. Koester, J. Magerlein and R. Puri. Interconnects in the third dimension: design challenges for 3D ICs. *Proceedings of the 44th annual Design Automation Conference, ACM*, **2007**, 562-567
- 16) Bohua, D., Q. Chengkang, W. Dezhi, W. Zhuangzhi, F. Zhen, Z. Yasong and W. Xing. Effect of Processing Parameters on Gelcasting Process for Mo/Cu Powders. *Rare Metal Materials and Engineering*, **2018**, 47(3): 766-772.
- 17) Bowler N. and Huang Y. Electrical conductivity measurement of metal plates using broadband eddy-current and four-point methods, *Measurement Science and Technology*, **2005** 16(11), 2193-2200.
- 18) Briant, C. L. New applications for refractory metals. *JOM*, **2000**,52(3): 36-36.
- 19) Brunschwiler, T., B. Michel, H. Rothuizen, U. Kloter, B. Wunderle, H. Oppermann and H. Reichl. Forced convective interlayer cooling in vertically integrated packages. *11th Intersociety Conference on Thermal and Thermomechanical Phenomena in Electronic Systems, IThERM*, **2008**, 1114-1125.
- 20) Buchanan, D. A. Scaling the gate dielectric: materials, integration, and reliability. *IBM journal of research and development*, **1999**, 43(3): 245-264.
- 21) Cesarano, J. Robocasting: Direct fabrication of ceramics from colloidal suspensions. *Proceedings of Solid Freeform Fabrication Symposium*, **1997**, 25-36

- 22) Chausse, P., M. Bouchoucha, D. Henry, N. Sillon and L. Chapelon. Polymer filling of medium density through silicon via for 3D-packaging. *Electronics Packaging Technology Conference, EPTC'09. 11th, IEEE, 2009*, 790-794
- 23) Chen, C.-F., M. Perisse, A. Ramirez, N. Padture and H. Chan. Effect of grain boundary phase on the thermal conductivity of aluminium nitride ceramics. *Journal of Materials Science, 1994*,29(6): 1595-1600.
- 24) Chen, L., Deng, C., Li, J., Yao, Q., Chang, J., Wang, L., & Wu, C. (2019). 3D printing of a lithium-calcium-silicate crystal bioscaffold with dual bioactivities for osteochondral interface reconstruction. *Biomaterials, 2019*, 196, 138-150.
- 25) Chen, L.-Y., P. G. Neudeck, D. J. Spry, G. M. Beheim and G. W. Hunter. Electrical Performance of a High Temperature 32-I/O HTCC Alumina Package. *HiTEC, 2016*, 000066-000072.
- 26) Chen, Q., T. Bandyopadhyay, Y. Suzuki, F. Liu, V. Sundaram, R. Pucha, M. Swaminathan and R. Tummala. Design and demonstration of low cost, panel-based polycrystalline silicon interposer with through-package-vias (TPVs). *Electronic Components and Technology Conference (ECTC), IEEE 61st, 2011*, 855-860
- 27) Chen, T.-C. Overcoming research challenges for CMOS scaling: Industry directions. *8th International Conference on Solid-State and Integrated Circuit Technology Proceedings, IEEE, 2006*, 4-7.
- 28) Cho, S., Y. Joshi, V. Sundaram, Y. Sato and R. Tummala. Comparison of

- thermal performance between glass and silicon interposers. *Electronic components and Technology conference (ECTC), 63rd, IEEE, 2013*, 1480-1487.
- 29) Cho, S., V. Sundaram, R. R. Tummala and Y. K. Joshi. Impact of Copper Through-Package Vias on Thermal Performance of Glass Interposers. *IEEE Transactions on Components, Packaging And Manufacturing Technology, 2015*, 5(8): 1075-1084.
- 30) Chua, C. K., K. F. Leong and C. S. Lim. Rapid Prototyping: Principles and Applications, *World Scientific Publishing Company, 2010*.
- 31) Chung, D. D. L. Materials for thermal conduction. *Applied Thermal Engineering, 2001*, 21(16): 1593-1605.
- 32) Claudionico~commons wiki (2013). Electron Interaction with Matter.
- 33) Cotofana, S. Emerging Phenomena-dependent Non-CMOS Nanoelectronic Devices-What Are They? *4th IEEE International Conference on Nano/Micro Engineered and Molecular Systems, IEEE-NEMS, Shenzhen, China, Jan 5-8 2009*, 1-2.
- 34) Crump, S. Fused deposition modeling (FDM): putting rapid back into prototyping. *The 2nd International Conference on Rapid Prototyping. Dayton, Ohio, 1991*, 354-357.
- 35) Cummins, G. and M. P. Desmulliez. Inkjet printing of conductive materials: a review. *Circuit World, 2012*, 38(4): 193-213.
- 36) Ćurković, L., A. Bakić, J. Kodvanj and T. Haramina. Flexural strength of



- alumina ceramics: Weibull analysis. *Transactions of FAMENA*, **2010**, 34(1): 13-19.
- 37) de Gans, B. J., P. C. Duineveld and U. S. Schubert. Inkjet printing of polymers: state of the art and future developments. *Advanced materials*, **2004**, 16(3): 203-213.
- 38) Dennard, R. H., F. H. Gaensslen, V. L. Rideout, E. Bassous and A. R. LeBlanc. Design of ion-implanted MOSFET's with very small physical dimensions. *IEEE Journal of Solid-State Circuits*, **1974**, 9(5): 256-268.
- 39) Dhara, S. Synthesis of nanocrystalline alumina using egg white. *Journal of the American Ceramic Society*, **2005**, 88(7): 2003-2004.
- 40) Dhara, S. and P. Bhargava. Egg white as an environmentally friendly low-cost binder for gelcasting of ceramics. *Journal of the American Ceramic Society*, **2001**, 84(12): 3048-3050.
- 41) DiStefano, J. R., B. A. Pint and J. H. DeVan. Oxidation of refractory metals in air and low pressure oxygen gas. *International Journal of Refractory Metals and Hard Materials*, **2000**, 18(4): 237-243.
- 42) Duan B, Qi. C., Wang D., Fu Z., Yin B. Preparation of Mo / Cu Alloy by Non-aqueous Gelcasting. *Nonferrous Metals Science and Engineering*, **2017**, 18(1), 56-62.
- 43) Eckel, Z. C., C. Zhou, J. H. Martin, A. J. Jacobsen, W. B. Carter and T. A. Schaedler. Additive manufacturing of polymer-derived ceramics. *Science*, **2016**, 351(6268): 58-62.

- 44) Eqtesadi, S., A. Motealleh, F. H. Perera, P. Miranda, A. Pajares, R. Wendelbo, F. Guiberteau and A. L. Ortiz. Fabricating geometrically-complex B4C ceramic components by robocasting and pressureless spark plasma sintering. *Scripta Materialia*, **2018**, 145(Supplement C): 14-18.
- 45) Espalin, D., D. W. Muse, E. MacDonald and R. B. Wicker. 3D Printing multifunctionality: structures with electronics. *The International Journal of Advanced Manufacturing Technology*, **2014**, 72(5-8): 963-978.
- 46) Fanelli, A. J., R. D. Silvers, W. S. Frei, J. V. Burlew and G. B. Marsh. New aqueous injection molding process for ceramic powders. *Journal of the American Ceramic Society*, **1989**, 72(10): 1833-1836.
- 47) Feilden, E., E. G.-T. Blanca, F. Giuliani, E. Saiz and L. Vandeperre. Robocasting of structural ceramic parts with hydrogel inks. *Journal of the European Ceramic Society*, **2016**, 36(10): 2525-2533.
- 48) Gagliardi, M. 3D Printed Technical Ceramics: Technologies and Global Markets Report, *BCC Research*, **2017**, 1-15.
- 49) Gao, W., Y. Zhang, D. Ramanujan, K. Ramani, Y. Chen, C. B. Williams, C. C. L. Wang, Y. C. Shin, S. Zhang and P. D. Zavattieri. The status, challenges, and future of additive manufacturing in engineering. *Computer-Aided Design*, **2015**, 69: 65-89.
- 50) Garrou, P. "IFTLE 269 IMAPS 2015 Part 2 High Density Packaging ASE STATS Nanium." **2015**, from <https://semimd.com/insights-from-leading-edge/2016/01/11/iftle-269-imaps-2015-part-2-high-density-packaging-ase->

stats-nanium/.

- 51) Garrou, P., M. Koyanagi and P. Ramm. Handbook of 3D Integration: Volume 3-3D Process Technology, *John Wiley & Sons*, **2014**.
- 52) Gibson, I., D. W. Rosen and B. Stucker. Additive manufacturing technologies, *Springer*. **2010**.
- 53) Golaszewski, M., Grygoruk, R., Giorgio, I., Laudato, M., & Di Cosmo, F. (2019). Metamaterials with relative displacements in their microstructure: technological challenges in 3D printing, experiments and numerical predictions. *Continuum Mechanics and Thermodynamics*, 31(4), 1015-1034
- Goplen, B. and S. S. Sapatnekar. Placement of thermal vias in 3-D ICs using various thermal objectives. *IEEE Transactions on Computer-Aided Design of Integrated Circuits and Systems*, **2006**, 25(4): 692-709.
- 54) Goser, K., P. Glösekötter and J. Dienstuhl. Nanoelectronics and nanosystems: from transistors to molecular and quantum devices, *Springer Science & Business Media*, **2004**
- 55) Greig, W. J. HDI substrate manufacturing technologies: Cofired ceramic. *Integrated Circuit Packaging, Assembly and Interconnections*, **2007**: 233-244.
- 56) Guenin, B. When Moore Is Less: Exploring the 3rd Dimension in IC Packaging. *Electronics Cooling*, **2009**, 15 (1), 1-9.
- 57) Guo, N. and M. C. Leu. Additive manufacturing: technology, applications and research needs. *Frontiers of Mechanical Engineering*, **2013**, 8(3): 215-

- 243.
- 58) Gupta, P. and A. B. Kahng. Manufacturing-aware physical design. *Proceedings of the IEEE/ACM International conference on Computer-aided design, IEEE Computer Society, 2003*, 681
- 59) Haron, N. Z. and S. Hamdioui. Why is CMOS scaling coming to an END? *3rd International Design and Test Workshop, IEEE, 2008*, 98-103.
- 60) Harriott, L. R. Limits of lithography. *Proceedings of the IEEE, 2001*, 89(3): 366-374.
- 61) He, X., B. Su, X. Zhou, J. Yang, B. Zhao, X. Wang, G. Yang, Z. Tang and H. Qiu. Gelcasting of alumina ceramic using an egg white protein binder system. *Ceram. Silik, 2011*, 55(1): 1-7.
- 62) Hellebrand, H. Processing of Ceramics. *Materials Science and Technology, 1996*, 190-265.
- 63) Hellings, G., M. Scholz, M. Detalle, D. Velenis, M. d. P. de ten Broeck, C. R. Neve, Y. Li, S. Van Huylenbroek, S.-H. Chen and E.-J. Marinissen (2015). Active-lite interposer for 2.5 & 3D integration. *Symposium on VLSI Technology (VLSI Technology), IEEE, 2015*, T222-T223.
- 64) Hensen, T. J., T. G. Aguirre, C. L. Cramer, A. S. Wand, K. Ma, D. A. Prawel, J. D. Williams and T. B. Holland. Additive Manufacturing of Ceramic Nanopowder by Direct Coagulation Printing. *Additive Manufacturing, 2018*, 23, 140-150.
- 65) Hielscher, K. Ultrasonic milling and dispersing technology for nano-

- particles. *MRS Online Proceedings Library Archive*, **2012**, 1479: 21-26.
- 66) Hillenius, S. The future of silicon microelectronics. *IEEE Workshop on Microelectronics and Electron Devices, IEEE*, **2004**, 3-4.
- 67) Ho, C., D. Chance, C. Bajorek and R. Acosta. The thin-film module as a high-performance semiconductor package. *IBM Journal of Research and Development*, **1982**, 26(3): 286-296.
- 68) Hoath, S. D. Fundamentals of inkjet printing: the science of inkjet and droplets, *John Wiley & Sons*, **2016**.
- 69) Homa, J. and M. Schwentenwein. A Novel Additive Manufacturing Technology for High-Performance Ceramics. *38th International Conference on Advanced Ceramics and Composites*, January 27-31, Daytona Beach, Florida, John Wiley & Sons, Inc., **2014**, 33-40
- 70) Hong, J.-P., S.-W. Yoon, T. Hwang, J.-S. Oh, S.-C. Hong, Y. Lee and J.-D. Nam. High thermal conductivity epoxy composites with bimodal distribution of aluminum nitride and boron nitride fillers. *Thermochimica Acta*, **2012**, 537: 70-75.
- 71) Hopewell, J., Dvorak, R., & Kosior, E. Plastics recycling: challenges and opportunities. *Philosophical Transactions of the Royal Society B: Biological Sciences*, **2009**, 364(1526), 2115–2126.
- 72) Hosseinizadeh, S., F. Tan and S. Moosania. Experimental and numerical studies on performance of PCM-based heat sink with different configurations of internal fins. *Applied Thermal Engineering*, **2011**, 31(17): 3827-3838.

- 73) Howatt, G., R. Breckenridge and J. Brownlow. Fabrication of thin ceramic sheets for capacitors. *Journal of the American Ceramic Society*, **1947**, 30(8): 237-242.
- 74) Hromadka, K., J. Stulik, J. Reboun and A. Hamacek. DBC Technology for Low Cost Power Electronic Substrate Manufacturing. *Procedia Engineering*, **2014**, 69: 1180-1183.
- 75) Huang, H. S. and K. S. Hwang. Deoxidation of molybdenum during vacuum sintering. *Metallurgical and Materials Transactions A*, **2002**, 33(3): 657-664.
- 76) Huang, T., M. S. Mason, G. E. Hilmas and M. C. Leu. Freeze-form extrusion fabrication of ceramics. *Solid Free. Fabr. Symp.*, Austin, TX, USA, **2005**, 73-85.
- 77) Huang, Y., D. K. Sarkar and X. G. Chen. A one-step process to engineer superhydrophobic copper surfaces. *Materials Letters*, **2010**, 64(24): 2722-2724.
- 78) Labadie, A. K., A. Schubring. Engineering Solutions in Ceramic Packaging: Meeting the Demand for Performance at Cost. *Advancing Microelectronics*. Washington, USA, IMAPS - International Microelectronics And Packaging Society, **2013**, 40: 8-14.
- 79) Isaac, R. D. The future of CMOS technology. *IBM Journal of Research and Development*, **2000**, 44(3): 369-378.
- 80) ITRS. International Technology Roadmap for Semiconductor 2007 Edition Executive Summary, **2007**,

<http://www.itrs.net/Links/2007ITRS/ExecSum2007.pdf>.

- 81) Iwai, H. CMOS Scaling for sub-90 nm to sub-10 nm. *17th International Conference on VLSI Design (VLSID04)*, **2004**, 30-35.
- 82) Jabbari, M., R. Bulatova, A. I. Y. Tok, C. R. H. Bahl, E. Mitsoulis and J. H. Hattel. Ceramic tape casting: A review of current methods and trends with emphasis on rheological behaviour and flow analysis. *Materials Science and Engineering: B*, **2016**, 212: 39-61.
- 83) Jacobs, P. F. Rapid prototyping & manufacturing: fundamentals of stereolithography, *Society of Manufacturing Engineers*, **1992**.
- 84) Jain, A. and S. Ramanathan. Theoretical investigation of sub-ambient on-chip microprocessor cooling. *Thermal and Thermomechanical Proceedings 10th Intersociety Conference on Phenomena in Electronics Systems, IITHERM*, **2006**, 765-770.
- 85) Janney, M. and O. Omateta. Method for molding ceramic powder using a water-based gelcasting process. *US Patent 5145908*, **1992**.
- 86) Janney, M. A. Method for molding ceramic powders, *U.S Patent 4894194*, **1990**.
- 87) Janney, M. A. and O. O. Omatete. Method for molding ceramic powders using a water-based gel casting, *U.S Patent 5028362*, **1991**.
- 88) Janney, M. A., O. O. Omatete, C. A. Walls, S. D. Nunn, R. J. Ogle and G. Westmoreland. Development of low-toxicity gelcasting systems. *Journal of the American Ceramic Society*, **1998**, 81(3): 581-591.

- 89) Janney, M. A., W. Ren, G. H. Kirby, S. D. Nunn and S. Viswanathan. Gelcast tooling: net shape casting and green machining. *Material And Manufacturing Process*, **1998**, 13(3): 389-403.
- 90) Jian, G., Q. Tai, Y. Jian, F. Yongbao, Z. Chao, Z. Wenpeng and G. Tianhao. Process dependant setting behavior of aqueous gelcast AlN slurries. *Ceramics International*, **2012**, 38(4): 2905-2911.
- 91) Jianfeng, X., D. Manjiang, L. Jun, Z. Guohong and W. Shiwei. Gelcasting of Aluminum Nitride Ceramics. *Journal of the American Ceramic Society*, **2010**, 93(4): 928-930.
- 92) Jiang, C., X. Gan, D. Zhang, R. Xie and K. Zhou. Gelcasting of aluminum nitride ceramics using hydantion epoxy resin as gelling agent. *Ceramics International*, **2013**, 39(8): 9429-9433.
- 93) Jiang, C., D. Zhang, X. Gan, R. Xie, F. Zhang and K. Zhou. Preparation of high performance AlN/Hydantion composite by gelcasting and infiltration processes. *Ceramics International*, **2014**, 40(1, Part B): 2535-2538.
- 94) Joe Lopes, A., E. MacDonald and R. B. Wicker. Integrating stereolithography and direct print technologies for 3D structural electronics fabrication. *Rapid Prototyping Journal*, **2012**, 18(2): 129-143.
- 95) Kamal, M. R. and Mutel, A. Rheological Properties of Suspensions in Newtonian and Non-Newtonian Fluids. *Journal of Polymer Engineering*, **1985**, 5(4), 293–382.
- 96) Kandasamy, R., X.-Q. Wang and A. S. Mujumdar. Application of phase



- change materials in thermal management of electronics. *Applied Thermal Engineering*, **2007**, 27(17–18): 2822-2832.
- 97) Kandasamy, R., X.-Q. Wang and A. S. Mujumdar. Transient cooling of electronics using phase change material (PCM)-based heat sinks. *Applied Thermal Engineering*, **2008**, 28(8–9): 1047-1057.
- 98) Karbasi, A., A. Hadjikhani and W. K. Jones. Effect of platinum metallization in cofired platinum/alumina microsystems for implantable medical applications. *CICMT*, **2013**, 000177-000182.
- 99) Kearney, D., T. Hilt and P. Pham. A liquid cooling solution for temperature redistribution in 3D IC architectures. *Microelectronics Journal*, **2012**, 43(9): 602-610.
- 100) Kemaloglu, S., G. Ozkoc and A. Aytac. Properties of thermally conductive micro and nano size boron nitride reinforced silicon rubber composites. *Thermochimica Acta*, **2010**, 499(1–2): 40-47.
- 101) Kim, N., D. Wu, D. Kim, A. Rahman and P. Wu. Interposer design optimization for high frequency signal transmission in passive and active interposer using through silicon via (TSV). *61st Electronic Components and Technology Conference (ECTC), IEEE*, **2011**, 1160-1167.
- 102) Klocke, F. Modern approaches for the production of ceramic components. *Journal of the European Ceramic Society*, **1997**, 17(2): 457-465.
- 103) Knapp, A. M. and J. W. Halloran. Binder Removal from Ceramic-

- Filled Thermoplastic Blends. *Journal of the American Ceramic Society*, **2006**, 89(9): 2776-2781.
- 104) Kocjan, A., Dakskobler, A., Krnel, K., & Kosmač, T.. The course of the hydrolysis and the reaction kinetics of AlN powder in diluted aqueous suspensions. *Journal of the European Ceramic Society*, 2011, 31(5), 815-823.
- 105) Kolobov, Y. R., B. Kieback, K. V. Ivanov, T. Weissgaerber, N. V. Girsova, Y. I. Pochivalov, G. P. Grabovetskaya, M. B. Ivanov, V. U. Kazyhanov and I. V. Alexandrov. The structure and microhardness evolution in submicrocrystalline molybdenum processed by severe plastic deformation followed by annealing. *International Journal of Refractory Metals and Hard Materials*, **2003**, 21(1): 69-73.
- 106) Kondo, K., M. Kada and K. Takahashi. Three-Dimensional Integration of Semiconductors: Processing, Materials, and Applications, *Springer*, **2016**.
- 107) Koski, J.A. Improved data-reduction methods for laser pulse-diffusivity determination with the use of minicomputers, *International Joint Conference on Thermophysical Properties*, **1981**
- 108) Kou, Y., S. Wang, J. Luo, K. Sun, J. Zhang, Z. Tan and Q. Shi. Thermal analysis and heat capacity study of polyethylene glycol (PEG) phase change materials for thermal energy storage applications. *The Journal of Chemical Thermodynamics*, **2019**, 128: 259-274.

- 109) Kraus, A. D. and A. Bar-Cohen. Thermal analysis and control of electronic equipment. Washington, DC, *Hemisphere Publishing Corp.*, **1983**, 633 p. 1.
- 110) Krum, A. ThermoMechanical Design. Ceramic Interconnect Technology Handbook, CRC Press, **2007**, 105-161.
- 111) Kuang, X., Chen, K., Dunn, C. K., Wu, J., Li, V. C., & Qi, H. J. (2018). 3D printing of highly stretchable, shape-memory, and self-healing elastomer toward novel 4D printing. *ACS applied materials & interfaces*, **2018**, 10(8), 7381-7388
- 112) Kuneman, J. E. and J. F. Dickson. Direct bond copper ceramic substrate for electronic applications, U.S Patents4563383, **1986**.
- 113) Kwon, Y.-S., A. A. Gromov and J. I. Strokova. Passivation of the surface of aluminum nanopowders by protective coatings of the different chemical origin. *Applied Surface Science*, **2007**, 253(12): 5558-5564.
- 114) Lee, G.-W., M. Park, J. Kim, J. I. Lee and H. G. Yoon. Enhanced thermal conductivity of polymer composites filled with hybrid filler. *Composites Part A: Applied Science and Manufacturing*, **2006**, 37(5): 727-734.
- 115) Leuven, K. Additive manufacturing of ceramics: a review. *Journal of Ceramic Science and Technology*, **2014**, 5(4): 245-260.
- 116) Levi, H. Changing the way we manufacture—AM in technical ceramics. *Metal Powder Report*, **2018**, 1.

- 117) Li, Y.-H., F. Wang and J.-J. Li. Current developments of biomedical porous Ti–Mo alloys. *International Journal of Materials Research*, **2017**, 108(8): 619-624.
- 118) Li, Y., Z. Guo, J. Hao and S. Ren. Gelcasting of metal powders in nontoxic cellulose ethers system. *Journal of Materials Processing Technology*, **2008**, 208(1): 457-462.
- 119) Li, Y., M. Song, Q. Yu and X. Zhang. Improvement of Anti-hydrolytic Property of AlN Powder Modified by the Rare-earth Salts. *Materials Science Forum*, **2015**, 816.
- 120) Liao, L. C. K., B. Peters, D. S. Krueger, A. Gordon, D. S. Viswanath and S. J. Lombardo. Role of length scale on pressure increase and yield of poly (vinyl butyral)–barium titanate–platinum multilayer ceramic capacitors during binder burnout. *Journal of the American Ceramic Society*, **2000**, 83(11): 2645-2653.
- 121) Liu, G., G. Zhang, F. Jiang, X. Ding, Y. Sun, J. Sun and E. Ma. Nanostructured high-strength molybdenum alloys with unprecedented tensile ductility. *Nature materials*, **2013**, 12(4): 344-350.
- 122) Liu, W., C. Jia, Y. Shi and Y. Han. Copper base materials prepared by gel-casting process. *Rare Metals*, **2008**, 27(1): 78-82.
- 123) Lundstrom, M. Moore's law forever? *Science*, **2003**, 299(5604): 210-211.
- 124) Lyckfeldt, O., J. Brandt and S. Lesca. Protein forming—a novel

- shaping technique for ceramics. *Journal of the European Ceramic Society*, **2000**, 20(14): 2551-2559.
- 125) MacCurdy, R., A. McNicoll and H. Lipson. Bitblox: Printable digital materials for electromechanical machines. *The International Journal of Robotics Research*, **2014**, 33(10): 1342-1360.
- 126) Maleksaeedi, S., M. H. Paydar and J. Ma. Centrifugal deairing of concentrated ceramic slurries. *Journal of the American Ceramic Society*, **2009**, 92(12): 2861-2869.
- 127) Matula R.A. Electrical resistivity of copper, gold, palladium, and silver. *Journal of Physical and Chemical Reference Data*. **1979**, 8(4), 1147-1298.
- 128) Mehmet D., Züriye Y. and Mahir A. Characterization and Rheological Properties of Kaolinite-Silicon Oil Pastes, *Ind. Eng. Chem. Res.* **2008**, 47, 8218–8227
- 129) Millán, A. J., R. Moreno and M. a. I. Nieto. Thermogelling polysaccharides for aqueous gelcasting—part I: a comparative study of gelling additives. *Journal of the European Ceramic Society*, **2002**, 22(13): 2209-2215.
- 130) Miložičić, D. IEEE Computer Society 2022 Report. *Joint Seminar on Computer Science and Applied Mathematics*, **2012**.
- 131) Mine, Y. Recent advances in the understanding of egg white protein functionality. *Trends in Food Science & Technology*, **1995**, 6(7): 225-232.

- 132) Mithal, P. Design of experimental based evaluation of thermal performance of a flichip electronic assembly. *ASME EEP Proceedings*, **1996**, 18: 109-115.
- 133) Monaghan, J. and D. Brazil. Modeling the sub-surface damage associated with the machining of a particle reinforced MMC. *Computational Materials Science*, **1997**, 9(1): 99-107.
- 134) Moore, A. L. and L. Shi. Emerging challenges and materials for thermal management of electronics. *Materials Today*, **2014**, 17(4): 163-174.
- 135) Moore, G. E. Cramming more components onto integrated circuits. *Electronics*, **1965**, 38 (8): 114-117.
- 136) Morrow, C. and D. Lockner. Hayward fault rocks: Porosity, density and strength measurements, *US Department of the Interior, US Geological Survey*, **2001**.
- 137) Mueller, A. J., R. Bianco and R. W. Buckman. Evaluation of oxide dispersion strengthened (ODS) molybdenum and molybdenum–rhenium alloys. *International Journal of Refractory Metals and Hard Materials*, **2000**, 18(4): 205-211.
- 138) Mueller, B. and D. Kochan. Laminated object manufacturing for rapid tooling and patternmaking in foundry industry. *Computers in Industry*, **1999**, 39(1): 47-53.
- 139) Mühler, T., C. M. Gomes, J. Heinrich and J. Günster. Slurry-Based Additive Manufacturing of Ceramics. *International Journal of Applied*

- Ceramic Technology*, **2015**, 12(1): 18-25.
- 140) Ng, W. F., M. H. Wong and F. T. Cheng. Stearic acid coating on magnesium for enhancing corrosion resistance in Hanks' solution. *Surface and Coatings Technology*, **2010**, 204(11): 1823-1830.
- 141) Ngo, T. D., A. Kashani, G. Imbalzano, K. T. Q. Nguyen and D. Hui. Additive manufacturing (3D printing): A review of materials, methods, applications and challenges. *Composites Part B: Engineering*, **2018**, 143: 172-196.
- 142) Novich, B. and C. Sundback. Quickset Injection Moulding of High Performance Ceramics. *Ceramic Transactions*, **1991**, 26: 157-164.
- 143) O'Donnell, J., M. Kim and H.-S. Yoon. A review on electromechanical devices fabricated by additive manufacturing. *Journal of Manufacturing Science and Engineering*, **2017**, 139(1): 010801-10..
- 144) Olhero, S., G. Tari, M. Coimbra and J. Ferreira. Synergy of polysaccharide mixtures in gelcasting of alumina. *Journal of the European Ceramic Society*, **2000**, 20(4): 423-429.
- 145) Omatete, O. O., M. A. Janney and S. D. Nunn. Gelcasting: From laboratory development toward industrial production. *Journal of the European Ceramic Society*, **1997**, 17(2-3): 407-413.
- 146) Omatete, O. O., M. A. Janney and R. A. Strehlow. Gelcasting: a new ceramic forming process. *American Ceramic Society Bulletin*, **1991**, 70(10): 1641-1649.

- 147) Onbattuvelli, V., G. Purdy, G. Kim, S. Laddha and S. Atre. Bimodal powder mixture for the powder injection molding of SiC and AlN. *Nanotech*, **2010**, 1: 800-803.
- 148) Onbattuvelli, V. P., R. K. Enneti, S.-J. Park and S. V. Atre. The effects of nanoparticle addition on binder removal from injection molded aluminum nitride. *International Journal of Refractory Metals and Hard Materials*, **2013**, 36: 77-84.
- 149) Onbattuvelli, V. P., R. K. Enneti, S.-J. Park and S. V. Atre. The effects of nanoparticle addition on SiC and AlN powder–polymer mixtures: Packing and flow behavior. *International Journal of Refractory Metals and Hard Materials*, **2013**, 36: 183-190.
- 150) Palmer, J., B. Jokieli, C. Nordquist, B. Kast, C. Atwood, E. Grant, F. Livingston, F. Medina and R. Wicker. Mesoscale RF relay enabled by integrated rapid manufacturing. *Rapid Prototyping Journal*, **2006**, 12(3): 148-155.
- 151) Pease, R. F. and S. Y. Chou. Lithography and other patterning techniques for future electronics. *Proceedings of the IEEE*, **2008**, 96(2): 248-270.
- 152) Pecora, R. Dynamic light scattering: applications of photon correlation spectroscopy, *Springer Science & Business Media*, **2013**.
- 153) Pelletier, J. AlN: a solid Al<sup>+</sup> ion source. *Vacuum*, **1986**, 36(11-12): 977-980.



- 154) Peng, E., D. Zhang and J. Ding. Ceramic Robocasting: Recent Achievements, Potential, and Future Developments. *Advanced Materials*, **2018**, 30: 1-14.
- 155) Piqué, A. and D. B. Chrisey. Direct-write technologies for rapid prototyping applications: sensors, electronics, and integrated power sources, *Academic Press*, **2001**.
- 156) Prakash, K. S., T. Nancharaih and V. V. S. Rao. Additive Manufacturing Techniques in Manufacturing -An Overview. *Materials Today: Proceedings*, **2018**, 5(2, Part 1): 3873-3882.
- 157) Prime, R. B., H. E. Bair, S. Vyazovkin, P. K. Gallagher and A. Riga. Thermogravimetric analysis (TGA). *Thermal analysis of polymers: Fundamentals and Applications*, **2009**, 241-317.
- 158) Qiu, J.-Y., Y. Hotta, K. Watari and K. Mitsuishi. Enhancement of Densification and Thermal Conductivity in AlN Ceramics by Addition of Nano-Sized Particles. *Journal of the American Ceramic Society*, **2006**, 89(1): 377-380.
- 159) Quinn, G. D., B. T. Sparenberg, P. Koshy, L. K. Ives, S. Jahanmir and D. D. Arola. Flexural strength of ceramic and glass rods. *Journal of Testing and Evaluation*, **2009**, 37(3): 1-23.
- 160) Rahman, A. and R. Reif. Thermal analysis of three-dimensional (3-D) integrated circuits (ICs). *Proceedings of the Interconnect Technology Conference*, IEEE, **2001**, 157-159.

- 161) Saha, S., K. Srinivasan and P. Dutta. Studies on optimum distribution of fins in heat sinks filled with phase change materials. *Journal of Heat Transfer*, **2008**, 130(3): 034505.
- 162) Sahoo, S. K., M. K. Das and P. Rath. Application of TCE-PCM based heat sinks for cooling of electronic components: A review. *Renewable and Sustainable Energy Reviews*, **2016**, 59: 550-582.
- 163) Sarvar, F., D. C. Whalley and P. P. Conway. Thermal interface materials-A review of the state of the art. *Electronics Systemintegration Technology Conference*, IEEE, **2006**, 157-159 .
- 164) Sato, K., J. G. Li, H. Kamiya and T. Ishigaki. Ultrasonic dispersion of TiO<sub>2</sub> nanoparticles in aqueous suspension. *Journal of the American Ceramic Society*, **2008**, 91(8): 2481-2487.
- 165) Schramm, G. A practical approach to rheology and rheometry, *Haake Karlsruhe*, **1994**.
- 166) Schwartz, B. and D. Wilcox. Laminated ceramics. *Ceram Age*, **1967**, 83(6): 40-44.
- 167) Scrantom, C. Q. and J. C. Lawson. LTCC technology: where we are and where we're going. *Symposium on Technologies for Wireless Applications*, IEEE, **1999**, 193-200
- 168) Serafy, C., A. Bar-Cohen, A. Srivastava and D. Yeung. Unlocking the true potential of 3-d cpus with microfluidic cooling. *IEEE Transactions on Very Large Scale Integration (VLSI) Systems*, **2016**, 24(4): 1515-1523.

- 169) Sergent, J. E. and C. A. Harper. Hybrid microelectronics handbook, *McGraw-Hill Companies*, **1995**.
- 170) Shabalin, I. L. Ultra-High Temperature Materials I Carbon (Graphene/Graphite) and Refractory Metals. *Dordrecht, Springer*, **2014**
- 171) Shen, L., X. Xu, W. Lu and B. Shi. Aluminum nitride shaping by non-aqueous gelcasting of low-viscosity and high solid-loading slurry. *Ceramics International*, **2016**, 42(4), 5569-5574.
- 172) Shi, Y. and Y. Zhang. Simulation of random packing of spherical particles with different size distributions. *Materials Science & Processing*, **2008**, 92(3): 621-626.
- 173) Shields, J. A. and P. Lipetzky. Molybdenum applications in the electronics market. *JOM*, **2000**, 52(3): 37-39.
- 174) Shinzato, K. and T. Baba. A laser flash apparatus for thermal diffusivity and specific heat capacity measurements. *Journal of Thermal Analysis and Calorimetry*, **2001**, 64(1): 413-422.
- 175) Shorey, A. B. and R. Lu. Progress and application of through glass via (TGV) technology. *Pan Pacific Microelectronics Symposium (Pan Pacific)*, *IEEE*, **2016**, 1-6.
- 176) Singh, M., H. M. Haverinen, P. Dhagat and G. E. Jabbour. Inkjet printing—process and its applications. *Advanced Materials*, **2010**, 22(6): 673-685.
- 177) Skotnicki, T., J. A. Hutchby, T.-J. King, H.-S. Wong and F. Boeuf.

- The end of CMOS scaling: toward the introduction of new materials and structural changes to improve MOSFET performance. *IEEE Circuits and Devices Magazine*, **2005**, 21(1): 16-26.
- 178) Song, J. and J. Evans. On the machinability of ceramic compacts. *Journal of the European Ceramic Society*, **1997**, 17(14): 1665-1673.
- 179) Srivatsa, P., R. Baby and C. Balaji. Numerical investigation of PCM based heat sinks with embedded metal foam/crossed plate fins. *Numerical Heat Transfer, Part A: Applications*, **2014**, 66(10): 1131-1153.
- 180) Srivatsan, T. S., B. G. Ravi, M. Petraroli and T. S. Sudarshan. The microhardness and microstructural characteristics of bulk molybdenum samples obtained by consolidating nanopowders by plasma pressure compaction. *International Journal of Refractory Metals and Hard Materials*, **2002**, 20(3): 181-186.
- 181) Standard, A. F2792. 2012. Standard Terminology for Additive Manufacturing Technologies. ASTM International, **2012**.
- 182) Stephens, B., P. Azimi, Z. El Orch and T. Ramos. Ultrafine particle emissions from desktop 3D printers. *Atmospheric Environment*, **2013**, 79: 334-339.
- 183) Strandjord, A. J. G. 3D Printing of LTCC. *Advancing Microelectronics: Ceramic Thick & Thin Materials. NC, IMAPS - International Microelectronics Assembly and Packaging Society*, **2014**, 41:

p4.

- 184) Sturdivant, R. 5G Systems and Packaging Opportunities. *51st International Symposium on Microelectronics*. Pasadena, CA, **2018**, 1-5.
- 185) Sui, G. and M. C. Leu. Investigation of layer thickness and surface roughness in rapid freeze prototyping. *Journal of Manufacturing Science and Engineering*, **2003**, 125(3): 556-563.
- 186) Sukumaran, V., T. Bandyopadhyay, V. Sundaram and R. Tummala. Low-cost thin glass interposers as a superior alternative to silicon and organic interposers for packaging of 3-D ICs. *IEEE Transactions on Components, Packaging and Manufacturing Technology*, **2012**, 2(9): 1426-1433.
- 187) Sultan, S., Abdelhamid, H. N., Zou, X., & Mathew, A. P. (2019). CelloMOF: nanocellulose enabled 3D printing of metal–organic frameworks. *Advanced Functional Materials*, 29(2), 1805372.
- 188) Sun, C., N. Fang, D. Wu and X. Zhang. Projection micro-stereolithography using digital micro-mirror dynamic mask. *Sensors and Actuators A: Physical*, **2005**, 121(1): 113-120.
- 189) Sun, Y., S. Shimai, X. Peng, M. Dong, H. Kamiya and S. Wang. A method for gelcasting high-strength alumina ceramics with low shrinkage. *Journal of Materials Research*, **2014**, 29(2): 247-251.
- 190) Sundaram, V., Q. Chen, Y. Suzuki, G. Kumar, F. Liu and R. Tummala. Low-cost and low-loss 3D silicon interposer for high bandwidth

- logic-to-memory interconnections without TSV in the logic IC. *62nd Electronic Components and Technology Conference (ECTC), IEEE, 2012*, 292-297.
- 191) Sunohara, M., T. Tokunaga, T. Kurihara and M. Higashi (2008). Silicon interposer with TSVs (Through Silicon Vias) and fine multilayer wiring. *58th Electronic Components and Technology Conference, ECTC., IEEE, 2008*, 847-852.
- 192) Sweetland, M. and Lienhard, J.H. Active thermal control of distributed parameter systems with application to testing of packaged IC devices. *Transactions-American Society of Mechanical Engineers Journal of Heat Transfer, 2003*, 125(1), 164-174.
- 193) Tabilo-Munizaga, G. and G. V. Barbosa-Cánovas. Rheology for the food industry. *Journal of Food Engineering, 2005*, 67(1): 147-156.
- 194) Tan, F. and C. Tso (2004). "Cooling of mobile electronic devices using phase change materials." *Applied Thermal Engineering, 2004*, 24(2): 159-169.
- 195) Tang, H.-H. and H.-C. Yen. Slurry-based additive manufacturing of ceramic parts by selective laser burn-out. *Journal of the European Ceramic Society, 2015*, 35(3): 981-987.
- 196) Tang, Y., Z. Ji, C. Jia, B. Karima, Y. Zhang and Z. Zhang. Effect of particle size on non-aqueous gel-casting process for copper powder. *Journal of Sol-Gel Science and Technology, 2016*, 79(3): 530-534.

- 197) Taur, Y. CMOS design near the limit of scaling. *IBM Journal of Research and Development*, **2002**, 46(2.3): 213-222.
- 198) Taylor, K. and C. Lenie. Some properties of aluminum nitride. *Journal of the Electrochemical Society*, **1960**, 107(4): 308-314.
- 199) Travitzky, N., A. Bonet, B. Dermeik, T. Fey, I. Filbert-Demut, L. Schlier, T. Schlordt and P. Greil. Additive Manufacturing of Ceramic-Based Materials. *Advanced Engineering Materials*, **2014**, 16(6): 729-754.
- 200) Tritt, T. M.. Thermal conductivity: theory, properties, and applications, *Springer Science & Business Media*, **2005**.
- 201) Trybula, W. Technology acceleration and the economics of lithography (cost containment and roi). *Future Fab Intl*, **2003**, 14(19).
- 202) Tummala, R. and V. Sundaram. Impact of 3D ICs with TSV is profound but complex and costly-is there a better way? *Chip Scale Rev.*, **2011**, 31-32.
- 203) Tyagi, S. (2007). Moore's Law: A CMOS Scaling Perspective. 2007 *14th International Symposium on the Physical and Failure Analysis of Integrated Circuits*, **2007**
- 204) V. Sundaram, R. R. T. Interposer Technology. Handbook of 3D Integration: 3D Process Technology. *Weinheim, Germany, Wiley-VCH*, **2014**, 41-63.
- 205) Veitl, A. and A. Dohn. Ceramic simplifies heat dissipation. *ATZ Elektronik Worldwide*, **2010**, 5(6): 12-15.

- 206) W.T Minehan, D. B., K. Adams, T. Shafer. High Temperature Co-Fired Ceramic (HTCC) Packages. *Advancing Microelectronics. USA, IMAPS - International Microelectronics Assembly and Packaging Society*, **2016**, 43: 16-19.
- 207) Wang, Q., B. Zhang, M. Qu, J. Zhang and D. He. Fabrication of superhydrophobic surfaces on engineering material surfaces with stearic acid. *Applied Surface Science*, **2008**, 254(7): 2009-2012.
- 208) Wang, X., R. Wang, Y. Feng, D. Zhang and C. Peng. Postcasting Contraction: Improving the Density of Gelcast Nanoparticle Green Bodies with Heated Liquid Desiccants. *Journal of the American Ceramic Society*, **2015**, 98(6): 1706-1710.
- 209) Wang, Y., R. Han, X. Liu and J. Kang. The challenges for physical limitations in Si microelectronics. *5th International Conference on Solid-State and Integrated Circuit Technology, IEEE*, **1998**, 25-30.
- 210) Wang, Y., W. Wang, L. Zhong, J. Wang, Q. Jiang and X. Guo. Superhydrophobic surface on pure magnesium substrate by wet chemical method. *Applied Surface Science*, **2010**, 256(12): 3837-3840.
- 211) Watari, K., H. J. Hwang, M. Toriyama and S. Kanzaki. Low-Temperature Sintering and High Thermal Conductivity of YLiO<sub>2</sub>-Doped AlN Ceramics. *Journal of the American Ceramic Society*, **1996**, 79(7): 1979-1981.
- 212) Watari, K., H. J. Hwang, M. Toriyama and S. Kanzaki. Effective



- sintering aids for low-temperature sintering of AlN ceramics. *Journal of Materials Research*, **1999**, 14(04): 1409-1417.
- 213) Watari, K., A. Tsuzuki and Y. Torii. Effect of rare-earth oxide addition on the thermal conductivity of sintered aluminium nitride. *Journal of Materials Science Letters*, **1992**, 11(22): 1508-1510.
- 214) White, J. L. and H. B. Dee. "Flow visualization for injection molding of polyethylene and polystyrene melts." *Polymer Engineering & Science*, **1974**, 14(3): 212-222.
- 215) Wicker, R. B., F. Medina and C. Elkins. Multiple material micro-fabrication: extending stereolithography to tissue engineering and other novel applications. *Proceedings of 15th Annual Solid Freeform Fabrication Symposium, Austin, TX*, **2004**, 754-764.
- 216) Wojtyła, S., Klama, P., and Baran, T, Is 3D printing safe? Analysis of the thermal treatment of thermoplastics: ABS, PLA, PET, and nylon. *Journal of Occupational and Environmental Hygiene*. **2017**, 14(6), D80-D85.
- 217) Wu, S.-T., J. H. Lau, H.-C. Chien, J.-F. Hung, M.-J. Dai, Y.-L. Chao, R.-M. Tain, W.-C. Lo and M.-J. Kao. Ultra low-cost through-silicon holes (TSHs) interposers for 3D IC integration SiPs. *62nd Electronic Components and Technology Conference (ECTC), IEEE*, **2012**, 1618-1624.
- 218) Xie, Z.-P., Y.-L. Chen and Y. Huang. A novel casting forming for ceramics by gelatine and enzyme catalysis. *Journal of the European Ceramic Society*, **2000**, 20(3): 253-257.

- 219) Xie, Z., J. Yang, D. Huang, Y. Chen and Y. Huang. Gelation forming of ceramic compacts using agarose. *British Ceramic Transactions*, **1999**, 98(2): 58-61.
- 220) Yang, H., J. C. Lim, Y. Liu, X. Qi, Y. L. Yap, V. Dikshit, W. Y. Yeong and J. Wei. Performance evaluation of projet multi-material jetting 3D printer. *Virtual and Physical Prototyping*, **2017**, 12(1): 95-103.
- 221) Yang, S. and Christou, A. Failure model for silver electrochemical migration. *IEEE Transactions on Device and Materials Reliability*, **2007**, 7(1), 188-196.
- 222) Yang, Y.-T. and Y.-H. Wang. Numerical simulation of three-dimensional transient cooling application on a portable electronic device using phase change material. *International Journal of Thermal Sciences*, **2012**, 51: 155-162.
- 223) Yen, H. C. Experimental studying on development of slurry-layer casting system for additive manufacturing of ceramics. *The International Journal of Advanced Manufacturing Technology*, **2015**, 77(5-8): 915-925.
- 224) Yijun, Y. and Q. Tai. Effect of  $Y_2O_3$  and  $Dy_2O_3$  on Microstructure and Mechanical Behaviors of Aluminum Nitride Ceramics. *Journal of Rare Earths*, **2006**, 24(1): 239-243.
- 225) Yijun, Y. and Q. Tai. "Effects of Behaviors of Aluminum Nitride Ceramics with Rare Earth Oxide Additives." *Journal of Rare Earths*, **2007**, 25: 58-63.

- 226) Yim, M. J., R. Strode, J. Brand, R. Adimula, J. J. Zhang and C. Yoo. Ultra thin PoP top package using compression mold: Its warpage control. *61st Electronic Components and Technology Conference (ECTC), IEEE, 2011*, 1141-1146.
- 227) Yin, S., K. J. Tseng and J. Zhao. Design of AlN-based micro-channel heat sink in direct bond copper for power electronics packaging. *Applied Thermal Engineering, 2013*, 52(1): 120-129.
- 228) Yoon, S. W., P. Tang, R. Emigh, Y. Lin, P. C. Marimuthu and R. Pendse. Fanout flipchip eWLB (embedded Wafer Level Ball Grid Array) technology as 2.5 D packaging solutions. *63rd Electronic Components and Technology Conference, IEEE, 2013*, 1855-1860.
- 229) Young, A. C., O. O. Omatete, M. A. Janney and P. A. Menchhofer. Gelcasting of alumina. *Journal of the American Ceramic Society, 1991*, 74(3): 612-618.
- 230) Yu, A., N. Khan, G. Archit, D. Pinjala, K. C. Toh, V. Kripesh, S. W. Yoon and J. H. Lau. Fabrication of silicon carriers with TSV electrical interconnections and embedded thermal solutions for high power 3-D package. *58th Electronic Components and Technology Conference, IEEE, 2008*, 24-28.
- 231) Yu, H., J. Liu, W. Zhang and S. Zhang. Ultra-low sintering temperature ceramics for LTCC applications: a review. *Journal of Materials Science: Materials in Electronics, 2015*, 26(12): 9414-9423.

- 232) Yuan, H.-y., Jia, C.-c. Wang, Y.-h. Chang, X.-x. Zhang, B. Karima and Wang, Z.-l. Effect of gelcasting conditions on quality of porous Al–Cu alloy. *Transactions of Nonferrous Metals Society of China*, **2015**, 25(6): 2018-2026.
- 233) Yung, K. and H. Liem. Enhanced thermal conductivity of boron nitride epoxy-matrix composite through multi-modal particle size mixing. *Journal of Applied Polymer Science*, **2007**, 106(6): 3587-3591.
- 234) Yuping, Z., J. Dongliang and P. Greil. Tape casting of aqueous Al<sub>2</sub>O<sub>3</sub> slurries." *Journal of the European Ceramic Society*, **2000**, 20(11): 1691-1697.
- 235) Zagorac, J., D. Zagorac, D. Jovanović, J. Luković and B. Matović. Ab initio investigations of structural, electronic and mechanical properties of aluminum nitride at standard and elevated pressures. *Journal of Physics and Chemistry of Solids*, **2018**, 122: 94-103.
- 236) Zhang, G., H. Chen and H. Zhou. Additive manufacturing of green ceramic by selective laser gasifying of frozen slurry. *Journal of the European Ceramic Society*, **2017**, 37(7): 2679-2684.
- 237) Zhang, K., Y. Chai, M. M. F. Yuen, D. Xiao and P. Chan. Carbon nanotube thermal interface material for high-brightness light-emitting-diode cooling. *Nanotechnology*, **2008**, 19(21): 215706.
- 238) Zhang, Y. and M. Bakir. Independent interlayer microfluidic cooling for heterogeneous 3D IC applications. *Electronics Letters*, **2013**, 49(6): 404-

406.

- 239) Zhang, Y., F. Di, Z.-Y. He and X.-C. Chen. Progress in joining ceramics to metals. *International Journal of Iron and Steel Research*, **2006**, 13(2): 1-5.
- 240) Zheng, L., Q. An, Y. Xie, Z. Sun and S.-N. Luo. Homogeneous nucleation and growth of melt in copper. *The Journal of Chemical Physics*, **2007**, 127(16): 164503.
- 241) Zhirnov, V. V., J. A. Hutchby, G. Bourianoffls and J. E. Brewer. Emerging research logic devices. *IEEE Circuits and Devices Magazine*, **2005**, 21(3): 37-46.
- 242) Zocca, A., P. Colombo, C. M. Gomes and J. Günster. Additive manufacturing of ceramics: issues, potentialities, and opportunities. *Journal of the American Ceramic Society*, **2015**, 98(7): 1983-2001.
- 243) Zocca, A., C. M. Gomes, T. Mühler and J. Günster (2014). "Powder-bed stabilization for powder-based additive manufacturing." *Advances in Mechanical Engineering*, **2014**,1-6 .